THE UNIVERSITY OF CHICAGO

TOWARD A PHYSICAL UNDERSTANDING OF THE DYNAMIC CIRCUMGALACTIC
MEDIUM

A DISSERTATION SUBMITTED TO
THE FACULTY OF THE DIVISION OF THE PHYSICAL SCIENCES
IN CANDIDACY FOR THE DEGREE OF
DOCTOR OF PHILOSOPHY

DEPARTMENT OF ASTRONOMY AND ASTROPHYSICS

BY
CUNCHENG CHEN

CHICAGO, ILLINOIS
AUGUST 2024

TABLE OF CONTENTS

v

LIST OF FIGURES

LIST OF TABLES

ACKNOWLEDGMENTS

extends to the administrative staff of the University of Chicago Astronomy & Astrophysics Department for their dedication to fostering a supportive and thriving community. Special thanks to Letty Rebeles and Jennifer Smith, who not only provided me with abundant tea bags and emotional support over the years but also ensured that I was on track at every checkpoint of this journey.

Moreover, the support and friendships I've gained while being in Chicago have been as integral to my life as my scientific pursuits, if not more so. I cannot be more grateful for the serendipity that brought our lives together. In particular, thank you Alex Alarcon, Amy Tang, Andrew Neil, Anowar Shajib, Clarke Esmerian, Dhayaa Anbajagane, Emily Simon, Giulia Giannini, Gourav Khullar, Jason Poh, Jose Maria Ezquiaga, Judit Prat, Junran Yang, Katie Harrington, Lucas Secco, Maya Mallaby-Kay, Nora Shipp, Phil Mansfield, Thao Do, and Vishesh Jain (in alphabetical order because each of you holds equal importance in my life in your unique way), for always being there for me, for making me a better person than I was, and for making this period of my life not only worthwhile but truly unforgettable.

Finally, I want to thank my mom, who tolerated me being thousands of miles away from home despite the mysteries of my research and why on earth I'd want to spend so much time in school to attain a PhD. The absence of a return home for four years during the COVID pandemic weighs heavily on me. Now, with international travel returning to normal and my PhD completed, I look forward to making up for lost time and sharing my life with you more intimately. Your patience, understanding, and love have been the bedrock of my journey and will continue to give me strength as I move on to the next stage of my career. And speaking of family, I must not forget to thank Jenny, my crazy feisty cat (not my words, just ask anyone that has ever met you). Your endearing yet occasionally dangerous presence and unparalleled prowess in pest control have been a constant source of warmth and comfort to my days.

ABSTRACT

The circumgalactic medium (CGM) is the outermost, gaseous envelope of a galaxy, spanning beyond the visible stellar disk and dominates the galaxy's baryonic mass. This expansive gas reservoir plays an influential role in cosmic structure formation and records critical information about a galaxy's past and ongoing interactions with the surrounding environment. Understanding the detailed physical properties of the CGM is a vital step to improving the current galaxy evolution theories. In particular, evidence has been mounting that the ebbs and flows of baryonic matter in the CGM play a crucial role in driving galaxy formation, maturation, and eventual quiescence. While recent CGM surveys have significantly tightened constraints on the spatial extent and column density of the gas, our direct observations of gas motions remain notably limited. In this thesis, I leveraged the exquisite sensitivity of the latest generation of integral-field spectrographs to provide empirical constraints on two key dynamical processes in the CGM: galactic superwinds driven by star-forming galaxies and the subsonic turbulent energy cascade in the low-density halo environment. Taking advantage of the magnifying power of strong gravitational lensing and employing Lyman-alpha radiative transfer models, I recovered highly organized velocity fields across galactic outflow regions at scales of ≈ 5–30 kpc surrounding star-forming galaxies at $z \approx 3$–4 (Chapter 2). Utilizing two-point statistical analyses derived from the spatially-resolved kinematic measures, I uncovered the subsonic nature of gas motions at scales of ≈ 10–60 kpc in the quasar CGM at $z \approx 0.5$–1 (Chapters 3 and 4). These empirical results shed light on the intimate connection between galaxies and their surrounding CGM, illuminating the role of star-formation/AGN feedback and galaxy environments on the evolution of the baryon cycle over cosmic time.

CHAPTER 1

INTRODUCTION

1.1   Motivation: the CGM and galaxy evolution

The motivation for this thesis is rooted in the quest to understand galaxy evolution. During the ~ 13 billion years between the formation of the first galaxies and the present day, galaxies have undergone drastic evolution in their internal properties (e.g., Strom et al., 2017; Tacconi et al., 2018). This evolution is paralleled by a steep rise in the star formation rate density in the early Universe at $z \gtrsim 2$, which rapidly declines from $z \approx 2$ to $z = 0$ (e.g., Behroozi et al., 2013). As we look around in the neighborhood of the Milky Way now, we notice that galaxies as a population tend to form new stars at a slower rate and exhibit more quiescent, well-ordered kinematic features compared with their high-redshift counterparts (e.g., Whitaker et al., 2012; Wisnioski et al., 2015). Understanding the full complexity of galaxy evolution throughout cosmic history requires a multifaceted approach, and tracing the evolution of the circumgalactic medium (CGM) presents a unique window into the baryon cycle that profoundly influences galaxy properties.

As the pivotal juncture bridging galaxies and the diffuse intergalactic medium (IGM), the CGM plays a critical role in a galaxy's evolution trajectory. As illustrated in Figure 1.1 (Newman et al., 2019), gas infalls from both the CGM and the IGM replenish the gas reservoir, fueling star formation and sustaining the growth of galaxies. Meanwhile, energetic feedback from stars and active galactic nuclei eject mass, momentum, and heavy metals into the lower-density halo environment, suppressing star formation activities. Through the flows of materials and energy, the formation and evolution of galaxies are intimately connected to the baryon cycle.

Gas falls
into galaxies
from the
CGM/IGM

$M_{halo} = 10^{12.0} M_{\odot}$

van de Voort + 2011

Stars & black
holes form

NASA/ESA

Galactic structures
emerge: disks,
clumps, and bulges

AURA/STScI/NASA

The Baryon Cycle   **Galaxy Evolution**

ESA

NASA

Stars & BHs
inject energy,
momentum,
and metals
into the ISM

NASA

Gas flow out
of galaxies
into the
CGM/IGM

Feedback
and dynamical evolution
change the internal
distribution of metals,
dust, and stars

Figure 1.1: Illustration of the baryon cycle and its connection to galaxy evolution, as presented in Newman et al. (2019). Gas infalls fuel star formation activities that sustain the growth of galaxies, while energetic feedback from black holes and massive stars ejects energy and materials back into the halo environments, suppressing the formation of new stars. These exchanges of mass and momentum are present in every stage of galaxy evolution, dictating a galaxy's trajectory through formation, maturation, and eventual quiescence. Figure reproduced with permission.

1.2 Direct detection of CGM emission with IFSs

Outside of the interstellar medium (ISM), the baryonic matter in the CGM consists of tenuous gas with a number density as low as $\sim 10^{-4}$ cm^{-3} (e.g., Tumlinson et al., 2017; Donahue & Voit, 2022). Due to the difficulty of detecting the low-density gas in emission, studies of the baryon cycle have largely relied on absorption-line spectroscopy (e.g., Chen, 2017; Rudie et al., 2019). However, without knowing the spatial distribution of the gas, uncertainties remain in connecting gas to galaxies. For example, at $z \gtrsim 1$, the ubiquitous presence of outflows in star-forming galaxies is demonstrated by the observed blue-shifted self-absorption that extends up to $\gtrsim 1000$ km/s in the spectra of these galaxies (e.g., Weiner et al., 2009; Rubin et al., 2010; Steidel et al., 2010; Heckman & Best, 2014). While these "down-the-barrel" observations are adept at uncovering fast-moving outflows, it is not clear whether the outflowing gas is located near star-forming regions or at large galactic distances beyond the stellar disks, thus hindering a robust characterization of the wind launching mechanism and the associated energetics.

To probe the spatial distribution of the CGM gas, traditional methods – such as narrow-band imaging and long-slit spectroscopy – require long exposure times in order to reveal the faint emissions (e.g., Rauch et al., 2008; Cantalupo et al., 2014). For example, with a total on-target science exposure of 10 hours on the 10-m Keck telescope and using a narrowband filter customized to detect Lyα emission at $z \approx 2.3$, Cantalupo et al. (2014) uncovered the extended CGM emission up to a scale of ~ 500 kpc around a luminous quasar (see Figure 1.2). However, such long exposures prohibit systematic detection of CGM emission for a sizable sample. In addition, narrowband imaging lacks the crucial kinematic information that significantly aids in downstream analyses.

In this context, the advent of high-throughput integral field spectrographs (IFSs) such as the Multi Unit Spectroscopic Explorer (MUSE) on the Very Large Telescopes (VLT) and the Keck Cosmic Web Imager (KCWI) on the Keck Telescopes has revolutionized investigations

3
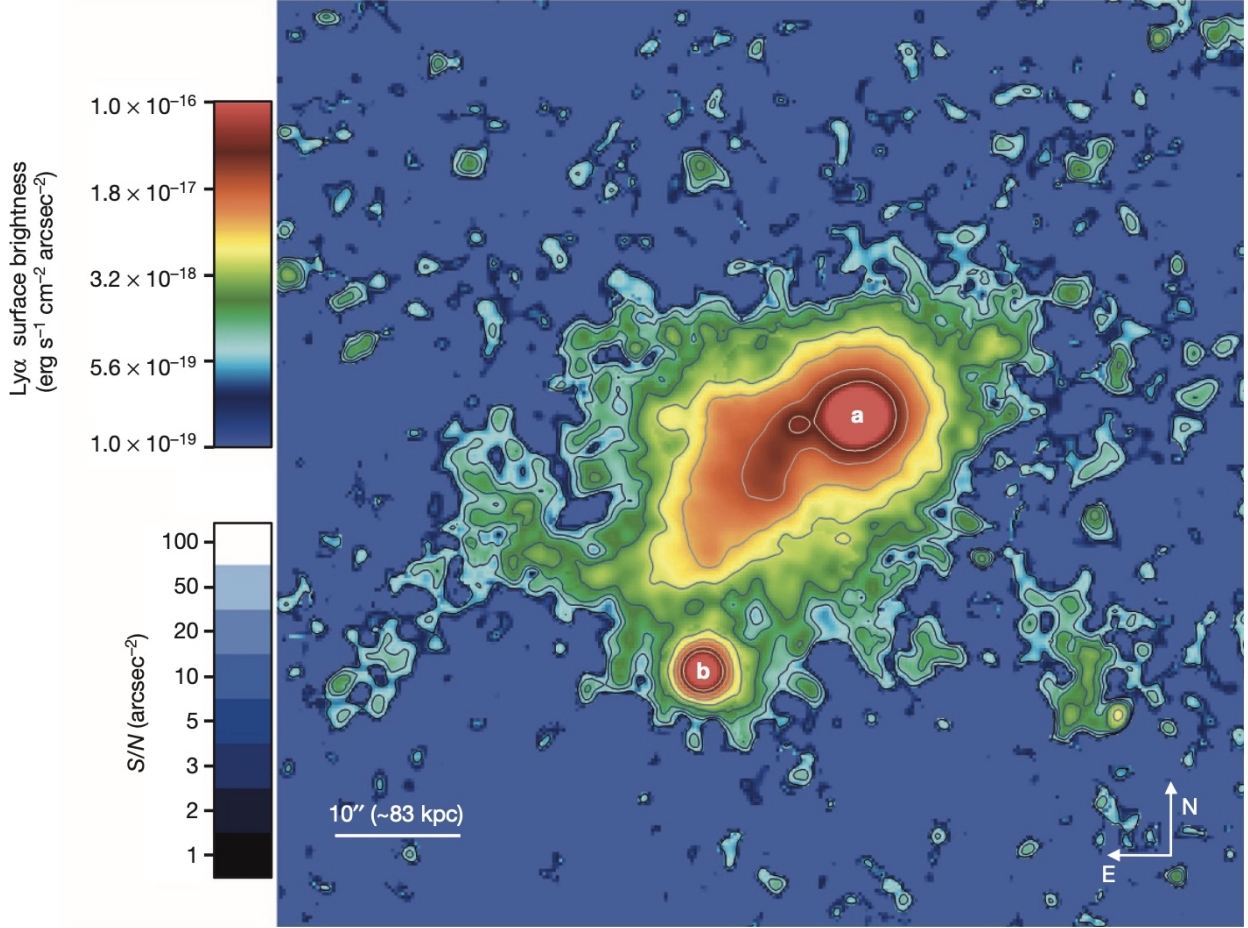
Figure 1.2: A ~ 500 kpc Lyα nebula at $z \approx 2.3$, as presented in Cantalupo et al. (2014). The detection was achieved with a total exposure time of 10 hours on Keck, using a custom narrowband filter. Figure reproduced with permission.

of the CGM by directly mapping out the faint CGM emission in the position and velocity space with unprecedented sensitivity (e.g., Bacon et al., 2010; Wisotzki et al., 2016; Borisova et al., 2016; Morrissey et al., 2018). For example, with an average exposure time as short as ≈ 45 minutes with MUSE, Arrigoni Battaia et al. (2019) found that extended Lyα emission is ubiquitous around quasars at $z \gtrsim 3$, as shown in Figure 1.3. Some of the Lyα nebulae detected by MUSE are as extended as the nebula discovered by Cantalupo et al. (2014) but with a much shorter exposure time than required in narrowband imaging.
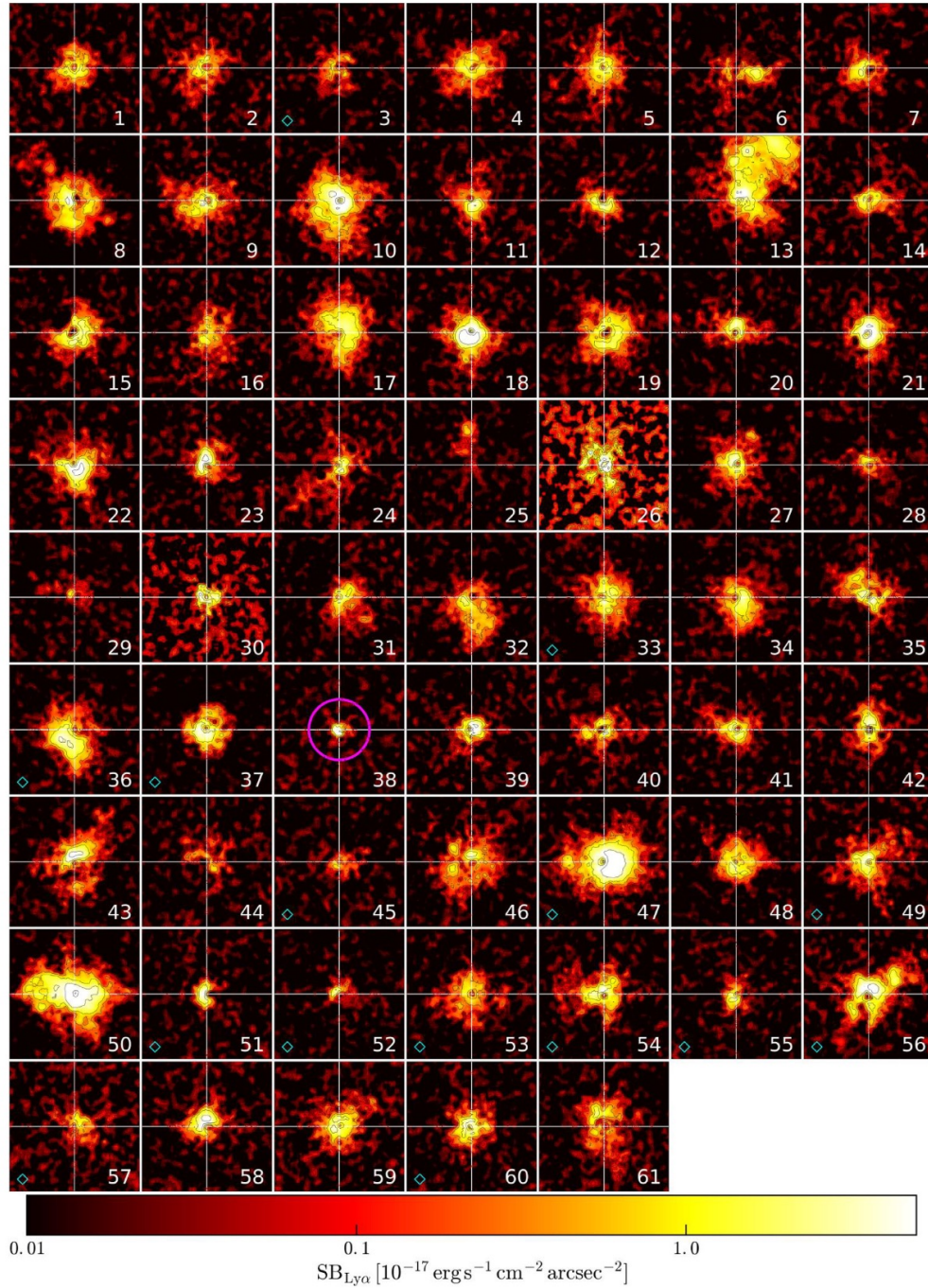
Figure 1.3: The QSO MUSEUM sample of 61 extended Lyα nebulae surrounding $z \sim 3$ quasars (Arrigoni Battaia et al., 2019). The emission is revealed by VLT/MUSE with an average exposure time of ≈ 45 minutes.
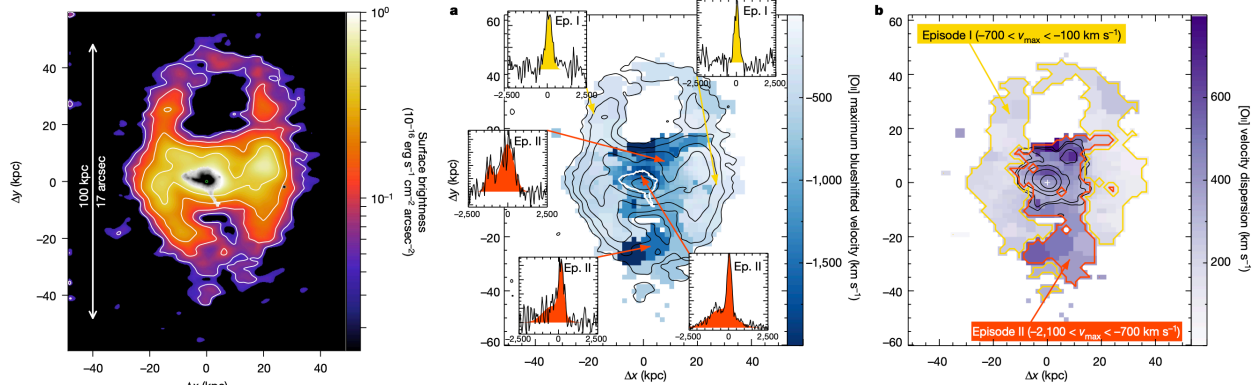
Figure 1.4: The "Makani" nebula at $z = 0.459$, where the spatially-resolved [O II] $\lambda\lambda\, 3727, 3729$ emission reveals two episodic galactic outflows driven by starbursts Rupke et al. (2019). Figure reproduced with permission.

1.3 Detailed insights into the dynamics of the CGM

Compared with absorption spectroscopy, IFS observations provide valuable morpho-kinematic constraints for resolving detailed density and velocity structures of the gas. At $z < 1.4$, extended gas is revealed through non-resonant lines (e.g., [OII], [OIII], Hα) in the optical window, enabling spatially-resolved measurements of the underlying velocity field. For example, an extended ~ 100-kpc-scale galactic outflow at $z = 0.459$ reported by Rupke et al. (2019) showcased the power of IFS data, where the spatially-resolved, blue-shifted [O II] $\lambda\lambda\, 3727, 3729$ line and its varying line width across the nebula indicated two episodic outflows driven by starbursts (see Figure 1.4). This nebula, dubbed "Makani", was observed by Keck/KCWI.

At higher redshifts, spatially-resolved emission from the CGM of high-redshift galaxies is pre-dominantly revealed through the hydrogen Lyα line (e.g., Leclercq et al., 2017; Arrigoni Battaia et al., 2019). This is because Lyα is the strongest emission line expected in photoionized gas at a temperature $T \sim 10^4$ K, and is also conveniently redshifted into the optical spectral window for sources at $z \approx 2$–7 and therefore accessible on the ground. However, while the extended Lyα emission unambiguously reveals the presence of tenuous gas surrounding these distant galaxies, interpreting the Lyα line is complicated by its resonant

nature (e.g., Cantalupo, 2017; Dijkstra, 2017). Constraining the physical properties of the line-emitting gas (e.g., density and velocity) with high accuracy therefore requires detailed modeling of the resonant process of Lyα photons.

In this thesis, I will present studies that robustly characterize the dynamics of the CGM. Leveraging the recent advent of high-throughput IFSs, I have built the first spatially-resolved constraints on galactic outflows and CGM turbulence in distant galaxies. Using Lyα, [O II], and [O III] emission lines as tracers, I initiated and led investigations of both non-active and active gaseous halos over a wide range of redshifts between $z \approx 0.5$ and $z \approx 4$. Chapter 2 presents a new approach of using gravitational lensing to trace galactic outflows directly – from their launching site near star-forming regions to large distances reaching over 30 kpc away from the galaxies. This innovative approach uncovered prominent Lyα nebulae surrounding two galaxy groups at redshifts $z = 3.038$ and $z = 3.754$, directly addressing the lack of spatial information in "down-the-barrel" observations. With Monte Carlo radiative transfer models, I conducted a careful Lyα profile analysis and recovered highly organized velocity fields across the nebulae. Chapters 3 and 4 present the first direct empirical constraints on CGM turbulence using an ensemble sample of eight quasar nebulae at $z \approx 0.5$–1. By measuring the velocity structure functions (VSFs) of these nebulae based on contiguous [O II] and [O III] emission detected by VLT/MUSE, I quantified the scale-dependent velocity variance in the quasar CGM at scales of ≈ 10–60 kpc. These measurements of quasar nebulae VSFs pioneer the use of IFS observations in spatially-resolved research on CGM dynamics, revealing detailed kinematic properties of the gas. Finally, Chapter 5 concludes this thesis and discusses ongoing as well as future observational efforts.

CHAPTER 2

RESOLVED GALACTIC SUPERWINDS RECONSTRUCTED AROUND THEIR HOST GALAXIES AT $z > 3$

This chapter is a modified version of Chen et al. (2021), published in the Monthly Notices of the Royal Astronomical Society, Volume 504, Issue 2, pp.2629-2657.

2.1 Introduction

The formation and evolution of galaxies are intimately connected to the properties of the circumgalactic medium (CGM). Characterizing the interactions between galaxies and their surrounding gas, such as gas infall and outflows, is a critical step toward improving our still patchy understanding of the life cycles of baryons and galaxy evolution over cosmic time. But because of the low-density nature of the CGM, studying such tenuous gas has historically relied on absorption spectroscopy along individual QSO sightlines. Over the past few decades, absorption-line studies have yielded sensitive, mostly one-dimensional constraints on the gas density, temperature, metallicity and kinematics in the circumgalactic space (see the review by Chen, 2017; Tumlinson et al., 2017; Rudie et al., 2019, and references therein). However, uncertainties remain in connecting gas to galaxies in the absence of a spatially-resolved two-dimensional map of the gas. To access the spatial information of gas distribution in the CGM, direct detections of the tenuous gas in emission provide a promising avenue. The hydrogen Lyα line, being the strongest emission line expected of photo-ionized gas at a temperature $T \sim 10,000$ K, provides a sensitive probe of the tenuous CGM (e.g., Osterbrock & Ferland, 2006; Draine, 2011). At $z \approx 2$–7, the Lyα line at 1215 Å is conveniently redshifted into the atmospheric transmission window and becomes accessible on the ground. In the past two decades, narrow-band imaging and deep long-slit spectroscopic observations have successfully revealed extended line-emitting gas around galaxies

(e.g., Adelberger et al., 2006; Rauch et al., 2008, 2011; Steidel et al., 2011; Xue et al., 2017) and QSOs (e.g., Hennawi et al., 2009; Cantalupo et al., 2012, 2014). Those observations have shed light on several important physical processes in the CGM, such as the ubiquity of large-scale gas flows on 10–100 physical kpc (pkpc) scales at high redshifts (e.g., Rauch et al., 2016) and the non-trivial contribution of star-forming galaxies to reionization (e.g., Dijkstra, 2014; Matthee et al., 2018).

The recent advent of high-throughput, wide-field optical integral field spectrographs (IFSs) on large ground-based telescopes, such as the Multi Unit Spectroscopic Explorer (MUSE) on the Very Large Telescopes (VLT) (Bacon et al., 2010) and the Keck Cosmic Web Imager (KCWI) on the Keck Telescopes (Morrissey et al., 2018) has brought a significant breakthrough in systematically uncovering extended Lyα emission in typical, low-mass galaxies as well as QSOs at $z \approx 2 - 7$ (e.g., Wisotzki et al., 2016, 2018; Borisova et al., 2016; Leclercq et al., 2017; Cai et al., 2017, 2019; Arrigoni Battaia et al., 2019). These sensitive IFS observations have uncovered extended Lyα emission out to > 20 times the spatial extent of the stellar continuum, and revealed key insights into the physical nature of these extended Lyα sources. For example, significant spatial variations of Lyα line profiles are directly observed within a single line-emitting nebula (e.g., Rauch et al., 2013; Vanzella et al., 2017; Erb et al., 2018). In addition, there exists a positive correlation between the full-width-at-half-maximum (FWHM) of the Lyα line and the continuum UV brightness of the associated star-forming galaxies (e.g., Wisotzki et al., 2018; Leclercq et al., 2020), indicating an intimate connection between the origin of the Lyα photons and star-forming activities (e.g., Dijkstra & Kramer, 2012; Cantalupo, 2017).

Multiple processes can lead to Lyα emission in the CGM, such as fluorescence powered by ionizing photons from star-forming regions or active galactic neuclei (AGN), cooling radiation, and scattering of Lyα photons by mostly neutral hydrogen gas (e.g., Hogan & Weymann, 1987; Gould & Weinberg, 1996; Cantalupo et al., 2005; Kollmeier et al., 2010;

Faucher-Giguère et al., 2010; Hennawi & Prochaska, 2013). Disentangling different processes that contribute to the observed Lyα signal is challenging due to the resonant scattering nature of Lyα photons, especially when Lyα is the only observable line feature from the emission regions. At the same time, the detailed double-peak profiles of spectrally-resolved Lyα lines provide a sensitive probe of the underlying gas kinematics. It is expected that Lyα emission originating in infalling and outflowing medium will result in blue-enhanced and red-enhanced peak, respectively (e.g., Dijkstra, 2017, and references therein). This has motivated increasingly sophisticated Monte Carlo radiative transfer models that incorporate different gas geometry and kinematics to accurately track Lyα photon scattering and infer the physical properties of the gaseous clouds (e.g., Dijkstra et al., 2006; Verhamme et al., 2006; Hansen & Oh, 2006; Laursen et al., 2009; Schaerer et al., 2011; Gronke et al., 2015).

These Monte Carlo Lyα radiative transfer codes can generally reproduce the observed Lyα line width based on a combination of thermal broadening and bulk motions, but significant discrepancies are also seen between observations and model predictions (Verhamme et al., 2008; Kulas et al., 2012; Orlitová et al., 2018). Such discrepancies have both theoretical and observational implications. Theoretically, there is a lot of room for better capturing the physical processes in radiative transfer simulations, such as a realistic treatment of dust attenuation and gas clumpiness (e.g., Laursen et al., 2009; Dijkstra & Kramer, 2012; Gronke et al., 2016). Observationally, as Lyα photons are scattered both in spectral and spacial dimensions, it is critical to obtain observations with not only high spectral resolution, but also high spatial resolution to provide the best constraints on the source environment.

Strong gravitational lensing provides sharpened images of the high-redshift Universe via an enhanced spatial resolution of highly magnified images of distant galaxies (e.g., Coe et al., 2013) and recently individual, luminous high redshift stars (Kelly et al., 2018). Massive galaxy and cluster lenses have revealed detailed properties of lensed background sources down to sub-kpc or even as detailed as tens of pc scales (e.g., Livermore et al., 2012; Bordoloi

et al., 2016; Johnson et al., 2017; Berg et al., 2018; Florian et al., 2020). Multiply-lensed QSOs and extended, lensed arcs of bright background sources have been used to spatially resolve the diffuse CGM in absorption spectroscopy (Rauch et al., 2002; Chen et al., 2014; Zahedy et al., 2016; Rubin et al., 2018; Lopez et al., 2018; Mortensen et al., 2020). Several gravitationally-lensed Lyα emitting nebulae have also been reported, in which the enhanced spatial resolution has aided to reveal the underlying physical environment of the source in greater details (Swinbank et al., 2007; Patrício et al., 2016; Caminha et al., 2017; Claeyssens et al., 2019; Erb et al., 2019).

Here we present a detailed analysis of two gravitationally-lensed Lyα emitting nebulae, System A at $z = 3.038$ (Figure 2.1) and System B at $z = 3.754$ (Figure 2.2), detected in deep MUSE observations of the field around the strong lensing cluster, MACS 1206−0847 at $z = 0.44$ (hereafter MACS 1206). Both nebulae are multiply-lensed to form giant tangential arcs in the image plane around the Einstein radius of the foreground cluster, and both exhibit a double-peaked Lyα profile. In particular, the serendipitous alignment of the nebula in System A results in an extended low surface brightness arc of $\mathrm{SB}_{\mathrm{Ly}\alpha} \approx 3 \times 10^{-18}\,\mathrm{erg\,s^{-1}\,cm^{-2}\,arcsec^{-2}}$ and $\approx 1'$ in length, comprising three contiguous lensed images (Caminha et al., 2017), while System B forms an arc of $\approx 15''$ in length with high surface brightness peaks exceeding $\mathrm{SB}_{\mathrm{Ly}\alpha} \approx 2 \times 10^{-17}\,\mathrm{erg\,s^{-1}\,cm^{-2}\,arcsec^{-2}}$. In addition, the Ly$\alpha$ emitting region in System A consists of two separate nebulae, detached from a group of three continuum sources with one being an $\approx 1.6\,L_*$ galaxy and the other two being sub-L_* galaxies. All three of these galaxies exhibit prominent interstellar absorption lines, including hydrogen damped Lyα absorption (DLA) in their spectra. One of the sub-L_* galaxies ($A3$ in Figure 2.1 below) is further resolved into two high-intensity peaks. In contrast, the Lyα nebula in System B exhibits a symmetric morphology in the source plane, centered approximately at two compact continuum sources separated by $\approx 0\rlap{.}''1$ ($\approx 0\rlap{.}''3$–$0\rlap{.}''5$ in the image plane), both of which are low-luminosity $\approx 0.03\,L_*$ Lyα emitters (LAE) with a

rest-frame Lyα equivalent width of $W(\text{Ly}\alpha) \approx 30\,\text{Å}$.

In this chapter, we examine the underlying gas flows by combining spatially-resolved Lyα emission profiles from MUSE and known star formation properties of the neighboring galaxies from available *Hubble Space Telescope* (*HST*) broadband photometry. This paper is organized as follows. First, the archival data included in our analysis are presented in Section 2.2, including broadband imaging data by *HST* and IFS data by VLT/MUSE. The lens models fine-tuned to best reproduce multiple images from Systems *A* and *B* are presented in Section 2.3. In Sections 2.4 and 2.5, we present a detailed analysis of UV continuum galaxies and the Lyα line-emitting gas, respectively. We discuss our results in Section 2.6, and conclude in Section 2.7. Throughout this paper, we adopt a Hubble constant of $H_0 = 70$ km/s/Mpc, $\Omega_{\text{M}} = 0.3$ and $\Omega_{\Lambda} = 0.7$ when deriving distances, masses and luminosities. All magnitudes quoted are in the AB system.

2.2   Observational Data

MACS 1206 is a well studied cluster, which was first identified as a luminous X-ray source in the ROSAT All Sky Survey (Voges et al., 1999; Böhringer et al., 2001) and later confirmed to be a massive, strong-lensing cluster by the Massive Cluster Survey (Ebeling et al., 2001, 2009). It was also selected as one of the 25 clusters in the *Cluster Lensing And Supernova Survey with Hubble* (CLASH) program (Postman et al., 2012). Exquisite imaging and spectroscopic data of this cluster field are available in public data archives, including high-quality multi-band imaging data from the *HST*, follow-up galaxy spectroscopic survey data from the CLASH-VLT redshift survey (Biviano et al., 2013; Rosati et al., 2014), and wide-field IFS data obtained using VLT/MUSE (Bacon et al., 2010; Caminha et al., 2017). High-level science products are retrieved from these public data archives for our study. In this section, we provide a summary of these data products.
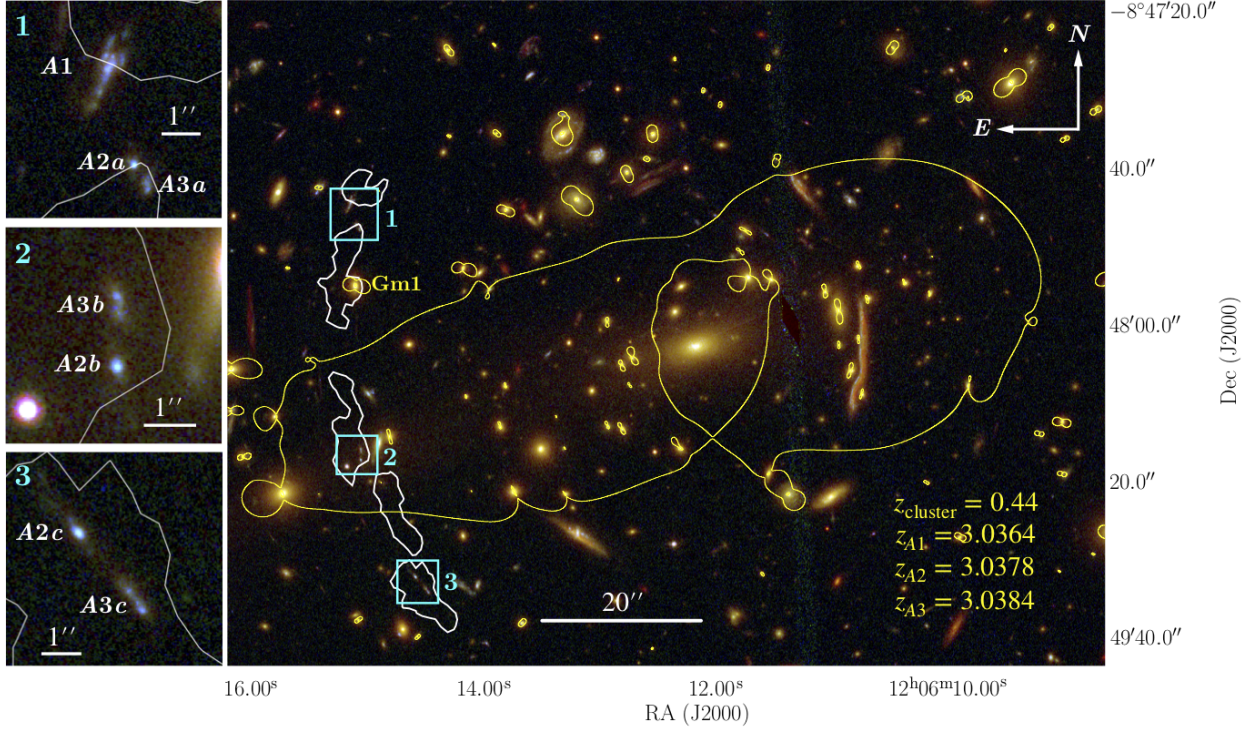
Figure 2.1: Composite image of the core region of MACS 1206, produced using *HST* F475W (blue), F814W (green) and F160W (red) images. White contours indicate the Lyα emission associated with System *A* at a surface brightness of $\mathrm{SB}_{\mathrm{Ly}\alpha} = 3.7 \times 10^{-18}\,\mathrm{erg\,s^{-1}\,cm^{-2}\,arcsec^{-2}}$, integrated over the spectral window of 4890-4930 Å (see §2.5.1 below). The surface brightness limit corresponds to a 3-σ limiting flux over a circular aperture of $1''$ in diameter, roughly the size of the PSF measured in the MUSE data. Yellow contours show the critical curve of the cluster lens for a source at $z = 3.038$. Left panels show zoomed-in regions around lensed images of galaxies *A*1, *A*2, and *A*3, along with the Lyα contours. Note that the galaxy *A*1 at $z = 3.0364$ is magnified but not multiply-lensed. Cluster member galaxy Gm1 is located close to lensed images of System *A* and is individually optimized in the lens modeling process as described in §2.3. After correcting for the lensing magnification, the total Lyα luminosity from the nebula is $L_{\mathrm{Ly}\alpha} = (5.2 \pm 0.1) \times 10^{42}\,\mathrm{erg\,s^{-1}}$ (see §2.5.1).

13
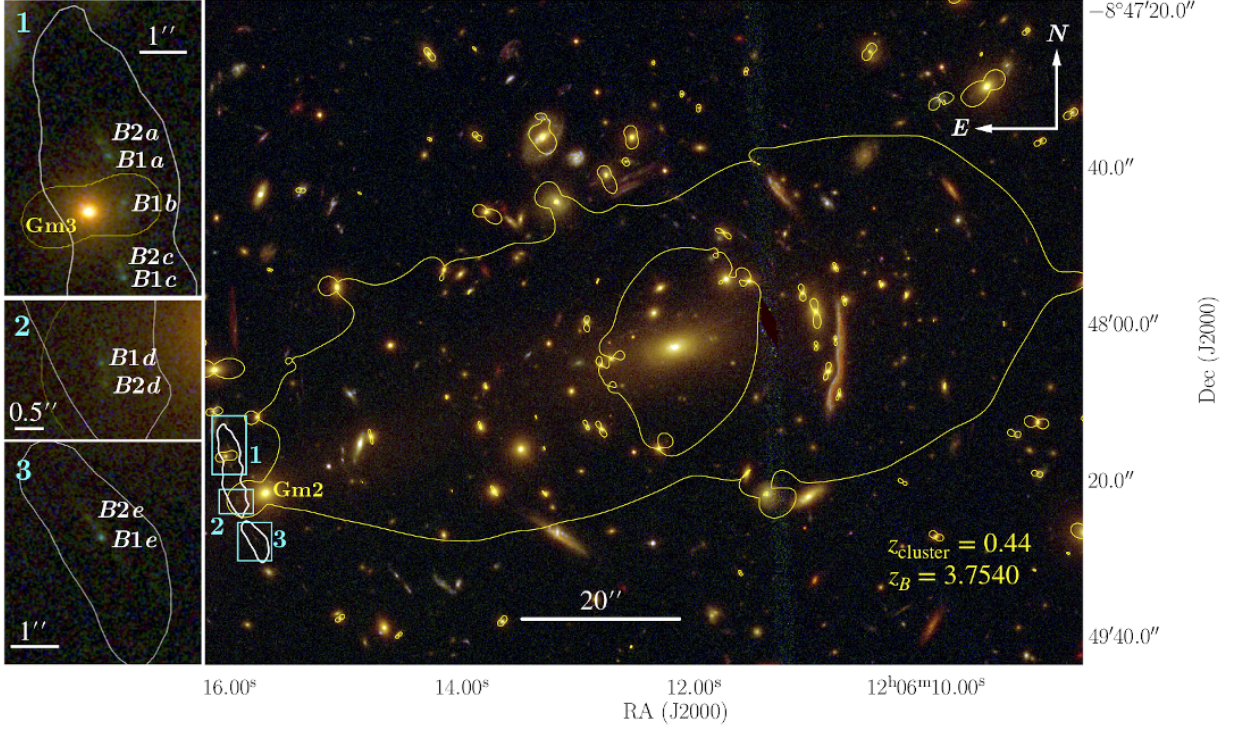
Figure 2.2: Same as Figure 2.1, while highlighting the configuration of System B. White contours indicate the Lyα emission associated with System B at $\mathrm{SB}_{\mathrm{Ly}\alpha} = 2.8 \times 10^{-18}\,\mathrm{erg\,s^{-1}\,cm^{-2}\,arcsec^{-2}}$, integrated over the spectral window of 5766-5796 Å (see § 2.5.1 below). The surface brightness limit corresponds to a 3-σ limiting flux over a circular aperture of $1''$ in diameter, roughly the size of the PSF measured in the MUSE data. Yellow contours show the critical curve of the cluster lens for a source at $z = 3.754$. Left panels show zoomed-in regions around the lensed images of galaxy B consisting of components $B1$ and $B2$, along with the Lyα contours. Cluster member galaxies Gm2 and Gm3 are located close to lensed images of System B and are individually optimised in the lens modeling process as described in §2.3. After correcting for the lensing magnification, the total Lyα luminosity from the nebula is $L_{\mathrm{Ly}\alpha} = (9.8 \pm 0.2) \times 10^{41}\,\mathrm{erg\,s^{-1}}$ (see §2.5.1).

14

2.2.1 HST images

High spatial resolution, UV, optical and near-infrared imaging data of the field around MACS 1206 obtained using the *HST* were retrieved from the Mikulski Archive for Space Telescopes (MAST) archive[1] (PI: M. Postman). These include images taken using the Advanced Camera for Surveys (ACS), the Wide Field Camera 3 (WFC3), and a suite of UV, optical, and near-infrared filters (see Table 2.2 below). Figures 2.1 and 2.2 show composite images of the central region of MACS 1206 from combining F475W (blue), F814W (green), and F160W (red) images, highlighting the lensing configurations of System A and System B, respectively. Detailed photometric properties of each system derived from these *HST* data are described in §2.4.

Given the close proximity of $B1$ and $B2$ in the source plane (see §2.5.1 below), it is possible that they correspond to distinct star-forming regions in the same galaxy at $z = 3.754$. However, without high-resolution infrared data, we cannot determine confidently whether or not $B1$ and $B2$ originate in the same galaxy. We therefore proceed with referring to $B1$ and $B2$ as individual galaxies for simplicity.

2.2.2 MUSE IFS Data

Wide-field IFS data of MACS 1206 were obtained using MUSE on the VLT UT4. The observations were carried out under Program ID's 095.A-0181(A) and 097.A-0269(A) to cover an effective area of 2.63 arcmin^2 around the cluster in three pointings (PI: J. Richard), which are part of a systematic survey of 12 strong lensing clusters using MUSE (Richard et al., 2020). In the region where lensed images of Systems A and B are found, a total exposure time of ≈ 4 hours were collected. Pipeline-processed and flux-calibrated data cubes were retrieved from the ESO Phase 3 Archive, covering a wavelength range of 4750-9300 Å with a spectral resolution of FWHM ≈ 170 (110) $\mathrm{km\,s^{-1}}$ at ≈ 5000 (7000) Å and a pixel scale of $0\rlap{.}''2 \times 0\rlap{.}''2$.

---

1. `https://archive.stsci.edu/pub/hlsp/clash/macs1206/data/hst/scale_30mas`

The mean point spread function (PSF) in the final combined data cube was determined using a bright star, and found to be $\approx 1''$ at 7000 Å. Astrometry of the combined MUSE data cube was re-calibrated to match the world coordinate system of available *HST* images. The pipeline generated combined data cube contains non-negligible sky residuals that affected the detection of faint emission features. Additional sky subtraction was therefore performed using a median sky residual spectrum generated from object-free spaxels in the data cube. Detailed spectroscopic properties of both continuum sources and Lyα emitting nebulae are described in §2.4 and §2.5, respectively. Finally, the wavelength array is converted to vacuum to facilitate accurate velocity calculations based on known rest-frame UV wavelengths.

2.3   Cluster lens modeling

To determine the intrinsic properties of both Systems A and B, it is necessary to construct a cluster lens model to correct for the gravitational lensing effect. Here we employ the software *LENSTOOL* (version 6.5) (Jullo et al., 2007) to construct a parametric cluster lens model of MACS 1206 by incorporating known multiply-lensed galaxies identified in the MUSE data (Caminha et al., 2017) and those reported in the literature (e.g., Zitrin et al., 2012; Umetsu et al., 2012; Eichner et al., 2013). As both Systems A and B are in the core region of the cluster, we only include the strong lensing constraints and do not consider weak lensing effect in our lens modeling process. We first obtain a fiducial cluster lens model that gives a good fit to a total of 72 multiple images from 21 background sources. Those images cover a field of view (FOV) of $\approx 2'$ relatively evenly, providing robust constraints for the projected cluster mass distribution within this FOV. We then fine-tune the lens model by considering only multiple images of Systems A and B, optimising the mass distribution projected close to those particular images as well as the multiply-lensed extended Lyα emitting nebulae. Details regarding the lens modeling process are described below.

2.3.1 Fiducial cluster lens model

Following Caminha et al. (2017), we adopt a parametric model based on a pseudo-isothermal elliptical mass distribution (PIEMD) (Kassiola & Kovner, 1993) of ellipticity ϵ and include two additional isothermal halo components to represent the cluster-scale diffuse mass. This three-halo configuration is found to minimize the dispersion between predicted and observed image positions for all multiply-lensed sources (see Caminha et al., 2017, for detailed discussions). The convergence of PIEMD is given by

$$\kappa_c = \frac{\sigma_v^2}{2\,G\,\Sigma_{cr}\,\sqrt{R_\epsilon^2 + r_c^2}}, \tag{2.1}$$

where R_ϵ is the distance from the center of the cluster, defined as

$$R_\epsilon^2 = \frac{x^2}{(1+\epsilon)^2} + \frac{y^2}{(1-\epsilon)^2}, \tag{2.2}$$

r_c is the core radius and Σ_{cr} is the projected critical mass density. Given the angular diameter distances between the observer and the lens (D_l), the lens and the source (D_{ls}), and the observer and the source (D_s), the projected critical mass density is defined as

$$\Sigma_{cr} = \frac{c^2}{4\pi G} \frac{D_s}{D_l D_{ls}}. \tag{2.3}$$

All six parameter of the three PIEMD halos (x, y, r_c, ϵ, position angle, velocity dispersion σ_v) are free to vary. We also include external shear (parameterized by the intensity γ_{shear} and position angle θ_{shear}) to account for possible massive structures in regions further away from the cluster core.

In addition to the cluster-scale diffuse mass distribution, we account for local perturbations in the vicinity of individual galaxies by including 128 cluster member galaxies in the lens model. These member galaxies are selected based on their redshifts in the catalog of

Molino et al. (2017), which is downloaded from the MAST archive [2]. We first eliminate galaxies fainter than $AB = 24$ mag in the F160W band. For galaxies with spectroscopic redshifts, we select those with $0.425 < z_{\mathrm{spec}} < 0.453$. For galaxies without z_{spec}, we apply the same criterion based on available photometric redshifts. A total of 128 cluster members are selected from this exercise. Note that in general, the cluster lensing potential is dominated by the large-scale diffuse mass distribution, which is primarily in the form of dark matter. Member galaxies only introduce perturbations local to the location of individual galaxies. Therefore, in cases where lensed images do not appear close to individual member galaxies ($\leq 5''$, corresponding to typical Einstein radius of individual galaxies), the variation in the selection of member galaxies does not introduce significant uncertainties to the cluster lensing potential. However, in cases where lensed images form close to individual galaxies, careful modeling of those individual galaxies is required to accurately reproduce the positions of nearby images. As our goal here is to obtain a good cluster-scale lens model instead of optimising individual galaxy mass distributions, we exclude image systems 2, 7, 13, 21, 24 and 27 in Caminha et al. (2017) (see their Fig. 1), whose multiple images fall very close to massive cluster member galaxies. This way we do not need to fine-tune every member galaxy with lensed images nearby and still maintain the accuracy of the large-scale cluster lens model.

We include cluster member galaxies as 128 dual pseudo-isothermal elliptical mass distributions (dPIE) (Elíasdóttir et al., 2007) located at their detected light centroids, with the ellipticity and position angle fixed to their observed values obtained from the Molino et al. (2017) catalog. The convergence of the dPIE profile is given by

$$\kappa_g = \frac{\sigma_{g,v}^2}{2\,G\,\Sigma_{cr}} \left(\frac{1}{R_{g,\epsilon}} - \frac{1}{\sqrt{R_{g,\epsilon}^2 + r_{g,t}^2}} \right), \tag{2.4}$$

Table 2.1: Mean lensing magnification of multiple images of Systems A and B. Calculated based on the fine-tuned lens model as described in Section 2.3.2.

Image	$\bar{\mu}$		Image	$\bar{\mu}$
$A1$	3.8		$B1a$	15.2
$A2a$	4.3		$B1c$	10.4
$A2b$	5.4		$B1d$	12.1
$A2c$	7.5		$B1e$	7.5
$A3a$	4.5		$B2a$	8.2
$A3b$	4.4		$B2c$	13.0
$A3c$	6.2		$B2d$	12.0
			$B2e$	8.4

where $r_{g,t}$ is the truncation radius. To reduce the total number of free parameters, we scale all 128 member galaxies with a constant mass-to-light ratio through

$$\sigma_{g,v} = \sigma_{g,v}^0 (\frac{L}{L_0})^{\frac{1}{4}}, \; r_{g,t} = r_{g,t}^0 (\frac{L}{L_0})^{\frac{1}{4}}, \tag{2.5}$$

where L_0 is the reference luminosity with magnitude $m_{\text{F814W}} = 19.6$. Hence there are only two free parameters for member galaxies: $\sigma_{g,v}^0$ and $r_{g,t}^0$.

Constraints of this fiducial cluster lens model are positions of 72 multiple images from 21 background sources identified by Caminha et al. (2017), excluding image systems 2, 7, 13, 21, 24 and 27 for reasons described above. The optimization is performed based on object positions in the source plane. We obtain similar best-fit parameters as Caminha et al. (2017). The root-mean-square positional offset between observed and predicted images is $\langle \text{rms} \rangle_{\text{im}} = 0\!''\!76$ in the image plane, averaged over all 72 images of 21 sources. The rms position offsets for Systems A and B are found to be $\langle \text{rms} \rangle_{\text{im}} = 0\!''\!38$ and $\langle \text{rms} \rangle_{\text{im}} = 0\!''\!73$, respectively. In the Appendix, we list the coordinates and redshifts of all 72 images used as constraints, as well as the best-fit model parameters.

2.3.2   Fine-tuned lens model for Systems A and B

Based on the fiducial cluster lens model described above, we now optimize the lens model for Systems A and B separately to ensure the highest accuracy in matching the observed locations of multiply-lensed images in these two systems. In the fiducial model, the respective centers of the three cluster-scale PIEMD halos are located at $\approx 2''$ from the brightest cluster galaxy (BCG), $\approx 13''$ northwest and $\approx 30''$ southeast of the BCG (see Table 2.8 for a summary). As the southeast cluster-scale PIEMD halo occurs close to the lensed images of Systems A and B, we obtain a refined lens model, leaving all parameters of this PIEMD halo free while fixing the other two cluster-scale PIEMD halos to their best-fit parameters in the fiducial model. We also notice that three of the cluster member galaxies (marked as Gm1, Gm2 and Gm3 in Figures 2.1 and 2.2) are located close to some images of Systems A and B. We therefore allow the velocity dispersion $\sigma_{g,v}$ and truncation radius $r_{g,t}$ of these three cluster members to vary freely in the fine-tuned model optimization, instead of being scaled together with the rest of member galaxies. Finally, the external shear parameters are fixed to their best-fit values in the fiducial model.

Because we are particularly interested in accurately producing the lensing effect for Systems A and B, we also include constraints from the two substructures of $A3$ (designated $A31$ and $A32$ in Table 2.7), and the fainter galaxy $B2$ in System B, which are not used in Caminha et al. (2017). With a total of 18 multiple images of A and B as constraints (the first 18 entries in Table 2.7), we then run *LENSTOOL* again with the above set-up, and obtain a fine-tuned model. This model places significantly more weight on the local perturbers (Gm1, Gm2, and Gm3) and provides much improved root-mean-square positional offsets for the systems of interest in this study. The rms position offsets for Systems A and B are reduced to $\mathrm{rms_{im}} = 0\!''\!1$ and $\mathrm{rms_{im}} = 0\!''\!21$, respectively. The best-fit parameters are listed Table 2.9 in the Appendix. In Figures 2.1 and 2.2, we show the predicted critical curves by this fine-tuned model for sources at the redshifts of Systems A and B. Mean lensing magni-

fication factors of multiple images of Systems A and B based on the fine-tuned lens model are presented in Table 2.1. Wherever required in subsequent analyses, we use this fine-tuned model to derive image position deflections and magnifications.

2.4 Analysis: galaxy properties

Both Systems A and B comprise two distinct components: (1) the continuum sources detected in the broadband *HST* images and (2) the Lyα emitting nebulae that are more spatially extended than the continuum sources and are only visible in the MUSE IFS data. Available broadband photometry and spectra of the galaxies provide important constraints for the star formation histories and the underlying stellar populations. In this section, we investigate the properties of the galaxies by analysing the photometric and spectroscopic data of the continuum sources. We will present the analysis of the associated Lyα emitting nebulae in §2.5.

2.4.1   Photometric properties

Accurate photometric measurements of galaxies in Systems A and B are challenging due to the crowding of members of the lensing cluster and non-negligible intracluster light (e.g., Figures 2.1 & 2.2). We first measure broadband magnitudes of individual lensed images of each galaxy in different bandpasses using a combination of circular and isophotal apertures determined by SExtractor (v.2.19.5; Bertin & Arnouts, 1996). These measurements (presented in the Appendix) are then corrected for lensing magnifications based on the fine-tuned lens model (see Table 2.1 presented in §2.3).

For galaxies $A2$ and $A3$ in System A, their b images occur between two bright foreground galaxies, resulting in uncertain background subtraction in the photometric measurements. The de-magnified apparent magnitudes of $A2$ and $A3$ are therefore determined based on an average of images a and c. The de-magnified magnitudes of $A2$ and $A3$ in image a are

Table 2.2: Summary of galaxy photometry for System A^a.

	redshift	M^b_{1500}	F300W^c	F390W	F435W	F475W	F606W	F625W
A1	3.0364	−21.52	> 26.14	25.85 ± 0.08	25.02 ± 0.03	24.59 ± 0.02	24.03 ± 0.07	23.90 ± 0.01
A2	3.0378	−19.87	> 28.37	26.97 ± 0.12	26.29 ± 0.05	26.10 ± 0.03	25.67 ± 0.04	25.43 ± 0.02
A3	3.0384	−19.63	> 28.57	27.53 ± 0.12	26.82 ± 0.05	26.46 ± 0.03	25.91 ± 0.04	25.76 ± 0.02
	F775W	F814W	F850LP	F105W	F110W	F125W	F140W	F160W
A1	23.76 ± 0.01	23.76 ± 0.01	23.73 ± 0.02	23.73 ± 0.01	23.71 ± 0.01	23.71 ± 0.01	23.52 ± 0.01	23.34 ± 0.01
A2	25.37 ± 0.02	25.32 ± 0.01	25.31 ± 0.03	25.47 ± 0.02	25.50 ± 0.01	25.54 ± 0.02	25.36 ± 0.01	25.32 ± 0.01
A3	25.66 ± 0.02	25.62 ± 0.01	25.61 ± 0.03	25.72 ± 0.02	25.70 ± 0.01	25.75 ± 0.02	25.51 ± 0.01	25.34 ± 0.01

^{a}All magnitudes are de-magnified based on the lens model described in §2.3, and averaged among images a and c.
^{b}At $z = 3$, typical star-forming galaxies have $M_{1500}* = −21.1 ± 0.2$ (e.g., Reddy et al., 2008)
^{c}2σ UV flux upper limit, averaged among the F225W, F275W and F336W bandpasses.

Table 2.3: Summary of galaxy photometry for System B^a.

	redshift	M^b_{1500}	F450W^c	F475W	F606W	F625W	F775W	F814W
B1	3.7540	-17.23	> 30.08	29.99 ± 0.20	29.15 ± 0.06	28.94 ± 0.08	28.69 ± 0.08	28.81 ± 0.05
B2	3.7540	-17.01	> 29.99	$> 30.68^d$	29.59 ± 0.11	29.57 ± 0.17	28.91 ± 0.11	28.95 ± 0.07

	F850LP	F105W	F110W	F125W	F140W	F160W
B1	28.80 ± 0.11	29.29 ± 0.09	29.13 ± 0.05	29.19 ± 0.09	29.28 ± 0.08	29.22 ± 0.08
B2	28.87 ± 0.15	29.15 ± 0.10	29.11 ± 0.06	29.12 ± 0.10	28.98 ± 0.07	28.83 ± 0.07

^{a}All magnitudes are de-magnified based on the lens model described in §2.3., and averaged among images a, c and d.
^{b}At $z = 4$, typical star-forming galaxies have $M_{1500}* = -21.1 \pm 0.1$ (e.g., Bouwens et al., 2007)
$^c2\sigma$ UV flux upper limit, averaged among the F225W, F275W, F336W, F390W and F435W bandpasses.
$^d2\sigma$ flux upper limit.

Table 2.4: SED fitting results, showing 16%–84% confidence interval for each parameter.

galaxy	redshift	$\log(M_{\rm star}/M_\odot)$	SFR $(M_\odot\,{\rm yr}^{-1})$	Age (Gyr)	τ (Gyr)	A_V
$A1$	3.0364	$[9.93, 9.98]$	$[89.84, 101.85]$	$[0.11, 0.14]$	$[1.37, 4.35]$	$[0.72, 0.77]$
$A2$	3.0378	$[8.95, 8.98]$	$[10.71, 11.45]$	$[0.05, 0.06]$	$[1.30, 4.38]$	$[0.62, 0.65]$
$A3$	3.0384	$[9.23, 9.27]$	$[13.02, 15.81]$	$[0.14, 0.19]$	$[1.44, 4.37]$	$[0.64, 0.71]$
$B1$	3.7540	$[7.59, 7.96]$	$[0.23, 0.40]$	$[0.13, 0.53]$	$[1.26, 4.25]$	$[0.05, 0.25]$
$B2$	3.7540	$[8.43, 8.72]$	$[0.50, 0.91]$	$[0.43, 1.31]$	$[1.31, 4.35]$	$[0.47, 0.74]$

≈ 0.2 magnitudes fainter than that in image c, suggesting that the true magnification factor for image a relative to image c is smaller than what is predicted by the lens model. In §2.5 below, we also show that the apparent Lyα surface brightness in the extended nebulae from image a is fainter than what is seen in images b and c, supporting a smaller relative magnification factor at the location of image a. Such a discrepancy in image brightnesses is commonly seen in strongly-lensed galaxies and quasars, and is often due to the limited accuracy of lens models and/or the presence of small-scale substructures in the lens (e.g. McKean et al., 2007; Hezaveh et al., 2016). The discrepancy of ≈ 0.2 magnitudes seen here is within the typical scatter of $\gtrsim 25\%$ between de-lensed magnitudes of multiply-lensed galaxies in cluster lenses (e.g. Lam et al., 2014; Caminha et al., 2016a). By averaging the de-lensed magnitudes between images a and c, we therefore mitigate the effect of lensing uncertainty on the magnification of these two galaxies.

Similarly, the b images of galaxies $B1$ and $B2$ are excluded due to the contamination from the nearby cluster member galaxy Gm3. In addition, image e of $B1$ is unusually bright compared with its counter part in images a, c and d, which are between 0.8 and 1.2 magnitudes fainter than image e across different bandpasses after the lensing correction. Such an enhancement in brightness is not observed in image e of $B2$. This brightness anomaly of $B1e$ can also be seen in the color image in Figure 2.2, and may be attributed to magnification perturbation caused by unseen substructures local to $B1e$ (e.g. McKean et al., 2007; Hezaveh et al., 2016). Consequently, the de-magnified apparent magnitudes of $B1$ and $B2$ are

determined by averaging measurements of images a, c and d. Finally, Galactic extinction corrections are calculated using the NED Galactic Extinction Calculator[3] and applied to the observed magnitudes in individual bandpasses following the Schlafly & Finkbeiner (2011) extinction map.

For galaxies in System A (B), the bandpasses bluer of F390W (F475W) correspond to rest-frame wavelengths $\lambda_{\text{rest}} < 912$Å, and no fluxes are detected above the background noise. We therefore place a 2-σ upper limit of the observed flux in each of these bandpasses. Unfortunately, these images are not sufficiently sensitive to provide meaningful constraints for the escape fraction of ionizing photons from these galaxies. The final de-magnified apparent magnitudes of galaxies A and B in different bandpasses are presented in Tables 2.2 and 2.3, while the direct measurements of individual images are presented in Table 2.10 for reference.

To characterize the intrinsic luminosities of these galaxies, we also estimate the rest-frame UV absolute magnitudes at 1500 Å, M_{1500}, using the observed F606W (F775W) brightness for galaxies in System A (B). At the respective redshifts of Systems A and B, these bandpasses correspond roughly to the rest-frame 1500 Å, and provide a robust estimate of the intrinsic UV luminosity. The absolute magnitudes of $A1$, $A2$, $A3$, $B1$ and $B2$, at rest-frame 1500Å are found to be $M_{1500} = -21.52$, -19.87, -19.63, -17.23 and -17.01, corresponding to 1.61, 0.35, 0.28, 0.03, 0.03 L_*, respectively, for a characteristic rest-frame absolute magnitude of $M_* = -21$ (e.g., Bouwens et al., 2007; Reddy et al., 2008).

2.4.2   Stellar population parameters

The observed broadband spectral energy distributions (SEDs) of galaxies in Systems A and B based on the photometric measurements presented in Tables 2.2 and 2.3 are typical of star-forming galaxies at $z = 3$–4 (e.g., Bouwens et al., 2007). To quantify the star formation histories, we perform a stellar population synthesis analysis using *Bayesian Analysis of*

---

3. `https://ned.ipac.caltech.edu/extinction_calculator`

Galaxies for Physical Inference and Parameter EStimation (BAGPIPES, Carnall et al., 2018), which employs the 2016 version of the Bruzual & Charlot (2003) stellar synthesis models. We assume an exponentially declining star formation model, $\mathrm{SFR}(t) \propto e^{-t/\tau}$, where τ represents the e-folding time and is a free parameter, and infer the stellar mass (M_{star}), star formation rate (SFR), age and dust extinction (A_V) of the continuum sources in both systems based on the observed SEDs from F606W to F160W. Because of a strong degeneracy between stellar age, metallicity, and dust attenuation (e.g., Conroy, 2013), we impose a metallicity prior based on the mass-metallicity relation for high-redshift galaxies (e.g., Ma et al., 2016) and fix the metallicity of $A1$ to 20% of the solar value, 10% for $A2$ and $A3$, and 5% for $B1$ and $B2$.

The 16%–84% confidence intervals in M_{star}, SFR, age, and A_V are presented in Table 2.4. All five galaxies are best characterized by a long star formation e-folding time that exceeds $\tau = 1$ Gyr, along with a relatively young, best-fit stellar age. In particular, the best-fit stellar ages for galaxies in System A are less than 200 Myr, making the adopted exponentially declining star formation model equivalent to a constant SFR scenario. This makes the inferred stellar age and SFR insensitive to the adopted star formation history, either exponentially declining or rising (Reddy et al., 2012). As discussed below, a constant star formation history is also consistent with the spectral features uncovered in the MUSE data. The inferred SFR for galaxies $A1$, $A2$, and $A3$ range between 10 and 100 $\mathrm{M}_\odot \, \mathrm{yr}^{-1}$ and M_{star} between 10^9 and $10^{10} \, \mathrm{M}_\odot$, typical of UV luminous star-forming galaxies at $z \approx 3$ (e.g. Shapley, 2011). In contrast, galaxies $B1$ and $B2$ have significantly lower SFR and stellar mass with $M_{\mathrm{star}} \approx 10^8 \, \mathrm{M}_\odot$, more typical of Ly$\alpha$ emitters (LAE) at $z \approx 3$ with a characteristic star formation time scale of $\lesssim 1$ Gyr (e.g. Feltre et al., 2020).
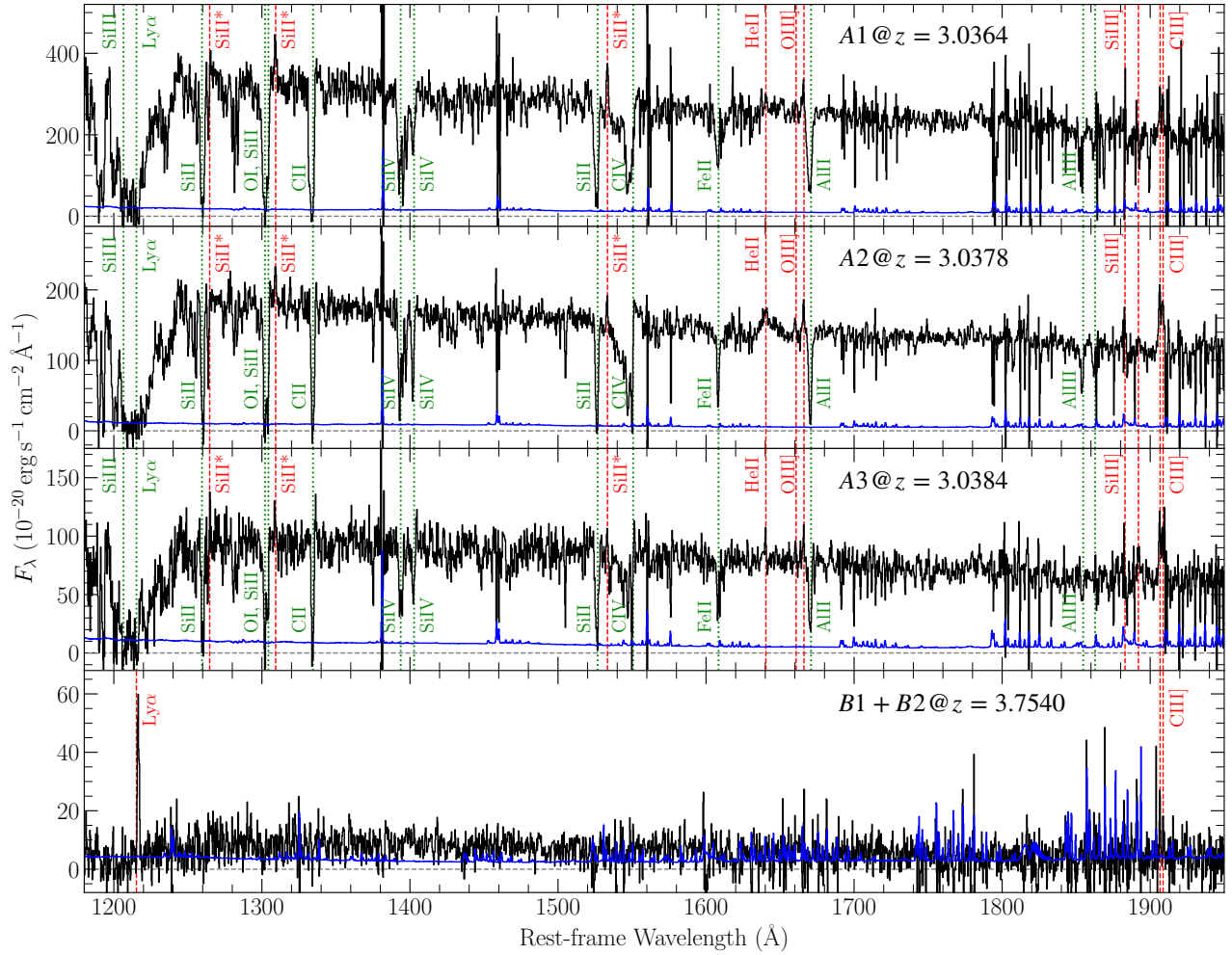
Figure 2.3: Sky-subtracted spectra of Systems A and B without lensing magnification corrections. For $A2$ and $A3$, multiple images a and c are stacked. For $B1+B2$ combined spectrum, images a, c, d and e are stacked. Rest-frame wavelength is calculated according to the best-fit redshift of each galaxy, as marked in their individual panels. The corresponding 1-σ error spectrum is shown in blue in each panel. Red dashed lines indicate major emission features while green dotted lines indicate major absorption features.

2.4.3 Spectroscopic properties

At $z = 3$–4, available MUSE data cover the rest-frame wavelength range from $\lambda_{\rm rest} > 1200$ Å to $\lambda_{\rm rest} < 1920$ Å, and provide additional constraints for the star-forming interstellar medium (ISM) and the stellar populations in Systems A and B. We extract individual galaxy spectra using spherical apertures centered on the location of the continuum sources, with varying sizes for different images depending on the intrinsic image size and magnification. Because galaxies $B1$ and $B2$ are blended in the ground-based MUSE data, we are only able to extract a single spectrum for these two galaxies. The extracted spectra (without lensing correction) are presented in Figure 2.3, along with the corresponding 1-σ error spectra. For galaxies $A2$ and $A3$, the spectra shown are combined from images a and c, while image b is excluded due to possible contamination from nearby cluster member galaxies. Similarly for $B1$ and $B2$, image b is excluded from the combined spectrum due to possible contamination from the nearby elliptical galaxy. Note that the brightness anomaly of $B1$e described in §2.4.1 does not affect the spectral features due to the achromatic nature of lensing. Image e is therefore included in the combined spectrum.

The spectra of galaxies $A1$, $A2$, and $A3$ are characterized by three distinct features: (1) a blue continuum consistent with the broadband photometry presented in Table 2.2; (2) strong interstellar absorption due to neutral hydrogen and heavy ions (marked in green, dotted line) that are commonly seen in $z \approx 3$ galaxies (e.g., Shapley et al., 2003; Erb et al., 2014), and (3) nebular emission lines due to He IIλ 1640, O III]$\lambda\lambda$ 1660, 1666, and C III]$\lambda\lambda$ 1906, 1908, as well as excited Si II*λ 1264, 1309, and 1530 lines. The strong DLA features observed in the spectra of galaxies $A1$, $A2$, and $A3$ reveal the presence of a significant amount of neutral gas in the ISM of these galaxies. A Voigt profile analysis of the red damping wing at the systemic redshifts of these galaxies (see below) yields best-fit H I column densities of $\log N({\rm HI})/{\rm cm}^{-2} = 20.9 \pm 0.1$, 21.3 ± 0.1, and 21.3 ± 0.1 for galaxies $A1$, $A2$, and $A3$, respectively, indicating a minimum surface neutral gas mass density of $\Sigma_{\rm gas} = 8$–$20 \, M_\odot \, {\rm pc}^{-2}$.
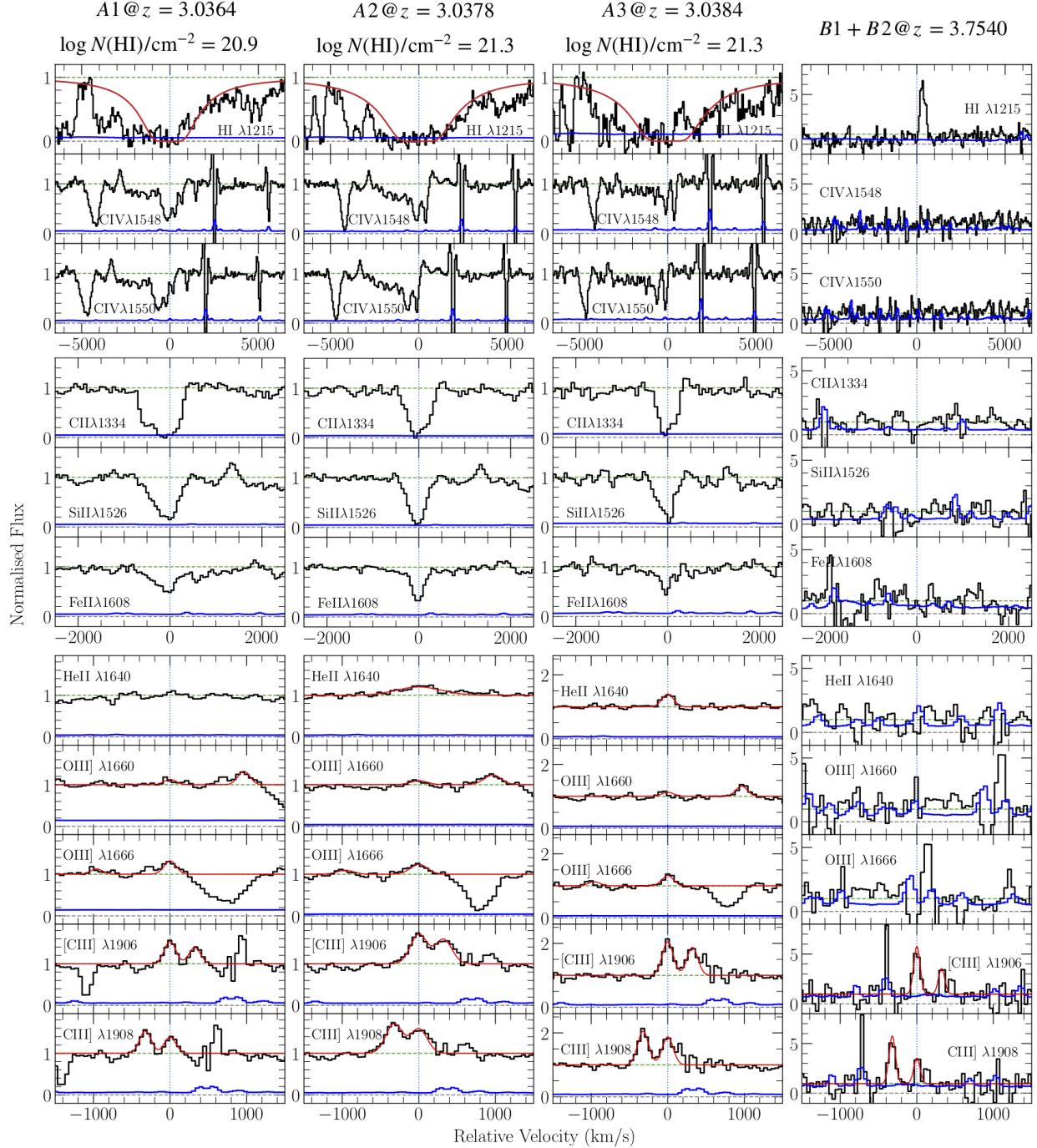
Figure 2.4: Summary of the ISM absorption and emission features of Systems A (left three columns) and B (right column). Zero velocity corresponds to the systemic redshift determined from nebular emission lines of each galaxy (see Table 2.5). The red curve in the H I panels shows the best-fit DLA profile with the estimated $N(\mathrm{H\,I})$ displayed at the top of each column. At negative velocities, the DLA profiles are contaminated by the forest of Lyα absorption lines in the foreground. The C IV$\lambda\lambda\,1548, 1550$ absorption profiles are presented in the second and third rows, showing blue absorption tail extending beyond -2500 km s^{-1}.

29

Figure 2.4: (continued) The 4th–6th rows show the low-ionization lines C $\textsc{ii}\lambda$ 1334, Si $\textsc{ii}\lambda$ 1526 and Fe $\textsc{ii}$1608, which exhibit asymmetric absorption profiles with extended blue tails, indicating the presence of gas outflows in the ISM. The best-fit Gaussian models of He $\textsc{ii}\lambda$1640, O $\textsc{iii}]\lambda\lambda$1660, 1666 and C $\textsc{iii}]\lambda\lambda$1906, 1908 emission lines are shown in red curves in bottom five rows. He $\textsc{ii}$1640 is fitted with a single Gaussian. The doublets are all fitted with a double Gaussian, and the separation between two Gaussian components are fixed by their rest-frame wavelength separation. We fix the flux ratio O $\textsc{iii}]\lambda$1666/O $\textsc{iii}]\lambda$1660 = 2.5. The redshift is tied to be consistent among all lines in each galaxy, and the best-fit values (shown at the top of each column) sets the zero velocity marked by the vertical dotted line. Data spectrum (continuum normalised) is shown in black, 1-σ error spectrum in blue and best-fit models in red. Flux and rest-frame equivalent width measured from the best-fit models for each emission line is listed in Table 2.5. While galaxies $B1/B2$ display a strong Lyα and modest C $\textsc{iii}]\lambda\lambda$1906, 1908 emission features, the data quality is not sufficient to place meaningful constraints on He $\textsc{ii}$, or O $\textsc{iii}]$.

The best-fit DLA profiles are presented in the top row of Figure 2.4. Note that the blue-side of the observed DLA profiles are contaminated by the forest of Lyα absorption lines in the foreground and therefore excluded from the fit.

Apart from the strong DLA features, the prominent C $\textsc{iv}\lambda\lambda$ 1548, 1550 absorption profiles in galaxies $A1$–3 show a blue tail extending beyond -2500 km s^{-1}, indicating the presence of stellar winds produced by massive young stars. The C $\textsc{iv}\lambda\lambda$ 1548, 1550 lines are shown in the second and third rows of Figure 2.4. In addition, low-ionization absorption lines, such as C $\textsc{ii}\lambda$ 1334, Si $\textsc{ii}\lambda$ 1526 and Fe $\textsc{ii}\lambda$ 1608 as presented in the 4th–6th rows of Figure 2.4, indicate the presence of outflowing gas in the ISM of these galaxies. These absorption lines are clearly asymmetric with an extended blue wing in $A1$. A weak, extended blue wing is also visible in Fe $\textsc{ii}\lambda$ 1608 for $A2$ and $A3$, while the core is more symmetrically distributed around the systemic velocity.

To quantify outflow velocities, we measure the absorption velocity centroid, v_{center}, and the maximum velocity of the absorption, v_{max}. Both quantities are measured with respect to the galaxy systemic velocities derived from nebular emission lines (see below). v_{center} is determined to be at the location of the deepest absorption trough. v_{max} measures the blueshifted velocity at which the absorption is consistent with the continuum to within 1-

σ level. It is determined through the relation $f(v_{\mathrm{max}}) = 1.0 - \delta(v_{\mathrm{max}})$, where f is the continuum-normalised flux and δ is the associated flux error (e.g. Martin et al., 2012). To estimate the uncertainties of both v_{max} and v_{center}, we repeat the measurements on 1000 random Gaussian generations of the spectra based on the observed intensities and error arrays, and report the mean and standard deviation of the 1000 measured values for both quantities. In addition, to quantify the internal velocity width of the absorption features, we fit a Gaussian profile to the red side of the absorption feature that is redward of the measured v_{center}, and obtain a $\mathrm{FWHM}_{\mathrm{red}}$ that is not affected by the extended blue wing. The model Gaussian profile is convolved with the instrument line spread function before fitting with the data.

Because both C IIλ 1334 and Si IIλ 1526 absorption lines are saturated, we make the measurements using Fe IIλ 1608 line. We find $[v_{\mathrm{center}}, v_{\mathrm{max}}, \mathrm{FWHM}_{\mathrm{red}}]$ of $[-42 \pm 58, -757 \pm 72, 474 \pm 52]$, $[-22 \pm 30, -614 \pm 147, 301 \pm 26]$ and $[-38 \pm 28, -480 \pm 140, 211 \pm 56]$ $\mathrm{km\,s}^{-1}$ for $A1$, $A2$ and $A3$, respectively. Both $A1$ and $A2$ exhibit an absorption velocity centroid consistent with $v = 0$ to within measurement uncertainties, while $A3$ displays a slightly more significant blueshift. At the same time, the maximum velocity v_{max} of ≈ 500–760 $\mathrm{km\,s}^{-1}$ observed in Fe IIλ 1608 exceeds the respective $\mathrm{FWHM}_{\mathrm{red}}$ measured for these galaxies, clearly indicating the presence of high-velocity outflows. We also note that the measured $\mathrm{FWHM}_{\mathrm{red}}$ is broader than the FWHM measured for nebular emission lines in all three galaxies (see below). In particular, for galaxy $A1$, the absorption line width is ≈ 3 times the width inferred from nebular emission lines (see Figure 2.4), suggesting the presence of turbulence ISM local to the star forming regions.

All three galaxies show significantly smaller outflow velocities in the line centroids in comparison to typical Lyα emitting galaxies, which is ~ 200 km/s as reported in (Shibuya et al., 2014). If the outflows originate in a biconical structure, the small outflow velocities in System A may suggest a large inclination angle of the cones of $\sim 80°$, assuming that the mean

v_{center} among the three galaxies of ~ 34 km/s is the projected velocity from an inclined cone flowing out with 200 km/s. Such a large inclination angle is also consistent with the side-lobe like morphology of the Lyα nebulae (i.e., the two clouds bracketing the continuum galaxies) and the elongated gap between the two clouds, as described below in §2.5.1. In addition, the fact that all three galaxies show similar uncharacteristically small outflow velocities might suggest that they all reside in the same outflow bubble likely originating from galaxy $A1$.

Different from galaxies in System A, galaxies $B1$ and $B2$ exhibit a strong Lyα emission with no apparent DLA trough, and resolved C III]$\lambda\lambda\,1906, 1908$ doublet features on top of a faint UV continuum. No strong absorption features are detected, but the spectrum does not have sufficient sensitivities for placing strong constraints. We measure a rest-frame equivalent width (EW$_{\text{rest}}$) of the Lyα emission line of galaxies $B1$ and $B2$ over the observed wavelength window from $\lambda_1 = 5760$ Å to $\lambda_2 = 5796$ Å, and obtain EW$_{\text{rest}}$(Lyα) $= 33.3 \pm 1.5$Å.

For all galaxies, we are able to determine an accurate systemic redshift for each of these galaxies by simultaneously fitting multiple emission lines with a Gaussian function, convolved with an appropriate instrument line spread function, which shares a common velocity centroid. Specifically for galaxies in System A, we adopt a single Gaussian model for He II$\lambda\,1640$ and a double Gaussian model for both O III]$\lambda\lambda\,1660, 1666$ and C III]$\lambda\lambda\,1906, 1908$ doublets. In addition, the flux ratio of O III]$\lambda\,1666$/O III]$\lambda\,1660$ is fixed at 2.5 as expected from their radiative transition probabilities. For galaxy $A1$, He II$\lambda\,1640$ is excluded from the fitting due to the lack of detection, and O III] and C III] doublets are fitted with a common line width. For galaxy $A2$, He II$\lambda\,1640$ is visibly broader than both O III] and C III] doublets. We therefore allow the width of He II$\lambda\,1640$ to be a free parameter while the the doublets share a common line width in the fit for $A2$. The difference in line width between He II$\lambda\,1640$ and O III]/C III] doublets is not surprising, as He II$\lambda\,1640$ emission is expected to have both stellar and nebular contributions which can sometimes lead to complex line structures (e.g. Berg et al., 2018; Kehrig et al., 2018; Nanayakkara et al., 2019; Feltre et al., 2020). For galaxy

$A3$, fittings with or without He $\textsc{ii}\lambda\,1640$ line width being a free parameter return consistent results within uncertainties. Therefore, we assign a common line width to all lines fitted for $A3$ for simplicity.

For galaxies $B1$ and $B2$, we fit a double Gaussian model with a fixed doublet separation to the C $\textsc{iii}]\lambda\lambda\,1906, 1908$ intercombination lines. The best-fit redshifts, line widths, integrated line fluxes, and $\mathrm{EW_{rest}}$, along with associated errors of individual galaxies are presented in Table 2.5. The best-fit line profiles of the emission features are also presented in Figure 2.4.

2.4.4 Emission line diagnostics

The UV emission line properties presented in Table 2.5 are typical of star-forming galaxies at $z \approx 3$ (e.g., Maseda et al., 2017; Nanayakkara et al., 2019; Feltre et al., 2020), and reveal a turbulent and high-density nature in the ISM with a radiation field dominated by massive young stars in these galaxies. The best-fit FWHMs of the emission lines correspond to velocity dispersions of $\approx 60\ \mathrm{km\,s^{-1}}$ in A1 and A3, and $\approx 100\ \mathrm{km\,s^{-1}}$ in A2, which are within the typical range measured for $z = 2$–3 galaxies (e.g., $108 \pm 86\ \mathrm{km\,s^{-1}}$ reported in Erb et al. 2006, and ≈ 50–$150\ \mathrm{km\,s^{-1}}$ reported in Kulas et al. 2012). The ratio between the C $\textsc{iii}]$ intercombination lines serves as an important UV diagnostic of the electron density, n_{e}, in the ISM, although it saturates at density below $n_{\mathrm{e}} \approx 10^3\,\mathrm{cm^{-3}}$ (e.g., Kewley et al., 2019). The observed [C $\textsc{iii}]\lambda\,1906/$C $\textsc{iii}]\lambda\,1908$ ratios of these galaxies range from 1.2 ± 0.2 for $A2$ and $A3$ to 1.9 ± 0.6 for $B1$ and $B2$, constraining the ISM electron density in both Systems A and B to be $\lesssim 2 \times 10^4\,\mathrm{cm^{-3}}$ for a gas temperature of $10{,}000$ K (Osterbrock & Ferland, 2006). The high-density limits are also comparable to what is seen in C $\textsc{iii}]$ emitters at $z \approx 3$ (e.g., Maseda et al., 2017). In addition, the detection of He $\textsc{ii}\lambda\,1640$ emission, along with the presence of a prominent P-Cygni profile in C $\textsc{iv}\lambda\lambda\,1548, 1550$ with blue absorption tail extending beyond $|\Delta\,v| \approx 2000\ \mathrm{km\,s^{-1}}$ (second and third rows in Figure 2.4), indicate the presence of massive young stars with $M \gtrsim 30\,M_{\odot}$ (e.g., Leitherer et al., 1999; Pettini

Table 2.5: Emission line fitting results, with lensing magnification corrected in all flux measurements based on mean magnification values listed in Table 2.1.

	FWHM ($\mathrm{km\,s^{-1}}$)	Flux ($10^{-20}\,\mathrm{erg\,s^{-1}\,cm^{-2}}$)	$\mathrm{EW}^b_{\mathrm{rest}}$ (Å)
*A*1 at $z = 3.0364 \pm 0.0001^a$			
He II $\lambda1640$		$< 45^c$	$< 0.18^d$
O III] $\lambda1660$	147 ± 34	35 ± 9	0.14 ± 0.04
O III] $\lambda1666$	...	86 ± 22	0.36 ± 0.11
[C III] $\lambda1906$	...	120 ± 30	0.64 ± 0.19
C III] $\lambda1908$	...	87 ± 25	0.47 ± 0.16
*A*2 at $z = 3.0378 \pm 0.0001^e$			
He II $\lambda1640$	673 ± 83^f	49 ± 7	0.79 ± 0.13
O III] $\lambda1660$	237 ± 14	9 ± 1	0.5 ± 0.02
O III] $\lambda1666$	...	22 ± 2	0.37 ± 0.05
[C III] $\lambda1906$	...	58 ± 4	1.23 ± 0.10
C III] $\lambda1908$	...	48 ± 3	1.02 ± 0.09
*A*3 at $z = 3.0384 \pm 0.0001$			
He II $\lambda1640$	136 ± 9	13 ± 2	0.41 ± 0.10
O III] $\lambda1660$	...	4 ± 1	0.13 ± 0.02
O III] $\lambda1666$	...	10 ± 1	0.34 ± 0.04
[C III] $\lambda1906$	...	32 ± 2	1.20 ± 0.10
C III] $\lambda1908$	...	26 ± 1	0.99 ± 0.08
*B*1/*B*2 at $z = 3.7540 \pm 0.0001$			
[C III] $\lambda1906$	43 ± 20	0.9 ± 0.2	3.36 ± 0.54
C III] $\lambda1908$	...	0.5 ± 0.2	1.80 ± 0.53

[a] Obtained from a simultaneous fit of O III]$\lambda\lambda\,1660, 1666$ and C III]$\lambda\lambda\,1906, 1908$

[b] Rest-frame equivalent width

[c] 2-σ upper limit

[d] 2-σ upper limit

[e] Obtained from a simultaneous fit of all lines listed; same for *A*3 and *B*1/*B*2

[f] FWHM of He II $\lambda1640$ in *A*2 is not tied with other lines due to its wide line width

34
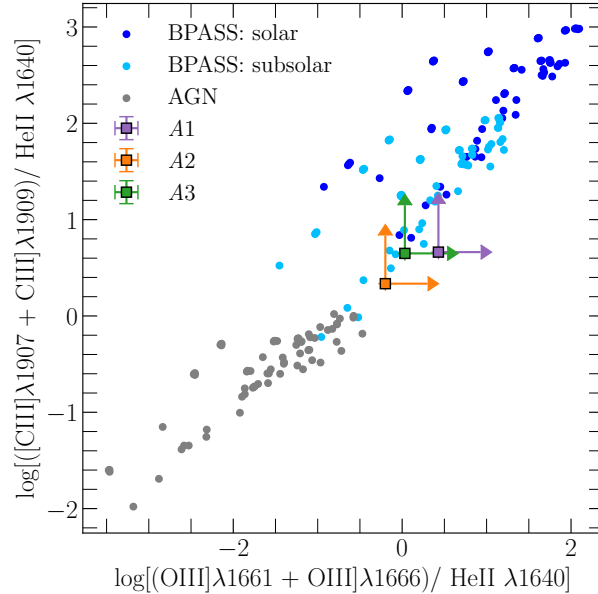
Figure 2.5: UV diagnostic diagram between AGN- (grey points) and stellar-dominated (blue and cyan points) radiation fields described in Section 2.4.4. Gas metallicities range from subsolar $Z = 0.002$ to supersolar $Z = 0.04$. The observed line ratios for galaxies $A1$, $A2$, and $A3$ are shown in squares. All three galaxies exhibit line ratios that are consistent with young stars (rather than AGN) dominating the ISM radiation field.

et al., 2000; Crowther, 2007; Brinchmann et al., 2008; Cabanac et al., 2008). The presence of broad He $\textsc{ii}\lambda 1640$ emission line in $A2$ is also a sign of Wolf-Rayet stars that have a short lifetime of ~ 5 Myr (e.g. Schaerer & Vacca, 1998; Crowther, 2007; Cabanac et al., 2008), in agreement with the constant SFR scenario suggested by photometric SED analysis (see Table 2.4 and discussion in §2.4.2).

Finally, we investigate the possibility of these galaxies hosting an active galactic nucleus (AGN) using emission line diagnostics in the UV. Specifically, Feltre et al. (2016) shows that the combination of collisionally excited nebular lines O $\textsc{iii}]\lambda\lambda 1660, 1666$, C $\textsc{iii}]\lambda\lambda 1906, 1908$ and the He $\textsc{ii}\lambda 1640$ recombination line can serve as a good indicator of the ISM ionization state. We compute the expected line ratios of O $\textsc{iii}]\lambda\lambda 1660, 1666/$He $\textsc{ii}\lambda 1640$ and C $\textsc{iii}]\lambda\lambda 1906, 1908/$He $\textsc{ii}\lambda 1640$ under different AGN and star formation (SF) ionization radiation fields, using the CLOUDY code (version 17.01; Ferland et al., 2017). For the AGN

spectrum, we adopt the model continuum specified in `CLOUDY` with an effective temperature of 10^6 K, an X-ray to UV ratio of $\alpha_{\mathrm{ox}} = -1.4$, a UV slope of $\alpha_{\mathrm{uv}} = -0.5$ and an X-ray slope of $\alpha_{\mathrm{x}} = -1$. For the SF model, we consider two stellar populations with sub-solar ($Z = 0.001$) and solar ($Z = 0.02$) metallicity, respectively. We use the FSPS code (v3.1; Conroy et al., 2009; Conroy & Gunn, 2010) to generate a composite SF spectrum at the age of 250 Myr with BPASS models, which assumes a Salpeter stellar initial mass function with an upper mass cutoff at $100\mathrm{M}_\odot$ (Eldridge et al., 2017). For each adopted AGN or SF spectrum, we generate a grid of models for the expected line ratios with the following parameters: gas metallicity $Z = [0.002, 0.02, 0.04]$, hydrogen density $n_{\mathrm{H}}/\mathrm{cm}^{-3} = [10, 10^2, 10^3, 10^4]$ and ionization parameter $U = [-4, -3.5, -3, -2.5, -2, -1.5]$. We set a temperature floor of 10,000 K. The predicted line flux ratios are shown in Figure 2.5, along with the observed values for galaxies $A1$, $A2$, and $A3$. The non-detection of He $\textsc{ii}\lambda 1640$ in galaxy $A1$ naturally leads to lower limits of both line flux ratios. We also treat the line flux ratios in both $A2$ and $A3$ as lower limits because of a possible stellar contribution to the measured He $\textsc{ii}\lambda1640$ flux.

Figure 2.5 shows that all three galaxies in System A are consistent with an ISM radiation field being dominated by massive young stars and that there is no evidence of an AGN dominating the radiation field in these galaxies. Furthermore, the lack of C $\textsc{iv}\lambda 1548, 1550$ in emission also suggests the absence of AGN as C $\textsc{iv}\lambda 1548, 1550$ emission is expected to be prominent with a hard ionization background (e.g. Gutkin et al., 2016). Due to the lack of relevant emission lines in the combined spectrum of $B1$ and $B2$, we cannot conduct the same exercise for System B. A close examination of available deep X-ray data taken by *Chandra* also shows that there is no apparent excess of X-ray signal at the locations of Systems A and B.

2.5 Analysis: Lyα nebula properties

The observed broadband photometric and spectroscopic properties of galaxies in System A indicate that these galaxies are typical of UV continuum selected star-forming galaxies at $z \approx 3$ with an ISM radiation field dominated by massive young stars, while galaxies in System B display properties that resemble low-mass LAEs in the early epoch. The large amount of ISM gas revealed in the spectra of galaxies $A1$, $A2$, and $A3$, coupled with a widespread Lyα nebula revealed in the MUSE data shows that this is a particularly gas-rich system. Here we present an analysis of the morphologies and line profiles of the extended Lyα nebulae in these two systems.

2.5.1 Pseudo narrow-band Lyα image and source plane reconstruction

To characterize the extended Lyα nebulae in both systems, we first form a pseudo narrowband Lyα image for each system. We first note that all three galaxies in System A exhibit asymmetric Lyα emission feature within the DLA trough, with an enhanced red peak at $\Delta v \approx +500$ km s^{-1} (e.g., top row of Figure 2.4) from the respective systemic redshifts. The observed asymmetric profile of these emergent Lyα photons is similar to what is seen in the extended nebulae (see §2.5.2 below) and is characteristic of large-scale outflows that have been commonly identified in high-redshift galaxies (e.g. Franx et al., 1997; Frye & Broadhurst, 1998; Pettini et al., 2000; Frye et al., 2002; Cabanac et al., 2008). An origin of the emergent Lyα photons in outflows is qualitatively consistent with the presence of gas outflows seen in absorption lines in galaxy spectra and the presence of massive young stars inferred from the UV spectral properties of the galaxies described in §2.4.4 (see also Pettini et al., 2000; Cabanac et al., 2008, for examples). Given the uncertainty of the lint-of-sight distance between the galaxies and the Lyα emission location, whether these photons originate in the star-forming ISM of the galaxies or in the extended nebulae that are blended with the galaxy image by projection remains uncertain. Therefore, we construct two versions of

the pseudo narrow-band Lyα image for System A: one without including the emergent Lyα photons in the DLA trough of the continuum sources, and a second one which incorporates both the Lyα photons in the DLA troughs and those in the extended nebulae. As discussed below and shown in Figures 2.6 and 2.7, this exercise enables a clearer understanding of the differences in the observed surface brightness profiles between multiple images, as well as establishing a direct connection between the galaxies and the line-emitting gas at large distances.

To construct a pseudo narrow-band Lyα image for System A without including the Lyα photons from the DLA troughs, we perform a local continuum subtraction per spaxel within the Lyα line. We determine a wavelength-dependent continuum level based on a linear interpolation of the continuum fluxes observed on the blue and red sides of the Lyα line. Specifically, we determine a medium flux over a spectral window of 4830-4863 Å on the blue side and a median flux over 4961-4994 Å on the red side. At $z \approx 3.04$, these correspond roughly to $[-5000, -3000]$ and $[+3000, +5000]$ km/s from the Lyα centroid (see Figure 2.10 below). The interpolated value is then subtracted from the observed flux at each spaxel. A pseudo narrow-band image of the Lyα emission is then created by integrating the flux of each spaxel over the wavelength range from 4890 Å to 4930Å, where Lyα flux is detected at a high level of significance (see Figure 2.10 below). A smoothed pseudo narrow-band Lyα image, using a Gaussian kernel of $\text{FWHM}_{\text{smooth}} = 1''$, is presented in Column (1) of Figure 2.6, which shows two nebulae separated roughly by $\approx 2''$ in the image plane and bracketing galaxies $A1$, $A2$, and $A3$ from the north and south. Furthermore, at the locations of galaxy continuum, there is a net absorption in this pseudo narrow-band image due to the presence of DLAs.

Next, we construct a pseudo narrow-band image that includes the emergent Lyα photons in the DLA troughs. This is accomplished by first identifying the spaxels within the continuum emitting regions of galaxies $A1$, $A2$, and $A3$ as defined by SExtractor (see §2.4.1).

38

Figure 2.6: Summary of the lensing configuration of the observed Lyα arc in System A. Column (1): pseudo narrow-band images without the emergent Lyα flux within the DLA troughs at the locations of galaxy continuum. The images have been smoothed using a Gaussian kernel of $\mathrm{FWHM_{smooth}} = 1''$. The contour marks constant surface brightness of $3.7 \times 10^{-18} \mathrm{erg\, s^{-1}\, cm^{-2}\, arcsec^{-2}}$, which is detected at the 3-σ level of significance in the smoothed image. Star symbols mark the positions of the associated star-forming galaxies identified in *HST* images. Column (2): same as Column (1) but includes Lyα flux from the DLA troughs at the locations of galaxy continuum (see text). Column (3): contours of multiply-lensed Lyα nebulae determined from Column (2) overlaid on individual galaxy images in the *HST* data to illustrate the relative alignment between star-forming regions and the line-emitting gas (see also Figure 2.1). Lyα surface brightness contours of of $3.7 \times 10^{-18} \mathrm{erg\, s^{-1}\, cm^{-2}\, arcsec^{-2}}$ and $7.3 \times 10^{-18} \mathrm{erg\, s^{-1}\, cm^{-2}\, arcsec^{-2}}$ are shown in white and red, respectively, and the yellow contours mark the critical curves of the cluster lens for sources at $z = 3.038$. Column (4): the magnification map overlaid with the same Lyα contours to illustrate the spatial variation of lensing magnification across the nebulae. Negative magnification factors indicate flipped parity of the image.

39
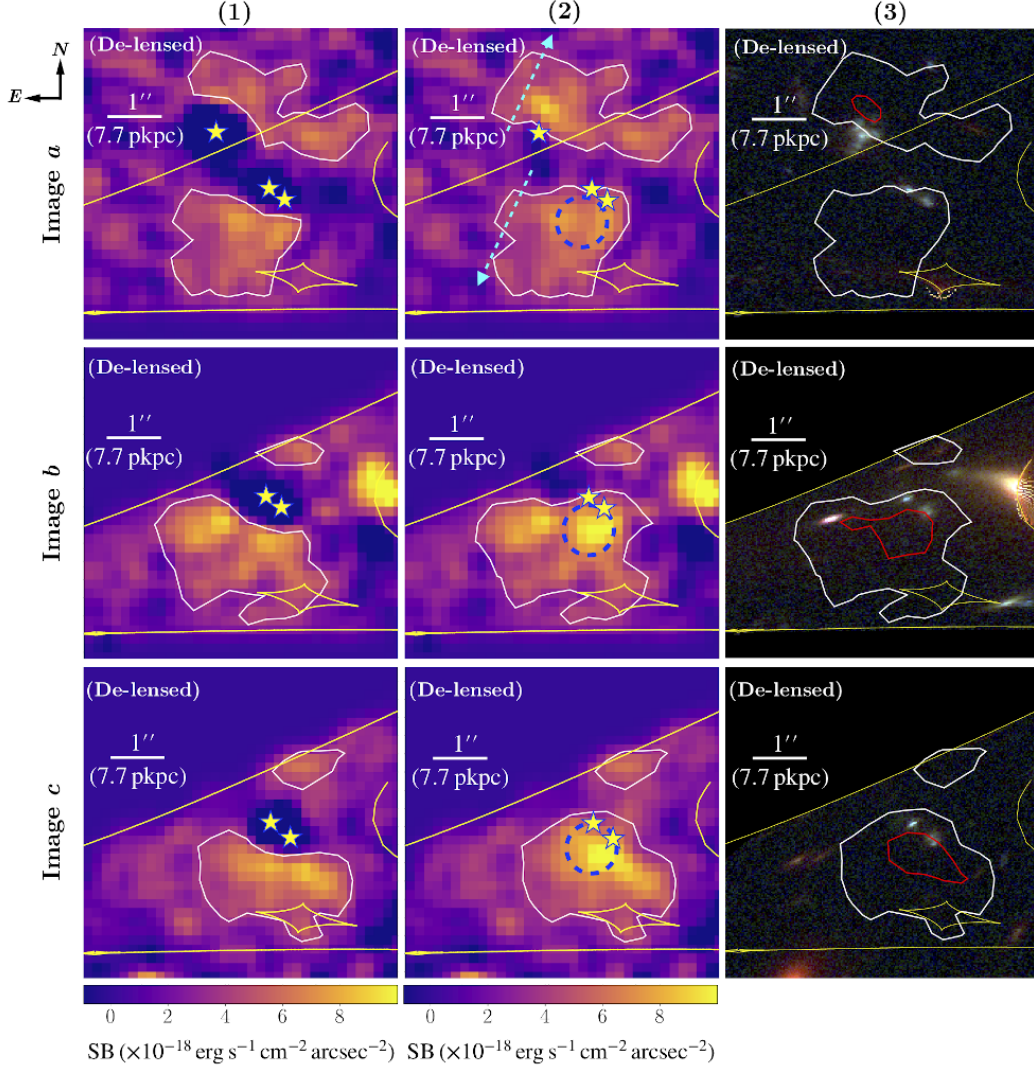
Figure 2.7: Column (*1*): de-lensed narrow-band image without Lyα flux from the DLA troughs at the locations of galaxy continuum. The images are smoothed using a Gaussian kernel of $\text{FWHM}_{\text{smooth}} = 0.5''$ in the source plane. The contour marks constant surface brightness of $3.7 \times 10^{-18} \text{erg s}^{-1} \text{cm}^{-2} \text{arcsec}^{-2}$, corresponding to the 3-σ level of significance detected in the image plane, same as contours shown in Column(*1*) of Figure 2.6. Star symbols mark the de-lensed positions of the associated star-forming galaxies identified in *HST* images. Column (*2*): same as Column (*1*) but includes Lyα flux from the DLA troughs at the locations of galaxy continuum. Column (*3*): de-lensed Lyα contours overlaid on de-lensed *HST* data, with the yellow contours showing the caustics in the source plane. The blue dashed circles in Column (*2*) mark the apertures for the template spectrum extraction, which we use for the shell model analysis (see §2.5.3). The cyan dashed arrows show the directions along which we extract the one-dimensional surface brightness profile (see Figure 2.9 below)

We then adopt the best-fit DLA model profile for each galaxy presented in Figure 2.4, and multiply the model by the best-fit continuum obtained using a low-order polynomial fit to line-free regions in the integrated continuum spectrum presented in Figure 2.3. Next, the combined DLA-continuum model spectrum is scaled to match the continuum level of the spectrum in each spaxel and subtracted from the data. The amplitude of the continuum model for each spaxel is determined using the spectrum in the wavelength window from 5430 Å to 5560 Å, corresponding to rest-frame wavelengths from 1345 Å to 1375 Å, where no narrow-line features are present. The resulting difference data cube is combined with the previous continuum-subtracted data cube in the extended nebula region. A pseudo narrow-band image is then created by integrating over the wavelength range from 4890 Å to 4930 Å. Similarly, we smooth the image using a Gaussian kernel of $\mathrm{FWHM_{smooth}} = 1''$, and present the smoothed pseudo narrow-band image in Column (2) of Figure 2.6.

In both versions of the pseudo narrow-band image presented in Columns (1) and (2) of Figure 2.6, the white contours mark a constant Lyα surface brightness of $3.7 \times 10^{-18}\,\mathrm{erg\,s^{-1}}$ $\mathrm{cm^{-2}\,arcsec^{-2}}$, which is detected at the 3-σ level of significance. A strong variation in Lyα surface brightness is clearly seen across both the northern and southern nebulae, suggesting large spatial fluctuations in the underlying gas properties. While there exists a clear gap between the northern and southern nebulae, after including the Lyα signal inside the DLA troughs, the overlap between the constant Lyα surface brightness contours and these galaxies supports a continuous flow of dense gas from star-forming regions into a low-density halo environment. Furthermore, the surface brightness of the southern nebula in the vicinity of the galaxy continuum in images b and c is relatively more enhanced than that in image a after incorporating the Lyα signal in the DLA troughs (also see Figures 2.7 and 2.9 below). Specifically, in Column (2) of Figure 2.6, the Lyα surface brightness in image a in the vicinity of galaxies $A2$ and $A3$ is fainter by $\approx 25\%$ compared with images b and c. The reduced Lyα surface brightness in images a suggests that the magnification factor of image a relative

to images b and c is smaller than what is predicted by the lens model. Such a difference in surface brightness of lensed Lyα nebulae is also seen in Caminha et al. (2016b), and is consistent with the discrepancy in de-lensed continuum brightnesses of $A2$ and $A3$, for which image a is fainter by ≈ 0.2 magnitude (see discussion in §2.4.1).

In Column (3) of Figure 2.6, Lyα surface brightness contours showing $3.7 \times 10^{-18}\,\mathrm{erg\,s^{-1}}$ $\mathrm{cm^{-2}\,arcsec^{-2}}$ and $7.3 \times 10^{-18}\,\mathrm{erg\,s^{-1}\,cm^{-2}\,arcsec^{-2}}$ (i.e., 3-σ and 6-σ determined from the pseudo narrow-band image shown in Column 2) are overlaid on top of the HST composite image from Figure 2.1. Note that image b is north-south flipped from images a and c in this lensing configuration. As a guide, we include the magnification map in Column (4) of Figure 2.6 (negative magnification factors indicate flipped parity of the image), overlaid with the same Lyα contours.

Through the deflection field calculated using the fine-tuned lens model (see § 2.3.2), we de-lens both the pseudo narrow-band image and the HST images back to the source plane. The de-lensed pseudo narrow-band image smoothed with a Gaussian kernel of $\mathrm{FWHM_{smooth}} = 0.5''$ in the source plane is presented in Columns (1) and (2) of Figure 2.7 for before and after including Lyα emission in the DLA troughs, respectively. The reconstructed source-plane images clearly show that most of the northern nebula is merely singly-lensed like galaxy $A1$, while the southern nebula stretches across the lensing field with rapidly changing magnification factors. Image a, covering the full extent of the nebulae in the source plane, constrains the projected size of the Lyα nebulae to approximately 30 pkpc from north to south. The de-lensed HST broadband images, as shown in Columns (3), are in excellent agreement among three multiple images, consistent with the low image position dispersion of $\mathrm{rms_{im}} = 0''1$ predicted by the fine-tuned lens model (see §2.3). The de-lensed pseudo narrow-band images show the same surface brightness discrepancy between multiple images as seen in the image plane (see Figure 2.6), where the surface brightness near the galaxy continuum regions is fainter in image a as discussed above. The white and red contours

in Figure 2.7 correspond to surface brightnesses of $3.7 \times 10^{-18}\,\mathrm{erg\,s^{-1}\,cm^{-2}\,arcsec^{-2}}$ and $7.3 \times 10^{-18}\,\mathrm{erg\,s^{-1}\,cm^{-2}\,arcsec^{-2}}$, same as the contours shown in Figure 2.6.

When computing the total Lyα flux in the nebulae, we consider image a for the northern nebula to avoid the confusion of partially lensed multiple images, and average images a and c for the southern nebula. Due to the contamination from a nearby galaxy at the east side of the southern nebula in image b, we leave out image b in the average. In contrast with the continuum sources, the Lyα nebulae span a much larger area in the image plane, within which the magnification factor can vary significantly (see Column(4) of Figure 2.6). Therefore, instead of using a mean magnification factor, we correct the lensing magnification for each spaxel within the extended nebulae before summing over all spaxels within the 3-σ contour for these images. We then integrate the flux over the wavelength range of 4890-4930 Å (the same wavelength window for constructing the narrow-band image described above). The total de-lensed Lyα flux of the southern nebula obtained from image a is $\approx 5\%$ (25%) lower than that from image c before (after) including the Lyα flux from the DLA troughs. This difference of Lyα flux between images a and c is in agreement with what is observed in the Lyα surface brightness and de-lensed magnitudes of galaxies $A2$ and $A3$ (see §2.4), suggesting again that the magnification factor near the continuum regions in image a is smaller than what is predicted by the lens model.

After excluding the Lyα flux from within the DLA troughs and correcting the lensing magnification, we obtain a total flux of $f_{\mathrm{Ly}\alpha}(A_{\mathrm{north}}) = (2.0 \pm 0.1) \times 10^{-17}\,\mathrm{erg\,s^{-1}\,cm^{-2}}$ for the northern nebula, and $f_{\mathrm{Ly}\alpha}(A_{\mathrm{south}}) = (2.9 \pm 0.1) \times 10^{-17}\,\mathrm{erg\,s^{-1}\,cm^{-2}}$ for the southern nebula. Including the Lyα flux from the DLA troughs, the total flux is increased to $f_{\mathrm{Ly}\alpha}^{\mathrm{tot}}(A_{\mathrm{north}}) = (2.7\pm0.1)\times10^{-17}\,\mathrm{erg\,s^{-1}\,cm^{-2}}$ for the northern nebula, and $f_{\mathrm{Ly}\alpha}^{\mathrm{tot}}(A_{\mathrm{south}}) = (3.8 \pm 0.1) \times 10^{-17}\,\mathrm{erg\,s^{-1}\,cm^{-2}}$ for the southern nebula. The Lyα signal inside the DLA troughs therefore accounts for $\approx 25\%$ of the total Lyα emission from both the northern and southern nebulae. At $z \approx 3.038$, these flux measurements (including the Lyα flux in the DLA
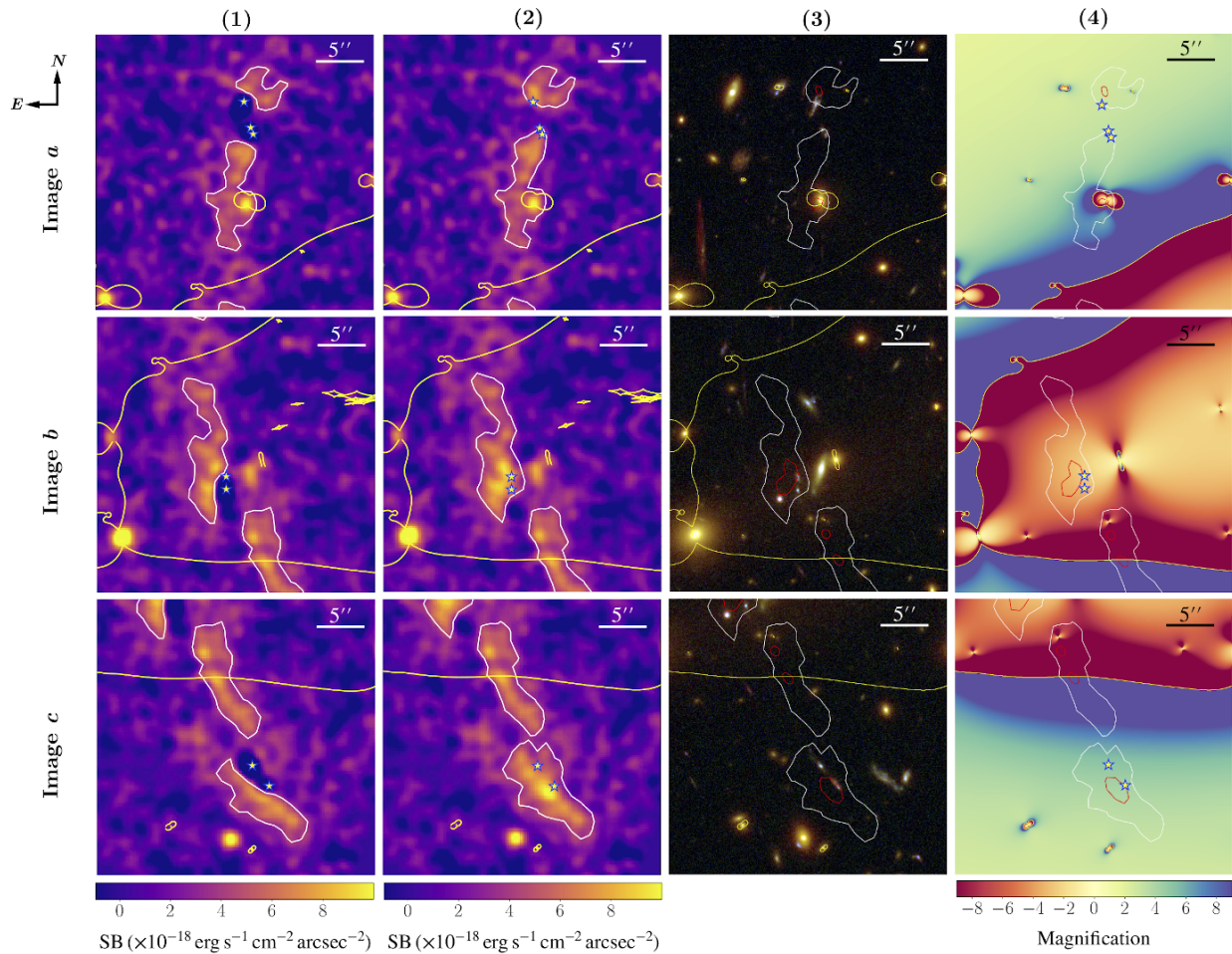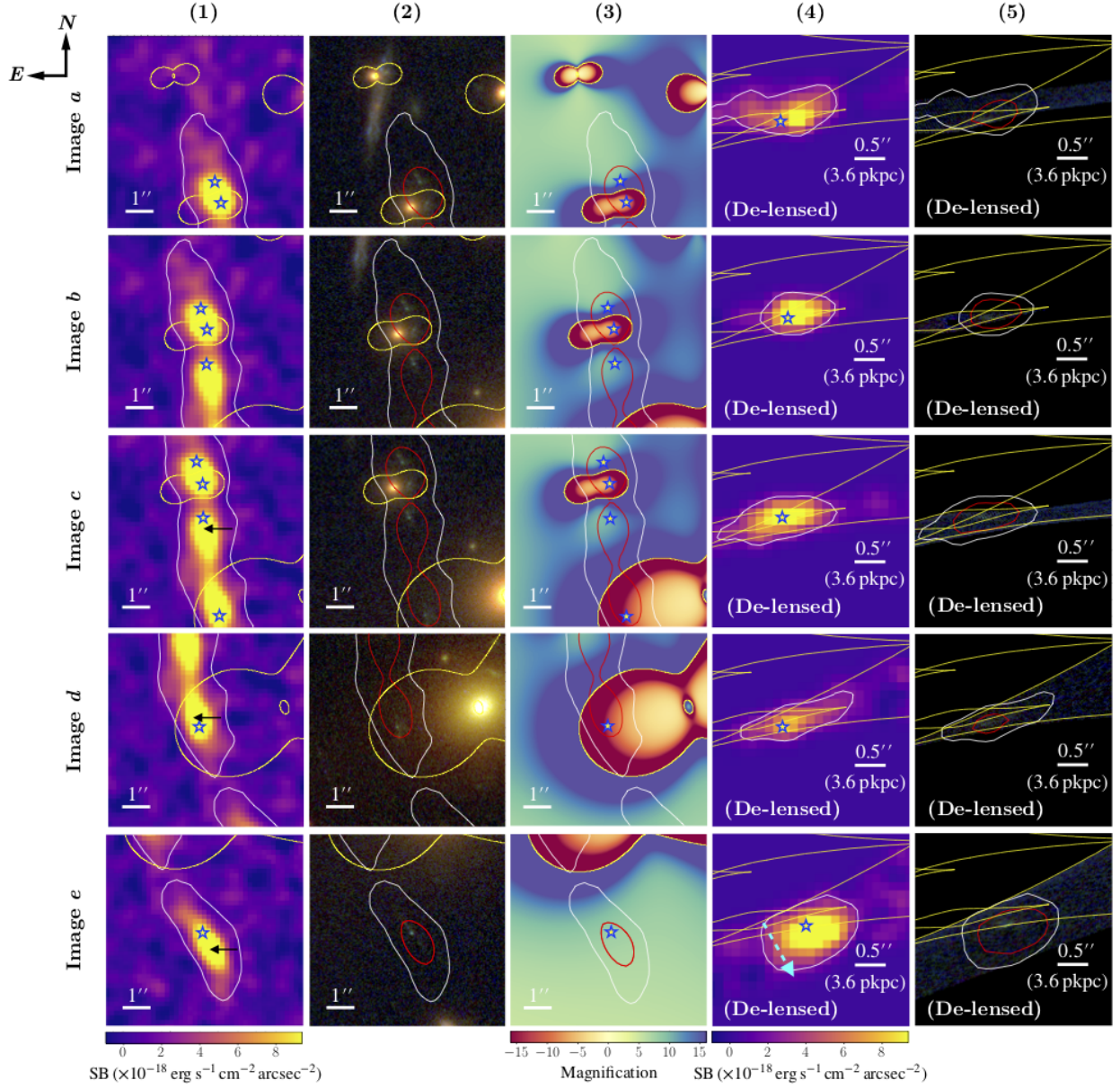
Figure 2.8: Summary of the lensing configuration of the observed Lyα arc in System B. Column (1): pseudo narrow-band image of the Lyα emission, smoothed with a Gaussian kernel of $\mathrm{FWHM_{smooth}} = 1''$. The contour marks constant surface brightness of $2.8 \times 10^{-18} \mathrm{erg \, s^{-1} \, cm^{-2} \, arcsec^{-2}}$, which is detected at the 3-σ level of significance. Star symbols mark the positions of the associated star-forming galaxies identified in HST images, and the yellow contours show the critical curve for a source at $z_{\mathrm{sys}} = 3.754$. Black arrows in the bottom three panels indicate the location of the brightest pixels in images c, d and e (one pixel from each image) that are included in the template Lyα spectrum used for shell model analysis (see §2.5.3). Column (2): contours of multiply-lensed Lyα nebulae overlaid on individual galaxy images in the HST data. Lyα surface brightness contours of $2.8 \times 10^{-18} \mathrm{erg \, s^{-1} \, cm^{-2} \, arcsec^{-2}}$ and $7.5 \times 10^{-18} \mathrm{erg \, s^{-1} \, cm^{-2} \, arcsec^{-2}}$ are shown in white

44

Figure 2.8: (continued) and red, respectively. Column (*3*): the magnification map overlaid with the same Lyα contours to illustrate the spatial variation of lensing magnification across the nebulae. Column (*4*): de-lensed narrow-band image, smoothed with a Gaussian kernel of $\mathrm{FWHM}_{\mathrm{smooth}} = 0.5''$ in the source plane. White contours mark constant surface brightness of $2.8 \times 10^{-18} \mathrm{erg\,s^{-1}\,cm^{-2}\,arcsec^{-2}}$, corresponding to the 3-σ level of significance detected in the image plane, same as contours shown in Column(*1*). Column (*5*): de-lensed Lyα contours overlaid on de-lensed *HST* data, with the yellow contours showing the caustics in the source plane. White and red contours mark the 3- and 8-σ Lyα surface brightness, same as the contours in Column(*2*). The cyan dashed arrow shows the direction along which we extract the one-dimensional surface brightness profile (see Figure 2.9 below). Compared with System *A*, the lensing configuration of System *B* is much more complicated, with images *a*-*d* being partial images with different levels of completeness. Image *e* is the only complete image of Lyα emission above 3-σ limiting surface brightness.

troughs) correspond to a Lyα luminosity of $L_{\mathrm{Ly}\alpha}(A_{\mathrm{north}}) = (2.15 \pm 0.07) \times 10^{42} \mathrm{erg\,s^{-1}}$ for the northern nebula, and $L_{\mathrm{Ly}\alpha}(A_{\mathrm{south}}) = (3.03 \pm 0.08) \times 10^{42} \mathrm{erg\,s^{-1}}$ for the southern nebula. Combining both northern and southern nebulae together leads to a total Lyα luminosity of $L_{\mathrm{Ly}\alpha}(A) = (5.2 \pm 0.1) \times 10^{42} \mathrm{erg\,s^{-1}}$.

For System *B*, no apparent DLA or strong ISM absorption features are detected in the MUSE spectra of the star-forming regions, but the low S/N as a result of a faint continuum makes gas column density estimates highly uncertain. The apparent discontinuity in the continuum blueward and redward of the Lyα emission line is consistent with the expectation from the Lyα forest in the intergalactic medium at $z \approx 3.75$ (e.g. Becker et al., 2007). To construct a pseudo narrow-band image for this system, we first subtract the expected continuum at the observed Lyα line. Following the approach described above for System *A*, we determine the continuum level in each spaxel of the star-forming regions by matching the low-order polynomial fit of the UV continuum presented in Figure 2.4 to the observed spectrum. For spaxels outside of the continuum emitting regions, the continuum level at the Lyα emission line is determined based on a linear interpolation between blue and red continuum fluxes observed within 5730–5760 Å and 5800–5830 Å, respectively. A pseudo narrow-band image is then constructed by integrating the flux in the wavelength range

from 5766 Å to 5796 Å. A smoothed version using a Gaussian kernel of FWHM = $1''$ is presented in Column (1) of Figure 2.8, overlaid with constant surface brightness contours of $2.8 \times 10^{-18} \, \mathrm{erg \, s^{-1} \, cm^{-2} \, arcsec^{-2}}$ detected at 3-σ. In Column (2) of Figure 2.8, contours of 2.8 and $7.5 \times 10^{-18} \, \mathrm{erg \, s^{-1} \, cm^{-2} \, arcsec^{-2}}$ (i.e., 3-σ and 8-σ) are presented along with the *HST* composite image to illustrate the relative alignment between the Lyα nebulae and the associated galaxies. The magnification map presented in Column (3) shows the fast changing magnification factors across all five lensed images in System B, as the lensed Lyα emitting regions straddles multiple critical curves in the image plane. De-lensed Lyα pseudo narrow-band images (smoothed using a a Gaussian kernel of FWHM = $0''.5$) and the *HST* images in the source plane, based on the fine-tuned lens model described in § 2.3.2, are also presented in Columns (4) and (5) of Figure 2.8, respectively. Compared with System A, the lensing configuration of System B is more complicated, with images a–d being partial images of different completeness levels. Image e is the only complete lensed image of the Lyα nebula defined at the 3-σ level of significance in surface brightness. The source plane reconstruction from image e reveals a relatively symmetric Lyα emission morphology, roughly centered near the UV continuum sources. Using image e, we estimate the projected size of the Lyα emitting nebula to be approximately 10 pkpc in diameter. A small spatial offset, $\approx 0''.1$, is seen between UV continuum sources and the peak of Lyα emission, corresponding to ≈ 0.7 pkpc at $z = 3.754$. It is commonly observed among LAEs that the Lyα emission signals can have an offset from the UV continuum, with a median 1D projected offset of ≈ 0.6 pkpc in previous slit spectroscopic data (e.g., Hoag et al., 2019; Ribeiro et al., 2020; Lemaux et al., 2020). Larger offsets have also been found in narrow-band imaging data (e.g., Shibuya et al., 2014). However, we note that the continuum fluxes of galaxies $B1$ and $B2$ are much fainter than the LAEs considered in those studies.

We use image e, the most complete image among all five multiple images of System B, to compute the total flux of the Lyα emission. Despite of the flux anomaly observed in
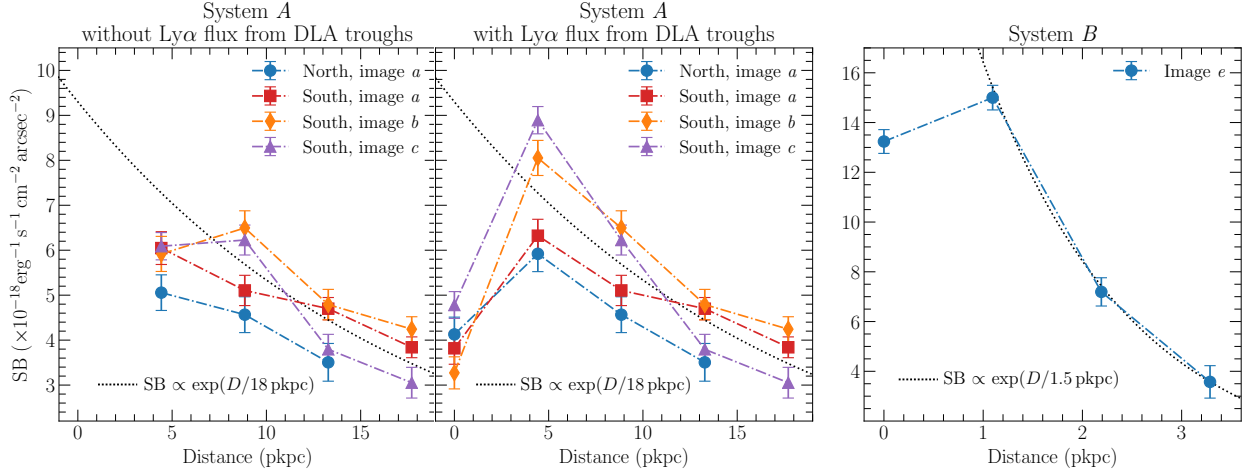
Figure 2.9: De-lensed Lyα surface brightness profile, extracted along the directions indicated in Figures 2.7 and 2.8. For System A, we present the surface brightness profile both before and after including the Lyα flux from the DLA troughs at the locations of galaxy continuum. Distance is measured from the location of $A1$ ($A2$ and $A3$) for the northern (southern) nebula. For System B, zero distance corresponds to the location of $B1$. Note that we use rectangle apertures to extract the surface brightness profile as guided by the velocity gradient within the nebulae, instead of circular annuli (see text). In both systems, there is a decrease in surface brightness at small distances. The suppression may be attributed to either attenuation by the observed high neutral gas column density and possibly high dust content in System A or by a reduced total gas column as a result of galactic scale outflows in System B.

image e of galaxy $B1$ as discussed in §2.4.1, the effect is likely localised (since image e of $B2$ does not show the same brightness enhancement) and therefore will not significantly bias the total Lyα flux from the extended nebula. After correcting the lensing magnification for each spaxel, we obtain a total flux of $f_{\mathrm{Ly}\alpha}(B) = (7.4 \pm 0.2) \times 10^{-18}\,\mathrm{erg\,s^{-1}\,cm^{-2}}$, integrated across the wavelength range of 5766-5796 Å (the same wavelength window for constructing the narrow-band image described above) and summed over all spaxels within the 3-σ contour in image e. At $z = 3.754$, the observed Lyα flux translates to a total luminosity of $L_{\mathrm{Ly}\alpha}(B) = (9.8 \pm 0.2) \times 10^{41}\,\mathrm{erg\,s^{-1}}$.

For both systems, we also extract the de-lensed one-dimensional Lyα surface brightness profile in the source plane starting from the galaxy continuum regions to the edge of each nebula (near the 3-σ surface brightness contours), as shown in Figure 2.9. In §2.5.3 below,

we derive the velocity gradient within the nebulae in both systems. As the velocity gradient suggests non-spherical gas flows in both systems, we therefore use a series of $2'' \times 0\!''6$ ($1'' \times 0\!''15$) pseudo slits for System A (System B), instead of circular annuli. We then extract the surface brightness profiles along directions guided by the velocity gradient within the nebulae (cyan dashed arrows in Figures 2.7 and 2.8; also see §2.5.3 below). The position angle of the pseudo slit is $25°$ north through east for System A and $60°$ north through west for System B. The first aperture (distance of zero) is centered on the de-lensed locations of galaxy $A1$ ($A2$ and $A3$) for the northern (southern) nebula in System A, and the distance of the subsequent apertures are measured from these corresponding continuum regions. For System B, the distance is measured from the location of $B1$, where we put the first aperture. We show the surface brightness profiles for System A both before and after including the Lyα flux inside the DLA troughs from star forming regions (see Figure 2.4).

As discussed above, Lyα surface brightness from the southern nebula agrees well across all three multiple images before including Lyα flux from DLA troughs, while image a becomes dimmer than images b and c after including the Lyα flux from the DLA troughs, suggesting a relatively smaller magnification factor in image a than what is predicted by the lens model at the locations of $A2a$ and $A3a$. Figure 2.9 shows that both Systems A and B exhibit a general decline in Lyα surface brightness with increasing projected distance. Applying a simple exponential profile to characterize the observed surface brightness, $\mathrm{SB}(\mathrm{Ly}\alpha) \propto \exp(-D/D_s)$, we find a best-fit scale radius of $D_s \approx 18$ pkpc for System A and $D_s \approx 1.5$ kpc for System B (see Figure 2.9), corresponding to a half-light radius of $r_e \approx 30$ and 2.5 pkpc for Systems A and B, respectively. These are consistent with the typical size found for Lyman break galaxies (e.g. Steidel et al., 2011) and LAEs (e.g. Wisotzki et al., 2016; Leclercq et al., 2017).

At the same time, we also see a suppressed Lyα surface brightness at the locations of the galaxies. The suppression resembles what is seen in the "net absorption" sub-sample of stacked Lyα surface brightness profiles of (Steidel et al., 2011). We propose that the

suppression may be attributed to attenuation by dusty outflows, which is supported by the observed high neutral gas column density and blueshifted low-ionization ISM absorption line in System A. Under the dusty outflow scenario, the radial extent of the observed dip in the center of the Lyα surface brightness profile is then a direct measure of the projected radius of the dusty outflows, which in the present cases amounts to $\lesssim 5$ pkpc for System A and $\lesssim 1$ pkpc for System B. Dust in the ISM could also contribute to the suppression of the Lyα signal in the gap, which would imply an anisotropic distribution of the dusty material in the ISM given the presence of extended Lyα nebulae at larger distances away from the line-of-sight. Alternatively, the suppression may be attributed to a reduced $N(\text{HI})$ as a result of galactic scale outflows or galaxy interactions (e.g., Johnson et al., 2014).

2.5.2   Spatial variation of line profiles

In addition to the surface brightness variation in the narrow-band images, the Lyα nebulae in both systems exhibit a double-peak profile with a significantly enhanced red peak that indicates expansion/outflowing motions. In the *top-left* panel of Figure 2.10, we present stacked Lyα spectra from the northern and southern nebulae in System A. The spectra are extracted separately from within the 3-σ contours in Column (2) of Figure 2.6. In the *top-right* panel of Figure 2.10, we present stacked Lyα spectra for System B, extracted from within the low-surface brightness (between 3-σ and 8-σ contours) and high-surface brightness (within the 8-σ contours) regions shown in Figure 2.8. An overall shift in wavelength, both in the peak locations and the location of the valley of the Lyα line, is clearly seen between the northern and southern nebulae in System A, with the northern nebula being blueshifted by ≈ 200 km s^{-1} relative to the southern one, suggesting a large velocity gradient across the line-emitting region. At the same time, no significant differences are seen between low- and high-surface brightness regions in System B.

To investigate in detail the velocity offset and possible spatial fluctuations in the Lyα
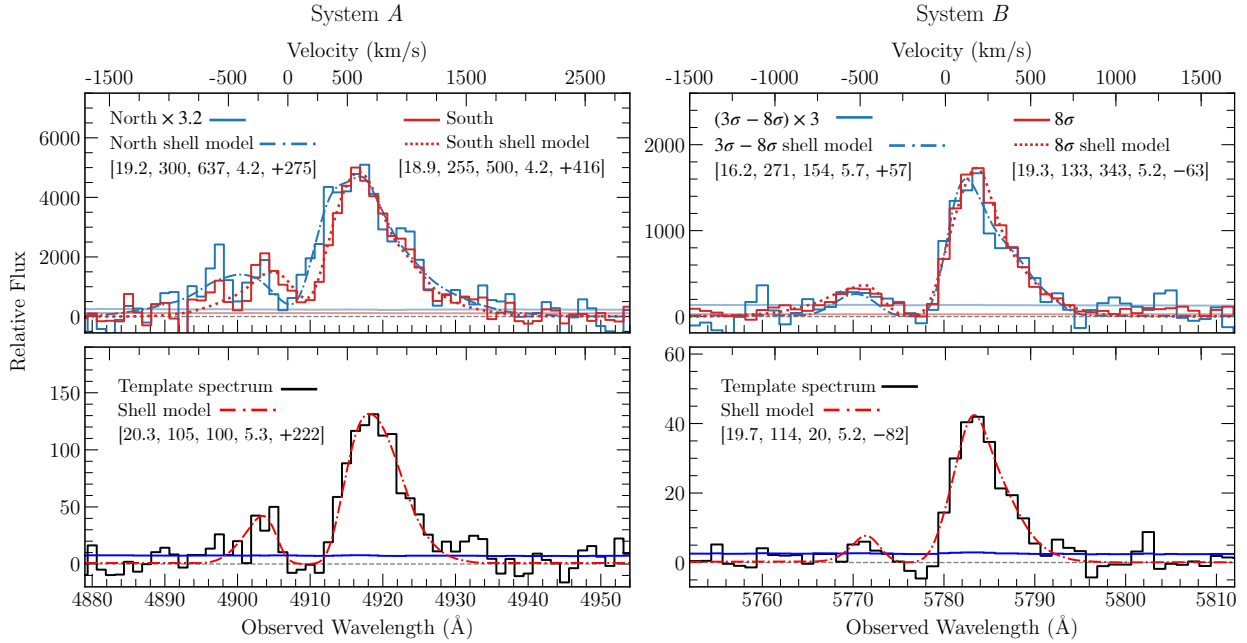
Figure 2.10: Spatial variation of the observed Lyα profiles and its impact on the best-fit shell model for Systems *A* (*left*) and *B* (*right*). *Top* panels display the summed Lyα line profiles over a large area, while *bottom* panels display the template Lyα profiles extracted from localized, small apertures indicated in Figure 2.7 for System *A* and stacked brightest pixels from multiple images *c*, *d* and *e* for System *B* (see text) . The corresponding best-fit model profiles from the expanding shell model described in the text are included as dotted and dash-dotted curves with the best-fit parameters summarized in the legend, following the order of [log $N(\mathrm{HI})/\mathrm{cm}^{-2}$, $v_{\mathrm{exp}}\,(\mathrm{km\,s}^{-1})$, $\sigma_i\,(\mathrm{km\,s}^{-1})$, log $T_{\mathrm{eff}}/\mathrm{K}$, $\Delta v\,(\mathrm{km\,s}^{-1})$]. For the large area sums in the *top* panels, System *A* is naturally divided into northern and southern nebulae, while System *B* is broadly divided by low- and high-surface brightness regions, between within and outside of the 8-σ contours. Zero velocity corresponds to $z_{\mathrm{sys}} = 3.0364$ for System *A*, which is the systemic redshift of *A*1, and $z_{\mathrm{sys}} = 3.7540$ for System *B*, which is the systemic redshift of *B*1 and *B*2. The largest distinction between large and small aperture stacks is seen in System *A*, both in terms of the flux level in the valley between the blue and red peak as well as the profile line width, which is captured by a combination of neutral hydrogen column density log $N(\mathrm{HI})/\mathrm{cm}^{-2}$, intrinsic line width ($\sigma_i$) and effective temperature (log $T_{\mathrm{eff}}/\mathrm{K}$). The line profiles are significantly broader in the stacked spectra obtained over a larger area. In contrast, such distinction is much less visible in System *B*.

profiles across both nebulae, we need to employ smaller apertures for extracting Lyα spectra. Specifically, we consider two competing factors when determining the extraction apertures: (1) the S/N necessary to obtain significant signal in both the blue and red peaks and (2) possible spatial smearing of the extracted Lyα profile over a large aperture that may lead to erroneous characteristics of the Lyα profile. Because of the low surface brightness nature across all regions in System A, the Lyα line per spaxel does not have sufficiently high signals. We therefore experiment with extracting Lyα spectra from a range of aperture sizes to identify an appropriate aperture size for achieving a sufficiently high S/N while limiting the smearing effect from combining different regions. We obtain the optimal extraction aperture from a localized, small area with a radius of $0\rlap{.}''5$ centered near the highest surface brightness peak in the reconstructed source-plane narrow-band image (blue dashed circles in Column (2) of Figure 2.7). We then identify the spaxels located whitin this area in the image plane in all three multiple images a, b and c, and construct a template spectrum for System A by coadding the spectra from all identified spaxels, which contains the information of gas properties in the brightest region of the nebula. The template spectrum is displayed in the *bottom-left* panel of Figure 2.10.

Although the S/N of the template spectrum is lower than what is seen in the large-area stacks (*upper-left* panel of Figure 2.10), the signal is strong enough to demonstrate the significant difference between the Lyα profiles extracted from small and large areas. Specifically, the template spectrum has a narrower width than the large-area stacks from both the northern and southern nebulae. In addition, the template spectrum exhibit a flux level that is consistent with zero at the bottom of the valley between the red and blue peaks. The observed zero flux in the valley is consistently seen across the nebulae in all spectra extracted from small apertures, and differs from the distinctly non-zero flux observed in the stacked spectra over the larger nebulae (see also Figure 3 of Caminha et al. 2017). Such difference can be naturally explained by the presence of a large velocity gradient in the

nebulae that results in smearing of the combined Lyα profile. But because a non-zero flux in the valley of a double-peak Lyα profile would lead to very different parameters constraints for the expanding shell model (e.g. Dijkstra et al., 2006; Verhamme et al., 2006; Hansen & Oh, 2006; Laursen et al., 2009; Schaerer et al., 2011; Gronke et al., 2015, also see below), the ability to spatially resolve the velocity field is necessary for obtaining accurate constraints for the underlying gas properties. In our study, we leverage lensing magnifications to resolve spatial variations on scales as small as ≈ 2 pkpc along both nebulae (Systems A and B) in ground-based, seeing-limited data, though we caution that variations on smaller scales may still be present in these clouds (e.g. Cantalupo et al., 2019).

For System B, because the nebula is significantly brighter than what is seen in System A and the distinction in the observed Lyα profile is subtle between different locations, we construct a template spectrum using only the brightest pixels in images c, d and e (one pixel from each image) to better constrain possible velocity gradient and spatial variation over a small area. The locations of the three brightest pixels included in the template spectrum are indicated by the black arrows in Column (*1*) of Figure 2.8. The template spectrum for System B is displayed in the *bottom-right* panel of Figure 2.10, and does not show significant differences from the stacked spectra from larger areas (*upper-right* panel of Figure 2.10).

2.5.3   *Physical properties of Lyα nebulae under an expanding shell model*

We utilize the spatially and spectrally resolved Lyα profiles from MUSE observations and a Lyα Monte Carlo radiative transfer code `tlac` (Gronke & Dijkstra, 2014; Gronke et al., 2015) to model the physical properties of the line-emitting gas. We adopt an expanding shell model that has successfully explained many observed Lyα spectra across a wide range of redshifts based on a finite set of parameters, including the neutral hydrogen column density, $N(\mathrm{H\,{\scriptstyle I}})$, the expansion velocity, v_{exp}, intrinsic line width, σ_i, effective temperature, T_{eff}, and systemic velocity, Δv (e.g. Verhamme et al., 2006; Yang et al., 2017; Gronke, 2017).

Table 2.6: Summary of the best-fit parameters (95% confidence interval) for characterizing the observed Lyα profile under an expanding shell model.

Spectrum	$\log N(\mathrm{HI})/\mathrm{cm}^{-2}$	v_{exp} (km/s)	σ_i^a (km/s)	$\log T_{\mathrm{eff}}/\mathrm{K}$	Δv^b (km/s)	χ_ν^2
System A, $z_{\mathrm{sys}} = 3.0364$						
North	$19.2_{-0.3}^{+0.2}$	300_{-30}^{+40}	637_{-51}^{+28}	$4.2_{-1.2}^{+0.6}$	275_{-37}^{+60}	6.6
South	$18.9_{-0.1}^{+0.2}$	255_{-36}^{+6}	500_{-7}^{+49}	$4.2_{-0.5}^{+0.1}$	416_{-44}^{+7}	10.6
Template spectrum	$20.3_{-0.2}^{+0.2}$	105_{-20}^{+27}	100	$5.3_{-0.2}^{+0.2}$	222_{-30}^{+22}	2.4
System B, $z_{\mathrm{sys}} = 3.7540$						
$3\sigma - 8\sigma$	$16.2_{-0.7}^{+3.4}$	271_{-174}^{+63}	154_{-57}^{+218}	$5.7_{-2.4}^{+0.2}$	57_{-138}^{+57}	0.9
8σ	$19.3_{-0.1}^{+0.2}$	133_{-15}^{+10}	343_{-22}^{+20}	$5.2_{-0.2}^{+0.0}$	-63_{-19}^{+13}	5.3
Template spectrum	$19.7_{-0.2}^{+0.1}$	114_{-19}^{+17}	20	$5.2_{-0.2}^{+0.2}$	-82_{-19}^{+25}	1.3

[a] Values without errors indicate a prior specified by the nebular emission lines (see Table 2.5).
[b] Relative velocity with respect to z_{sys}.

As illustrated in Verhamme et al. (2006), while there are considerable degeneracies between different parameters of the shell model, the peak separation increases primarily with $N(\mathrm{HI})$, and the red-to-blue peak ratio increases with v_{exp}, while T_{eff} and σ_i set the overall line width (see also Gronke et al., 2015, for a more detailed discussion on the effect of these parameters). In most cases this simple shell model provides a crude estimate of the underlying kinematic properties of the gas, but there are also known cases where the model failed to provide a good fit to data (e.g. Kulas et al., 2012; Orlitová et al., 2018).

We note that the shell models are developed for a spherical shell expanding radially outward, which may work better for unresolved Lya nebulae under the assumption that the emission sources are at the center of the gas. In applying these models to System A, for which the Lyα photons may originate outside of the nebulae, we attribute the enhanced red peak in the observed Lyα profile per spaxel to cloud expansion relative to a fiducial reference point interior to the cloud along the observer's line of sight. In addition, we attribute the observed velocity shear to the motion of this reference point relative to the systemic redshift of the galaxies. Although the source of photons likely lies outside of the nebulae (see §2.6 below for discussions on the origin of Lyα photons), the problem is equivalent to extracting the

Lyα signal from one hemisphere of a spherical shell. Because of spherical isotropy inherent to the shell model, we expect that considering one hemisphere would result in an overall reduction in the amplitude of the signal, instead of altering the line profile. Guided by this understanding, we proceed with approximating the signal in each spaxel with expectations from an expanding shell model for constraining the systemic velocity at each location.

For our analysis, we assume a homogeneous medium of constant gas density and compare the observed Lyα profiles with predictions over a grid of model parameters. To fully explore the allowed parameter space, we construct a model grid that covers $\log N(\mathrm{H\,I})/\mathrm{cm}^{-2}$ from 15.1 to 21.1, v_{exp} from 10 to 400 $\mathrm{km\,s}^{-1}$, σ_i from 25 to 700 $\mathrm{km\,s}^{-1}$, $\log T_{\mathrm{eff}}/\mathrm{K}$ from 3.0 to 6.0, and Δv from -100 to 550 $\mathrm{km\,s}^{-1}$. The velocity offset, Δv, is calculated with respect to the systemic redshift z_{sys} listed in Table 2.6. We use 10,000 photons and 100 frequency bins to generate each model profile. Each model profile is also convolved with MUSE line spread function before compared to observations. Given the uncertainty of the dust attenuation effect on Lyα photons, we do not include dust in our models and it will be explored separately in the future. For each model, we compute a likelihood function $\mathscr{L}$ defined as

$$
\begin{aligned}
&\mathscr{L}(N_{\mathrm{H\,I}}, v_{\mathrm{exp}}, \sigma_i, T_{\mathrm{eff}}, \Delta v) \\
&= \prod_j \exp\left\{ -\frac{[D(\lambda_j) - M(\lambda_j | N_{\mathrm{H\,I}}, v_{\mathrm{exp}}, \sigma_i, T_{\mathrm{eff}}, \Delta v)]^2}{2\, S^2(\lambda_j)} \right\},
\end{aligned}
$$

(2.6)

where $D(\lambda_j)$ and $M(\lambda_j)$ are the observed and model spectra, respectively, and $S(\lambda_j)$ is the corresponding error spectrum. The likelihood function is computed over the wavelength range of 4890-4930 Å (5766-5796 Å) for System A (System B), and can be translated to χ^2 following $\chi^2 = -2 \ln \mathscr{L}$. We then construct a marginalised likelihood function for each parameter by integrating $\mathscr{L}$ over all other parameters, and find the 95% confidence interval
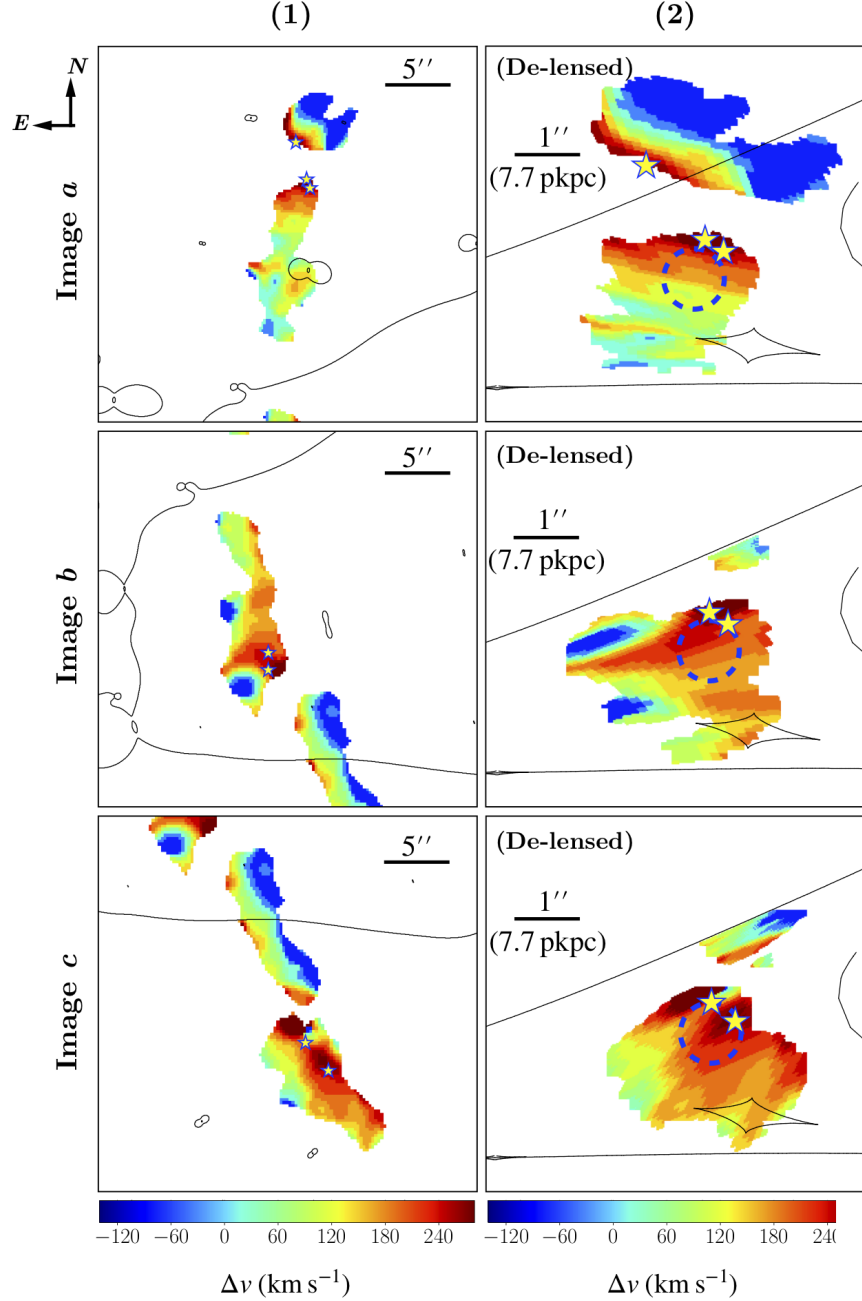
Figure 2.11: Column (*1*): velocity map of multiple images *a*, *b* and *c* in System *A*, derived from cross-correlating the best-fit shell model for the template spectrum (*bottom-left* panel of Figure 2.10) and spectra extracted from spaxels within the 3-σ contours. Zero velocity corresponds to $z_{\rm sys} = 3.0364$, which is the systemic redshift of *A*1 derived from nebular emission lines. Column (*2*): de-lensed velocity map of individual images in the source plane. Star symbols mark the positions of the associated star-forming galaxies identified in *HST* images (see Figures 2.6 and 2.7). The blue dashed circles, same as in Column (*2*) of Figure 2.7, mark the apertures for the template spectrum extraction, which we use for the shell model analysis.
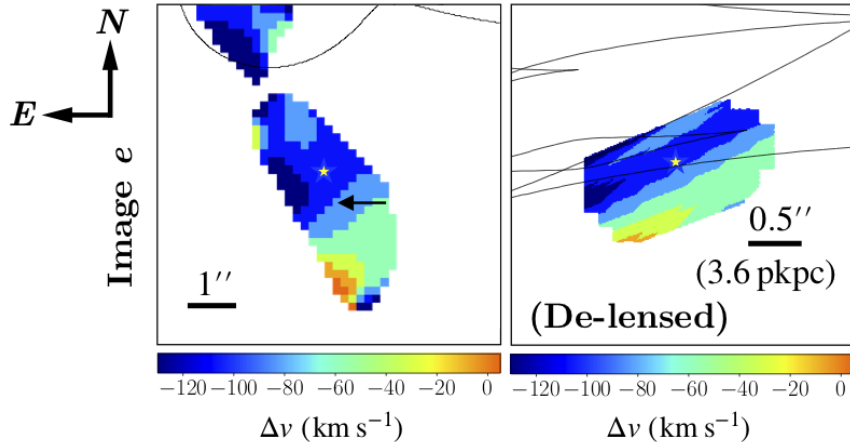
Figure 2.12: *Left*: velocity map of image e in System B, derived from cross-correlating the best-fit shell model for the template spectrum (*bottom-right* panel of Figure 2.10) and spectra extracted from spaxels within the 3-σ contour. Zero velocity corresponds to $z_{\rm sys} = 3.7540$, which is the systemic redshift of $B1/B2$ derived from nebular emission lines *Right*: de-lensed velocity map of image e in the source plane. Star symbols mark the position of $B1/B2$ determined from *HST* images (see Figure 2.8). The black arrow, same as in Column (*1*) of Figure 2.8, indicate the brightest pixel in image e that is included in the template spectrum.

centered around the best-fit value. Note that since we do not explicitly include turbulent broadening in the models here, the temperature inferred from the model represents an effective temperature that includes non-thermal motion. For reference, for an intrinsic gas temperature of $T = 10^4$ K, an inferred effective temperature of $T_{\rm eff} = 10^5$ (10^6) K implies an underlying bulk flow of $\sigma_v^{\rm bulk} \approx 30$ (90) km s^{-1}.

To illustrate the impact of velocity smearing on the Lyα profile analysis, we first consider stacked spectra obtained over a large area along with the best-fit model profiles (*top* panels of Figure 2.10). The best-fit parameters and the associated 95% confidence intervals are presented in Table 2.6. The large χ_ν^2 values in Table 2.6 show that an expanding shell model fails to provide a good fit for the high S/N stacked Lyα spectra for both systems. A close examination of the profiles in the *top* panels of Figure 2.10 shows that the best-fit models with an uncharacteristically large intrinsic line width of $\sigma_i \approx 500$-650 km s^{-1} provide a poor fit to the blue peak of the northern and southern nebulae in System A. The best-fit σ_i is substantially broader than either what is seen in the nebular emission lines (see Table 2.5)

or what is expected for the velocity dispersion in halos of a comparable mass scale for the host galaxies (e.g. $M_{\mathrm{halo}} < 10^{12}\,M_\odot$; Trainor & Steidel, 2012). For System B, while the small χ^2_ν for the stacked spectrum from low-surface brightness regions suggests a good fit to the data, the model remains poorly constrained with large associated uncertainties due to the low S/N of the data. At the same time, the best-fit shell model produces a relatively poor fit to the blue peak of high S/N, high-surface brightness regions, leading to a large χ^2_ν.

To improve the precision and accuracy of the model constraints, we perform the profile analysis for the template spectra extracted from localized, small apertures presented in the *bottom* panels of Figure 2.10. In addition, we adopt the observed nebular line width (see Table 2.5) as a prior for modelling the Lyα profiles. This is justified by the understanding that these Lyα photons likely originate in the star-forming regions of the associated galaxies (see §2.6 below). Specifically, we set $\sigma_i = 100\ \mathrm{km\,s^{-1}}$ for System A based on the observed FWHM of $\approx 240\ \mathrm{km\,s^{-1}}$ in galaxy $A2$, and $\sigma_i = 20\ \mathrm{km\,s^{-1}}$ for System B based on the observed FWHM of $\approx 40\ \mathrm{km\,s^{-1}}$ in galaxies $B1/B2$. The best-fit model profiles are shown in dotted and dash-dotted curves and best-fit parameters are presented in Table 2.6. It is immediately clear that the resulting χ^2_ν is reduced substantially and the parameters are well-constrained. In contrast, setting the same prior on σ_i when fitting the stacked spectra from larger apertures results in poor model fits with larger χ^2_ν values (see Appendix). This again underscores the smearing effect on stacked Lyα profiles extracted from larger areas, which can significantly bias the constrained gas properties with the presence of velocity gradient and spatial variations in the line emitting region. The best-fit models also suggest that both Systems A and B consistently require a large neutral hydrogen column density, $\log N(\mathrm{H\,I})/\mathrm{cm}^{-2} \gtrsim 19$ for explaining the observed Lyα profiles from localized locations.

Because of the competing factors between spectral qualities (i.e., S/N) and velocity smearing, in addition to a strong degeneracy between different model parameters with modest S/N data, we continue the analysis with a focus on constraining the velocity field, Δv,

across the Lyα nebulae. This is achieved by cross-correlating the best-fit shell model for the template Lyα spectra with each spaxel within the 3-σ contours in both systems to measure velocity offsets at different locations. To optimize the cross-correlation analysis, we spatially smooth the data cube with a Gaussian filter of $\text{FHWM}_{\text{smooth}} = 1''$ before extracting individual spectra. The resulting velocity maps are presented in Figure 2.11 for System A and Figure 2.12 for System B. We also present de-lensed velocity maps of both nebulae in the source plane. We have also experimented with constraining the velocity gradient by fitting an asymmetric Gaussian function (e.g., see Eq.1 of Leclercq et al., 2020) to the red peak of the Lyα profile from every spaxel within the 3-σ contour in both systems, and we obtain a similar velocity gradient as shown in Figures 2.11 and 2.12. Our method utilising the best-fit model of the template spectra enables us to determine the systemic velocity offset Δv of the line-emitting gas in the frame of the nearby star-forming region, thereby connecting the nebulae with the associated star-forming regions.

Our analysis of System A has uncovered a highly organized velocity field across the Lyα emitting nebulae, with increasing velocity offset from $\Delta v \approx 0$ km s^{-1} at ≈ 11 pkpc south of galaxies $A2$ and $A3$ to $\Delta v \approx +250$ km s^{-1} at the locations of these galaxies (Figure 2.11). In the north, the velocity offset decreases from $\Delta v \gtrsim +200$ km s^{-1} at the location of galaxy $A1$ to $\Delta v \approx -150$ km s^{-1} at ≈ 13 pkpc northwest of $A1$. The inferred velocity offset shows that the line-emitting gas closest to the galaxies is receding from the galaxies. Different from the extended blue wings seen in ISM absorption lines, this velocity offset seen in Lyα emission places the gas behind the star-forming region. The observed steep velocity gradient, $|\Delta v / \Delta r_{\perp}| \approx 22 - 27$ km s^{-1} pkpc^{-1}, together with a large best-fit $N(\text{H\,I})$ and an enhanced red peak in the Lyα profile across the nebula supports a scenario in which high column density gas is driven outward from the galaxies to beyond 10 pkpc in projected distance into the low-density surroundings. Due to a lack of AGN activities (see §2.4.4), the outflows are likely driven by star formation in these young galaxies.

It is interesting that there exists an apparent gap in Lyα signal between the northern and southern nebulae. One possible explanation for this gap is a reduced N(HI) as a result of galaxy interactions. A lack of strong Lyα absorber has been seen at projected distances of < 20 pkpc from an interacting galaxy pair at low redshift with an upper limit of log N(HI)/cm$^{-2} \lesssim 13.7$ (e.g. Johnson et al., 2014). In the optically thin regime, we estimate a 2-σ upper limit of log N(H I)/cm$^{-2} < 16.4$ at ≈ 5 pkpc based on the observed 2-σ upper limit in Lyα surface brightness and an assumption of 100% escape fraction of ionizing photons from the galaxies. While at this limit, the gas would still be optically thick to Lyα photons, we cannot rule out the possibility of a significantly lower N(HI). Other plausible explanations for the gap also include a lack of illumination from young stars due to anisotropic leakage of Lyα and ionizing photons, and attenuation of Lyα signal due to highly neutral, dusty gas in-between these galaxies (also see discussion in §2.6 below).

In contrast, System B exhibits distinct properties from System A. The Lyα nebula appears to be distributed symmetrically around galaxies B1 and B2 with the peak intensity located close to star forming regions. The inferred line-of-sight velocity offset of ≈ -100 km s^{-1} near the location of the galaxies, coupled with the observed Lyα profile, again supports an outflow scenario from the galaxies. The observed velocity gradient of $|\Delta v/\Delta r_\perp| \approx 20$ km s^{-1} kpc^{-1} toward the outer edge of the nebula may be explained by a line-of-sight projection effect.

2.6   Discussion

We have shown that by accounting for spatial variations in the observed Lyα line profiles, we are able to determine the velocity field and constrain gas flows across the nebulae. Given the proximity of the line-emitting gas to star-forming galaxies and the relatively small velocity offset between gas and galaxies, we argue that the gas is being driven out of the star-forming regions at a modest speed. Specifically, the Lyα nebula of System B exhibits a

relatively symmetrical morphology with the peak of the Lyα emission located close to the star-forming regions. This configuration is typical of low-mass LAEs at high redshifts (e.g. Wisotzki et al., 2016; Leclercq et al., 2017), and suggests that gas flows outward from the star-forming regions into the low-density halo environment. At the same time, galaxies $A1$, $A2$ and $A3$ share similar spectral and photometric properties (see §2.4). The close proximity of these three galaxies suggest that they may share an interactive group environment and are part of a common CGM. The Lyα nebulae are clearly offset to one side of the galaxies with the highest surface brightness regions bordering the continuum-emitting regions (see Figures 2.6 and 2.7). While the star-forming regions contribute significantly to the extended Lyα emission, the connection between the star-forming regions and the large-scale outflows remains uncertain.

We consider two plausible scenarios for the origin of the outflows. First, the northern nebula originates in gas flowing out of $A1$, while the southern nebula originates in gas flowing out of galaxies $A2$ and $A3$. This is plausible if all three galaxies are capable of driving galactic scale super winds. Applying the conversion factor of Madau & Dickinson (2014), we estimate an unobscured SFR of $\approx$ 22, 5 and 4 $M_\odot\,\mathrm{yr}^{-1}$ for galaxies $A1$, $A2$, and $A3$, respectively, based on the observed rest-frame UV absolute magnitudes M_{1500} presented in Table 2.2. In the presence of dust, this observed M_{1500} and inferred SFR are likely lower limits to the intrinsic values. In addition, we estimate a total projected area based on the continuum regions determined by SExtractor (see §2.4.1) and apply lensing magnification corrections based on the fine-tuned lens model (see §2.3). We find the intrinsic projected area of $A1$, $A2$, and $A3$ to be $\approx$ 50, 11 and 11 pkpc^2, respectively. For galaxies $A2$ and $A3$, these are based on an average over all three images, a, b, and c after lensing magnification corrections. Combining the estimated unobscured SFR and projected area leads to an estimate of SFR per unit area of $\gtrsim 0.4\,M_\odot\,\mathrm{yr}^{-1}\,\mathrm{pkpc}^{-2}$ in these individual galaxies. This exceeds the empirical threshold seen in driving galactic scale super winds in local starburst galaxies (e.g. Heckman

et al., 2015).

Alternatively, galaxy $A1$ may be the single dominant source driving the outflows seen in both the northern and southern nebulae. Apart from being the most massive galaxy with the highest SFR in the group, $A1$ also shows more extended blue wings in the low-ionization ISM absorption lines (see Figure 2.4), suggesting the presence of galactic outflows that are more prominent than what is seen from the same line features in galaxies $A2$ and $A3$. In this scenario where galaxy $A1$ is the origin of the outflows on both sides, the gap in Lyα emission between the northern and southern nebulae is likely due to dusty outflow materials from galaxy $A1$ that cover the gap area along the line-of-sight.

A remaining question of the observed line-emitting nebulae is the origin of Lyα photons. As described earlier, multiple mechanisms can lead to Lyα emission in diffuse gas, including cooling radiation, fluorescence powered by ionizing photons from either star-forming regions or AGN, and resonant scattering by neutral hydrogen gas (e.g., Hogan & Weymann, 1987; Gould & Weinberg, 1996; Cantalupo et al., 2005; Kollmeier et al., 2010; Faucher-Giguère et al., 2010; Hennawi & Prochaska, 2013). Disentangling between different mechanisms that are responsible for the observed Lyα signals is challenging, especially when the Lyα line is the only observable feature in the nebulae.

For the two systems in our study, however, the observed spectral properties of the Lyα line enable us to rule out cooling radiation and photo-ionization due to the cosmic UV background radiation as a dominant mechanism for powering the observed emission. Specifically, radiatively cooled gas is expected to condense and sink through the hot ambient medium, resulting in infall, and the majority of the photons will travel through the infalling clouds before escaping the medium (e.g., Faucher-Giguère et al., 2010). The expectation of an enhanced blue-peak from infalling gas in inconsistent with the observations. In addition, the expected Lyα fluorescence signal from cosmic UV background alone is low with surface brightness of $\lesssim 10^{-19}\,\mathrm{erg\,s^{-1}\,cm^{-2}\,arcsec^{-2}}$ (e.g., Kollmeier et al., 2010).

We therefore proceed with considerations of the two remaining scenarios: (1) Lyα photons arising as a result of fluorescence powered by ionizing photons from star-forming regions and (2) Lyα photons produced in the galaxies and resonantly scattered by neutral hydrogen in the nebulae. The first scenario requires a non-zero escape fraction of ionizing photons from the galaxies, while the second scenario corresponds to the shell model analysis described in §2.5.3. Here we also discuss the implications of these scenarios.

2.6.1 Lyα emission from recombination radiation and implications for the escape fraction of ionizing radiation from star-forming galaxies

We first consider the possibility that the observed Lyα signals are powered by *in situ* star formation directly underneath the nebulae. Available deep *HST* F606W image places strong constraints on the rest-frame UV continuum flux at the location of the nebulae. Using the integrated Lyα luminosity of $L_{\rm Ly\alpha} = (2.15\pm0.07)\times10^{42}\,{\rm erg\,s}^{-1}$ ($[3.49\pm0.08]\times10^{42}\,{\rm erg\,s}^{-1}$) for the northern (southern) nebula of System A, we infer an SFR of $\approx 1.1\,(2.3)\,{\rm M}_\odot\,{\rm yr}^{-1}$ based on a conversion factor of Lyα/Hα = 8.7 (Hayes, 2015, and references therein) and the Hα-SFR relation of Kennicutt & Evans (2012). From the inferred SFR, we derive the expected apparent magnitude in the F606W bandpass (corresponding to 1500 Å in the rest frame at $z \approx 3$) of AB(F606W) ≈ 27.3 (26.5) using the FUV flux-SFR relation of Madau & Dickinson (2014) for the underlying star-forming regions in the northern (southern) nebula. The inferred F606W magnitude is roughly more than two magnitudes brighter than the 2-σ detection limit in the F606W bandpass (AB(F606W) ≈ 29 within an aperture of $0\rlap{.}''5$ in diameter), but no flux is detected at the location of the nebulae away from the galaxies. While we consider *in situ* star formation an unlikely scenario for powering the Lyα signals, we cannot rule out the possibility that dust obscurations may have played a role in blocking the FUV photons along the line of sight. Deeper imaging data at submillimeter are needed for constraining the effect of dust. In the following discussion, we proceed with considerations

of external sources for powering the observed Lyα signals.

For photo-ionization by the nearby galaxies, the observed Lyα intensity is connected to the incident ionizing radiation field and the discussion often involves considerations of two different regimes, optically thin versus optically thick gas. For the purpose of our study, both Systems A and B consistently require a large $N(\mathrm{H\,I})$, exceeding $\log N(\mathrm{H\,I})/\mathrm{cm}^{-2} \approx 19$ (Table 2.6), for explaining the observed Lyα profile. We therefore consider only optically-thick regime in the subsequent discussion.

In optically-thick regime, ionization occurs in the surface of a cloud illuminated by the ionizing source and roughly 66% of all ionizing photons are converted into Lyα photons through recombination cascades in the surface layer (i.e., $\eta_{\mathrm{B}} = 0.66$) (Osterbrock & Ferland, 2006). The surface brightness of Lyα emission is connected to ionizing photon flux according to

$$
\begin{aligned}
\mathrm{SB}_{\mathrm{Ly}\alpha} &= f_g\, f_{\mathrm{esc}}\, \frac{\eta_{\mathrm{B}}\, h\, \nu_{\mathrm{Ly}\alpha}}{(1+z)^4}\, \frac{\Phi}{\pi} \\
&= 3.2 \times 10^{-18} f_g\, f_{\mathrm{esc}} \left(\frac{1+z}{4.0}\right)^{-4} \left(\frac{D}{10\,\mathrm{pkpc}}\right)^{-2} \\
&\quad \left(\frac{\Phi_0}{10^7\,\mathrm{s}^{-1}\,\mathrm{cm}^{-2}}\right)\ \mathrm{erg\, s}^{-1}\,\mathrm{cm}^{-2}\,\mathrm{arcsec}^{-2}
\end{aligned}
\tag{2.7}
$$

where f_g is the geometric correction coefficient to account for partial illumination of the nebula and redistribution of Lyα photons, f_{esc} is the fraction of ionizing photons that escape the galaxies, D is the distance of the cloud from the ionizing source, and Φ_0 is the ionizing photon flux at a distance of 1 kpc from the source. In principle, comparing the observed Lyα surface brightness with the expected ionizing radiation field from the SED analysis of the galaxies constrains f_{g} and f_{esc} based on Eq. 2.7. In practice, uncertainties in the inferred galaxy spectra are large. Therefore, it is not trivial to obtain accurate constraints for f_g and f_{esc}.

For System A, we estimate the total ionizing photon fluxes from $A1$, $A2$ and $A3$ us-

ing the best-fit BAGPIPES model spectra and find respectively $\Phi_0 \approx 3.4 \times 10^8$, 8.1×10^7, $5.1 \times 10^7\,\mathrm{s}^{-1}\,\mathrm{cm}^{-2}$ at $D = 10$ pkpc. Assuming $f_\mathrm{g} = 0.5$ from numerical simulations (e.g., Cantalupo et al., 2005; Kollmeier et al., 2010) and $f_\mathrm{esc} < 10\%$ as a fiducial upper limit for ionizing photon escape fraction (e.g. Chen et al., 2007; Vanzella et al., 2010; Grazian et al., 2017), the observed peak Lyα surface brightness of $7.3 \times 10^{-18}\,\mathrm{erg}\,\mathrm{s}^{-1}\,\mathrm{cm}^{-2}\,\mathrm{arcsec}^{-2}$ (the 6-σ contour in Figure 2.7) implies a distance limit of $D < 8.5$ pkpc from $A1$ and $D < 3.3$ pkpc from $A3$. Adopting the low-intensity contour of $3.7 \times 10^{-18}\,\mathrm{erg}\,\mathrm{s}^{-1}\,\mathrm{cm}^{-2}\,\mathrm{arcsec}^{-2}$ would increase the distance limit by 40% to $D < 12$ pkpc from $A1$ and $D < 4.6$ pkpc from $A3$. The observed extent of Lyα emission of $\gtrsim 10$ pkpc (see Figure 2.7) therefore requires $A1$ to be the dominant source of ionizing photons with an escape fraction $\sim 10\%$. Current observations suggest that the escape fraction of ionizing photons from massive ($>L_*$) galaxies at $z \approx 3$ is much smaller than 10% (e.g. Grazian et al., 2017). The inferred large $\log(\mathrm{H\,I})$ based on Lyα line profiles also suggests that f_esc is likely to be small. In addition, in §2.6.2 below, we show that resonant scattering of Lyα photons produced in the star-forming regions can account for the full extent of the Lyα nebulae. We therefore conclude that recombination radiation from photo-ionized gas alone is unlikely to dominate the observed Lyα signal in System A.

We repeat the same exercise for System B. Due to the smaller physical scale of System B, we estimate the ionizing photon flux at a distance of $D = 1$ pkpc. Using the best-fit BAGPIPES model spectra, we obtain the total ionizing photon flux from $B1$ and $B2$ combined to be $\Phi \approx 1.4 \times 10^8\,\mathrm{s}^{-1}\,\mathrm{cm}^{-2}$ at 1 pkpc. The observed surface brightness of $7.5 \times 10^{-18}\,\mathrm{erg}\,\mathrm{s}^{-1}\,\mathrm{cm}^{-2}\,\mathrm{arcsec}^{-2}$ (the 8-σ contour in Figure 2.8) leads to $(f_\mathrm{g} f_\mathrm{esc}) \approx 33\%$, or $f_\mathrm{esc} = 66\%$ assuming $f_\mathrm{g} = 0.5$. At the limit of $f_\mathrm{esc} < 1$, we infer the distance limit of $D < 1.2$ pkpc for the high-intensity contours. With the low-intensity surface brightness of $2.8 \times 10^{-18}\,\mathrm{erg}\,\mathrm{s}^{-1}\,\mathrm{cm}^{-2}\,\mathrm{arcsec}^{-2}$ (the 3-σ contour in Figure 2.8), the inferred distance limit is increased to $D < 2$ pkpc. Because the observed Lyα emission extends to $\gtrsim 4$ pkpc in the source plane (see Figure 2.8), we conclude that recombination radiation from photo-ionized

gas alone *cannot* explain all of the observed Lyα photons away from the galaxies in System B.

2.6.2 Lyα emission from scattering and implications for dust attenuation

Given the star-forming nature of the galaxies in both Systems A and B, we now consider the scenario in which the Lyα photons are produced in the star-forming ISM of the galaxies and resonantly scattered through the spatially extended nebulae. Using the estimated SFR in the 16%–84% confidence interval for galaxies A1, A2 and A3 (see Table 2.4), we infer a total intrinsic Lyα luminosity of $L_{\mathrm{Ly}\alpha}^{\mathrm{int}}/(10^{44}\,\mathrm{erg\,s^{-1}}) = 1.46$–1.65, 0.17–0.19, and 0.21–0.26 for galaxies A1, A2, and A3, respectively, using the conversion factor of Lyα/Hα = 8.7 (Hayes, 2015, and references therein) and the Hα-SFR relation of Kennicutt & Evans (2012). For System B, the same exercise leads to an intrinsic Lyα luminosity of $L_{\mathrm{Ly}\alpha}^{\mathrm{int}} = (1.2$–2.1)$\times 10^{42}\,\mathrm{erg\,s^{-1}}$ for galaxies B1 and B2 combined.

While these star-forming galaxies may be intrinsically luminous in Lyα, we expect that a large fraction of these Lyα photons are unable to escape the ISM due to a substantial amount of dust attenuation. We obtain an empirical estimate of the attenuation factor $k_{\mathrm{dust}} = 1 - L_{\mathrm{Ly}\alpha}^{\mathrm{obs}}/L_{\mathrm{Ly}\alpha}^{\mathrm{int}}$ based on the observed Lyα luminosity of $2.15 \times 10^{42}\,\mathrm{erg\,s^{-1}}$ for the northern nebula and $3.43 \times 10^{42}\,\mathrm{erg\,s^{-1}}$ for the southern nebula, and the intrinsic Lyα luminosity from star-forming regions described above. Attributing the Lyα emission of the northern (southern) nebula to the scattering of Lyα photons from galaxy A1 (galaxies A2 and A3), we estimate k_{dust} to be $\approx 98\%$ and $\approx 92\%$ for the northern and southern nebula, respectively.

Following the optically-thick prescription from Equation 2.7 and replacing ionizing photon flux with Lyα photon flux $\Phi_{\mathrm{Ly}\alpha}$, we can now connect the Lyα scattering surface brightness

to $L^{int}_{Ly\alpha}$ following

$$
\begin{aligned}
\mathrm{SB}_{Ly\alpha} &= \frac{h\,\nu_{Ly\alpha}}{(1+z)^4}\frac{\Phi_{Ly\alpha}}{\pi} \\
&= \frac{h\,\nu_{Ly\alpha}}{(1+z)^4}\frac{(1-k_{dust})\,L^{int}_{Ly\alpha}}{4\pi^2\,D^2\,h\,\nu_{Ly\alpha}} \\
&= 2.4\times10^{-18}\left(\frac{1+z}{4.0}\right)^{-4}\left(\frac{D}{10\,\mathrm{pkpc}}\right)^{-2} \\
&\quad \frac{(1-k_{dust})\,L^{int}_{Ly\alpha}}{10^{42}\,\mathrm{erg\,s^{-1}}}\ \mathrm{erg\,s^{-1}\,cm^{-2}\,arcsec^{-2}}.
\end{aligned}
\tag{2.8}
$$

Eq. 2.8 leads to a distance estimate of $D_{north} \approx 14$ pkpc between the northern nebula and galaxy $A1$ for an observed Lyα surface brightness of 3.7×10^{-18} erg s^{-1} cm^{-2} arcsec^{-2} (the 3-σ contour in Figure 2.7), an intrinsic Lyα luminosity of $L^{int}_{Ly\alpha} = (1.46\text{–}1.65)\times10^{44}$ erg s^{-1} for $A1$, and an attenuation factor of 98%. At higher intensity of 7.3×10^{-18} erg s^{-1} cm^{-2} arcsec^{-2} (the 6-σ contour in Figure 2.7), the distance is reduced to ≈ 10 pkpc. The inferred distance range is fully consistent with the extent of the northern nebula relative to $A1$. In addition, the estimated amount of dust attenuation agrees with $A_V \approx 0.7$ mag inferred from the SED analysis presented in §2.4.2 (see also Table 2.4). Based on the Calzetti et al. (2000) extinction law for starburst galaxies, the estimated stellar extinction of $A_V \approx 0.7$ mag corresponds to an extinction magnitude of $A_{1215} \approx 5.2$ mag for the Lyα emission line, or $k_{dust} \approx 99\%$ for the Lyα photons. It suggests that resonant scattering alone can fully account for the observed Lyα brightness in the northern nebula.

For the southern nebula, galaxies $A2$ and $A3$ together contribute to a total intrinsic Lyα luminosity of $L^{int}_{Ly\alpha} = 3.8\text{-}4.5\times10^{43}$ erg s^{-1}. Adopting $k_{dust} = 92\%$ leads to a distance estimate of $D_{south} \approx 10$ pkpc for the high-intensity region and $D_{south} \approx 15$ pkpc for the low-intensity region between galaxies $A2/A3$ and the southern nebula. Similarly, the estimated size is consistent with the observed extent of the southern nebula (see §2.5.1). Although the dust attenuation of 92% is in tension with the estimated $k_{dust} \approx 99\%$ based on the SED

analysis, we argue that a possible contribution of Lyα photons from galaxy $A1$, together with uncertainties in $f_{\rm esc}$ (see §2.6.1) and $k_{\rm dust}$ in an inhomogeneous, clumpy medium could account for the observed extent of Lyα signals in the southern nebula (e.g., Neufeld, 1991; Hansen & Oh, 2006).

For galaxies $B1$ and $B2$, the uncertainty in $k_{\rm dust} = 1 - L_{{\rm Ly}\alpha}^{\rm obs}/L_{{\rm Ly}\alpha}^{\rm int}$ is larger, ranging between $\approx$ 20–50%. Meanwhile, uncertainties in A_V are also larger, ranging between $A_V \approx$ 0.05-0.25 for $B1$ and $A_V \approx$ 0.5-0.7 for $B2$ (see Table 2.4), corresponding to a wide range of dust attenuation of $\approx$ 30–99% for Lyα photons, in agreement with the emprical $k_{\rm dust}$ of $\approx$ 20–50%. Adopting $k_{\rm dust} = 50\%$, Eq. 2.8 leads to a distance estimate of $D \approx 3$ pkpc between galaxies $B1/B2$ and the observed Lyα intensity peak of $7.5 \times 10^{-18}\,{\rm erg\,s^{-1}\,cm^{-2}\,arcsec^{-2}}$ (the 8-σ contour in Figure 2.8). At ${\rm SB}_{{\rm Ly}\alpha} = 2.8 \times 10^{-18}\,{\rm erg\,s^{-1}\,cm^{-2}\,arcsec^{-2}}$ (the 3-σ contour in Figure 2.8), we estimate a distance of ≈ 5 pkpc, which agrees well with the observed extent of the nebula.

The above exercise shows that resonant scattering of Lyα photons produced in nearby star-forming regions may be sufficient for explaining the observed Lyα signals in both systems without invoking additional emission sources. This is in contrast to the recombination radiation scenario discussed in §2.6.1. It shows that even at 100% escape fraction of ionizing photons, recombination is insufficient for explaining the observed Lyα flux in System B and that it would require an escape fraction of $\sim$10% from $A1$ for recombination to contribute significantly to the emission signal.

2.6.3 Systematics in interpreting the spatial and spectral profiles of the nebulae

Due to the clumpy nature of line-emitting gas, the surface brightness profile of extended nebulae is subject to the spatial variation of lensing magnification and its associated uncertainties in the image plane. In principle, gravitational lensing conserves surface brightness

of a light-emitting source. However, the conservation of surface brightness does not apply when the lensed image of the source is not resolved in the data. In our study, the spatial resolution is limited by the size of the seeing disk in ground-based observations. We see that the source-plane image reconstructed from less magnified regions appear to be fainter (e.g., image a of System A) than those reconstructed from more highly magnified images (e.g., images b and c of System A). This surface brightness discrepancy suggests that the individual clumps, even after being magnified by the cluster lens, are still not resolved by the data. Apart from the decrease of surface brightness in image a of System A as discussed in §2.5.1, we also see discrepancy of Lyα surface brightness near critical curves where the magnification factor is much larger (e.g., in System B, the Lyα emitting region that straddles the critical curve between images a and b shows the highest apparent surface brightness across the whole lensed arc). Adopting $\mu \approx 20$ as the fiducial magnification factor near the critical curves, we estimate that the clump size should be $\lesssim 1.5$ kpc in order for the gas clumps to remain unresolved in lensed images recorded under $1''$ seeing. This upper limit is in agreement with clump sizes of cold gas in the CGM constrained in absorption studies (e.g. Zahedy et al., 2019). Furthermore, small-scale substructures in the lens can also introduce additional perturbations to the lensing effect across an extended source (e.g., the unusually large magnification at the location of image $B1e$, see §2.4.1). In order to accurately quantify the intrinsic surface brightness distribution of extended and clumpy sources in strong lensing fields, a better understanding of the systematic uncertainties of lensing magnification as a function of image position is necessary.

Systematic uncertainties also remain in the shell model analysis on the Lyα line profiles and the interpretation of the velocity gradient derived from spatially-varying Lyα lines in both Systems A and B. For example, our shell model does not include radiative transfer effects inside the galaxies, which would re-shape the input Lyα line from a single Gaussian into a double-peak profile. This provides a likely explanation for the large redshift observed

at the location of the continuum regions in System A (see Figure 2.11). However, a clumpy ISM may also be transparent to Lya photons, resulting in a wider Gaussian linewidth instead. In addition, because the signal strength is dominated by the much stronger red peak in the Lyα line (see Figure 2.10), the inferred velocity offset could simply represent a shift in the location of the red peak. The observed blueshifted velocity with increasing projected distance in System A (see Figure 2.11) may also be explained in part due to line-of-sight projection of a uniformly expanding sphere. While a complete 3D radiative transfer model to consider different possible cloud geometry is beyond the scope of this paper, an initial exercise that explores different cloud geometry and velocity field shows that the emergent spectrum will be increasingly blueshifted (redshifted) from the center to the edge of the cloud with decelerating (accelerating) gas expansions. We show one example of such exercise in Appendix 2.8.4, where we extract the emergent Lyα line profile as a function of projected distance from the center of a spherical cloud that is undergoing expansion with an accelerating or decelerating velocity field. We therefore argue that System A is likely decelerating while System B is accelerating as the gas move outward from the star-forming regions.

In summary, the observed Lyα emission morphology in System A clearly indicates a more complicated gas geometry than what is assumed in current radiative transfer simulations. In addition, significant uncertainties remain in terms of the origin and the spatial distribution of Lyα emission sources, the effect of local ISM on the Lyα spectra emergent from the the star-forming regions prior to the scattering of large-scale gas in the CGM, as well as the effect of dust and gas clumpiness. All of these factors can alter the shape of the emerging line profile, the surface brightness profile, and the velocity gradient of Lyα emission in an extended gas cloud. A more sophisticated radiative transfer model is needed to fully explore the parameter space.

2.7   Summary and Conclusions

Combining the strong cluster lensing power with deep wide-field integral field spectroscopic data, we have carried out a detailed analysis of two giant Lyα arcs to spatially and spectrally resolve gas flows around two active star-forming regions at $z > 3$. Both Lyα nebulae are found to be spatially offset from the associated star-forming region and both exhibit a double-peak profile with a significantly enhanced red peak that indicates expansion/outflowing motions. One of the arcs with Lyα surface brightness of $3.7 \times 10^{-18} \mathrm{erg\,s^{-1}\,cm^{-2}\,arcsec^{-2}}$, detected at the 3-$\sigma$ level of significance, stretches over $1'$ around the Einstein radius of the cluster, resolving the velocity field of the line-emitting gas on sub-kpc scales around a group of three star-forming galaxies of 0.3-1.6 L_* at $z = 3.038$. Based on a lens model constructed from deep *HST* images, the de-magnified source-plane Lyα image exhibits a symmetric double-lobe structure of $\approx$ 30 pkpc across, encompassing the galaxy group. The total integrated Lyα flux across the nebula is $(6.5 \pm 0.1) \times 10^{-17}\,\mathrm{erg\,s^{-1}\,cm^{-2}}$ after correcting lensing magnifications, corresponding to a total Lyα luminosity of $L_{\mathrm{Ly}\alpha} = (5.2 \pm 0.1) \times 10^{42}\,\mathrm{erg\,s^{-1}}$ at $z \approx 3.038$. The second arc with Lyα surface brightness of $2.8 \times 10^{-18}\,\mathrm{erg\,s^{-1}\,cm^{-2}\,arcsec^{-2}}$ (3-σ) spans $15''$ in size, roughly centered around a pair of low-mass dwarf Lyα emitters of $\approx 0.03\,L_*$ at $z = 3.754$. The total integrated Lyα flux is $(7.4 \pm 0.2) \times 10^{-18}\,\mathrm{erg\,s^{-1}\,cm^{-2}}$, corresponding to a total luminosity of $L_{\mathrm{Ly}\alpha} = (9.8 \pm 0.2) \times 10^{41}\,\mathrm{erg\,s^{-1}}$ at $z \approx 3.754$. Here we summarize the main findings of our study:

(1) A strong variation in the observed Lyα surface brightness is clearly seen across both nebulae, suggesting large spatial fluctuations in the underlying gas properties. While the nebulae at $z = 3.038$ is split into northern and southern lobes bracketing the group of luminous star-forming galaxies, the one at $z = 3.754$ appears to be more symmetrically distributed around the associated low-mass galaxies.

(2) Spatial variations in the kinematics profile of the Lyα emission line are also detected

in both nebulae, revealing highly organized velocity fields across the nebulae. We show that such spatial variations, if unaccounted for in integrated Lyα profiles, may lead to biased results in constraining the underlying gas kinematics. By applying a simple expanding shell model to the spatially-varying Lyα line, we infer a large velocity gradient of $|\Delta v/\Delta r_\perp| \approx 22-27\ \mathrm{km\,s^{-1}\,pkpc^{-1}}$ and high neutral hydrogen column density of $\log N(\mathrm{H\,I})/\mathrm{cm^{-2}} \gtrsim 19.5$ for both nebulae. The result supports a scenario in which high column density gas is driven outward from the galaxies to beyond 10 pkpc in projected distance into the low-density surroundings.

(3) Combining known star formation properties of the galaxies and the observed extent and surface brightness of the Lyα signals, we show that the observed Lyα photons likely originate from a combination of resonant scattering of Lyα photons from the nearby star-forming regions and recombination radiation due to escaping ionizing photons, although the relative contribution of these two mechanisms cannot be accurately determined with the current data.

Both nebulae provide clear-cut examples of gas outflows that are thought to be widespread at high redshift and may be responsible for metal enrichment of the Lyα forest in general. While the hydrogen Lyα line, being the strongest emission line in diffuse, photo-ionized gas, enables sensitive studies of spatially extended outflows beyond active star-forming regions, large uncertainties remain due to the resonant nature of this transition. Future observations targeting non-resonant transitions, such as [O II]$\lambda\lambda$3727, 3730, H$\beta\lambda$4863, [O III]λ5008, and H$\alpha\lambda$6565, within the line-emitting nebulae will provide the necessary discriminating power to resolve the degeneracy between different physical parameters. Based on the observed Lyα surface brightness in Systems A and B and under the assumption that the Lyα emission arises from recombination radiation of photo-ionized gas, we estimate the expected Hα and Hβ surface brightness to be approximately 3 and $1 \times 10^{-19}\ \mathrm{erg\,s^{-1}\,cm^{-2}\,arcsec^{-2}}$, respectively. The [O III]λ5008 line is expected to be between 3 and 10 times brighter than Hβ in

photo-ionized, low-metallicity gas (e.g. Kewley et al., 2019). While the Hα line is redshifted out of the detection window with existing near-infrared spectrographs on the ground, it is possible to detect H$\beta\lambda$4863 and [O III]λ5008 lines in under $\approx$ 20 hours, within the reach of current observing facilities. We therefore argue that follow-up near-infrared integral field observations, targeting rest-frame optical, non-resonant lines in known Lyα nebulae, will greatly improve the physical constraints of gas flows around distant star-forming galaxies.

2.8   Appendix

2.8.1   Lens constraints and parameters

In Table A1, we list the coordinates of all multiple images used as constraints in our lens modeling process, while the best-fit parameters for the fiducial and fine-tuned model are listed in Tables A2 and A3, respectively.

2.8.2   Photometry for individual images of Systems A and B

In §2.4.1, we presented the photometric magnitudes of galaxies in Systems A and B after correcting the lensing magnification and averaging among multiple images. Here in Table 2.10, we list the direct measurements from the data for each individual images without correcting for lensing effect. Note that the Galactic extinction is corrected for each bandpass.

Table 2.7: Coordinates and redshifts of multiple images included for lens modeling.

Image ID	RA	DEC	Redshift
$A2a$	181.562648	-8.796683	3.0378
$A2b$	181.562497	-8.804908	3.0378
$A2c$	181.560573	-8.808988	3.0378
$A31a$	181.562535	-8.796884	3.0384
$A31b$	181.562501	-8.804524	3.0384
$A31c$	181.560104	-8.809551	3.0384
$A32a$	181.562551	-8.796809	3.0384
$A32b$	181.562492	-8.804617	3.0384
$A32c$	181.560204	-8.809411	3.0384
$B1a$	181.566558	-8.804480	3.7540
$B1b$	181.566475	-8.804733	3.7540
$B1c$	181.566475	-8.805147	3.7540
$B1d$	181.566275	-8.806328	3.7540
$B1e$	181.565591	-8.807690	3.7540
$B2a$	181.566605	-8.804400	3.7540
$B2c$	181.566494	-8.805077	3.7540
$B2d$	181.566250	-8.806446	3.7540
$B2e$	181.565675	-8.807566	3.7540
$1a$	181.550916	-8.797422	1.0121
$1b$	181.549604	-8.799294	1.0121
$1c$	181.548870	-8.806655	1.0121
$3a$	181.550570	-8.795568	1.0433
$3b$	181.547611	-8.799811	1.0433
$3c$	181.548607	-8.805281	1.0433
$4a$	181.552987	-8.794699	1.4248
$4b$	181.548830	-8.800057	1.4248
$4c$	181.549752	-8.807965	1.4248
$5a$	181.553557	-8.795189	1.4254
$5b$	181.554237	-8.801552	1.4254
$5c$	181.550005	-8.808098	1.4254
$6a$	181.549979	-8.796362	1.4255
$6b$	181.548139	-8.797058	1.4255
$6c$	181.548050	-8.809283	1.4255
$8a$	181.553657	-8.795756	1.4864
$8b$	181.554524	-8.801104	1.4864
$8c$	181.549957	-8.808887	1.4864
$9a$	181.546741	-8.793144	1.9600
$9b$	181.543273	-8.797812	1.9600
$9c$	181.544378	-8.807486	1.9600
$10a$	181.552450	-8.795001	2.5393
$10b$	181.546604	-8.797465	2.5393
$10c$	181.550487	-8.799957	2.5393
$10d$	181.554894	-8.800160	2.5393

Image ID	RA	DEC	Redshift
10e	181.548827	−8.811813	2.5393
12a	181.548632	−8.793717	3.3890
12b	181.546121	−8.795387	3.3890
12c	181.553268	−8.800197	3.3890
15a	181.555962	−8.791635	3.7611
15b	181.557600	−8.803056	3.7611
15c	181.551748	−8.810964	3.7611
16a	181.554584	−8.791202	3.7617
16b	181.546465	−8.799671	3.7617
16c	181.556520	−8.802471	3.7617
17a	181.556136	−8.795620	3.8224
17b	181.556958	−8.799422	3.8224
18a	181.555376	−8.796714	4.0400
18b	181.555927	−8.798595	4.0400
19a	181.562084	−8.794875	4.0520
19b	181.561873	−8.805239	4.0520
19c	181.559788	−8.809463	4.0520
20a	181.547472	−8.800476	4.0553
20b	181.556839	−8.803813	4.0553
22a	181.544328	−8.791418	4.2913
22b	181.540282	−8.796562	4.2913
22c	181.540884	−8.806094	4.2913
23a	181.563252	−8.796893	4.7293
23b	181.563537	−8.803670	4.7293
23c	181.559832	−8.811526	4.7293
25a	181.559714	−8.796562	5.7927
25b	181.560102	−8.800177	5.7927
26a	181.550711	−8.803112	6.0106
26b	181.551211	−8.803668	6.0106

Table Note –

We adopt the multiple image identifications from Caminha et al. (2017), while excluding image systems 2, 7, 13, 21, 24 and 27 (see §2.3 for detailed discussions). We rename their image system 11 to be $A2$, and add $A31$ and $A32$ (the north and south substructures of $A3$). Similarly, we rename image system 14 to be $B1$, and add $B2$ (the fainter structure near $B1$ at the same redshift). We also update redshifts for $A2$, $A3$, $B1$ and $B2$ to be their best-fit values from fitting the observed emission lines (see §2.4). For the fiducial model, we use all images listed except for $A31$, $A32$ and $B2$. For the fine-tuned model, we only use systems $A2$, $A31$, $A32$, $B1$ and $B2$, excluding all other lensed systems, in order to optimise the model specifically for A and B.

Table 2.8: Best-fit *LENSTOOL* parameters of the fiducial lens model.

First cluster-scale PIEMD halo	
x ($''$)	$-1.420^{+0.314}_{-0.157}$
y ($''$)	$1.047^{+0.149}_{-0.109}$
ϵ	$0.598^{+0.036}_{-0.005}$
θ (deg)	$19.790^{+1.265}_{-0.268}$
r_c (kpc)	$35.941^{+0.814}_{-1.984}$
σ_v (km/s)	$986.284^{+14.338}_{-8.487}$
Second cluster-scale PIEMD halo	
x ($''$)	$-11.592^{+0.347}_{-0.291}$
y ($''$)	$5.729^{+0.001}_{-2.367}$
ϵ	$0.429^{+0.076}_{-0.0}$
θ (deg)	$100.850^{+3.853}_{-1.232}$
r_c (kpc)	$212.843^{+9.732}_{-28.724}$
σ_v (km/s)	$1078.762^{+5.161}_{-63.885}$
Third cluster-scale PIEMD halo	
x ($''$)	$29.401^{+0.629}_{-0.437}$
y ($''$)	$-8.171^{+0.710}_{-0.239}$
ϵ	$0.453^{+0.009}_{-0.074}$
θ (deg)	$8.895^{+3.891}_{-2.322}$
r_c (kpc)	$88.386^{+5.336}_{-6.934}$
σ_v (km/s)	$746.233^{+31.612}_{-18.050}$
External Shear	
γ_{shear}	$0.334^{+0.031}_{-0.022}$
θ_{shear} (deg)	$92.177^{+1.939}_{-1.357}$
Galaxy members	
$r^0_{g,t}$ (kpc)	$22.940^{+2.600}_{-2.840}$
$\sigma^0_{g,v}$ (km/s)	$197.907^{+14.636}_{-11.880}$

Positions x and y are relative to the position of the BCG at RA = $181.550648°$ and DEC = $-8.800952°$, with positive offsets point to west and north.

Table 2.9: Best-fit *LENSTOOL* parameters of the fine-tuned lens model.

Third cluster-scale PIEMD halo	
x ($''$)	$13.847^{+0.497}_{-9.301}$
y ($''$)	$-5.008^{+0.063}_{-1.849}$
ϵ	$0.573^{+0.102}_{-0.098}$
θ (deg)	$9.202^{+1.418}_{-1.431}$
r_c (kpc)	$97.114^{+3.834}_{-11.217}$
σ_v (km/s)	$799.654^{+8.018}_{-43.115}$
Gm1 PIEMD halo	
$r_{g,t}$ (kpc)	$28.104^{+22.0}_{-20.0}$
$\sigma_{g,v}$ (km/s)	$203.412^{+68.500}_{-63.907}$
Gm2 PIEMD halo	
$r_{g,t}$ (kpc)	$24.369^{+26.0}_{-20.0}$
$\sigma_{g,v}$ (km/s)	$210.705^{+61.428}_{-52.603}$
Gm3 PIEMD halo	
$r_{g,t}$ (kpc)	$7.272^{+12.8}_{-6.0}$
$\sigma_{g,v}$ (km/s)	$83.873^{+28.112}_{-23.457}$

Positions x and y are relative to the position of the BCG at RA = $181.550648°$ and DEC = $-8.800952°$, with positive offsets point to west and north. The first and second cluster-scale PIEMD halos, external shear, and galaxy members are fixed to their best-fit values from the fiducial model, as listed in Table 2.8.

Table 2.10: Photometry from *HST* data, directly measured for each individual image without correcting for lensing magnification. The foreground Galactic extinction is corrected (see §2.4.1 for details).

	F330W[a]	F390W	F435W	F475W	F606W	F625W	F775W	F814W
A1	> 23.94	24.16 ± 0.08	23.35 ± 0.03	22.94 ± 0.02	22.42 ± 0.07	22.31 ± 0.01	22.21 ± 0.01	22.22 ± 0.01
A2a	> 26.07	25.18 ± 0.13	24.57 ± 0.05	24.33 ± 0.03	24.05 ± 0.03	23.77 ± 0.02	23.72 ± 0.03	23.70 ± 0.01
A2b	> 26.80	24.87 ± 0.09	24.22 ± 0.05	24.07 ± 0.03	23.53 ± 0.02	23.31 ± 0.02	23.19 ± 0.02	23.17 ± 0.01
A2c	> 27.26	24.51 ± 0.32	23.78 ± 0.04	23.69 ± 0.03	23.22 ± 0.02	23.04 ± 0.02	23.04 ± 0.02	22.98 ± 0.01
A3a	> 26.59	25.98 ± 0.21	25.04 ± 0.07	24.67 ± 0.05	24.24 ± 0.08	24.09 ± 0.03	24.08 ± 0.03	24.05 ± 0.02
A3b	> 27.85	25.45 ± 0.15	25.03 ± 0.10	24.52 ± 0.05	23.83 ± 0.02	23.70 ± 0.03	23.51 ± 0.03	23.43 ± 0.01
A3c	> 26.49	24.99 ± 0.11	24.55 ± 0.08	24.23 ± 0.04	23.67 ± 0.02	23.54 ± 0.03	23.43 ± 0.03	23.39 ± 0.02

	F850LP	F105W	F110W	F125W	F140W	F160W
A1	22.20 ± 0.02	22.22 ± 0.01	22.20 ± 0.01	22.21 ± 0.01	22.03 ± 0.01	21.86 ± 0.01
A2a	23.67 ± 0.03	23.82 ± 0.02	23.86 ± 0.02	23.90 ± 0.02	23.73 ± 0.02	23.68 ± 0.02
A2b	23.21 ± 0.03	23.20 ± 0.01	23.18 ± 0.01	23.21 ± 0.02	23.04 ± 0.01	22.92 ± 0.01
A2c	23.01 ± 0.03	23.24 ± 0.02	23.26 ± 0.01	23.31 ± 0.02	23.14 ± 0.01	23.12 ± 0.01
A3a	24.08 ± 0.05	24.16 ± 0.03	24.14 ± 0.02	24.22 ± 0.03	23.96 ± 0.02	23.86 ± 0.02
A3b	23.29 ± 0.03	23.33 ± 0.01	23.30 ± 0.01	23.26 ± 0.01	23.10 ± 0.01	22.95 ± 0.01
A3c	23.38 ± 0.03	23.54 ± 0.02	23.54 ± 0.01	23.59 ± 0.02	23.38 ± 0.02	23.15 ± 0.01

	F450W[b]	F475W	F606W	F625W	F775W	F814W	F850LP	F105W
B1a	> 27.42	27.25 ± 0.32	26.48 ± 0.11	26.38 ± 0.16	25.95 ± 0.13	25.98 ± 0.09	25.82 ± 0.15	26.36 ± 0.13
B1c	> 27.39	27.09 ± 0.27	26.34 ± 0.09	26.07 ± 0.11	25.78 ± 0.11	26.00 ± 0.08	26.23 ± 0.21	26.48 ± 0.14
B1d	> 27.25	27.46 ± 0.41	26.43 ± 0.10	26.17 ± 0.13	26.14 ± 0.15	26.26 ± 0.11	26.15 ± 0.21	26.82 ± 0.19
B1e	> 27.41	26.97 ± 0.25	26.17 ± 0.24	25.73 ± 0.09	25.62 ± 0.09	25.77 ± 0.07	25.63 ± 0.13	25.81 ± 0.09
B2a	> 27.39	> 27.81[c]	27.04 ± 0.19	26.67 ± 0.21	26.40 ± 0.20	26.23 ± 0.10	26.78 ± 0.37	26.45 ± 0.14
B2c	> 27.37	> 27.82[c]	26.74 ± 0.13	26.85 ± 0.24	26.37 ± 0.18	26.36 ± 0.12	25.97 ± 0.17	26.25 ± 0.12
B2d	> 27.43	27.69 ± 0.49	27.24 ± 0.22	27.41 ± 0.41	26.18 ± 0.17	26.48 ± 0.13	26.08 ± 0.20	26.97 ± 0.22
B2e	> 27.24	27.62 ± 0.49	27.22 ± 0.20	26.51 ± 0.19	26.93 ± 0.34	26.80 ± 0.18	26.56 ± 0.30	26.74 ± 0.20

	F110W	F125W	F140W	F160W
B1a	26.41 ± 0.10	26.24 ± 0.13	26.41 ± 0.13	26.69 ± 0.17
B1c	26.39 ± 0.09	26.44 ± 0.15	26.44 ± 0.13	26.30 ± 0.12
B1d	26.39 ± 0.09	26.67 ± 0.19	26.77 ± 0.17	26.47 ± 0.14
B1e	25.74 ± 0.10	25.97 ± 0.10	26.02 ± 0.11	26.26 ± 0.15
B2a	26.39 ± 0.10	26.49 ± 0.16	26.29 ± 0.11	26.09 ± 0.10
B2c	26.33 ± 0.09	26.22 ± 0.13	26.19 ± 0.10	26.00 ± 0.09
B2d	26.84 ± 0.14	26.88 ± 0.23	26.68 ± 0.16	26.66 ± 0.16
B2e	27.09 ± 0.10	26.36 ± 0.14	26.44 ± 0.15	26.45 ± 0.15

[a] 2σ UV flux upper limit, averaged among the F225W, F275W and F336W bandpasses.
[b] 2σ UV flux upper limit, averaged among the F225W, F275W, F336W, F390W and F435W bandpasses.
[c] 2σ flux upper limit.

2.8.3 Fitting a shell model to stacked spectra obtained over a large area with fixed intrinsic Lyα line width σ_i

In §2.5.3, we have shown that the best-fit shell models for stacked spectra extracted from a large area in both Systems A and B require the intrinsic Lyα line width σ_i to be much larger than the observed nebular emission line width. We argue that the large σ_i is caused by the smearing effect due to the velocity gradient in the nebulae. Here in Figure 2.13, we show the best-fit models for the same spectra shown in the top row of Figure 2.10 in the main text, and demonstrate that by fixing σ_i to the observed values from galaxy spectra, the best-fit models provide a worse fit to the data.

2.8.4 Lyα line profile from accelerating and decelerating expanding clouds

We present the Lyα line profiles emergent at different distances from the center of a spherical cloud undergoing, respectively, an accelerating and decelerating expansion. The physical parameters of the cloud are $\log N(\text{H\,{\sc i}})/\text{cm}^{-2} = 20$, $\sigma_i = 0$ km/s (i.e., all Lyα photons are emitted at the same frequency), and $T_{\text{eff}} = 10^4$ K. The accelerating cloud has a velocity field changing from 0 km/s at the center to 400 km/s at the outer edge of the cloud with a constant radial acceleration, while the decelerating cloud has a reverse gradient changing from 0 to 400 km/s from the outer edge to the center of the cloud. We extract the emergent Lyα line profiles in two projected distance bins from the cloud center, with an inner bin corresponding to the distance range $[0, 0.5R_{\text{max}}]$ and an outter bin corresponding to $[0.5R_{\text{max}}, R_{\text{max}}]$, where R_{max} is the radius of the cloud. Note that given a fixed $N(\text{H\,{\sc i}})$, changing the physical value of R_{max} does not change the shape of the emergent Lyα profile and therefore R_{max} is not a parameter in the model.

The Lyα profiles from these two bins are shown in Figure 2.14. For the decelerating cloud, the dominant red peak is more blueshifted in the outer bin, while the opposite trend is observed for the accelerating cloud. While the amount of shift in velocity and the profile
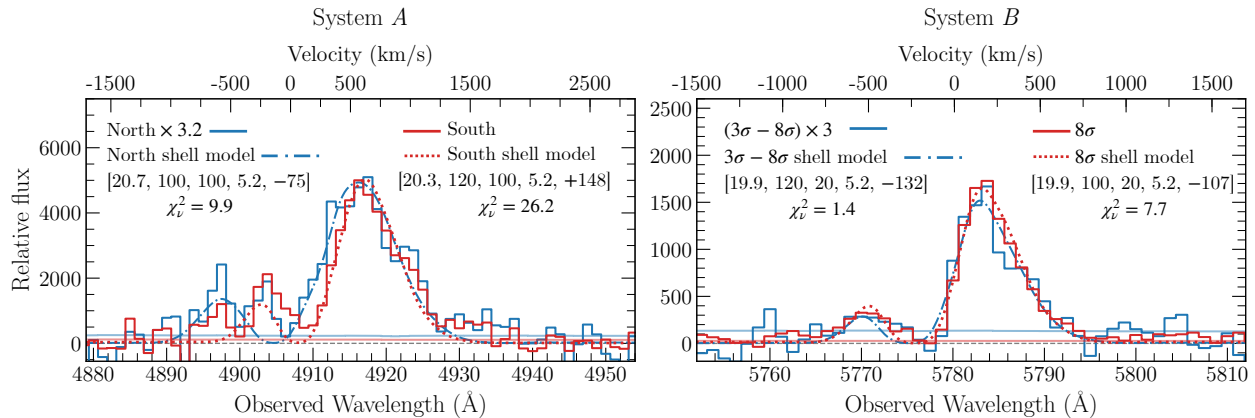
Figure 2.13: *Left:* Stacked spectra from all spaxels within the 3-σ contour in System A, divided into northern and southern nebulae (see Figures 2.1 and 2.6). The best-fit models are shown in dash-dotted and dotted curves for the northern and southern nebula, respectively. To obtain the best-fit models, we fix the intrinsic Lyα line width σ_i to be 95 km/s, corresponding to the observed line width measured from the nebular emission lines (see §2.4.3 and Table 2.5). Compared with the best-fit models shown in Figure 2.10 in the main text where σ_i is a free parameter, the models shown here with a fixed σ_i provide a worse fit to the data (particularly on the blue peak), which is also reflected with the increased χ^2_ν. *Right:* Stacked spectral from low- and high-surface brightness regions in System B, extracted from within and outside of the 8-σ contours. The best-fit models are shown in dash-dotted and dotted curves for low- and high-surface brightness spectra, respectively. Similar to the models for System A, we fix σ_i to be 20 km/s as measured from the galaxy spectrum. Although these models with fixed σ_i also provide a worse fit to the data compared with the models presented in Figure 2.10 where σ_i is a free parameter, the difference in χ^2_ν is not as significant as the difference seen in System A. This is consistent with System A having a steeper velocity gradient across the nebulae, leading to a more significant smearing effect in the stacked spectra from a large area.
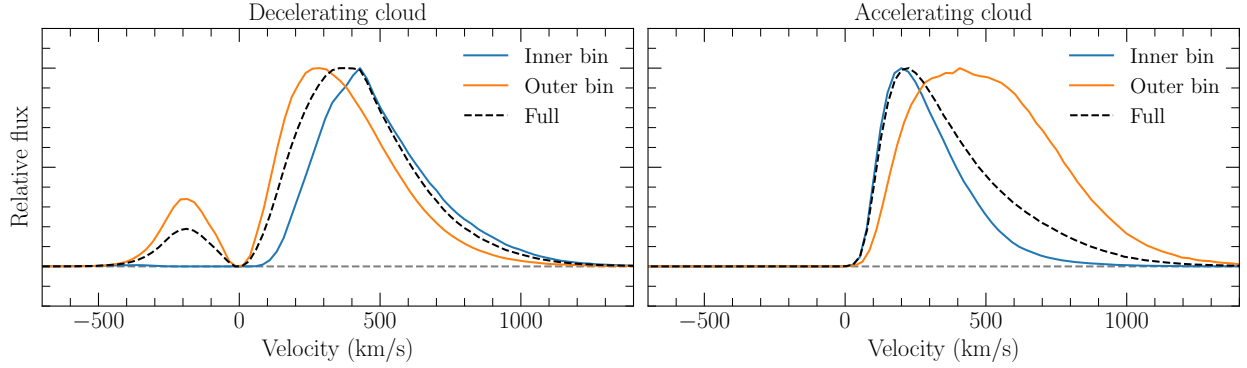
Figure 2.14: *Left:* Emergent Lyα profiles extracted from the inner and outer bins of a decelerating expanding cloud. The inner and outer bins correspond to the projected distance range of $[0, 0.5R_{\max}]$ and $[0.5R_{\max}, R_{\max}]$ from the center of the cloud, respectively, where $R_{\max}$ is the radius of the cloud. The dominant red peak of the Lyα profiles is more blueshifted in the outer bin. The full spectrum extracted from the entire cloud is shown in the dashed black curve. *Right:* same as the left panel but for an accelerating expanding cloud. The profile is more redshifted in the outer bin, contrary to the trend observed for a decelerating cloud.

shapes do not match well with the observed Lyα profiles presented in the this work, this simple exercise demonstrates that differential velocity fields in expanding clouds might be a plausible mechanism to produce velocity gradients seen in spatially-resolved Lyα profiles.

CHAPTER 3

EMPIRICAL CONSTRAINTS ON THE TURBULENCE IN QSO HOST NEBULAE FROM VELOCITY STRUCTURE FUNCTION MEASUREMENTS

This chapter is a modified version of Chen et al. (2023c), published in the Monthly Notices of the Royal Astronomical Society, Volume 518, Issue 2, pp.2354-2372.

3.1   Introduction

The tenuous gas residing in the circumgalactic medium (CGM) contains a critical record of the past and ongoing interactions between galaxies and their surrounding environment. Characterizing the detailed physical properties of the CGM is an important step in improving current galaxy evolution models. Over the past three decades, absorption spectroscopy using predominantly QSO sightlines has yielded sensitive constraints on various properties of the CGM, and provided us with an increasingly intricate picture of the gaseous halo ecosystem (see e.g. Chen, 2017; Tumlinson et al., 2017; Rudie et al., 2019, and references therein). Observations have shown that the CGM contains multiphase gas spanning a wide range in density, temperature, ionization state, and metallicity (e.g., Savage et al., 2005; Zahedy et al., 2019, 2021; Cooper et al., 2021). Numerical simulations have also shown that different dynamical processes, such as gas infall, outflow, and tidal interactions, can also happen in the CGM to drive and regulate galaxy growth over cosmic time (e.g., van de Voort, 2017; Anglés-Alcázar et al., 2017; Mitchell & Schaye, 2022).

However, the lack of spatial information from the "pencil-beam" probe of absorption spectroscopy has hindered our ability to robustly characterize the thermodynamic state of the gas. While the Doppler width of absorption profiles exceeding the value of thermal broadening may provide evidence for the presence of non-thermal pressure support in the CGM (e.g.

Rauch et al., 1996a; Rudie et al., 2019), interpretations of the physical origin of the non-thermal motions remain ambiguous because both large-scale coherent flows and turbulent motions contribute to the observed line broadening. Similar ambiguities exist in kinematic studies of emission signals obtained through long-slit or single-aperture spectroscopy.

Diffuse, ionized plasmas such as the CGM are expected to be turbulent, because of the expected high Reynolds number (see Burkhart, 2021, for a recent review). The presence of turbulence in the diffuse halo gas and the degree of such turbulence have profound implications for the thermal and dynamic properties of the CGM. Turbulent energy can be a significant source of heating to offset cooling in the hot halo through non-linear interactions between large and small eddies (e.g., McNamara & Nulsen, 2007; Zhuravleva et al., 2014). In addition, turbulence produces density fluctuations, triggering and facilitating multiphase condensation in the hot halo (e.g., Gaspari et al., 2018; Fielding et al., 2020; Gronke et al., 2022). Turbulent mixing also provides an efficient transport mechanism for metals from star-forming regions to the CGM/IGM, and can facilitate the mixing of metals within the CGM (e.g. Pan & Scannapieco, 2010). Given these vital scientific implications, it is of great interest to obtain direct empirical constraints on turbulence in the CGM.

In this context, the recent advent of high-throughput, wide-field integral field spectrographs (IFSs) such as the Multi-Unit Spectroscopic Explorer (MUSE; Bacon et al., 2010) on the Very Large Telescope (VLT) has transformed CGM investigations by providing two-dimensional contiguous maps of large-scale line-emitting signals with unprecedented sensitivities and efficiency. Compared with absorption spectroscopy, the spatial information provided by these IFS data reveals new insights into the detailed physical processes of these low-density regions. In particular, spatially-resolved kinematic properties now enable two-point statistical measurements of the velocity field, providing an exciting opportunity to probe turbulence beyond a single sightline/aperture approach.

One of the standard two-point probes is the velocity structure function (VSF), defined
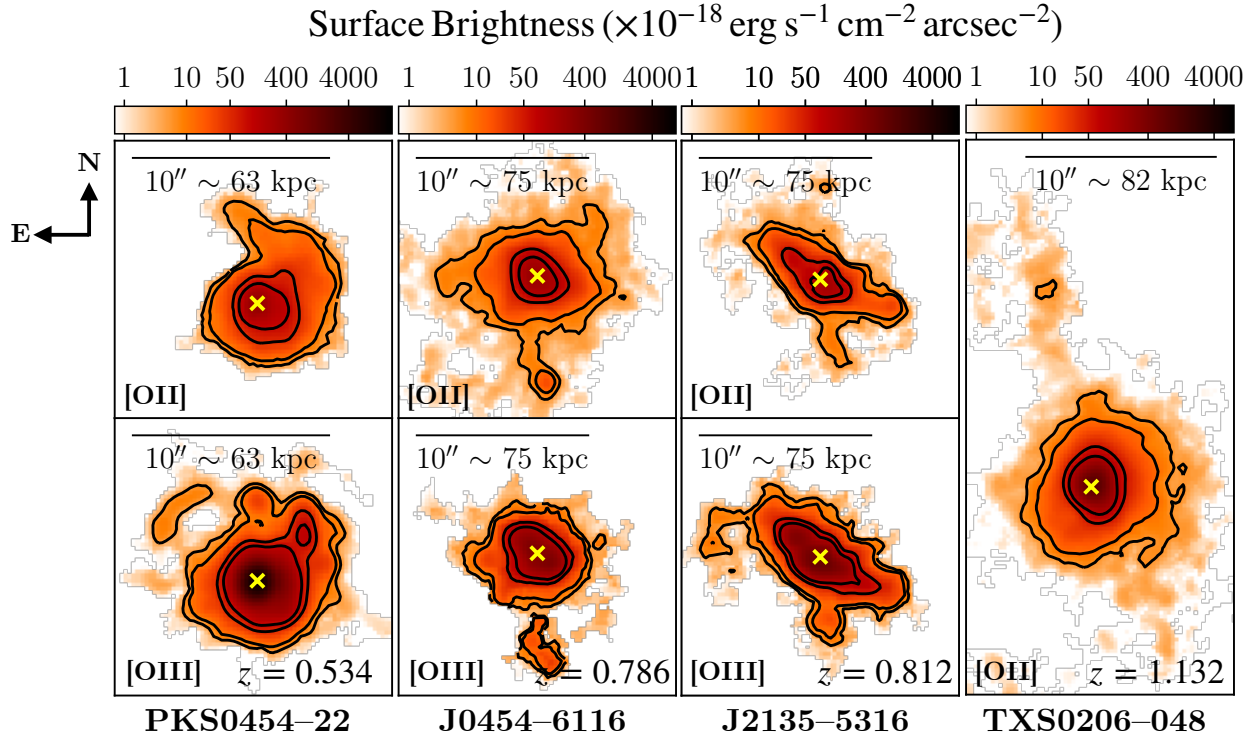
Figure 3.1: Continuum- and QSO-subtracted narrow-band images of the [O II] and [O III] emission from the four fields studied in this paper, based on the MUSE-WFM observations. The fields are shown in the order of increasing redshift from left to right. For TXS0206−048, the [O III] line is redshifted out of the MUSE wavelength coverage and is therefore not shown here. Contours are at surface brightness levels of $[5, 10, 50, 100] \times 10^{-18} \, \mathrm{erg \, s^{-1} \, cm^{-2} \, arcsec^{-2}}$. The yellow cross in each panel marks the quasar position.

as

$$S_p(r) = \langle |\boldsymbol{v}(\boldsymbol{x}) - \boldsymbol{v}(\boldsymbol{x} + \boldsymbol{r})|^p \rangle, \tag{3.1}$$

where $\boldsymbol{x}$ and $\boldsymbol{r}$ represent respectively the spatial location of a starting point and the distance between the starting point and a second location for calculating the pair velocity difference (e.g., Frisch, 1995). Different variants of the VSFs record the mean pair velocity difference to the power of p averaged over all available pair configurations for a given separation $r \equiv |\boldsymbol{r}|$. There have been extensive efforts, both in observations and numerical simulations, in using VSFs to probe the thermodynamic state of the interstellar medium (ISM) in local H II regions and in molecular clouds (e.g. Wen & O'dell, 1993; Ossenkopf & Mac Low, 2002; Federrath, 2013; Padoan et al., 2016; Arthur et al., 2016; Anorve-Zeferino, 2019; Chira et al., 2019; Melnick et al., 2021; Hu et al., 2022). Recently, VSFs have also been measured for Milky Way stars using GAIA data (Ha et al., 2021, 2022). These studies in the local Universe have shown that not only is turbulence ubiquitous in the ISM, but it also plays a critical role in shaping the star-formation processes inside a galaxy (see, e.g. Burkhart, 2021, for a review).

For the CGM, measuring VSFs becomes more challenging because of faint emission signals and because of a lack of two-dimensional velocity maps with sufficiently fine spatial sampling, particularly for sources beyond the local Universe where cosmological surface brightness dimming further weakens the signal strength. Rauch et al. (2001) attempted the first second-order VSF measurements in the low-density circum- and intergalactic gas at redshift $z \approx 2-3$, using C IV absorbers identified along multiply-lensed QSO sightlines. The VSFs in Rauch et al. (2001) were found to be consistent with expectations from the Kolmogorov turbulence (Kolmogorov, 1941, also see the discussion below in § 3.2), but the uncertainties were large and the spatial sampling was sparse. Recently, Li et al. (2020) measured the first-order VSF using Hα filaments detected in IFS data near the centers of nearby cool core clusters. These authors identified a bump in the VSFs at 20-30 kpc, which they attributed to energy injections by rising bubbles powered by the supermassive black holes at the centers of these

galaxy clusters. Studies such as these demonstrate that measuring the VSF provides a promising tracer of energy coupling and cascades from the source at the galactic center to the diffuse gas reservoir on 10–30 kpc scales.

Motivated by Li et al. (2020), we have carried out a detailed analysis of the velocity field observed in four QSO-host nebulae. These nebulae are revealed by extended emission (up to a scale of ~ 100 physical kpc in diameter) in [O II] $\lambda\lambda\,3727, 3729$ and/or [O III] $\lambda\,5008$ lines (see Figure 3.1). These four fields span a range in redshift from $z_{\mathrm{QSO}} \approx 0.5$ to $z_{\mathrm{QSO}} \approx 1.1$, constituting the first $z \gtrsim 0.5$ sample with two-point characterisations of the CGM velocity field. While all fields host a bright QSO with a bolometric luminosity of $\sim 10^{47}$ erg s^{-1}, these QSOs span a range in radio luminosity and reside in diverse group environments with different numbers of neighboring galaxies found (see Table 3.1 for a summary of the QSO properties). We have measured the second- and third-order VSFs over a range of scales, from $\lesssim 5$ kpc to ≈ 20-50 kpc in these nebulae. While no constraints on the energy injection and dissipation scales can be obtained from the current data, we are able to determine a robust power-law slope after accounting for the effects of atmospheric seeing, spatial smoothing, and large-scale bulk flows. This work represents the first empirical study to resolve the turbulent velocity field in the CGM beyond the nearby Universe.

This paper is organized as follows. First, we illustrate the basic formalism of VSFs in § 3.2, and discuss how the smoothing and projection effects in observational data can affect the VSF measurement. In § 3.3, we present the IFS data used in this work, the subsequent emission line analyses, as well as the VSF measurements. The results are presented in § 3.4. We discuss our results in § 3.5, and conclude in § 3.6. Throughout this paper, we adopt a Hubble constant of $H_0 = 70$ km/s/Mpc, $\Omega_{\mathrm{M}} = 0.3$ and $\Omega_\Lambda = 0.7$ when deriving distances, masses and luminosities. All distances quoted are in physical units.

Table 3.1: Summery of the QSO properties.

Field name	Redshift	N_{group}^a	$\sigma_{v,\text{group}}^b$ (km/s)	Radio mode
PKS0454$-$22^c	0.5335	23	≈ 320	Loud
J0454$-$6116^d	0.7861	18	≈ 300	Quiet
J2135$-$5316	0.8115	2	$-$	Quiet
TXS0206$-$048^e	1.1317	27	≈ 550	Loud

Notes.
[a] Number of spectroscopically-identified group member galaxies.
[b] Velocity dispersion of the group.
[c] QSO properties of PKS0454$-$22 are adopted from Helton et al. (2021). While the authors identified 23 galaxies with $|\Delta v| < 1500$ km/s and $d \lesssim 300$ kpc from the QSO location, the velocity distribution of these galaxies is clearly asymmetric with a tail extending to ≈ 1500 km/s. The velocity dispersion referenced here is calculated using 19 galaxies with $|\Delta v| < 1000$ km/s.
[d] For both J0454$-$6116 and J2135$-$5316, group member galaxies are found with $|\Delta v| < 1000$ km/s from the QSO redshift and $d \lesssim 250$ kpc from the QSO location (J. Li, privare communication).
[e] For TXS0206$-$048, group member galaxies are found with $|\Delta v| < 1500$ km/s from the QSO redshift and $d \lesssim 500$ kpc from the QSO location (Johnson et al., 2022).

3.2 Velocity structure functions as a tracer of turbulence

As defined in Equation 3.1, the VSF quantifies the kinetic energy fluctuations as a function of scale in a velocity field. Kolmogorov (1941) showed that for isotropic, homogeneous, and incompressible flows with sufficiently large Reynolds numbers, the VSF should follow a power-law scaling of $S_p(r) \propto r^{p/3}$. In particular, the second-order VSF $S_2(r) \propto r^{2/3}$ is directly related to the auto-correlation function $\Gamma(r)$ and the kinetic energy power spectrum E_k of an isotropic velocity field through

$$S_2(r) = 2[\Gamma(0) - \Gamma(r)] = 2 \int (1 - e^{ikr}) E_k dk, \qquad (3.2)$$

where

$$\Gamma(r) = \langle \boldsymbol{v}(\boldsymbol{x}) \boldsymbol{v}(\boldsymbol{x} + \boldsymbol{r}) \rangle \qquad (3.3)$$

and $k = 2\pi/r$. The energy power spectrum then scales with k following $E_k \propto k^{-5/3}$. Similarly, the third-order VSF $S_3(r) \propto r$ can be derived exactly to follow $S_3(r) = -(4/5)\,\epsilon\,r$, where ϵ represents the energy cascade rate (also see § 3.5.1 below for a discussion on ϵ).

While these theoretical expectations of VSFs are established in three dimensional space, empirical data are limited to projected quantities. Specifically, the velocity differences are measured along the line of sight based on the observed Doppler shifts, and only projected separations r_{proj} along the plane of the sky are accessible instead of the true three-dimensional distances between two locations. Such limitations need to be accounted for explicitly when interpreting observational results.

The effect of projections in the observed VSFs has been investigated extensively by previous authors. When viewing a cloud with well-established three-dimensional Kolmogorov turbulence in projection, von Hoerner (1951) demonstrated that the shape of the measured VSF depends on the depth, L, of the cloud along the line of sight. At separations $r_{\mathrm{proj}} < L$, the VSF is expected to steepen, with a power-law slope of $5p/6$, but it recovers to the theo-

retical value of $p/3$ at larger separations $r_{\mathrm{proj}} > L$. There is a smooth transition between the two regimes that could be used as a probe of the cloud depth L (von Hoerner, 1951). This effect, sometimes referred to as "projection smoothing", is also verified by several other studies both analytically (e.g. O'dell & Castaneda, 1987; Xu, 2020) and in numerical simulations (e.g., Mohapatra et al., 2022). Meanwhile, a recent study by Zhang et al. (2022) suggests that if the emission source is more spatially-confined (e.g., Hα filaments at the center of some galaxy clusters), the projection effect will flatten the VSF as opposed to making it steeper.

In addition to line-of-sight projection effects, the spatial correlation due to atmospheric seeing in ground-based data will also alter the shape of the measured VSF. Additional spatial smoothing often applied to enhance the signal-to-noise ratio (SNR) of noisy data would further increase the scale of the spatially-correlated signal. Fortunately, this effect can be analytically incorporated into the theoretical models of the second-order VSF S_2, allowing a more accurate comparison between data and model expectations. Based on Equation 3.2, the second-order VSF of a spatially-smoothed velocity field can be written as

$$S_2'(r) = 2[\Gamma'(0) - \Gamma'(r)]. \tag{3.4}$$

$\Gamma'(r)$ is the auto-correlation function of the smoothed velocity field and can be calculated by

$$\Gamma'(r) = \langle \boldsymbol{v}'(\boldsymbol{x})\boldsymbol{v}'(\boldsymbol{x}+\boldsymbol{r}) \rangle = \boldsymbol{v}' \otimes \boldsymbol{v}', \tag{3.5}$$

where $\boldsymbol{v}'$ is the smoothed velocity field. If we designate $\boldsymbol{g}(\boldsymbol{x})$ as the spatial smoothing kernel, then the smoothed velocity field can be expressed as convolution of $\boldsymbol{v}$ with a Gaussian kernel representing the total point-spread-function (PSF), $\boldsymbol{v}'(\boldsymbol{x}) = \boldsymbol{g}(\boldsymbol{x}) * \boldsymbol{v}(\boldsymbol{x})$. Equation 3.5 can now be rewritten as

$$\Gamma'(r) = \boldsymbol{v}' \otimes \boldsymbol{v}' = (\boldsymbol{g} * \boldsymbol{v}) \otimes (\boldsymbol{g} * \boldsymbol{v}) \tag{3.6}$$
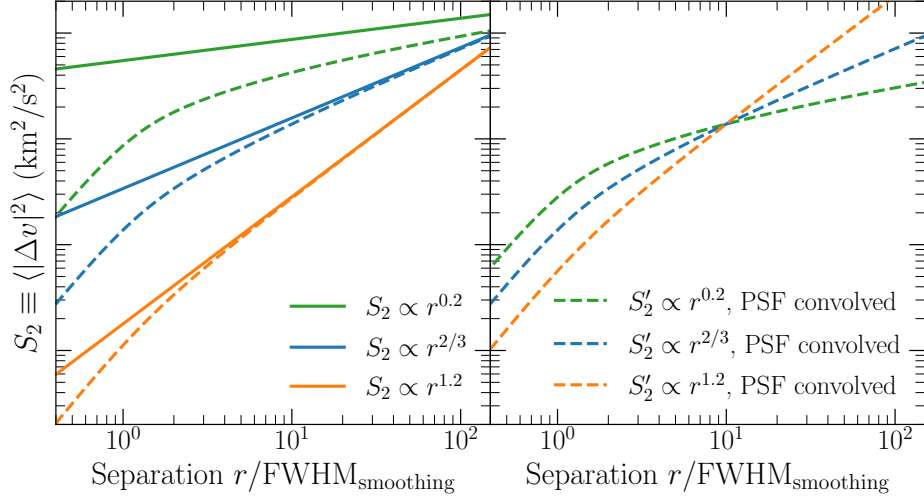
Figure 3.2: *Left*: Illustration of the spatial smoothing effect on the shape of the second-order VSF. Green, blue and orange solid lines show power-law $S_2(r)$ with an intrinsic slope of $\gamma_2 = 0.2, 2/3$ (i.e., Kolmogorov slope) and 1.2, respectively. The corresponding dashed curves show the shapes of $S'_2(r)$ after convolving with a Gaussian smoothing kernel, calculated with Equations 3.4–3.7. It can be seen that spatial smoothing significantly steepens the VSF at $r \lesssim 2 \times \text{FWHM}_{\text{smoothing}}$, and the discrepancy is stronger for a flatter intrinsic VSF, as discussed in the text. *Right*: Smoothed $S'_2(r)$ curves, same as shown in the left column, re-normalised to the same value at $r = 10 \times \text{FWHM}_{\text{smoothing}}$. This panel shows that with an accurate estimate of the smoothing kernel size, the intrinsic VSF slope can be obtained with high-SNR measurements even if the probed spatial scale does not cover a large dynamic range.

Equation 3.6 can be rearranged to a simple analytic form of

$$\Gamma'(r) = (\boldsymbol{g} \otimes \boldsymbol{g}) * (\boldsymbol{v} \otimes \boldsymbol{v}) = \Gamma_g(r) * \Gamma(r). \tag{3.7}$$

Equation 3.7 shows that the auto-correlation function of a smoothed velocity field can be calculated through a convolution of two functions: the auto-correlation function of the smoothing kernel, and the auto-correlation function of the intrinsic, unsmoothed velocity field. When both $\Gamma_g(r)$ and $\Gamma(r)$ have analytical expressions, such as the case for a Gaussian smoothing kernel and a power-law auto-correlation function, $\Gamma'(r)$ can be calculated explicitly and an exact expression for S'_2 can be obtained through Equation 3.4.

To visualize this spatial smoothing effect, we perform a series of calculations, adopting

three different intrinsic power-law slopes for S_2, corresponding to a relatively flat VSF with a slope of $\gamma_2 = 0.2$, a Kolmogorov VSF of $\gamma_2 = 2/3$, and a steeper VSF of $\gamma_2 = 1.2$. Assuming a Gaussian kernel for spatial smoothing, the comparisons of the intrinsic S_2 and the smoothed S_2' are shown in Figure 3.2. It is clear that the smoothing effect is more significant for a flatter intrinsic VSF. This can be understood intuitively by noting that a flatter VSF carries significantly more relative power on small scales, corresponding to large k modes. As a result, spatial smoothing, which by design removes the power from large k modes, will have a more significant impact in systems with a flatter energy power spectrum. Taking the Kolmogorov VSF for reference, Figure 3.2 shows that the measured VSF begins to recover the intrinsic, unsmoothed VSF at separations $\gtrsim 4$ times the full-width-at-half-maximum (FWHM) of the smoothing kernel. We, therefore, emphasize the importance of explicitly taking into account this smoothing effect in VSF measurements, especially when working with data where the seeing size is relatively large compared with the scales probed.

For the QSO nebulae included in the current study, the spatial scales probed are restricted to $\lesssim 10$ times the FWHM of the PSF (see § 3.3 below). Fortunately, as we show in the right-hand panel of Figure 3.2, with sufficient SNR in the VSF measurements and an accurate estimate of the PSF size, the intrinsic VSF slope can still be recovered even when working with a limited dynamic range. Similarly, for the VSF measurements of Hα filaments in cluster cores (Li et al., 2020), the steeper slopes may be partially attributed to the spatial smoothing effect due to the limited dynamic range compared to the size of the seeing disk in the data.

We have demonstrated that it is straightforward to incorporate any spatial smoothing present in the data to the second-order VSF measurements, thanks to the convenient relation between S_2 and the auto-correlation function $\Gamma(r)$. It is less straightforward to do so for the third-order VSFs, from which we expect to infer the energy cascade rate based on the exact relation of $S_3(r) \propto \epsilon\, r$ (see the discussion in § 3.5.1 below). Benzi et al. (1993) reported

the existence of an extended self-similarity (ESS), where VSFs of different orders are tightly correlated with each other and roughly following a simple power-law function. The ESS is useful because it applies to cases with both high and low Reynolds numbers. For example, for cases with low Reynolds numbers, the second-order VSFs may not follow the expected power-law scaling relation due to a lack of a well-established inertial range. However, with ESS, the third-order VSFs can still be inferred to constrain the energy cascade rate. In addition, with a simulated velocity field generated using Fourier series (see e.g. Saad et al., 2017), we have tested that the spatial smoothing effect does not alter the power-law scaling relation for ESS. In other words, if a velocity field exhibits an ESS relation of $S_p = \alpha S_3^{\gamma_p/\gamma_3}$, then this scaling relation is preserved as $S_p' = \alpha S_3'^{\gamma_p/\gamma_3}$ after the velocity field is smoothed. In §3.4.1 & §3.5.3 below, we show that the ESS is observed in all systems and discuss the caveats associated with this observation.

3.3   Observations and measurements

To measure the VSFs in extended nebulae, spatially-resolved velocity maps are necessary. In this section, we described the wide-field IFS observations available for detecting extended nebulae around four QSO hosts and the constructions of velocity maps based on line profile analyses of [O II] $\lambda\lambda\, 3727, 3729$ and [O III] $\lambda\, 5008$ emission lines.

3.3.1   IFS Observations

Wide-field IFS data of the QSO fields were obtained using the Multi-Unit Spectroscopic Explorer (MUSE; Bacon et al., 2010) on the VLT UT4. All four fields were observed under the Wide-Field-Mode (WFM), which provides a contiguous field-of-view (FOV) of $1' \times 1'$ in a single pointing, with $0''\!.2$ per pixel spatial sampling. MUSE covers a wavelength range of 4750–9350 Å with a resolving power of $R \approx 2000$–4000 (higher at the longer wavelength end).

Table 3.2: Journal of MUSE observations.

Field name	RA(J2000)	Dec.(J2000)	$t_{\exp}$ (s)	seeing[a] ($''$)
PKS0454$-$22	04:56:08.90	$-$21:59.09.1	2700	$0\overset{''}{.}6$
J0454$-$6116	04:54:15.95	$-$61:16:26.6	5100	$0\overset{''}{.}7$
J2135$-$5316	21:35:53.20	$-$53:16:55.8	6840	$0\overset{''}{.}6$
TXS0206$-$048	02:09:30.74	$-$04:38:26.5	28800	$0\overset{''}{.}7$

Notes.
[a] Atmospheric seeing FWHM measured using the QSO at 7000Å. To improve the quality of line fitting, each combined data cube was convolved with a Gaussian kernel of FWHM= $0\overset{''}{.}7$. This yielded a total PSF FWHM of $\approx 0\overset{''}{.}9$-$1\overset{''}{.}0$ (see § 3.3.3), corresponding to a projected separation of 6-8 kpc at the redshifts of these QSOs.

Table 3.3: Summery of emission properties in spatially-extended QSO nebulae[a].

Field name	Surface Brightness Limit[b]		Luminosity (erg s^{-1})		Nebula area (kpc^2)	
	[O II]	[O III]	[O II]	[O III]	[O II]	[O III]
PKS0454$-$22	2.3×10^{-19}	1.7×10^{-19}	1.9×10^{42}	2.2×10^{43}	1552	2202
J0454$-$6116	1.2×10^{-19}	2.4×10^{-19}	3.5×10^{42}	5.3×10^{42}	3821	2128
J2135$-$5316	1.4×10^{-19}	2.6×10^{-19}	2.5×10^{42}	9.2×10^{42}	1614	2190
TXS0206$-$048	6.3×10^{-20}	$-$	2.0×10^{43}	$-$	6239	$-$

Notes.
[a] Luminosities and nebula sizes are summed over the areas used for the subsequent VSF analysis, which are smaller than the areas shown in Figure 3.1. See velocity maps (e.g. Figure 3.3) for the areas included in the VSF calculation. Note that for the nebula in TXS0206$-$048, the $r < 1''$ region centered on the QSO contributes to $\approx 50\%$ of the total luminosity. Excluding this central region results in a luminosity estimate consistent with the reported value in Johnson et al. (2022).
[b] 1-σ limit in units of $\mathrm{erg\,s^{-1}\,cm^{-2}\,arcsec^{-2}}$ over a single wavelength slice (i.e., 1.25Å) at the observed wavelength of the corresponding emission line.

Out of the four fields, J0454$-$6116 and J2135$-$5316 were obtained as part of the Cosmic Ultraviolet Baryon Survey (CUBS) using adaptive optics assisted WFM under program ID, 0104.A-0147 (PI: H.-W. Chen; Chen et al., 2020). The total exposure time was 5100s for J0454$-$6116 and 6840s for J2135$-$5316. PKS0454$-$22 was observed under program ID 0100.A-0753 (PI: C. Péroux; Péroux et al., 2019), with a total exposure time of 2700s. TXS0206$-$048 was part of the MUSE Quasar-field Blind Emitters Survey (MUSEQuBES) under program IDs 097.A-0089(A) and 094.A-0131(B) (PI: J. Schaye; Muzahid et al., 2020) with a total exposure time of 28,800s. All observations were carried out under good seeing conditions, with the mean seeing FWHM measured to be $\approx 0\rlap{.}''6$–$0\rlap{.}''7$ at the location of the QSOs at 7000Å. A summary of the MUSE observations, including the mean seeing in the final combined data cube, is listed in Table 3.2.

Raw science exposures and the associated raw calibration files were retrieved from the ESO science archive. We reduced the data of all four fields using the standard ESO MUSE pipeline (v.2.8.4; Weilbacher et al., 2020), and applied an additional sky subtraction in the final combined cubes using the median sky spectrum obtained from object-free regions in each field.

The pipeline-generated variance cube has been known to underestimate the data uncertainties (e.g. Bacon et al., 2017). Using the wavelength range of 6000–7000Å, we obtained an empirical estimate of the uncertainties in each field and found that on average this empirical noise level is ≈ 1.6 times higher than the noise level inferred from the pipeline generated variance cube. We, therefore, scaled up the pipeline-produced variance cube by a factor of 1.6^2. This correction factor is similar to what has been adopted in previous studies (e.g. Borisova et al., 2016; Sanderson et al., 2021).

3.3.2   QSO light subtraction

To better reveal the emission from the extended nebulae, we removed the QSO light following a method similar to the high-resolution spectral differential imaging technique discussed in Haffert et al. (2019) and Xie et al. (2020). Below we briefly describe the main steps.

We first constructed a QSO template spectrum using the mean spectrum from the central 5 spaxels (i.e., within a radius of $0''\!.2$) around the QSO. Next, for each spaxel contaminated by the QSO light, we divided the data in this spaxel by the QSO template spectrum to obtain a ratio spectrum. We then smooth this ratio spectrum with a median rolling filter with a window width of ~ 100 spectral pixels (i.e., ~ 125Å). The exact window size is decided through trial and error and is slightly different for different fields. This smoothing step will maintain the low-order variation in the ratio spectrum while removing high-order features, such as strong emission lines and noise. Finally, we scale the QSO template spectrum by the smoothed ratio spectrum and subtract it from the spaxel to remove the QSO contamination. These steps were repeated for every spaxel within a radius of 30 pixels (i.e., $6''$) from the QSO center in each field.

Comparing with other commonly used QSO light subtraction methods, such as principle component analysis (and similarly, non-negative matrix factorization) (e.g. Johnson et al., 2018; Helton et al., 2021) and a joint analysis of the QSO spectrum and the host galaxy spectrum incorporating stellar population synthesis models (e.g. Rupke et al., 2017), the method described above has the advantage of being relatively simple while delivering very clean residual spectra. However, a couple of caveats should also be noted. By using a QSO template spectrum that is scaled according to the smoothed ratio spectrum, this method removes all low-order features, including continuum and broad emission lines, indiscriminate to the origin of such features. As a result, it removes the low-order signal from the QSO host galaxy as well as other possible continuum sources located underneath the QSO PSF. Hence

this method works well for revealing spectral features narrower than typical QSO broad lines, such as the extended nebula emission studied here, but it is not suitable for studies of host galaxies and continuum sources. Meanwhile, in the QSO template spectrum constructed around the core region of the QSO PSF, there are possible contributions from the template to the targeted narrow emission line, and therefore the line flux in the nebula after QSO light subtraction could be underestimated. We, therefore, take extra caution when forming the QSO template and exclude spaxels with relatively strong narrow signals at the wavelength of the lines of interest.

3.3.3 Narrow-band images

Additional continuum subtraction was applied to the full data cube across the FOV to further remove background continuum flux in spaxels not included in the QSO light subtraction step. In general, we used a continuum spectrum determined through linear interpolation using the median value in a blue (red) window that was approximately $[-3000, -1500]$ ($[+1500, +3000]$) km/s away from the expected line center. In practice, based on the observed wavelength of the line of interest in each field, the spectral windows were adjusted to avoid noisy regions due to strong skylines and other artifacts in the data cube.

To enhance the SNR of the extended faint emission in the outskirts of each QSO nebula, we smoothed the data in the spatial dimension with a Gaussian kernel. The FWHM of the Gaussian kernel is chosen to be 3.5 pixels (i.e., $0''.7$) for all four fields. In Table 3.2, we list the atmospheric seeing size for each field measured at the position of the QSO at 7000Å before applying the additional spatial smoothing. The total PSF FWHM after smoothing was $\approx 50\%$ larger than the seeing disk. No additional smoothing was applied along the spectral dimension. The 1-σ surface brightness limit in a single wavelength slice (i.e., width of 1.25Å) at the observed wavelengths of the [O II] $\lambda\lambda\,3727, 3729$ and [O III] $\lambda\,5008$ lines for each field ranges from approximately $6 \times 10^{-20}\mathrm{erg\,s^{-1}\,cm^{-2}\,arcsec^{-2}}$

to $3 \times 10^{-19} \mathrm{erg\, s^{-1}\, cm^{-2}\, arcsec^{-2}}$, as listed in Table 3.3. TXS0206$-$048 has the lowest noise level at the observed [O II] $\lambda\lambda\, 3727, 3729$ wavelength due to a significantly longer total integration time.

With the smoothed, continuum- and QSO light-subtracted data cube, optimally-extracted narrow-band images were constructed for both [O II] $\lambda\lambda\, 3727, 3729$ and [O III] $\lambda\, 5008$ lines for the three lower redshift fields. For TXS0206$-$048, the [O III] $\lambda\, 5008$ line is redshifted out of the MUSE spectral coverage and therefore no results based on [O III] $\lambda\, 5008$ are available. Optimal extraction using a 3D mask that takes advantage of the information along both the spatial and the spectral dimension was carried out to maximize the SNR in the resulting narrow-band images. Detailed descriptions of the procedure can be found in, e.g., Borisova et al. (2016) and Sanderson et al. (2021). In short, the 3D mask was created based on an SNR threshold chosen for each voxel (i.e., volume pixel) of the data cube, and the minimum number of consecutive spectral pixels in a given spaxel to be included in the mask. For this study, we chose a voxel SNR threshold of 1 and a minimum number of consecutive spectral pixels of 3. The narrow-band images constructed using such 3D masks are shown in Figure 3.1 for all four fields.

3.3.4 Emission line analysis and velocity measurements

To determine the line-of-sight velocities at different locations across the nebulae, we performed a line profile analysis by adopting a Gaussian profile convolved with an appropriate instrumental line spread function. For fields with both [O II] $\lambda\lambda\, 3727, 3729$ and [O III] $\lambda\, 5008$ detections, we carried out the analysis of these two lines separately. The [O II] $\lambda\lambda\, 3727, 3729$ doublet is mostly unresolved for all fields at the MUSE resolution. Furthermore, both the [O II] $\lambda\lambda\, 3727, 3729$ and [O III] $\lambda\, 5008$ emission lines exhibit complex line profiles showing evidence for multiple velocity components, particularly in the inner regions closer to the QSOs. For some individual velocity components, spatial variation is observed in the [O III]/[O II] line

ratio, leading to different flux-weighted mean velocities at the same locations for these two lines. We, therefore, decided to take a simpler approach and fit these two lines separately.

We adopted an MCMC approach to search for the best-fit parameters of individual Gaussian components, which was implemented with the Python module `emcee` (Foreman-Mackey et al., 2013). Compared with least-square-based fitting methods, an MCMC approach provides a more robust posterior probability density distribution for the model parameters, naturally accounting for non-Gaussian posteriors as well as upper/lower limits. For the [O II] $\lambda\lambda\, 3727, 3729$ blended doublet, we only included one Gaussian component in the model profile for all spaxels, as the current MUSE data do not provide sufficient spectral resolution to break the degeneracy between the centroids of multiple velocity components and the doublet line ratios. For the [O III] $\lambda\, 5008$ line, we conducted the fitting with up to four independent Gaussian components and determined the number of components in each spaxel based on the Bayesian information criterion (BIC) (see e.g. Sharma, 2017). We required that a complex model with more Gaussian components can be accepted only when its BIC value was smaller than the BIC value of a simpler model by at least 30. We chose this more stringent threshold than the commonly adopted value of ΔBIC > 10 because the spectra from the data cubes often displayed complicated noise spikes that were not fully accounted for in the error arrays, and a more conservative approach was required to avoid over-fitting when using multiple components.

However, as we will discuss in §3.4.4 and show in Figure 3.14 below, for spaxels with multiple Gaussian components to model the observed [O III] $\lambda\, 5008$ line, adopting a flux-weighted mean velocity leads to similar VSF measurements as adopting a one-component model (i.e., ignoring the multi-component nature of the line). For simplicity, we, therefore, opted to focus on the VSF measurements based on the one-component model even for spaxels with complex line profiles. We will present and discuss results from the multi-component fitting process of the [O III] $\lambda\, 5008$ line in a subsequent paper.

97

3.3.5   VSF measurements

Before carrying out the VSF measurements, we performed a series of checks to ensure that the results are robust. First, we examined possible contamination resulting from overlapping continuum sources due to projection effects. In particular, a large velocity contrast would suggest that such continuum sources might not belong to the same dynamic system as the rest of the line-emitting gas, and therefore should be excluded from the VSF measurements. For the PKS0454−22 and TXS0206−048 fields, we used the archival broadband *HST* data to identify continuum sources (Helton et al., 2021; Johnson et al. in prep). For the J0454−6116 and J2135−5316 fields, due to a lack of higher spatial resolution imaging data, continuum sources were identified using a MUSE white-light image. We flipped the white-light image of each field along the x-axis (using the QSO centroid as the center), and subtracted the flipped image from the original image. Strong continuum sources underneath the QSO PSF will lead to a pattern of significant residual flux at the original locations of such sources paired with significant over-subtraction at their flipped locations. This method helps to identify sources that might be easy to miss due to the QSO PSF. Flipping along the y-axis of the image would have achieved the same effect. Out of the four fields, we only identified two strong continuum sources in the J0454−6116 field that stood out in the velocity map and excluded the spaxels inside a circular aperture centered on each of these two continuum sources. The size of the aperture was chosen to enclose most of the continuum flux. For the remaining three fields, the continuum sources overlapping with the nebulae showed consistent velocities with the rest of the nebulae, and no spaxels were excluded from the VSF measurements.

In addition, we masked spaxels with highly uncertain velocity measurements. Because we adopted a generous voxel SNR threshold when forming the 3D masks (see § 3.3.3), some spaxels included in the line fitting step had relatively faint signals and large measurement uncertainties that would significantly impact the VSF measurement uncertainties. We excluded spaxels with a velocity uncertainty larger than 45 km/s. This threshold was approximately

two to three times the median uncertainty of the fitting results based on the [O III] λ 5008 line, and was about the median uncertainty for measurements based on the [O II] $\lambda\lambda$ 3727, 3729 line among all fields. We verified that changing this threshold by a small amount (i.e., ± 15 km/s) did not lead to significant differences in the subsequent analyses. Finally, we examined the probability density distribution of the observed velocities among the rest of the spaxels in each field, and filtered out spaxels that are outliers (i.e., either too blue or too red in velocity, defined to be the $\approx 2\%$ tail on both ends). We also excluded the central $r \leq 3$ pixels region for both J0454−6116 and J2135−5316 fields due to noisy residuals from the QSO light removal, which was not necessary for PKS0454−22 and TXS0206−048.

All spaxels left after the above filtering steps were included in subsequent VSF measurements. Summing over all these spaxels, we report the total luminosity in [O II] $\lambda\lambda$ 3727, 3729 and [O III] λ 5008 line emission as well as the total area (in kpc^2) for each field in Table 3.3. Out of the four fields, TXS0206−048 has the largest area. In fact, in terms of the area and the total line emission luminosity of the [O II] nebula, TXS0206−048 exceeds the "Makani" nebula at $z = 0.459$, the largest [O II] nebula detected hitherto (Rupke et al., 2019)[1]. The filtered [O II] velocity map of the TXS0206−048 field is shown in the left panel of Figure 3.3, together with its corresponding velocity uncertainty map on the whole 3D mask footprint for comparison. The filtered velocity maps of the other three fields, for both [O II] and [O III] lines, are shown in Figures 3.7–3.12 in the Appendix.

Because of the spatial correlation between adjacent spaxels, when measuring the VSF, individual velocity pairs within a distance separation bin are not independent of each other. We therefore cannot directly propagate the measurement uncertainties of the velocity centroids in each spaxel to estimate the uncertainties of the VSFs. To robustly estimate the

---

1. Note that the size and [O II] line luminosity of TXS0206−048 reported in Table 3.3 were obtained at a surface brightness level of $\sim 10^{-19}$erg s^{-1} cm^{-2} arcsec^{-2}, significantly lower than the surface brightness threshold of 5×10^{-18}erg s^{-1} cm^{-2} arcsec^{-2} used in Rupke et al. (2019). At the level of 5×10^{-18}erg s^{-1} cm^{-2} arcsec^{-2}, the TXS0206−048 [O II] nebula has an area ≈ 4100 kpc^2, slightly smaller than 4900 kpc^2 covered by "Makani".
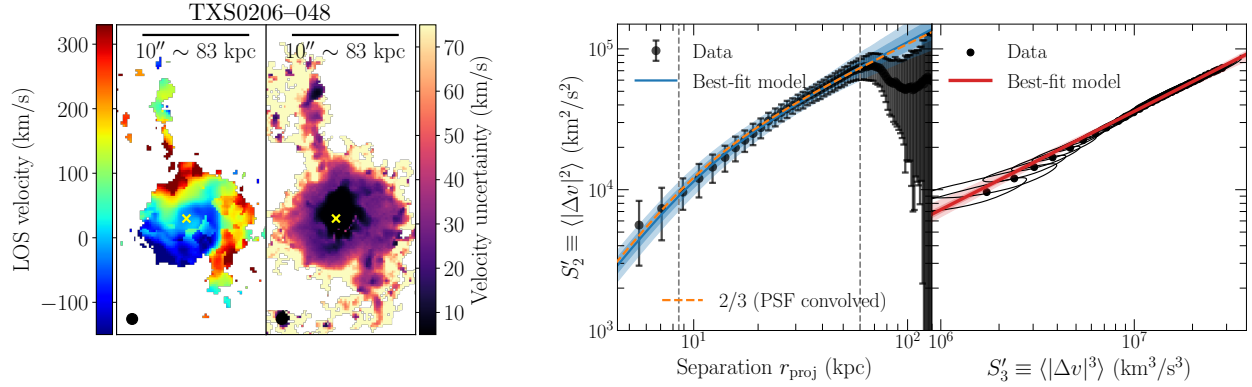
Figure 3.3: *Left panels:* The observed velocity map and the associated measurement uncertainties of the extended nebula around TXS0206−048 using the [O II] $\lambda\lambda\,3727, 3729$ emission lines. The yellow cross in both panels marks the QSO position. Only pixels included in the VSF calculation are shown in the velocity map (see §3.3.5), while the velocity uncertainty panel contains all pixels from the 3D mask (see §3.3.3). The black circle at the bottom left represents the total PSF of this field, after convolving the atmospheric seeing with the smoothing kernel applied to improve the SNR. *Right panels:* The second-order VSF $S_2'(r)$ constructed using the velocity map displayed in the left panel, along with the S_2' vs. S_3' correlation. Vertical dashed lines mark the fitting boundaries in r_{proj}, with the left line indicating the $\mathrm{FWHM}_{\mathrm{total}}$ of the field and the right line indicating the maximum r_{proj} beyond which a single power-law model does not provide a good fit anymore. The best-fit model of S_2', after being convolved with the total PSF, is shown as the blue solid curve. The dark (light) blue shaded region represents the 16th–84th (2nd–98th) quantile range for the model. The orange dashed curve shows the PSF-convolved Kolmogorov mode for S_2' with a theoretical slope of $\gamma_2 = 2/3$. In the right panel, the best-fit power-law model for the S_2' vs. S_3' relation is shown as the red solid line with the model uncertainty represented by the red shaded region. Only the data points within the same distance separation range for the fitting of S_2' are shown in the S_2'-S_3' panel, with the ellipses showing the correlated 1-σ error area determined by the eigen vectors and eigen values of the covariance matrix within each distance bin. We measure an intrinsic power-law slope of $\gamma_2 = 0.72^{+0.12}_{-0.11}$ and $\gamma_3 = 1.03^{+0.18}_{-0.16}$ for S_2 and S_3, respectively (see Table 3.4).

uncertainty of the VSF, we proceeded with the following steps. First, we divided the whole nebula in each field into smaller sub-regions. The size of these sub-regions was roughly the FWHM of the total PSF in each field (see Table 3.1). Most of these sub-regions were squares while some sub-regions located near the edge of the nebula had irregular shapes. Next, we randomly selected one spaxel per sub-region and constructed a VSF based only on the selected spaxels. We then repeated the step of randomly selecting one spaxel per sub-region 1000 times, and each time obtained a VSF measurement. In addition, for each iteration, we perturbed the velocity map to within the measurement uncertainties by randomly assigning a new velocity value drawn from the MCMC chain to each spaxel. By restricting the pair formation to one spaxel per sub-region defined by the PSF, we were able to minimize correlated noise between adjacent bins in the VSF and recover small-scale power lost due to smoothing. We refer to this procedure as a modified bootstrap method. We obtained a mean and standard deviation of the 1000 VSFs as the measurement and associated uncertainty of the final VSF. Note that while all VSFs were measured using a distance bin size of one spaxel, only measurements separated by scales larger than the size of the total PSF were included when quantifying the slope of the VSFs (see § 3.4.1 below for details of constraining the VSF slopes).

3.4 Results

Of the four QSO nebulae studied here, TXS0206−048 has the most constraining IFS data and the largest spatial extent (see Figure 3.1 and Table 3.3). Together, these characteristics ensure the best-determined velocity map and well-constrained VSFs. In this section, we present the VSFs measured for extended QSO nebulae at $z_{\mathrm{QSO}} \approx 0.5$–1.1 with a focus on the line-emitting gas detected around TXS0206−048 at $z_{\mathrm{QSO}} \approx 1.1$. In addition, we investigate the impact on the observed VSFs due to possible underlying coherent bulk flows in these nebulae. We consider the presence of unidirectional velocity gradient, radial, and

tangential motions in the observed velocity field of each nebula, and compare the measured VSFs before and after removing these smooth velocity components.

3.4.1   The observed VSFs of TXS0206−048

The velocity and velocity uncertainty maps of the [O II] $\lambda\lambda\,3727, 3729$ nebula around TXS0206−048 displayed in Figure 3.3 show that the line-emitting gas is highly disturbed with well-determined line-of-sight velocities spanning a wide range from ≈ -150 km/s to $\gtrsim 300$ km/s across the full extent of nearly 200 kpc defined by the narrow stream-like feature toward the northeast and southwest (Johnson et al., 2022). However, most of the statistical power in the VSF measurements lies in the main, more spherically distributed nebula of ≈ 90 kpc in diameter centered on the QSO. The observed second-order VSF, S_2', is well characterized by a single power-law scaling up to $r_{\text{proj}} \approx 60$ kpc over the projected distance range from $r_{\text{proj}} < 6$ kpc to $r_{\text{proj}} \approx 60$ kpc (Figure 3.3).

To quantify the second-order VSF slope, we apply a power-law model convolved with the total PSF to characterize the reconstructed S_2' from each of the 1000 realizations obtained through the modified bootstrap method described above. We adopt a Gaussian function with an FWHM of 8.3 kpc for the PSF in TXS0206−048 (see Table 3.1), and we follow the steps discussed in §3.2 to calculate the shape of the power-law model after the PSF convolution. Note that we only consider non-negative power-law slopes, as negative slopes are not motivated by the data here and would lead to divergence at $r = 0$ for a simple power-law parameterization. The model fitting is done over the distance range of 8.3 kpc$< r_{\text{proj}} <$60 kpc, using the `Scipy` curve_fit routine. The small-scale cutoff at 8.3 kpc is to minimize systematic uncertainties due to spatial smoothing, while the large-scale threshold at 60 kpc is determined based on a series of trials and errors to optimize the fitting precision and accuracy. For S_2 of TXS0206−048 obtained using the [O II] $\lambda\lambda\,3727, 3729$ emission line, we measure a slope of $\gamma_2 = 0.72^{+0.12}_{-0.11}$. The best-fit value corresponds to the median value among

the 1000 fitting results, and the 16th and 84th quantiles represent the lower and upper limit, respectively.

In Figure 3.3, the best-fit model is shown in the blue solid curve, with the dark (light) blue shaded region representing the 16th–84th (2nd–98th) quantile range for the models. This measurement is consistent with the Kolmogorov slope of 2/3 (orange dashed curve in Figure 3.3) for isotropic, homogeneous, and incompressible turbulence. We have experimented with removing the stream-like features both north- and south-ward of the main nebula, and we obtained consistent VSF measurements.

In addition to S'_2, for each of the 1000 modified bootstrap samples described above, we also calculate the VSF S'_p for other orders up to $p = 6$, and examined if the ESS discussed in §3.2 applies to this data set. Limited by the data quality, VSFs for $p > 6$ become too noisy to result in meaningful constraints. In the right-most panel of Figure 3.3, we show the measurement of S'_2 as a function of S'_3 for TXS0206$-$048. Note that the S'_2 and S'_3 measurements are highly correlated. Therefore, we use ellipses to show the 1-σ confidence intervals with the elongations and sizes determined by the eigen vectors and eigen values of the data covariance matrix in each distance bin.

Similar to the ESS presented in Benzi et al. (1993) (see their Figure 3), we observe a well-defined power-law relation of $S'_2 \propto S'^{0.70\pm0.03}_3$. The measurement of this power-law slope is obtained using the 1000 realizations of the velocity map, and only the data points within the same distance range of 8–60 kpc are included in the model fitting. Due to the tight correlation between S'_2 and S'_3, the ESS scaling slope is much better constrained than the individual slopes γ_2 and γ_3. Because we can analytically incorporate the effect of PSF smoothing into a power-law S_2 but not for S_3, the presence of the ESS in this data set conveniently allows us to measure a slope and amplitude of S_3 accurately. In addition, as discussed in §3.2, the smoothing effect does not change the power-law scaling relation for ESS. Combining the measured S_2 slope of $\gamma_2 = 0.72^{+0.12}_{-0.11}$ and the S_2-S_3 power-law scaling of
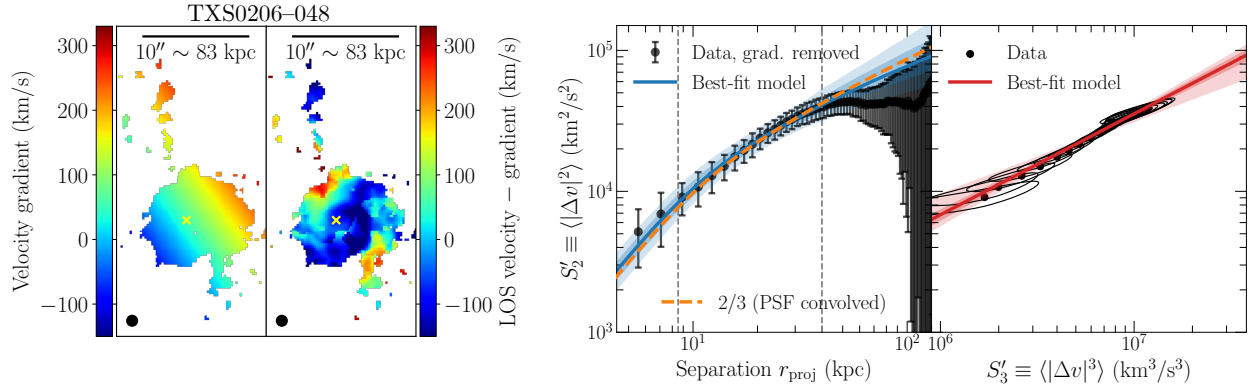
Figure 3.4: *Left panels:* The best-fit 2D velocity gradient model and the residual velocity map after subtracting the velocity gradient from the observed velocity map for TXS0206−048. The yellow cross in both panels marks the QSO position. Similarly to the left-most panel of Figure 3.3, only pixels included in the VSF calculation are shown. *Right panels:* $S'_2(r)$ and the S'_2-S'_3 ESS relation constructed using the gradient-subtracted velocity map displayed on the left. Similar to the right panels of Figure 3.3 but calculated with the gradient removed velocity map. We measure an intrinsic power-law slope of $\gamma_2 = 0.56^{+0.16}_{-0.17}$ and $\gamma_3 = 0.78^{+0.28}_{-0.25}$ for S_2 and S_3, respectively (see also Table 3.4).

$\gamma_2/\gamma_3 = 0.70 \pm 0.03$, we obtain a slope of $\gamma_3 = 1.03^{+0.18}_{-0.16}$ for S_3 in TXS0206−048. Consistent with the result for S_2, the S_3 slope is in excellent agreement with the expectation of $\gamma_3 = 1$ for Kolmogorov turbulence. Discussions on the slopes of higher-order VSFs are presented in §3.5.3.

3.4.2   Effect of large-scale velocity gradients

While the measured S_2 and S_3 are both consistent with Kolmogorov turbulence for the nebula surrounding TXS0206−048, a caveat remains regarding the presence of large-scale coherent flows which could contribute to the observed power in the velocity structure functions (e.g. Zhang et al., 2022, for a discussion). In this section, we address this issue by considering a unidirectional flow model for removing the bulk flow in the observed velocity map.

We first adopt a simple model velocity map parameterized as $v(x, y) = ax + by + c$, where x and y are the coordinates of individual spaxels within the nebula, and a, b, and c are free

104

parameters used to capture any potential large-scale velocity gradient. We apply this model to the empirical velocity map displayed in the left-most panel of Figure 3.3, and obtain the best-fit velocity gradient map as shown in the left-most panel of Figure 3.4. The gradient in the model is ≈ 3.7 km/s/kpc. We estimate the uncertainty of this gradient by fitting 1000 velocity maps that are randomly generated based on the MCMC line fitting chain for each spaxel. Due to the relatively large number of spaxels included in the analysis (i.e., over 2000 in the field of TXS0206$-$048), the velocity gradient based on this simple three-parameter model is well-determined. We then subtract the best-fit 2D velocity gradient from the original velocity map and obtain the residual velocity map shown in Figure 3.4.

At first look, the best-fit unidirectional flow model does not completely capture the coherent flows displayed in Figure 3.3. While it captures the apparent velocity shear along the east-west direction, the velocity gradient visible along the north-south direction remains. This motivates a different approach to consider the presence of radial/tangential flows, which is discussed in § 3.4.3 below. Here we proceed with the discussion using the residual map displayed in Figure 3.4. We repeat the VSF measurements described in § 3.3.5 and obtain both the S_2' and the S_2'-S_3' ESS relation. The results are shown in the right panels of Figure 3.4.

As expected, subtracting a large-scale velocity gradient has a larger impact on larger scales, and S_2', in general, becomes flatter compared to the results in Figure 3.3 using the original velocity map. Instead of continuing to rise to larger scales, S_2' appears to flatten at $r_{\mathrm{proj}} \approx 40$ kpc. The S_2' vs. S_3' ESS still holds for the gradient removed velocity map. We estimate an intrinsic power-law slope of $\gamma_2 = 0.56^{+0.16}_{-0.17}$ for S_2 and $\gamma_3 = 0.78^{+0.28}_{-0.25}$ for S_3. Note that the fitting range is now restricted to 8.3 kpc$< r_{\mathrm{proj}} <$40 kpc due to the flattening at 40 kpc, resulting in larger uncertainties in the best-fit slopes. While the slope is flatter than what is obtained before removing the velocity gradient model, the two results are consistent to within the uncertainties. Similarly, we also overplot the expected Kolmogorov S_2' with a

slope of 2/3 after convolving with the PSF as the orange dashed curve in Figure 3.4. It is clear that despite the data points exhibiting a flatter overall trend, the measurements still agree with the Kolmogorov slope over the scales probed.

Based on the morphology of the nebulae (see Figure 3.1) and the velocity measurements, the nebulae in all four fields do not show signatures of well-established rotation disks. We, therefore, do not consider a more elaborate disk model with additional parameters such as inclination and maximum rotation velocity.

3.4.3   Effects of radial and tangential motions

Complementary to the simple, unidirectional coherent flows discussed above, here we investigate whether there exist significant differences between the VSFs constructed along the radial vs. tangential directions. This is a physically motivated scenario as gas outflows can manifest as coherent, radial motions while gas infalls are more likely to form large-scale tangential motions due to the conservation of angular momentum. For instance, if a nebula is mostly comprised of isotropic supergalactic winds, we would expect that the measured S_2 is driven by the power associated with radial motions with the best-fit slope γ_2 indicative of the acceleration of the wind. In addition, this test can also reveal anisotropy if the radial vs. tangential VSFs exhibit distinctive shapes.

Using the velocity map presented in Figure 3.3, we classify the velocity pairs into two groups based on their spatial configuration with respect to the QSO location. The classification criterion is illustrated in the left panel of Figure 3.5. In this classification, we require both pixels in a pair to reside in the same quadrant of the nebula with the angle ϕ (see Figure 3.5) being equal to or smaller than 90°. Velocity pairs taken from pixels located in different quadrants of the nebula are not considered to avoid ambiguities between radial and tangential pairs. We then calculate θ, which is the angle between the vector that connects the two points in a pair and the vector that connects the pair mid-point to the QSO loca-
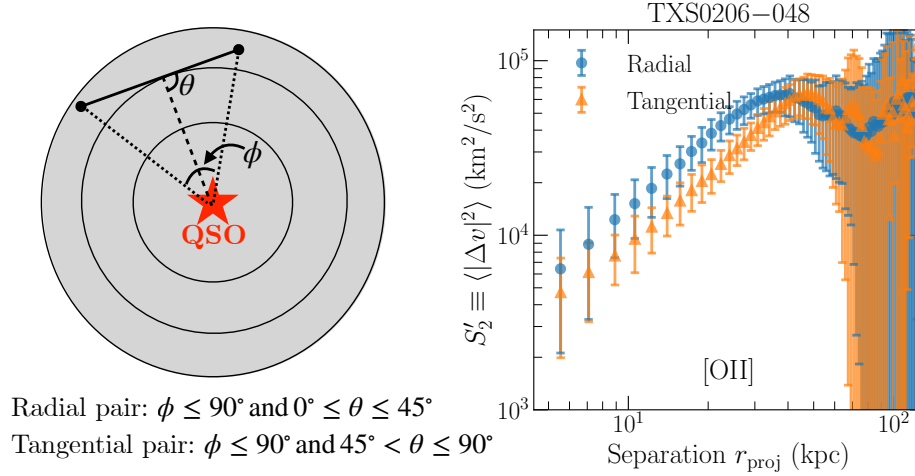
Figure 3.5: *Left:* Illustration of the radial vs. tangential pair classifications. *Right:* The second-order VSFs S_2' measured using radial and tangential pairs, respectively, based on the velocity map presented in Figure 3.3. The shapes of S_2' for the radial and tangential pairs are consistent with each other, while the radial pairs exhibit a higher amplitude in the VSF.

tion, as shown in Figure 3.5. We assign any pairs with $0° \leq \theta \leq 45°$ ($45° < \theta \leq 90°$) as radial (tangential) pairs, and repeat the VSF measurements using these two groups of pairs separately. The results are shown in the right panel of Figure 3.5.

The shapes of S_2' for the radial and tangential pairs are consistent with each other, while the radial pairs exhibit a slightly higher amplitude in the VSF. This test demonstrates that the nebula gas undergoes dynamical processes with similar turbulence energy cascade characteristics along the radial and tangential directions, and that both directions have comparable contributions to the signal in the total VSF presented in Figure 3.3. Repeating this exercise with the gradient-removed velocity map leads to the same conclusion.

3.4.4   The observed VSFs of PKS0454−22, J0454−6116 and J2135−5316

For the remaining three fields, PKS0454−22, J0454−6116 and J2135−5316, both the [O II] $\lambda\lambda\,3727, 3729$ and [O III] $\lambda\,5008$ lines are detected in the MUSE cubes. We present the VSF measurements based on both lines, which are shown in Figures 3.7-3.12 in the Appendix. Constraints on the slopes of the VSFs are summarized in Table 3.4.

Table 3.4: Summary of the power-law slopes of the VSFs constructed using [O II] and [O III] lines[a].

Field name	[O II]		[O II] grad. removed[b]		[O III]		[O III] grad. removed[b]	
	γ_2	γ_3	γ_2	γ_3	γ_2	γ_3	γ_2	γ_3
PKS0454−22	< 0.78	< 1.15	< 0.66	< 0.99	< 0.67	< 0.94	< 1.45	< 2.3
J0454−6116	< 0.51	< 0.77	< 0.45	< 0.74	< 0.84	< 1.26	< 0.33	< 0.48
J2135−5316	< 0.50	< 0.76	< 0.65	< 1.02	< 1.23	< 1.81	< 1.12	< 1.75
TXS0206−048	$0.72^{+0.12}_{-0.11}$	$1.03^{+0.18}_{-0.16}$	$0.56^{+0.16}_{-0.17}$	$0.78^{+0.28}_{-0.25}$	−	−	−	−

Notes.

[a] Constraints for the best-fit slopes listed here are based on the 1000 modified bootstrap samples (see §3.3.5). These slopes are the intrinsic power-law slopes for S_2 and S_3, as our fitting procedure explicitly accounts for the smoothing effect in the measured S_2' and S_3' (see §3.4.1). For PKS0454−22, J0454−6116, and J2135−5316, we present 95% upper limits for the slope under the assumption that the observed pair separations are within the inertial range. If the available pair separations are close to injection scales, then no robust constraints can be obtained. For TXS0206−048, we list the median value as well as the 16th and 84th quantiles as lower and upper limits. Note that, as discussed in §3.4.1, we only consider non-negative power-law slopes.

[b] Measurements obtained after removing a 2D velocity gradient (see §3.4.2).

Compared with the results for TXS0206−048, the constraints on the slopes of the VSFs for these three QSO nebulae are weaker. The large uncertainties can be attributed to the limited dynamic range in spatial scale when comparing the spatial extent of the line-emitting nebulae with the size of the PSF in the data (see §3.2). As listed in Table 3.3, the [O II] nebula included in the VSF measurements for TXS0206−048 is ≈ 2–4 times larger than that of these three fields. The larger area leads to smaller uncertainties in the VSF measurements in each distance bin, and a larger dynamic range in distance separation, both contributing to a better-constrained VSF. In contrast, a limited dynamic range in the pair separations for the remaining three nebulae inevitably pushes the VSF measurements closer to the injection scale, where we expect the VSF to flatter (e.g., Benzi et al., 1993). If this is the case, then no robust constraints can be obtained for the VSF slopes in the inertial range.

Similar to the result of TXS0206−048, removing a large-scale unidirectional velocity gradient from the velocity maps results in a flatter VSF. However, the measured slopes are consistent before and after the gradient removal, particularly with the large uncertainties for these fields. The VSFs calculated with radial vs. tangential pairs are also consistent in terms of the general shape and amplitude within each field, as shown in Figure 3.13. Despite poorly constrained S'_2, a strong correlation between S'_2 and S'_3 remains with $\gamma_2/\gamma_3 \approx 0.7$. (see Figures 3.7–3.12).

3.4.5   Effects of line-of-sight projections

The availability of both [O II] $\lambda\lambda\, 3727, 3729$ and [O III] $\lambda\, 5008$ emission signals for three of the QSO nebulae studied here also offers an opportunity to investigate the effect of line-of-sight projection. In particular, while velocity measurements of [O II] $\lambda\lambda\, 3727, 3729$ and [O III] $\lambda\, 5008$ for PKS0454−22, J0454−6116 and J2135−5316 are mostly consistent with each other, there are regions with significantly different values between the two velocity maps, revealing not only that the emission signals are a blend of multiple components along the

sightline but also that there exists a large variation in the [O III]/[O II] line flux ratio between different components. Such variations indicate changing ionization conditions between different gas clumps that overlap along the line-of-sight and/or are unresolved along the plane of the sky (see § 3.5.4 for further discussion).

Here we test how the measured VSFs change with different treatments of regions showing multi-component [O III] $\lambda\,5008$ line profiles. Specifically, we compare three different scenarios where we assign to each multi-component spaxel (1) the velocity of the component with the largest line flux, (2) the velocity obtained by forcing a one-component fit, and (3) the flux-weighted mean velocity across all components. We present the VSF comparison under these three scenarios in Figure 3.14. While the uncertainties are large, this data set indicates that using the velocity of the dominant component in flux for multi-component spaxels may lead to a flatter VSF with higher amplitudes on small scales. Using the flux-weighted mean velocity and adopting a one-component fitting velocity results in similar VSFs, which motivates our decision to present the single-component fitting result in the VSF measurements.

3.5   Discussion

Of the four QSO nebulae studied in this work, we have shown that the VSFs of one QSO nebula, TXS0206−048, are in spectacular agreement with expectations from the Kolmogorov law. The Kolmogorov model applies to isotropic, homogeneous, and incompressible flows. The observed agreement, therefore, implies that gas flows in the nebula are subsonic and that the turbulent energy is being transferred at a constant rate between different spatial scales. Given the expectation that the observed [O II] emission traces cool gas of temperature $T \sim 10^4$ K with a sound speed of $c_s^{\rm cool} \approx 10$ km/s, the observed velocity difference of $\Delta\,v \gtrsim 100$ km/s on scales greater than 10 kpc would lead to a conclusion of supersonic motions within the cool gas. On the other hand, the QSO is found to reside in a massive halo of $M_{\rm halo} \approx 5\times10^{13}{\rm M}_\odot$ (see § 3.5.1 below) with an anticipated temperature of $T \sim 10^7$ K

for the hot halo and a sound speed of $c_s^{\text{hot}} \approx 300$ km/s. If the [O II]-emitting gas originates in cool clumps condensed out of the surrounding hot halo, then the observed VSFs capture the subsonic motions of individual clumps relative to the hot medium. For the remaining three nebulae around PKS0454−22, J0454−6116, and J2135−5316, however, no robust constraints for the VSFs can be determined due to a limited dynamic range in seeing-limited data.

In this section, we discuss the implications for the energy balance in the diffuse CGM in these QSO host nebulae. We first estimate the turbulence energy transfer rate, using TXS0206−048 as an example, and explore possible causes for the observed differences in the VSFs between the different QSO nebulae. Finally, we review the limitations and caveats in the observations.

3.5.1   Constant turbulent energy cascade in TXS0206−048

For turbulent gas that follows the Kolmogorov law, the mean energy transfer rate per unit mass ϵ is expected to be constant within the inertial range and can be estimated following

$$\epsilon = \frac{5}{4} \left[\frac{|\langle \Delta v(r)^3 \rangle|}{r} \right] \approx \frac{5}{4} \left[\frac{\langle |\Delta v(r)|^3 \rangle}{r} \right]. \tag{3.8}$$

This is commonly referred to as the "four-fifths law" in fully developed turbulence, and is an exact result derived from the Navier-Stokes equations (Kolmogorov, 1941; Frisch, 1995). As stated in Benzi et al. (1993), the relation $|\langle \Delta v(r)^3 \rangle| \approx \langle |\Delta v(r)|^3 \rangle$ is not obvious from first principles but has been experimentally verified. Using the S_3 measurement for TXS0206−048, we obtain $\epsilon \approx 0.2$ cm^2 s^{-3}. This energy transfer rate is comparable to the value measured with Hα filaments in the Perseus cluster (Li et al., 2020), as well as the 0.1–1 cm^2 s^{-3} rate estimated for the Orion Nebula (e.g. Kaplan & Pikelner, 1970). Rauch et al. (2001) reported a lower ϵ of $\sim 10^{-3}$ cm^2 s^{-3} for C IV absorbers at $z \approx 3$, suggesting that the CGM in high-redshift star-forming halos is less turbulent with a lower energy cascade rate

(see also Rudie et al., 2019). However, due to the unspecified uncertainty in the VSF measurement in Rauch et al. (2001) and the different data set used, it is not conclusive whether the current discrepancy between our result and that of Rauch et al. (2001) is significant.

Figures 3.3 and 3.4 show that the VSF of TXS0206−048 flattens at around 50 kpc. Given that the statistical uncertainty in the VSF does not increase significantly until a scale of ≈ 80 kpc, the turnover point at 50 kpc may be interpreted as the energy injection scale in this system. In contrast, we do not detect signatures of the dissipation scale in all systems due to a fundamental limitation on the spatial resolution in seeing-limited observations.

In addition, the estimated ϵ suggests that turbulent energy is subdominant in QSO host halos, as can be shown through the following calculations. The total mass of the dark matter halo hosting TXS0206−048 is estimated to be $M_{\mathrm{halo}} \approx 5 \times 10^{13} \mathrm{M}_\odot$ (Johnson et al., 2022). Adopting a baryon fraction of $f_b \approx 0.15$ (Planck Collaboration et al., 2020), we calculate a total baryonic mass within a radius of 50 kpc to be $\sim 3 \times 10^{11} \mathrm{M}_\odot$ for an NFW halo with a reasonable choice of halo concentration (i.e., between 4 and 10). This gives us a total turbulent energy transfer rate of $\dot{E}_{\mathrm{turb}} \sim 10^{44}$ erg s^{-1}, assuming that gas of all phases is perfectly coupled dynamically and that the turbulence cascade does not affect gas residing at distances much larger than ≈ 50 kpc (i.e., the injection scale) from the halo center. Keeping these assumptions in mind, the turbulent energy that will eventually dissipate and heat up the gas in the CGM is $\sim 0.05\%$ of the bolometric luminosity of the QSO (see Table 3.1), which is similar to the wind energy fraction observed in AGN outflows (e.g., Fabian, 2012; Sun et al., 2017). At the same time, this turbulent heating rate has the same order of magnitude as the [O II] $\lambda\lambda\, 3727, 3729$ line luminosity. As we expect the gas to also cool through other forms of emission (e.g., [O III] $\lambda\, 5008$, Hα and Lyαlines for the $\sim 10^4$ K ionized phase), the turbulent heating rate is not sufficient to offset cooling of this gas in the vicinity of a luminous QSO.

Finally, we note that in comparison to the remaining three QSO nebulae included in

this study (see Table 3.1), TXS0206−048 occurs at the highest redshift QSO, $z_{\mathrm{QSO}} \approx 1.13$, and appears to reside in the highest-mass halo with a significant number of group members being super-L_* galaxies and a large velocity dispersion (Johnson et al., 2022). The associated galactic environment may also play a significant role in driving the turbulence in the CGM, in addition to QSO outflows.

3.5.2   Implications of the VSF slopes

While the Kolmogorov theory has explicit predictions for the slopes of the VSF, a number of factors can impact the empirical measurements and should therefore be taken into account when interpreting the results. As discussed in §3.2, if the thickness of the nebulae along the line of sight is larger than the scales probed in the VSF, the projection effect will steepen the VSF. If the nebulae identified around these four QSOs are more sheet-like than spherical, then we would expect the intrinsic slope to be flatter than measured. Of the four nebulae studied here, J2135−5316 exhibits an elongated morphology and is most likely affected by such projection effect.

One possible explanation for the flat slopes is the presence of dynamically important magnetic fields, where the kinetic energy cascade is suppressed due to magnetic tensions (e.g., Boldyrev, 2006; Brandenburg & Lazarian, 2013; Grete et al., 2021; Mohapatra et al., 2022). Another interesting scenario for flattened VSFs is one where energy injections happen at multiple different length scales, instead of one scale that defines the canonical upper limit of the turbulent inertial range. When combining multiple kinetic energy power spectra with different injection scales, the resulting VSF reflects the superposition of the different components, leading to a flatter slope due to elevated power at scales smaller than the largest injection scale of the system (e.g., ZuHone et al., 2016). This scenario is consistent with a diverse range of dynamical processes expected to be present in the CGM of a QSO halo, such as gas outflows, mergers, AGN-inflated bubbles, and relativistic jets (e.g., Fabian,

2012). While the detailed mechanisms through which these processes transfer kinetic energy to the gas are poorly understood at the current moment, it is likely that different processes have different characteristic scales for energy injection. Irrespective of what the detailed mechanisms are, if the pair separations are indeed closer to the injection scale, then no conclusive constraints can be obtained for the VSF slopes in the inertial range.

Alternatively, the range of VSF slopes across the four fields could also be suggestive of a time-dependent evolution of these nebulae. As the energy injection from QSO outflows is expected to be episodic, turbulent energy may be dissipated during the off cycle, leading to a flat VSF. For virialised systems with a complete absence of turbulence, Melnick et al. (2021) indeed obtains flat VSFs based on N-body simulations. Taking TXS0206$-$048 as a reference, turbulent energy on scales of ~ 50 kpc is expected to be dissipated on a time scale of $\langle |\Delta v|^2 \rangle / \epsilon \sim 100$ Myr, and the time scale will be shorter for smaller spatial scales. Under this scenario, the observed flatter VSFs in the three lower redshift QSO nebulae suggest that the most recent episode of significant energy injection occurred more than ~ 100 Myr ago. Because such time scale exceeds the typical QSO lifetime of $\sim 0.1 - 10$ Myr (e.g. Schawinski et al., 2015; Sun et al., 2017; Shen, 2021), this would make the radiative feedback during the luminous phase of an AGN an unlikely source for driving the observed turbulence.

At the same time, recall that the four QSOs reside in a diverse range of galactic environments, with TXS0206$-$048 in a rich dynamic galaxy group while J2135$-$5316 in a relatively isolated environment with only two neighboring galaxies found (see Table 3.1). If galaxy/satellite interactions are a main driver of the turbulent CGM, then a flat VSF found for J2135$-$5316 may be attributed to the quiescent state of its galactic environment.

3.5.3 Extended self-similarity scaling slopes

In addition to the slopes γ_p of individual VSFs, the ESS scaling slopes between different orders can also shed light on the dynamic state of the gas. We have measured the slopes

114

of VSFs of each nebulae for up to $p = 6$. As mentioned in §3.4.1, with the current data set, VSFs for $p > 6$ become too noisy to deliver meaningful constraints. The results are presented in Figure 3.15, along with theoretical expectations presented in She & Leveque (1994) and Boldyrev (2002). These models account for Kolmogorov turbulence with the intermittency correction and supersonic magnetohydrodynamic turbulence, respectively. The simulation results for transonic and supersonic hydrodynamic turbulence presented in Pan & Scannapieco (2011) are also included in Figure 3.15 for comparison.

It is clear that the strongest discriminating power between these different scenarios lies in the higher-order VSFs with $p \geq 4$. Due to large uncertainties in our measurements particularly for higher orders, we can only rule out the scenario for supersonic hydrodynamic turbulence with a Mach number of 6.1 from Pan & Scannapieco (2011). While the measurements appear to support the presence of subsonic turbulence in all four quasar nebulae, we note that the simple $p/3$ scaling relative to S_3 is also expected from a simple dimensional inference. Consequently, in the absence of direct measurements of S_2, the relative scaling between different orders alone does not provide conclusive evidence for whether or not the gas follows subsonic turbulence.

3.5.4   [O II] and [O III] surface brightness profiles

As mentioned in §3.4.5, examinations of the observed [O III]/[O II] line flux ratio across the nebulae have revealed intrinsic differences in the gas traced by the [O II] and [O III] emission features. Here we investigate the circularly-averaged radial surface brightness profiles for [O II] and [O III] lines, as shown in Figure 3.6, in order to gain insights into the difference in the spatial distribution of the gas probed by different emission features. The observed one-dimensional surface brightness profile also facilitates a direct comparison of the gas properties across the four fields and with high-redshift quasars. Similar to the practice in Borisova et al. (2016), to obtain a more robust uncertainty estimate for the surface brightness level, we use
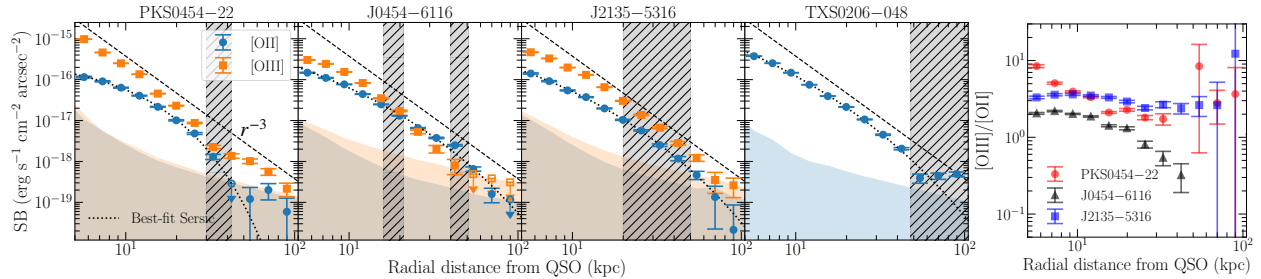
Figure 3.6: Surface brightness profiles of the four fields, and the corresponding [O III]/[O II] line flux ratios for the three lower redshift fields. The surface brightness profiles are circularly averaged within annuli at different distances from the QSOs. For the first three fields, vertical shaded regions indicate radii with relatively strong flux contributions from areas that are eliminated from the VSF measurements (see § 3.3.5). For TXS0206−048, the vertical shaded region indicates the radii of the stream-like structures away from the main nebula (see Fig. 3.1). Blue and orange shaded regions at the bottom of each panel show the 2σ limit of the [O II] and [O III] surface brightness level as a function of radius. Dotted curves show the best-fit Sérsic profiles for the [O II] line, with half-light radius $R_e \approx [10, 10, 9, 6]$ kpc and Sérsic index $n \approx [1.1, 2.6, 2.5, 3.0]$ for the four fields from left to right. For the [O III] profiles, however, we cannot find a good fit with Sérsic, exponential, or cored isothermal profiles. Instead, we overplot a power-law with -3 slope in dashed lines for comparison, as it provides a good match to the [O III] profile in PKS0454−22, as well as the [O II] and [O III] profiles outside of the core (≈ 10 kpc) region in other fields. In the right-most panel, [O III]/[O II] line flux ratios are shown for the three lower redshift fields, and data points with only upper limits on [O II] or [O III] are not included.

narrow-band images collapsed over a fixed range of wavelength slices across the whole field, instead of the optimally subtracted images shown in Figure 3.1. The wavelength range used for the narrow-band images here is decided based on the largest range along the wavelength dimension in the corresponding 3D masks (see § 3.3.3). We also manually remove additional residuals in the narrow-band images that are not associated with the nebulae. This step is necessary because taking the circularly averaged value within each annulus could pick out faint spurious signals, especially in the noise-dominated regions. For the areas that are filtered out in the VSF measurement step (see § 3.3.5), we indicate their corresponding radii with vertical shaded regions in Figure 3.6 to guide the visual comparison. For TXS0206−048, the vertical shaded region denotes where the stream structures away from the main nebula contribute significantly to the averaged surface brightness level.

We find a good fit for the [O II] emission with Sérsic profiles (Sersic, 1968), with the best-fit half-light radius $R_e \approx [10, 10, 9, 6]$ kpc and the best-fit Sérsic index $n \approx [1.1, 2.6, 2.5, 3.0]$, for the four fields with increasing redshifts. The best-fit models for the [O II] profiles are shown in dotted curves in Figure 3.6. For the [O III] profiles, however, we cannot find a good fit with Sérsic, exponential, or cored isothermal profiles. Instead, a single power-law with a slope of ≈ -3 can provide a good match to the [O III] profiles, except for the flat core regions (approximately inner 10 kpc) of J0454−6116 and J2135−5316. We therefore simply overplot this power-law with a slope of -3 in Figure 3.6 for comparison. This slope also roughly matches the slopes of the [O II] profiles outside of the core region.

Note that the [O II] and [O III] surface brightness profiles in the optical nebulae here are much steeper than the spatial profiles observed in extended Lyαnebulae around $z \approx 3$ QSOs, which have characteristic power-law slopes of ≈ -2 (e.g., Steidel et al., 2011; Borisova et al., 2016; Arrigoni Battaia et al., 2019). This contrast in slope between optical nebulae and Lyαnebulae can be explained by the resonant nature of Lyαphotons, resulting in more extended Lyαemission with shallower spatial profiles compared with the continuum and non-

117

resonant line emission (e.g., Steidel et al., 2011; Wisotzki et al., 2016; Patrício et al., 2016; Leclercq et al., 2017; Chen et al., 2021).

In the right-most panel of Figure 3.6, we show the [O III]/[O II] line flux ratios as a function of radial distance from the QSOs for the three lower redshift fields. Here we see the manifestation of the extreme ionization condition in the vicinity of these bright QSOs, with the line ratios far exceeding the nominal values of [O III]/[O II]< 1 for typical star-forming and even AGN regions (e.g., Kewley et al., 2001; Kauffmann et al., 2003). Particularly for PKS0454$-$22, the [O III]/[O II] ratio is significantly enhanced in the central 10 kpc, reaching a value of ≈ 10 at its peak. Interestingly, among the three lower redshift fields, the [O III]/[O II] line flux ratios as a function of spatial distance from the QSO exhibit different profiles. This difference confirms that significant variations in the underlying physical conditions, such as density, metallicity, and local ionizing radiation intensities, are present both within individual nebulae and between fields. However, quantifying the impact on the VSF measurements will require higher signal-to-noise data.

3.5.5 On the detection rate of QSO nebulae and its implications for turbulence studies

While the four QSO nebulae studied here exhibit a range of VSF slopes, a remaining question is how the results from this sample bear on quasar host halos as a whole. A fundamental limitation of the VSF measurements is the detectability of the diffuse gas, which is a combined result of instrument sensitivity and the physical conditions of the gas. Using the CUBS sample of 15 UV-bright QSOs (Chen et al., 2020), the detection rate of extended optical QSO nebulae (i.e., $\gtrsim 30$ kpc above the surface brightness level of $\sim 10^{-18}$ erg s^{-1} cm^{-2} arcsec^{-2}) at $z \lesssim 1.5$ is $\approx 25\%$[2]. While a more comprehensive search of the

---

2. Two of the four fields are presented in this study (i.e., J0454$-$6116 and J2135$-$5316), and two are not considered here due to their smaller sizes.

MUSE data archive is needed to better quantify the detection rate of extended optical nebulae around QSOs, the $\approx 25\%$ detection rate from the CUBS program most likely represents a conservative lower limit to the rate of incidence of extended nebulae around luminous QSOs. It remains to be determined as to whether deeper observations will both increase the detection rate of extended nebulae and uncover missing light at larger distances and lower flux levels.

With the current small sample size, no clear correlation is found between global QSO properties (e.g., luminosity, radio-loudness, number of group member galaxies) and the presence (or lack thereof) of extended optical nebulae. The current detection rate of extended nebulae around low-redshfit QSOs is in stark contrast with the 100% detection rate of extended Lyαnebulae around QSOs at $z \approx 3$, and could be a result of the possible redshift evolution of the cool ($\sim 10^4$ K) gas content at different epochs (e.g., Borisova et al., 2016; Arrigoni Battaia et al., 2019). However, a statistical sample of sources observed both in Ly$\alpha$and non-resonant lines over cosmic time has yet to be established for a rigorous investigation of the apparent discrepancy in the incidence of extended nebulae between QSOs at low and high redshifts.

Meanwhile, evidence suggests that these nebulae could have a diverse range of physical origins. In addition to different [O III]/[O II] ratios (see §3.5.4 and Figure 3.6), the morphology and the kinematics of nebulae also provide important clues. For example, the "Makani" nebula exhibits morpho-kinematics that strongly suggests supergalactic winds being a predominant driver of the line-emitting region (Rupke et al., 2019). For PKS0454−22, the morpho-kinematics of the nebula and the continuum sources in the immediate vicinity of the QSO have led Helton et al. (2021) to argue that the extended nebula mostly consists of striped ISM through interactions between gas-rich galaxies. A similar case is made for the nebula in PKS0405−123 in Johnson et al. (2018) and TXS0206−048 (Johnson et al., 2022). However, this scenario of ISM stripping does not seem to be plausible for J0454−6116 and

J2135−5316 studied here. For J2135−5316, only two group member galaxies (both far away from the location of the nebula) are found in the QSO field with the current data set (see Table 3.1). Similarly for the J0454−6116 field, although two continuum sources are found near the QSO, their velocities are inconsistent with the rest of the nebula and are likely not in a coherent dynamical system with the line-emitting gas (see §3.3.5). No additional companion continuum sources are found in this field that overlap with the nebula footprint. Interestingly, both J0454−6116 and J2135−5316 exhibit a relatively flat VSF. Future studies based on a larger sample are needed to investigate the respective roles of supergalactic winds and galactic environments in driving the turbulence of the CGM.

3.5.6   Limitations and caveats

A primary limitation of the current study is the relatively small dynamic range of length scales available for the VSF measurements. Specifically, the smallest scale accessible is limited by the FWHM of the effective PSF, which is a combination of the seeing disk in ground-based observations and the smoothing kernel applied to the final combined cubes to increase the SNR in the data (see §3.3.1). The largest scale is dictated by the size of the nebulae over which robust line signals can be measured. When measuring the slope of the VSF, the dynamic range is further restricted to where a single power-law can provide an adequate description (see §3.4.1). Uncertainties in the VSF have also led to ambiguities in drawing conclusions on the dynamical properties of the gas. Even for TXS0206−048, the range of distance scales probed is less than a decade. One possible way to increase the dynamic range is to target nebulae at lower redshifts. For example, at the same physical size, a nebula at $z \approx 0.1$ will be approximately 5× larger in the apparent angular size than those at $z \approx 1$, enabling VSF measurements on smaller scales for a fixed seeing disk size. Alternatively, to improve the measurements for nebulae at high redshifts, it is necessary to reduce the size of effective PSF in the data. The infrared spectrograph, NIRSpec, onboard

the *James Webb Space Telescope* (*JWST*) will deliver a PSF 10 times smaller than the natural seeing disk on the ground. Using the upgraded adaptive optics assisted Narrow-Field-Mode provided by MUSE will also offer additional spatial resolving power for probing the energy power spectrum on scales as small as ~ 1 kpc, but will require long exposures to reach sufficient SNR.

An improved spatial resolution also helps to reduce systematic uncertainties in the two-dimensional VSF measurements due to blending of distinct structures between adjacent sightlines. In analysing the [O II] $\lambda\lambda\, 3727, 3729$ emission lines in all four fields, there is clear evidence for large density variations across individual nebulae based on the doublet ratio. If a large density contrast exists on scales smaller than the spatial resolution kernel, then blending would also suppress the power on small scales. Despite these caveats, it is interesting to see that the VSF measurements of three out of four nebulae in this study display a non-zero slope, indicating a clear scale-dependent power in the velocity structures.

3.6   Conclusion

In this study, we present measurements of the velocity structure functions for four optical nebulae detected in the vicinities of UV-luminous QSOs at $z \approx 0.5$-1.1. Using wide-field integral field spectroscopic data obtained from VLT/MUSE, we measure spatially-resolved kinematics using the [O II] $\lambda\lambda\, 3727, 3729$ and [O III] $\lambda\, 5008$ emission lines, and construct VSFs based on these velocity maps. Out of the four field, one field (i.e., TXS0206$-$048 with the largest nebula area and the highest SNR in the VSF measurement) exhibits a second-order VSF consistent with Kolmogorov, suggesting that the gas flows are isotropic and subsonic. We estimate a turbulent energy cascade rate of $\epsilon \approx 0.2$ cm^2 s^{-3}. The remaining three fields show a range of VSF slopes, while all being flatter than the Kolmogorov slope. Possible interpretations of the range of VSF slopes across the four fields include the presence of a dynamically important magnetic field, turbulent energy injection at multiple spatial scales,

a time-dependent evolution of the turbulent motions in the nebulae, and the impact from the diverse range of galactic environment associated with different fields. Alternatively, the apparent flat slopes in the VSFs may simply be due to a lack of dynamic range in the pair separations for probing the inertial range, which can be directly tested with high spatial resolution IFS data to extend the VSF measurements to smaller scales.

We develop the methodology to explicitly account for the spatial correlation in the data due to atmospheric seeing and smoothing. We also investigate possible contributions to the VSF measurements from a unidirectional velocity gradient, and large-scale radial or tangential rotational flows. These methods can be applied in future studies to obtain more robust VSF measurements. Our results improve upon traditional line width studies for inferring turbulent velocity fields in diffuse gas and provide a robust description of the energy power spectrum of the velocity field. The findings of this study can be compared with high-resolution numerical simulations to further our understanding of the driving and development of turbulence in the CGM, and the impact of quasar feedback on the CGM dynamics specifically in the case of quasar nebulae.

3.7   Appendix

Here we present the VSFs measurements for PKS0454−22, J0454−6116 and J2135−5316. The results are discussed in § 3.4.4 and § 3.5.
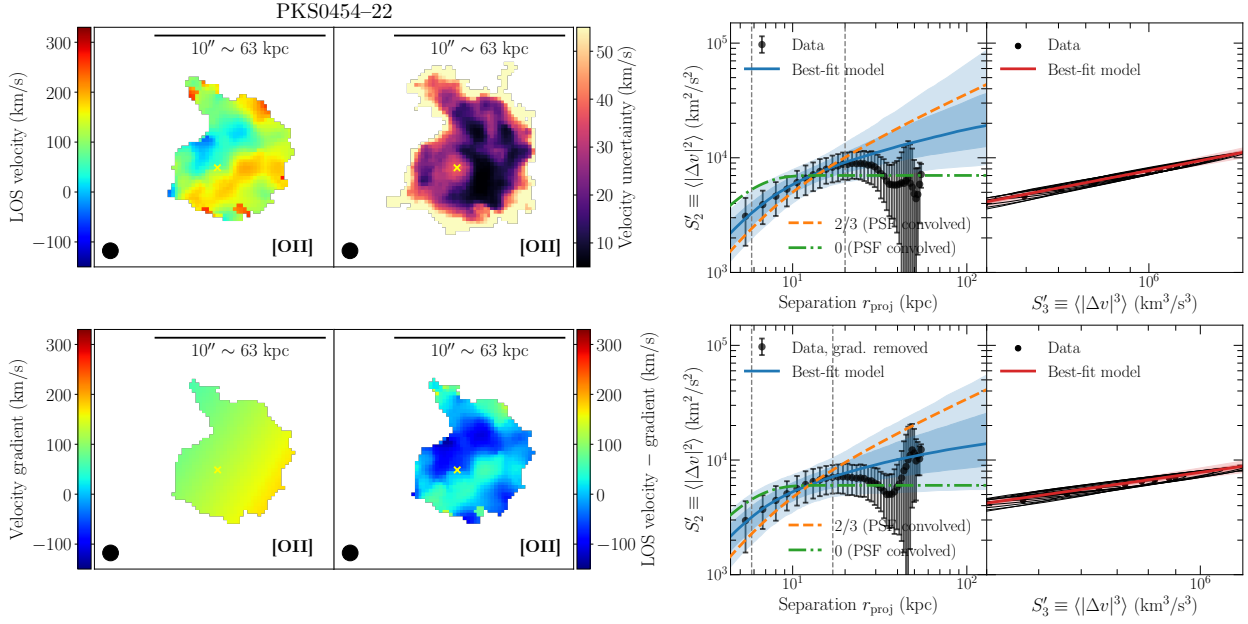
Figure 3.7: Same as Figs. 3.3 and 3.4 in the main text, but for the field of PKS0454−22 using the [O II] $\lambda\lambda\,3727, 3729$ emission line. Here a flat VSF (with a slope of 0) is also shown by the dotted-dash green line for comparison.
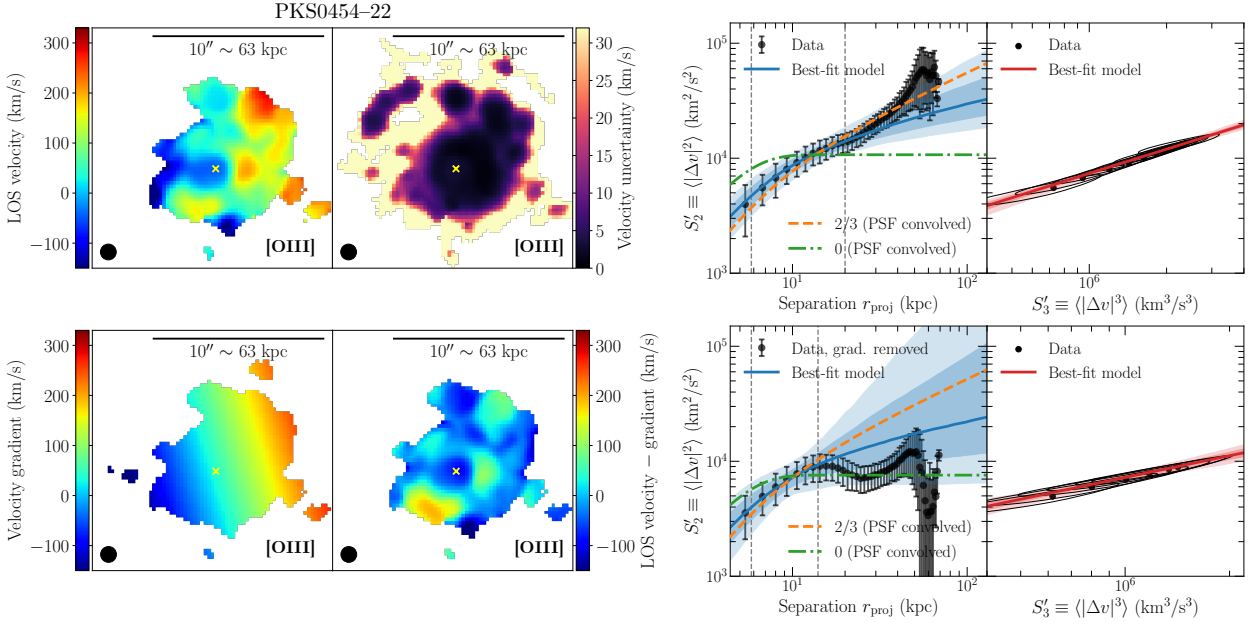
Figure 3.8: Same as Figs. 3.3 and 3.4 in the main text, but for the field of PKS0454−22 using the [O III] $\lambda\,5008$ emission line. Here a flat VSF (with a slope of 0) is also shown by the dotted-dash green line for comparison.
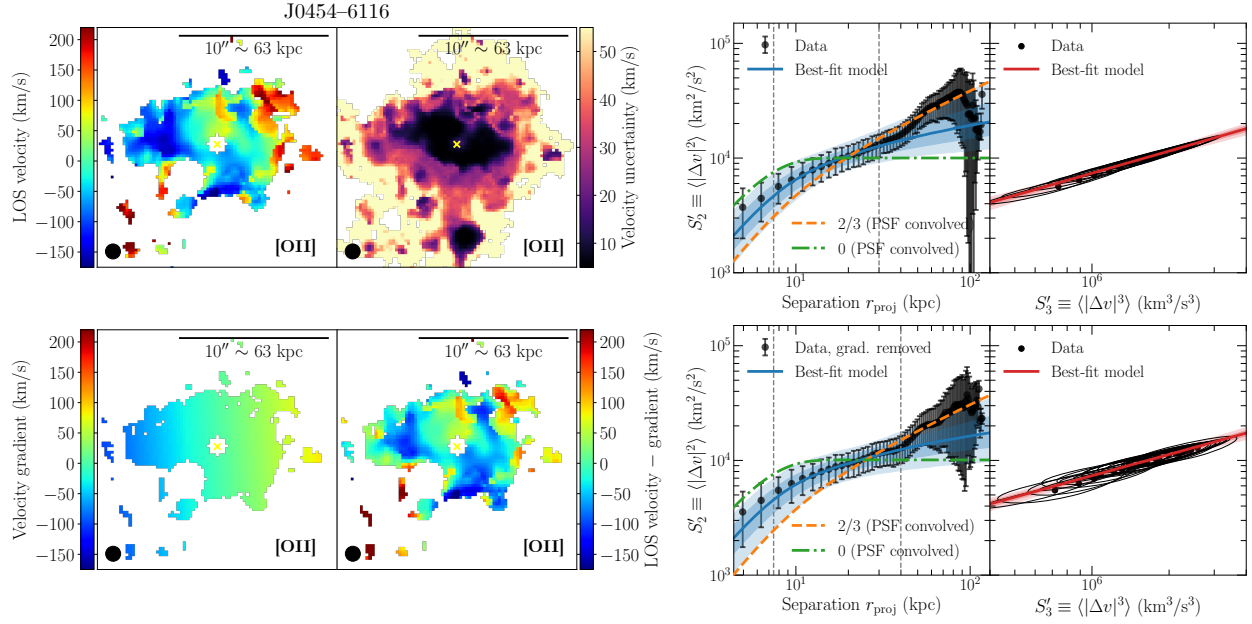
Figure 3.9: Same as Figs. 3.3 and 3.4 in the main text, but for the field of J0454−6116 using the [O II] $\lambda\lambda$ 3727, 3729 emission line. Here a flat VSF (with a slope of 0) is also shown by the dotted-dash green line for comparison.
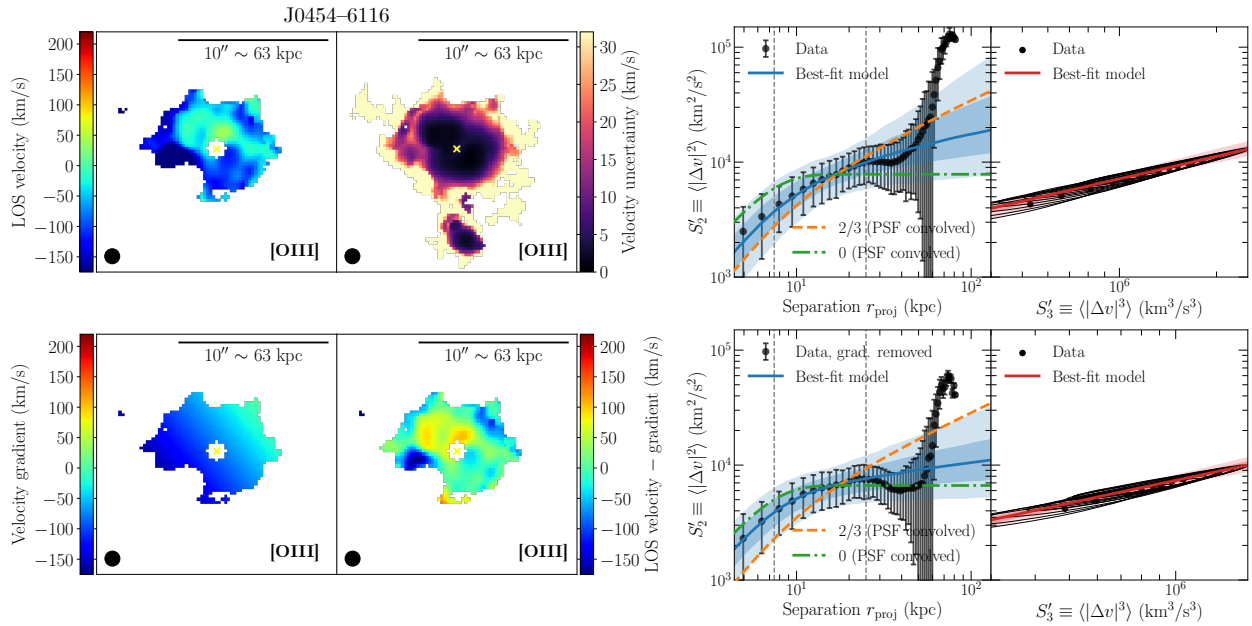
Figure 3.10: Same as Figs. 3.3 and 3.4 in the main text, but for the field of J0454−6116 using the [O III] λ 5008 emission line. Here a flat VSF (with a slope of 0) is also shown by the dotted-dash green line for comparison.
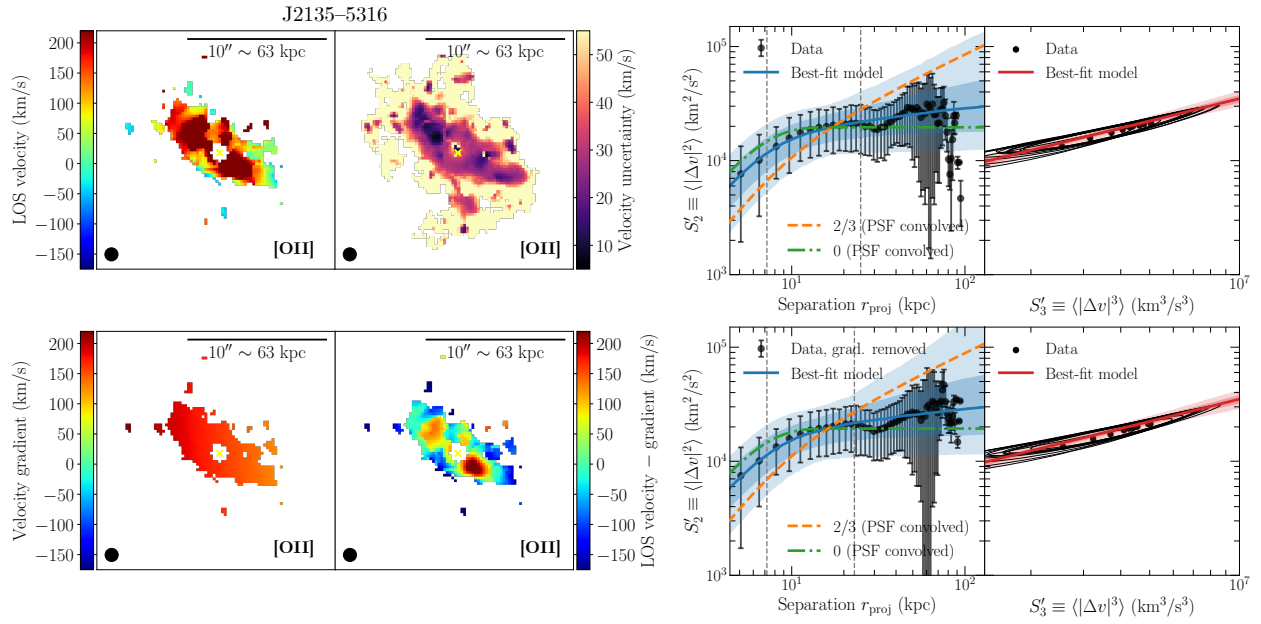
Figure 3.11: Same as Figs. 3.3 and 3.4 in the main text, but for the field of J2135−5316 using the [O II] $\lambda\lambda\,3727, 3729$ emission line. Here a flat VSF (with a slope of 0) is also shown by the dotted-dash green line for comparison.
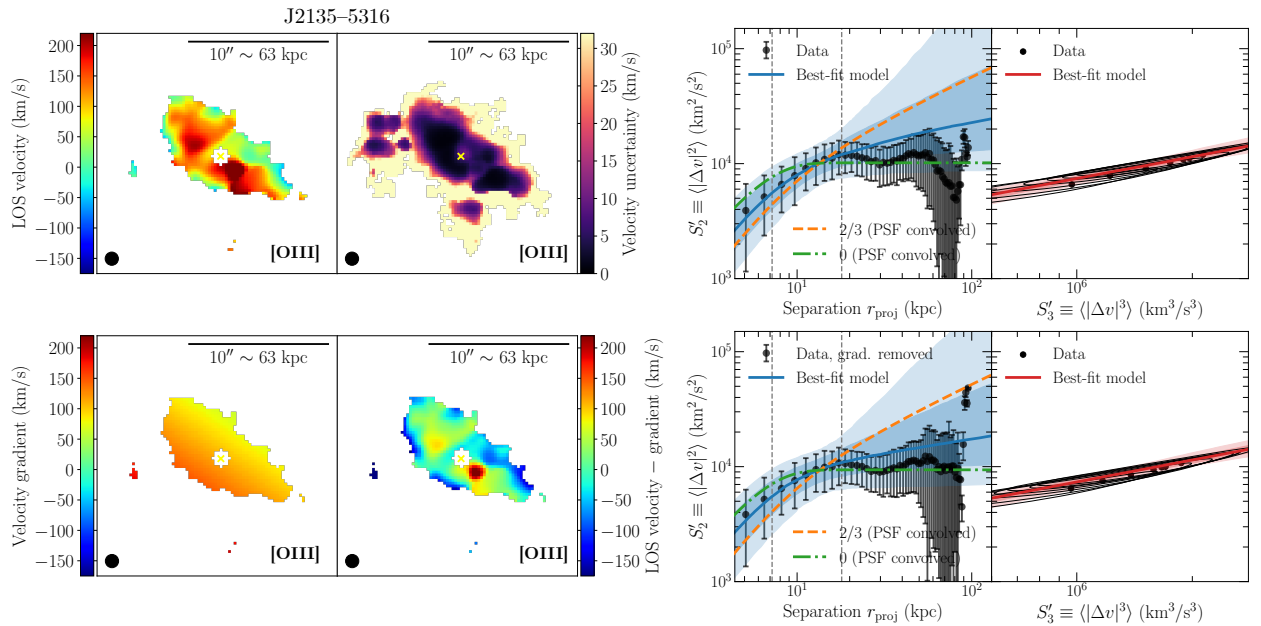
Figure 3.12: Same as Figs. 3.3 and 3.4 in the main text, but for the field of J2135−5316 using the [O III] $\lambda\,5008$ emission line. Here a flat VSF (with a slope of 0) is also shown by the dotted-dash green line for comparison.
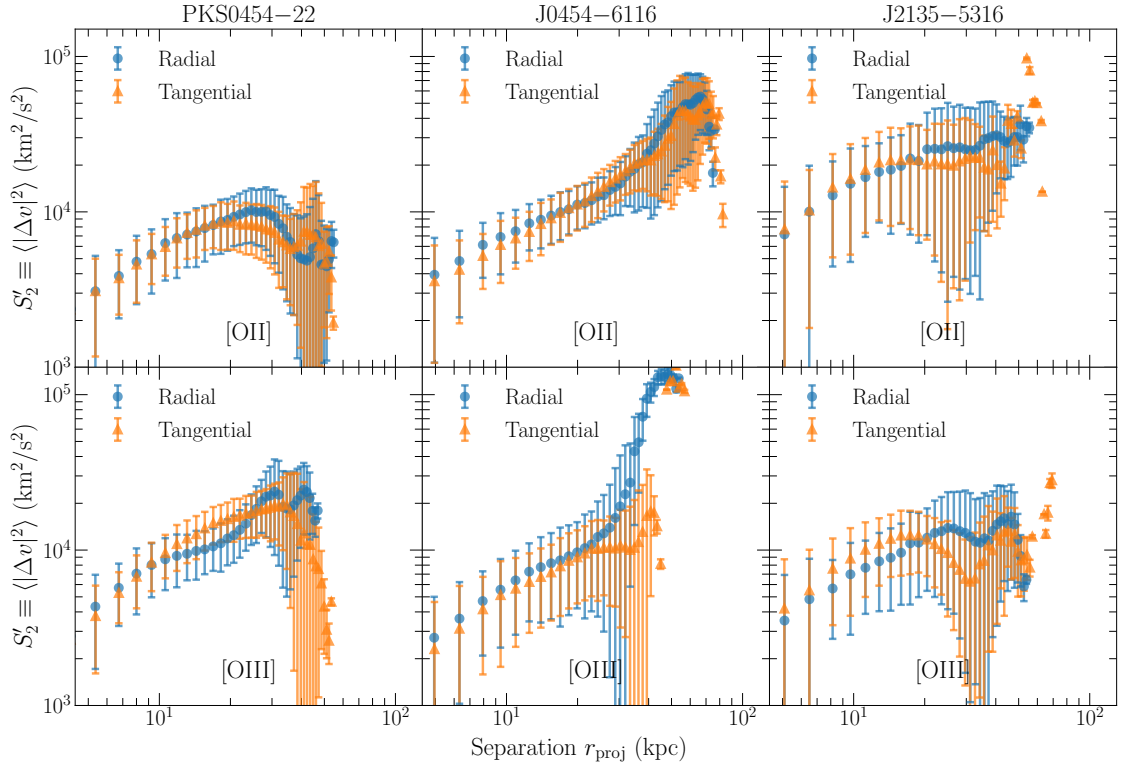
Figure 3.13: Same as the right panel of Fig 3.5, but for the fields of PKS0454−22, J0454−6116, and J2135−5316, including results based on both [O II] $\lambda\lambda\,3727, 3729$ and [O III] $\lambda\,5008$ emission lines.
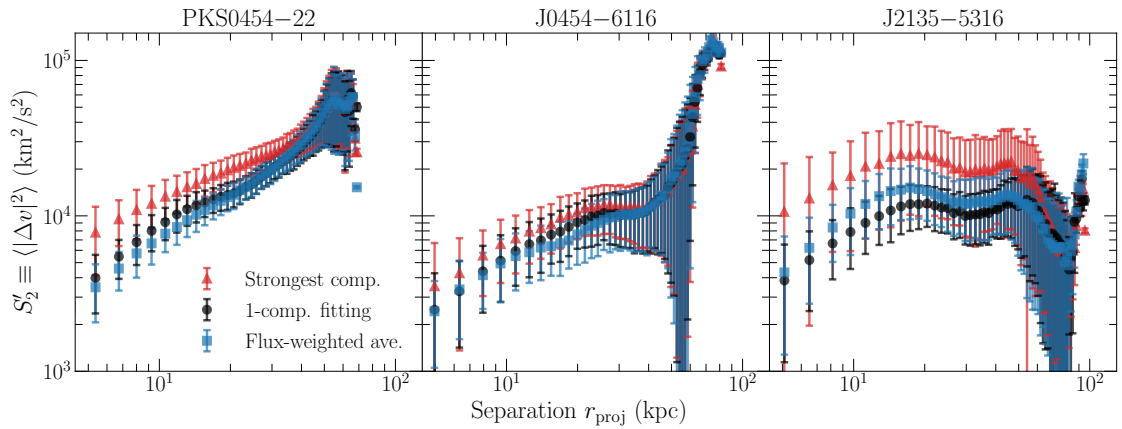
Figure 3.14: Comparison of the VSF measurement under three different scenarios where we assign to the multi-component spaxels (1) the velocity of the components with the most flux in each spaxel (i.e., the strongest component), (2) the velocity obtained by a one-component fit (i.e., ignoring the presence of multiple components), and (3) the flux-weighted mean velocity among all components.
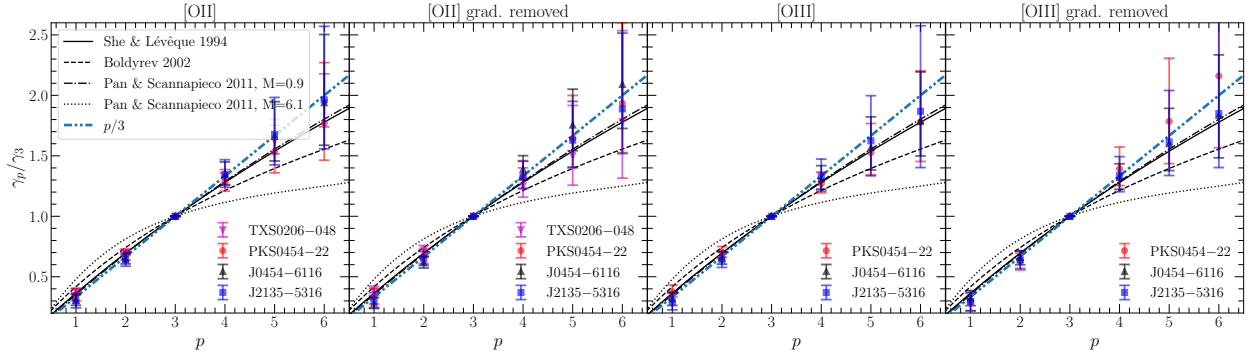
Figure 3.15: Estimated power-law slopes γ_p of S_p with p ranging from $p = 1$ to $p = 6$ for all four nebulae. Different γ_p's are normalized to γ_3 for measurements based on [O II] $\lambda\lambda\, 3727, 3729$ and [O III] $\lambda\, 5008$ velocity maps as well as their corresponding velocity residual maps after removing a unidirectional coherent gradient (see § 3.4.2). Data points represent the median values obtained with the 1000 modified bootstrap samples (see § 3.3.5), and the error bars indicate the 16th and 84th quantiles. Note that the ratio γ_p/γ_3 only equals to γ_p if $\gamma_3 = 1$. The solid curve shows the expected γ_p/γ_3 ratio for subsonic Kolmogorov turbulence with the intermittency correction presented in She & Leveque (1994). The expected γ_p/γ_3 ratio for supersonic magnetohydrodynamic turbulence presented in Boldyrev (2002) is shown by the dashed curve. The dash-dotted (dotted) curve indicates the γ_p/γ_3 ratio derived from numerical hydrodynamic turbulent simulations for Mach number $M = 0.9$ ($M = 6.1$) as presented in Pan & Scannapieco (2011). Finally, the blue loosely dash-dotted curve shows the expected γ_p/γ_3 ratio for Kolmogorov turbulence without the intermittency correction, which simply scales as $p/3$. See § 3.5.3 for further discussions.

CHAPTER 4

AN ENSEMBLE STUDY OF TURBULENCE IN EXTENDED

QSO NEBULAE AT $z \approx 0.5$–1

This chapter is a modified version of Chen et al. (2023b), published in the Astrophysical Journal, Volume 962, Issue 1, id.98, 18 pp.

4.1   Introduction

The circumgalactic medium (CGM) is the outermost, gaseous envelope of a galaxy, extending beyond the visible stellar disk and containing the majority of the baryons in the galaxy. This main gas reservoir records critical information about a galaxy's past and ongoing interactions with the surrounding environment. Due to the tenuous nature of the CGM, absorption spectroscopy using bright background sources – predominantly quasi-stellar objects (QSOs) – has been the main probe of gaseous halos, yielding sensitive constraints on gas density, temperature, metallicity, and ionization state (e.g., Chen, 2017; Tumlinson et al., 2017; Rudie et al., 2019; Péroux & Howk, 2020; Donahue & Voit, 2022; Faucher-Giguère & Oh, 2023).

Over the past decade, the advent of wide-field, high-throughput integral field spectrographs (IFSs) has provided a spatial resolving power that complements the pencil-beam probe from QSO absorption spectroscopy, greatly aiding in the investigation of the CGM. Various dynamical processes in the CGM, such as infalls, outflows, and tidal interactions, can now be spatially and spectrally mapped by IFSs via strong nebular emission lines (e.g., Epinat et al., 2018; Johnson et al., 2018; Rupke et al., 2019; Chen et al., 2019). One particularly exciting prospect with these resolved kinematic measurements is the robust constraint of turbulent motions in low-density gas.

With a high Reynolds number, ionized, diffuse plasma such as the CGM is expected to be

turbulent (see e.g., Burkhart, 2021, for a recent review), which can manifest as large density fluctuations commonly observed in extended emission at tens of kpc scales in gaseous halos (e.g., Travascio et al, in prep). Turbulence plays a critical role in several key processes in the CGM, such as mixing/transporting metals (e.g, Pan & Scannapieco, 2010), facilitating multiphase structure formation (e.g., Gaspari et al., 2018; Fielding et al., 2020), and offsetting radiative cooling (e.g., Zhuravleva et al., 2014). Until recently, observing turbulence in circumgalactic/intergalactic gas has had to rely on two approaches employing high-resolution absorption line spectra of background QSOs. One approach is to observe line widths of ions with different masses and isolate the turbulent contribution to the velocity profile along the line of sight (e.g., Rauch et al., 1996b; Rudie et al., 2019; Qu et al., 2022; Chen et al., 2023a). Alternatively, if multiple lines of sight (e.g., to gravitationally lensed QSO images) are available, turbulence can be measured as a function of transverse separation between the lines of sight to form the structure functions for the line-of-sight velocities (Rauch et al., 2001). With the advent of IFS, spatially-resolved velocity maps of entire gaseous galactic halos can now be obtained in one shot, enabling the simultaneous measurement of the turbulent power spectrum over a wide range of scales, thus providing multiple independent constraints on the nature of turbulence and the turbulent energy transfer in the gas.

Recently, Chen et al. (2023c) (hereafter Paper I) obtained two-dimensional line-of-sight velocity maps of line-emitting gas around four QSOs up to scales of ~ 100 kpc using IFS data. Taking advantage of the spatially-resolved velocity maps from IFS observations, these authors constructed velocity structure functions (VSFs), S_p, defined as

$$S_p(r) = \langle |\boldsymbol{v}(\boldsymbol{x}) - \boldsymbol{v}(\boldsymbol{x} + \boldsymbol{r})|^p \rangle, \tag{4.1}$$

where $\boldsymbol{x}$ and $\boldsymbol{r}$ represent, respectively, a position in the velocity map and the distance vector between two positions separated by $\boldsymbol{r}$. The exponent p is generally referred to as the order of the VSFs, and $\langle \rangle$ denotes the mean value averaged over all available velocity pairs separated

Table 4.1: Summary of the QSO properties.

Field name[a]	$z_{\rm QSO}$	$L_{\rm bol}$ (erg s^{-1})	$N_{\rm group}^b$	$\sigma_{v,\rm group}^c$ (km s^{-1})	Radio mode	References
PKS0454−22*	0.5335	$\approx 10^{47.0}$	23	≈ 320	Loud	Helton et al. (2021)
PKS0405−123	0.5731	$\approx 10^{47.3}$	20	≈ 430	Loud	Johnson et al. (2018)
HE0238−1904	0.6282	$\approx 10^{47.2}$	34	≈ 400	Quiet	Liu et al. (2023)
PKS0552−640	0.6824	$\approx 10^{47.4}$	10	≈ 335	Loud	Johnson et al. (2023)
J0454−6116*	0.7861	$\approx 10^{46.9}$	19	≈ 300	Quiet	Li et al. in prep.
J2135−5316*	0.8115	$\approx 10^{47.3}$	3	–	Quiet	Li et al. in prep.
TXS0206−048*	1.1317	$\approx 10^{47.3}$	27	≈ 550	Loud	Johnson et al. (2022)

[a] VSF analyses for fields marked with * (i.e., PKS0454−22, J0454−6116, J2135−5316 and TXS0206−048) were presented in Paper I; PKS0405−123, HE0238−1904 and PKS0552−640 are three newly included fields in this work (see Section 4.2).

[b] Number of spectroscopically-identified group member galaxies, including the QSO host.

[c] Velocity dispersion of the group.

by r. As can be seen from the definition, S_p quantifies the scale-dependent variance of a velocity field (e.g., Frisch, 1995), and has been commonly used to probe the dynamical state of the interstellar medium (ISM) in local H 2 regions (e.g., Wen & O'dell, 1993; Ossenkopf & Mac Low, 2002; Federrath, 2013; Arthur et al., 2016; Padoan et al., 2016; Melnick et al., 2021; García-Vázquez et al., 2023) as well as in the intracluster medium (ICM) in nearby cool-core clusters (Li et al., 2020; Ganguly et al., 2023).

While the uncertainties remained large for three QSO nebulae, Paper I found that in one particular nebula, the gas dynamics can be unambiguously characterized by the Kolmogorov relation, expected for subsonic, isotropic and homogeneous turbulent flows. Building upon the sample studied in Paper I, in this follow-up paper, we include results from four nebulae discovered in three new QSO fields. Combining this new sample with the previous one establishes a sample of eight QSO nebulae that allows us to carry out an ensemble study of the empirical properties of CGM turbulence in distant QSO host halos. The QSOs are all luminous, with a bolometric luminosity of $\sim 10^{47}$ erg s^{-1}, and span a range in redshift from $z \approx 0.5$ to $z \approx 1.1$. The nebulae are revealed in [O II] $\lambda\lambda\,3727, 3729$ and/or [O III] $\lambda\,5008$ line emission (see Figure 4.1) and are selected to have an extended, contiguous emission area $\gtrsim 1500$ kpc^2. Table 4.1 summarises the properties of the QSOs in the sample. Out of the seven QSOs, four are radio-loud, and three are radio-quiet.

This paper is organized as follows. In Section 4.2, we describe the observations of the ensemble sample and the subsequent velocity measurements using the emission line features. Based on the spatially-resolved velocity maps, we present the VSFs for all eight nebulae in Section 4.3. We discuss the implications of the results in Section 4.4 and conclude in Section 4.5. Throughout this paper, we adopt a flat ΛCDM cosmology with $H_0 = 70$ km s^{-1} Mpc^{-1}, $\Omega_{\mathrm{M}} = 0.3$ and $\Omega_{\Lambda} = 0.7$ when deriving distances, masses and luminosities. All distances quoted are in physical/proper units.

Table 4.2: Journal of MUSE observations.

Field name	RA(J2000)	Dec.(J2000)	$t_{\exp}$ (s)	Seeing[a] (arcsec)
PKS0454−22	04:56:08.90	−21:59:09.1	2700	0.″6
PKS0405−123	04:07:48.48	−12:11:36.1	35100	0.″7
HE0238−1904	02:40:32.58	−18:51:51.4	31500	0.″8
PKS0552−640	05:52:24.60	−64:02:10.9	6000	0.″8
J0454−6116	04:54:15.95	−61:16:26.6	5100	0.″7
J2135−5316	21:35:53.20	−53:16:55.8	6840	0.″6
TXS0206−048	02:09:30.74	−04:38:26.5	28800	0.″7

[a] Atmospheric seeing FWHM measured using the QSO at 7000Å. To improve the quality of line fitting, each combined data cube was convolved with a Gaussian kernel of FWHM= 0.″7. This yielded a total PSF FWHM of $\approx$ 0.″9–1.″0, corresponding to a projected separation of 6-9 kpc at the redshifts of these QSOs.

4.2 Observations and data analysis

To constrain the turbulent energy spectrum, we follow the approach described in Paper I to construct the VSFs of four nebulae found in three new QSO fields, PKS 0405−123, HE 0238−1904, and PKS 0552−640. In this section, we briefly summarize the IFS observations and the steps we took to construct a spatially-resolved velocity map based on a line profile analysis of [O II]$\lambda\lambda$3727, 3729 and [O III]λ5008 emission lines in these QSO fields.

4.2.1 IFS observations

To measure the spatially-resolved kinematics in the plane of the sky for the QSO nebulae in our sample, we use the IFS observations obtained using the Multi-Unit Spectroscopic Explorer (MUSE; Bacon et al., 2010) on the VLT UT4. The Wide-Field-Mode (WFM) was used to observe all seven fields, offering a field-of-view (FOV) of $1' \times 1'$ for a single pointing and a spatial sampling of 0.″2 per pixel. MUSE covers a wavelength range of 4750–9350Å and has a spectral resolving power of $R \approx 2000$–4000, with a higher resolution at longer wavelengths.

Table 4.2 lists the coordinates, exposure time, and atmospheric seeing conditions of

our sample. Out of the seven QSO fields, the measurements for four fields (PKS0454$-$22, J0454$-$6116, J2135$-$5316, and TXS0206$-$048) were presented in Paper I. The three newly included fields (PKS0405$-$123, HE0238$-$1904, and PKS0552$-$640) are all part of the MUSE Quasar-field Blind Emitters Survey (MUSEQuBES) program, and we use the MUSE-DEEP datacubes directly downloaded from the ESO phase-3 archive with program IDs 097.A-0089(A) and 094.A-0131(B) (PI: J. Schaye; Muzahid et al., 2020).

4.2.2 Construction of velocity maps

As described in Paper I, the main steps to construct a two-dimensional velocity map include removing the contamination from the QSO point spread function (PSF), subtracting continuum flux across the whole MUSE FOV, constructing optimally extracted narrow-band images for $[\text{O\,\textsc{ii}}]\,\lambda\lambda\,3727, 3729$ and $[\text{O\,\textsc{iii}}]\,\lambda\,5008$ lines using three-dimensional masks, and finally fitting Gaussian components to the emission signals and optimizing the parameters via an MCMC analysis. Readers can find the detailed descriptions and associated technical considerations of each step in Paper I. Note that to increase the signal-to-noise ratio for faint spaxels in the outskirts of a nebula, we smooth the data cubes in the spatial dimension with a two-dimensional Gaussian kernel of full-width-at-half-maximum of FWHM $= 0\rlap{.}''7$, leading to a total PSF FWHM of $\approx 0\rlap{.}''9$–$1\rlap{.}''0$ (see Table 4.2), corresponding to ≈ 6–9 kpc at the QSO redshifts.

A subset ($\approx$10–20%) of spaxels in the nebulae (mostly towards the inner region in the vicinity of the QSOs) exhibit multiple velocity components, which can be identified clearly with the $[\text{O\,\textsc{iii}}]\,\lambda\,5008$ line. With MUSE spectral resolution and due to the doublet nature of the $[\text{O\,\textsc{ii}}]\,\lambda\lambda\,3727, 3729$ line, multiple velocity components are only obvious for narrow features with a velocity dispersion $\lesssim 50$ km/s. In Paper I, we demonstrated that different ways of handling the multi-component spaxels (e.g., adopting the flux-weighted mean velocity versus using the velocity of the strongest component) do not lead to significant differences in

the VSF measurements. The insensitivity of the VSFs to the treatment of multi-component spaxels can be attributed to the relatively small proportion of spaxels requiring a multi-component fit, and that the majority of such spaxels exhibit a single prominent component that dominates the kinematics. Therefore, we opt to take the simple approach of using a single Gaussian function when fitting the lines.

We also treat [O II] $\lambda\lambda\, 3727, 3729$ and [O III] $\lambda\, 5008$ from the same spaxels separately when conducting the line fitting, allowing the two lines to have different velocities and line widths. This decision is motivated by the observation that for spaxels requiring multiple velocity components, there exists spatial variation in the [O III]/[O II] ratio across different components, resulting in a different flux-weighted mean velocity for the two lines. In addition, the two lines have different footprints within the same nebula due to different signal-to-noise ratios and emission strengths. Therefore, to keep the analyses simple without sacrificing the accuracy of the velocity measurements, we opt to measure [O II] and [O III] separately.

4.2.3   VSF measurements

For the three new QSO fields presented in this paper, we show the continuum- and QSO-subtracted narrow-band images in Figure 4.1. The narrow-band images for PKS0454−22, J0454−6116, J2135−5316 and TXS0206−048 have already been presented in Figure 1 of Paper I.

As described in Section 3.5 of Paper I, to ensure the robustness of the VSF measurements, we exclude spaxels with a velocity uncertainty larger than 45 km/s. We also examine the velocity map for each nebula in tandem with the broadband images from either MUSE or *HST* to identify spaxels that are likely to originate from continuum sources. If such spaxels exhibit distinctly different velocities and line widths from the rest of the nebula, we exclude them because such continuum sources are likely to be separate from the rest of the nebula, and are simply projected to be within the nebula footprint. Finally, we exclude spaxels that

Table 4.3: Summary of emission properties in QSO nebulae[a].

	Luminosity (erg s^{-1})		Nebula area (kpc^2)	
Field name	[O II]	[O III]	[O II]	[O III]
PKS0454−22	1.9×10^{42}	2.2×10^{43}	1552	2202
PKS0405−123 S	1.2×10^{42}	2.8×10^{42}	2765	3171
PKS0405−123 E	1.6×10^{42}	3.2×10^{42}	3839	4667
HE0238−1904	3.2×10^{42}	4.2×10^{42}	5081	5356
PKS0552−640	4.0×10^{42}	1.2×10^{43}	4105	3533
J0454−6116	3.5×10^{42}	5.3×10^{42}	3821	2128
J2135−5316	2.5×10^{42}	9.2×10^{42}	1614	2190
TXS0206−048	2.0×10^{43}	–	6239	–

[a] Luminosities and nebula sizes are summed over the spaxels used for the subsequent VSF analyses, which encompass a smaller area than shown in Figure 4.1. Refer to velocity maps (e.g. Figures 4.9–4.16) for the regions included in the VSF calculation.

are outliers ($\approx$ 2 per cent tail on both the blue and red ends) in the probability density distribution of the velocities in each field. After the above-mentioned steps, all spaxels left in the velocity maps are included in the subsequent VSF calculation, as shown in the top left panels of Figures 4.9–4.16. Summing over all spaxels included in the VSF analyses, the total luminosity and area for each nebula are listed in Table 4.3.

Within the spectral coverage of MUSE, we observe both [O II] $\lambda\lambda\, 3727, 3729$ and [O III] $\lambda\, 5008$ emission for six out of seven QSO fields in our sample, and we present the results based on both lines for these fields. For TXS0206−048 at $z \approx 1.1$, the [O III] $\lambda\, 5008$ line is redshifted out of the MUSE spectral window, and therefore only results based on [O II] $\lambda\lambda\, 3727, 3729$ are presented. PKS0405−123 consists of three main nebulae that are cleanly separated in velocity-position space (see Figures 4.1 and 4.9–4.12; also see Figure 2 of Johnson et al., 2018). For the purpose of this paper, we analyze the southern and eastern nebulae of PKS0405−123 separately and refer to them as PKS0405−123 S and PKS0405−123 E, and we do not include the nebula immediately surrounding the QSO in this field due to its relatively small size.

We measure the VSFs up to order $p = 6$ for all eight nebulae following the definition of Equation 4.1. VSFs with $p > 6$ become too noisy to provide meaningful constraints. Due
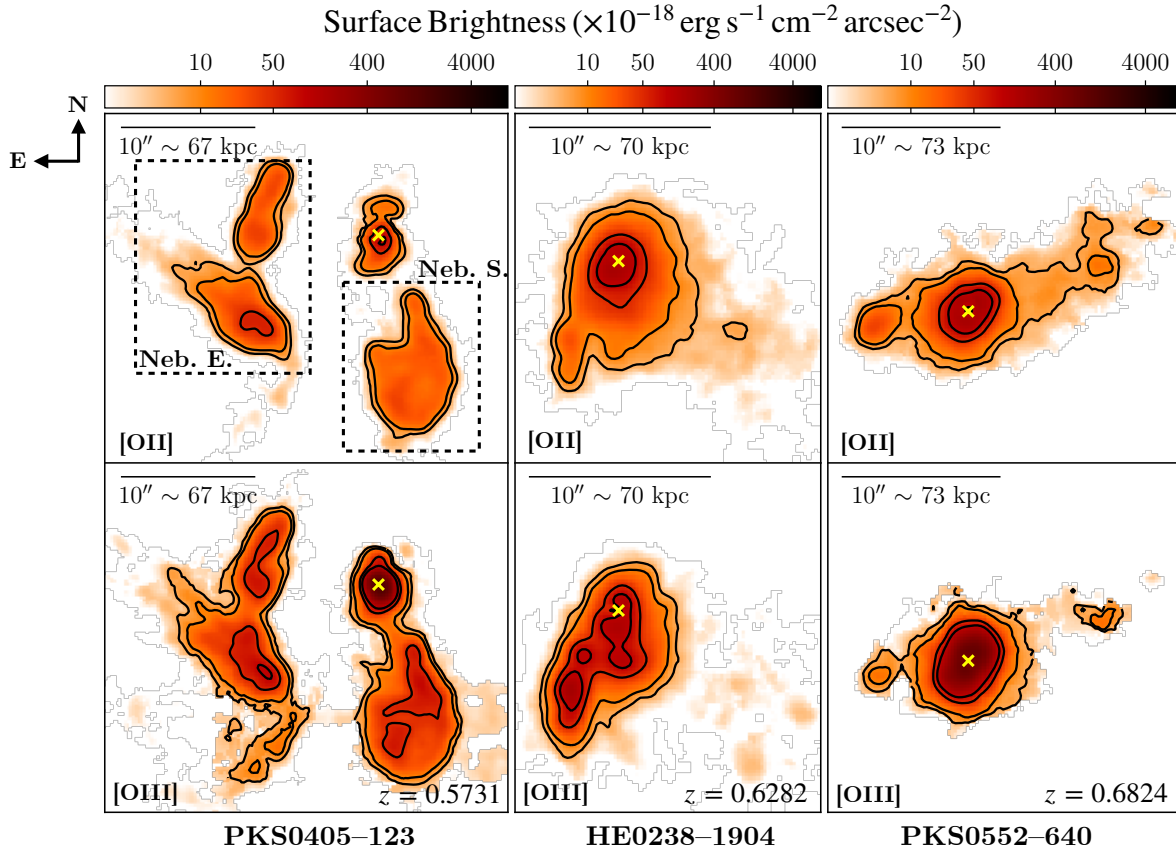
Figure 4.1: Continuum- and QSO-subtracted narrow-band images of the [O II] and [O III] emission from the three fields studied in this paper, based on the MUSE-WFM observations. The fields are shown in order of increasing redshift from left to right. Contours are at surface brightness levels of $[5, 10, 50, 100] \times 10^{-18}\,\mathrm{erg\,s^{-1}\,cm^{-2}\,arcsec^{-2}}$. The yellow cross in each panel marks the quasar position. For PKS0405$-$123, we indicate the eastern nebula (Neb. E.) and the southern nebula (Neb. S.) with dashed boxes (same for both [O II] and [O III] emission), as these two nebulae are treated as separate systems despite originating from the same QSO field (see text for details). The narrow-band images for PKS0454$-$22, J0454$-$6116, J2135$-$5316 and TXS0206$-$048 were presented in Paper I.

to the spatial correlation between spaxels that are separated by distances less than the size of the total PSF, not all velocity pairs in each distance bin are independent. Therefore, to obtain a more robust estimate of the uncertainty in the VSF measurements, we adopt the modified bootstrap method described in Paper I. In addition, as shown in Paper I, the spatial correlation due to atmospheric seeing and the additional Gaussian smoothing applied to the datacubes preferentially removes power from small scales and steepens the VSFs. This smoothing effect can be explicitly accounted for by employing a Gaussian-convolved 2nd-order VSF, S_2',

$$S_2'(r) = 2[\Gamma'(0) - \Gamma'(r)], \tag{4.2}$$

where Γ' is a Gaussian-convolved velocity autocorrelation function,

$$\Gamma'(r) = \Gamma(r) * \Gamma_g(r). \tag{4.3}$$

Here $\Gamma(r)$ and $\Gamma_g(r)$ are the autocorrelation function of the velocity field and the smoothing kernel, respectively. A more detailed derivation for Equation 4.3 can be found in Equations 2–7 of Paper I.

To quantify the slopes of the 2nd-order VSFs, we adopt a single power-law model:

$$S_2 \propto r^{\gamma_2}. \tag{4.4}$$

When fitting the observed S_2' with a power-law model, we conduct the convolution in Equation 4.3 numerically, and find the best-fitting γ_2 with the `Scipy curve_fit` routine for each of the 1000 modified bootstrap samples described above to obtain the mean and dispersion of γ_2. Note that we only consider non-negative slopes of γ_2, which is motivated by data and avoids divergent values at $r = 0$.

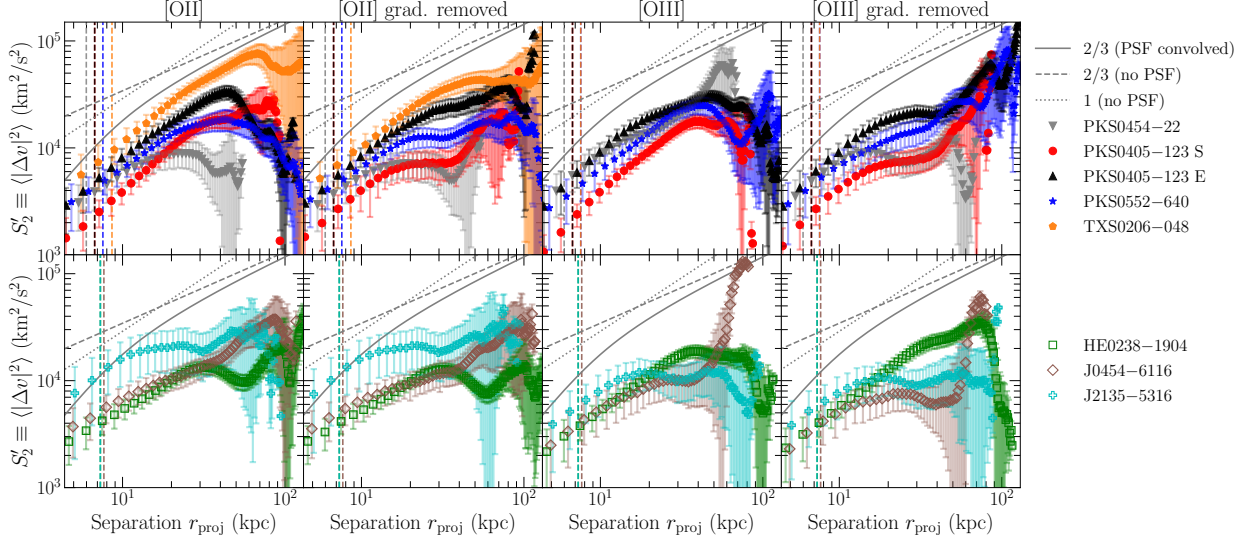With the IFS data, observations are confined to projected quantities both in velocity

Figure 4.2: *Top row:* The observed 2nd-order VSF $S_2'(r)$ for the nebulae of radio loud QSOs. Vertical dashed lines mark the size of the total PSF FWHM for each field. The data points and the error bars show the mean and the standard deviation for the 1000 measurements obtained through the modified bootstrap method (see Section 4.2). The dashed and solid gray lines show, respectively, the expected S_2 for Kolmogorov turbulence before and after convolving with an appropriate PSF. As different fields have slightly different PSF sizes, we use the mean value of the PSF FWHM for all radio-loud fields included in the panels when constructing the expected Kolmogorov VSF. The dotted gray lines show a power-law with a slope of 1 (i.e., Burger's turbulence). The four panels from left to right show the results using the [O II] and [O III] lines, both from direct measurements and after removing a unidirectional gradient (see text). *Bottom row:* Same as the top row but for radio-quiet fields. All nebulae exhibit VSFs with an increasing amplitude in velocity variance as a function of separation distance. PSF smoothing significantly steepens the apparent slopes of the VSFs and we will explicitly take into account this smoothing effect when fitting the VSFs with a power-law (see Section 4.3.2).

and spatial separations. Therefore, we report the VSF measurements using the line-of-sight velocities and the projected spatial separation r_{proj} in the plane of the sky. The potential limitations due to the projection effect will be discussed in further detail in Section 4.4.5.

4.3   Results

Using the velocity maps constructed for individual nebulae, we proceed with the VSF analysis using the full sample of eight extended nebulae. Recall that while it is relatively

138

straightforward to measure the VSFs using spatially-resolved velocity maps, a primary systematic uncertainty is possible contributions to the observed signal from coherent bulk motions projected in the plane of the sky. To account for this uncertainty, we follow the approach adopted by Paper I and consider a simple, unidirectional velocity gradient model parameterized as $v(x, y) = ax + by + c$, where x and y are coordinates of individual spaxels, and a, b, and c are the free parameters. For each nebula, we measure the VSFs with and without the best-fitting two-dimensional bulk-flow model subtracted. The amplitudes of the best-fitting gradient for the [O II] $\lambda\lambda\, 3727, 3729$ and [O III] $\lambda\, 5008$ emission lines in each field are listed in Table 4.4. We estimate the uncertainty of this velocity gradient by repeating the fitting with 1000 randomly perturbed velocity maps based on the MCMC chains for each spaxel and find that the uncertainties are small ($\lesssim 0.1$ km s^{-1}) for all nebulae. Therefore, we do not list the uncertainties in Table 4.4. To identify possible coherent motions dominant along the radial or tangential directions (for example in the case of strong outflows or inflows), Paper I also calculated the VSFs using radial and tangential velocity pairs separately and found the VSF measurements to be comparable along these two directions. For the newly analyzed nebulae in this paper, we find a similar trend where radial and tangential VSFs show no clear differences and are therefore not included in the presentation here.

In this section, we first examine the general trend displayed in the second-order VSF across all eight QSO nebulae. Then we quantify and compare the best-fitting VSF slope over a finite range of spatial scale where the measurements can be characterized by a power-law function. Finally, we explore the presence or absence of extended self-similarity (ESS; see, e.g., Benzi et al., 1993) in turbulent flows in QSO host halos by measuring the higher-order VSFs.

4.3.1 The overall shape of VSFs

Figure 4.2 shows the observed 2nd-order VSFs, S_2', for the eight nebulae in our sample. Radio-loud and radio-quiet fields are shown in the top and bottom rows, respectively. The vertical dashed lines mark the FWHM of the total PSF for each field (see Table 4.2). To guide the visual comparison, we overplot the expected S_2 for Kolmogorov turbulence, with the dashed gray line showing the intrinsic 2/3 slope and the solid gray line showing the observed shape of S_2' after convolving with an appropriate PSF. Because different fields have slightly different PSF sizes, we use the mean value of the PSF FWHM for radio-loud (-quiet) fields when constructing the expected Kolmogorov S_2' for the top (bottom) row. We also show the power-law with a slope of 1 (e.g., Burger's turbulence), without convolving with a PSF, in dotted gray lines. The comparison between the data and the model S_2 with slopes 2/3 and 1 underlines the importance of including the PSF effect when quantifying the observed VSF slopes. In particular, if the probed distance separation, r_{proj}, is $\lesssim$ 10–20 times the PSF FWHM, the PSF smoothing effect can significantly steepen the apparent slope of the VSFs and a naive visual inspection will lead to the wrong conclusion that the VSF slopes are steeper than their intrinsic values. The VSFs obtained using the gradient-removed velocity maps are also included in Figure 4.2 for comparison.

As shown in Figure 4.2, all nebulae in our sample exhibit an overall increasing trend of velocity fluctuations with increasing spatial scale. The values of $\langle \Delta v^2 \rangle$ range from $\approx$ 5000–10,000 km^2/s^2 at $r_{\text{proj}} \approx 10$ kpc to $\approx 10,000$–80,000 km^2/s^2 at $r_{\text{proj}} \approx 50$ kpc. The results based on the [O II] $\lambda\lambda\, 3727, 3729$ and [O III] $\lambda\, 5008$ lines are consistent within the uncertainty for fields with both lines. In general, we do not expect the VSFs constructed from [O II] $\lambda\lambda\, 3727, 3729$ and [O III] $\lambda\, 5008$ lines to be identical, because the footprints of the two emission lines in the nebulae do not overlap completely due to the different signal-to-noise ratios of the two lines at different locations. For regions with overlapping footprints from both [O II] $\lambda\lambda\, 3727, 3729$ and [O III] $\lambda\, 5008$ emission, the line-of-sight velocities can also

differ for spaxels with multiple velocity components and varying [O III]/[O II] line ratios between components, as discussed in Section 4.2.2. We will show below that the VSFs from [O II] and [O III] lines lead to consistent constraints on the dynamical state of the gas. In addition, the removal of a large-scale, unidirectional velocity gradient generally flattens the VSFs via preferentially reducing the power at larger distance separations. Nonetheless, the constrained slopes for a single power-law fit are consistent before and after the removal of the gradient, as we will discuss in the following section.

4.3.2 2nd-order VSF slopes

As shown in Figure 4.2, all VSFs exhibit structures that deviate from a single power-law. In particular, at larger separations, the VSFs can show an overall decreased amplitude (e.g., TXS0206$-$048 at $r_{\rm proj} \gtrsim 60$ kpc), an overall enhanced power (e.g., J0454$-$6116 at $r_{\rm proj} \gtrsim 30$ kpc), or an oscillatory behavior (e.g., HE0238$-$1904 at $r_{\rm proj} \gtrsim 30$ kpc). Such deviations may reflect different levels of velocity fluctuations in the central regions of the nebulae versus the outskirts, as velocity pairs at larger separations are predominantly constructed from spaxels in the outskirts. In addition, large-scale periodic oscillations in the velocity fields can manifest as oscillations in the VSFs at large separations (e.g., García-Vázquez et al., 2023). The VSF measurements at larger separations are also more uncertain due to a combined effect of fewer pair counts and uncertain velocity centroids as a result of fainter signals in the outskirts of a nebula.

Taking into account the above-mentioned factors, we restrict the fitting to be within a finite range of spatial scales, $[r_1, r_2]$, when employing a single power-law model to quantify the slopes of the VSFs. The lower limit r_1 is chosen to be the FWHM of the total PSF for each field (see Table 4.2), while the upper limit r_2 is chosen through a series of trial and error such that we obtain the lowest reduced χ^2 for the best-fitting model within this range. We refer to r_2 as the VSF turnover scale and will discuss its correlation with the nebula

141

Table 4.4: Summary of the power-law slopes of the VSFs constructed using [O II] and [O III] lines[a].

Field name	[O II]			[O II] grad. removed[b]		[O III]			[O III] grad. removed	
	$[r_1, r_2]^c$	γ_2	Gradient[d]	$[r_1, r_2]$	γ_2	$[r_1, r_2]$	γ_2	Gradient	$[r_1, r_2]$	γ_2
PKS0454−22	[5.8, 20]	< 0.78	2.2	[5.8, 17]	< 0.66	[5.8, 20]	< 0.67	5.0	[5.8, 14]	< 1.45
PKS0405−123 S	[7.4, 29]	$1.07^{+0.20}_{-0.18}$	5.8	[7.4, 17]	< 1.54	[7.4, 34]	$0.97^{+0.15}_{-0.15}$	6.2	[7.4, 17]	< 1.41
PKS0405−123 E	[7.4, 37]	$0.76^{+0.19}_{-0.16}$	6.0	[7.4, 30]	$0.55^{+0.22}_{-0.21}$	[7.4, 46]	$0.33^{+0.11}_{-0.11}$	5.8	[7.4, 22]	< 1.04
HE0238−1904	[8, 29]	$0.48^{+0.17}_{-0.18}$	0.9	[8, 30]	$0.43^{+0.18}_{-0.18}$	[8, 33]	$0.75^{+0.15}_{-0.15}$	2.2	[8, 33]	$0.88^{+0.17}_{-0.17}$
PKS0552−640	[8.3, 25]	$0.55^{+0.28}_{-0.28}$	5.0	[8.3, 22]	< 0.97	[8.3, 32]	$0.88^{+0.20}_{-0.22}$	8.7	[8.3, 37]	< 0.50
J0454−6116	[7.5, 30]	< 0.51	1.6	[7.5, 40]	< 0.45	[7.5, 25]	< 0.84	2.8	[7.5, 25]	< 0.33
J2135−5316	[7.2, 25]	< 0.50	0.9	[7.2, 23]	< 0.65	[7.2, 18]	< 1.23	1.8	[7.2, 18]	< 1.12
TXS0206−048	[8.5, 60]	$0.72^{+0.12}_{-0.11}$	3.7	[8.5, 40]	$0.56^{+0.16}_{-0.17}$	–	–	–	–	–

Notes.

[a] The best-fitting slopes are derived from 1000 modified bootstrap samples, as discussed in Section 4.2. These slopes correspond to the intrinsic power-law slopes for S_2, with our fitting process explicitly addressing the PSF smoothing effect in the measured S_2'. The reported values are medians along with the 16th and 84th percentiles. The 3th and 97th percentiles are approximately double the uncertainty estimates listed here for all fields. For the unconstrained results, we present 95% upper limits for the slope, assuming the observed pair separations fall within the inertial range. If the available pair separations are close to injection scales, then no robust constraints can be obtained. We exclusively consider non-negative power-law slopes, in line with the discussion in Section 4.2.

[b] Measurements obtained after removing a 2D velocity gradient (see § 4.3).

[c] Lower and upper bounds in the projected distance separation, $r_{\rm proj}$, in the unit of kpc, within which the power-law slopes of the VSFs are constrained (see §4.3.2).

[d] Best-fitting 2D velocity gradient, in the unit of km/s/kpc.

142

size later in Section 4.4.4. When constraining the VSF slopes, we explicitly incorporate the smoothing effect in the 2nd-order VSF models before comparing them with the data, as described in Section 4.2.3. The $[r_1, r_2]$ values as well as the best-fitting slopes for the 2nd-order VSF, γ_2, are listed in Table 4.4 using both the directly measured line-of-sight velocity maps and the gradient-removed velocity maps. As mentioned above, removing a large-scale, unidirectional gradient tends to flatten the VSF, leading to a smaller r_2 and weaker constraints on the VSF slopes. The comparisons between best-fitting power-law models and the data for PKS0454$-$22, J0454$-$6116, J2135$-$5316, and TXS0206$-$048 are shown in Paper I, while the models for PKS0405$-$123 S, PKS0405$-$123 E, HE0238$-$1904, and PKS0552$-$640 are shown in Figures 4.9–4.16 in the Appendix of this paper.

Based on the line-of-sight velocity maps directly measured using the [O II] $\lambda\lambda\,3727, 3729$ and [O III] $\lambda\,5008$ emission lines (top left panels of Figures 4.9–4.16), the slope γ_2 for the eight nebulae in our sample shows a range of values. Specifically, the 16th–84th measurement percentiles of four nebulae are consistent with the Kolmogorov expectation of $\gamma_2 = 2/3$ (PKS 0405$-$123 E, HE 0238$-$1904, PKS 0552$-$640, and TXS 0206$-$048), while three nebulae show flatter VSFs (PKS 0454$-$22, J0454$-$6116 and J2135$-$5316). PKS 0405$-$123 S exhibits a steeper slope but this is also a system that shows a large-scale velocity gradient across the nebula. After removing a unidirectional velocity gradient, the VSF is consistent with the Kolmogorov expectation. Below we discuss these three categories individually.

Nebulae with γ_2 consistent with 2/3: the VSF measurements for PKS0405$-$123 E, HE0238$-$1904, PKS0552$-$640 and TXS0206$-$048 lead to a constrained 2nd-order slope in agreement with the value 2/3. For HE0238$-$1904 and PKS0552$-$640, the measurements for both [O II] $\lambda\lambda\,3727, 3729$ and [O III] $\lambda\,5008$ within the 16th–84th percentiles are consistent with the Kolmogorov slope. For TXS0206$-$048, only measurements with [O II] $\lambda\lambda\,3727, 3729$ are available and the result is consistent with $\gamma_2 = 2/3$. While the VSF slope for the nebula PKS0405$-$123 E based on [O III] $\lambda\,5008$ is flatter than 2/3 within the 16th–84th percentiles,

the values within the 3th–97th percentiles using both [O II] $\lambda\lambda\,3727, 3729$ and [O III] $\lambda\,5008$ emission are in agreement with the Kolmogorov slope and therefore we consider the VSFs of this nebula consistent with the Kolmogorov expectation.

Nebulae with $\gamma_2 < 2/3$: for the three nebulae in PKS 0454−22, J0454−6116 and J2135−5316, only upper limits of γ_2 can be obtained and the 95% limits derived from [O II] $\lambda\lambda\,3727, 3729$ measurements are below 2/3. While the γ_2 upper limits obtained from the [O III] $\lambda\,5008$ measurements are larger than 2/3, the smaller γ_2 upper limits obtained using [O II] $\lambda\lambda\,3727, 3729$ suggest that the VSF slopes for these three nebulae are likely flatter than the Kolmogorov expectation. As we discussed in Paper I, the flatter VSFs may indicate the presence of multiple energy injection scales (e.g, ZuHone et al., 2016) and/or the effect of a dynamically important magnetic field (e.g., Boldyrev, 2006; Brandenburg & Lazarian, 2013; Grete et al., 2021; Mohapatra et al., 2022).

Nebulae with $\gamma_2 > 2/3$: Based on the directly measured velocity fields, PKS0405−123 S exhibits VSFs that are steeper than the expectation of Kolmogorov turbulence. The constraints are consistent using the [O II] $\lambda\lambda\,3727, 3729$ and [O III] $\lambda\,5008$ measurements. One possible explanation for the steepening of the VSF in this nebula is a strong effect of projection smoothing if the depth of the nebula is larger than the projected distance scales in the plane of the sky (see discussions in Section 4.4.5). Moreover, the line-of-sight velocity maps for both [O II] and [O III] show a possible velocity shear along the NW-SE direction (see Figures 4.9 and 4.10). The best-fitting direction and amplitude for the velocity gradient are consistent between both emission lines, suggesting that the bulk flow can plausibly contribute to the VSF measurements, leading to steeper VSF slopes. Indeed, the VSFs become flatter after we remove a unidirectional velocity gradient, resulting in slope upper limits consistent with the Kolmogorov expectation albeit with larger uncertainties.

In summary, using the direct measurements of the line-of-sight velocity fields based on the [O II] $\lambda\lambda\,3727, 3729$ and/or [O III] $\lambda\,5008$ emission lines, five out of eight nebulae exhibit
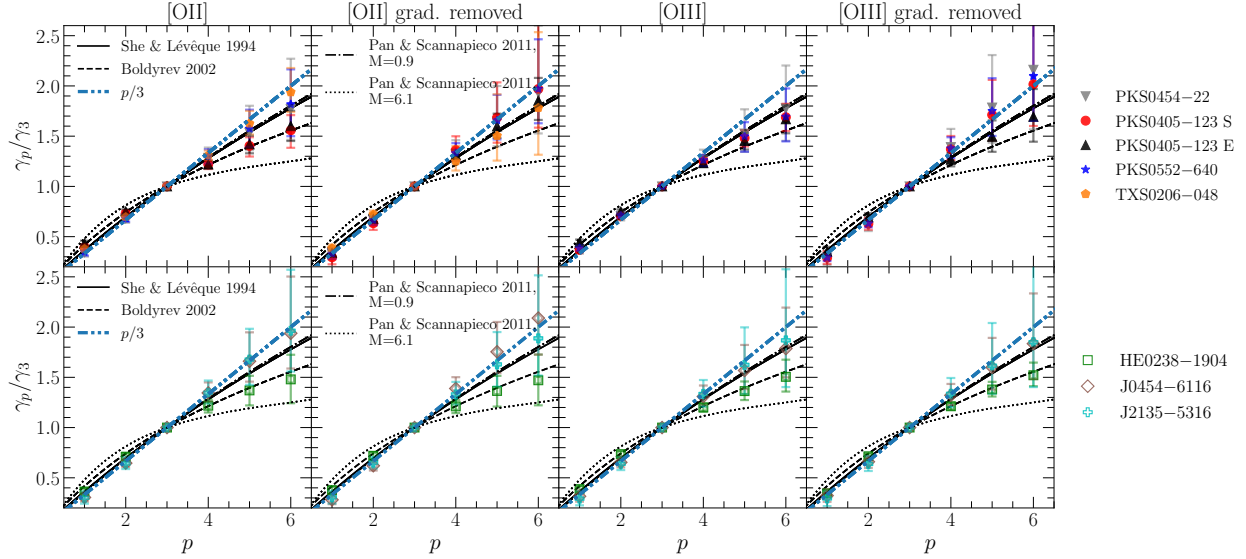
Figure 4.3: Ratios γ_p/γ_3 for all eight nebulae in the sample based on both [O II] $\lambda\lambda\,3727, 3729$ and [O III] $\lambda\,5008$ measurements, as well as their corresponding velocity residual maps after removing a coherent, unidirectional gradient. γ_p/γ_3 is the best-fitting power-law slope for the relation between the observed pth-order VSF, S'_p, and S'_3. The data points represent the median values obtained from fitting the 1000 modified bootstrap samples (see Section 4.2.3), and the error bars indicate the 16th and 84th percentiles. The solid curves represent the expected ratio of γ_p/γ_3 for subsonic Kolmogorov turbulence, taking into account the intermittency correction presented in She & Leveque (1994). The dashed curves represent the expected ratio for supersonic magnetohydrodynamic turbulence, as presented in Boldyrev (2002). The dash-dotted (dotted) curves indicate the γ_p/γ_3 ratio derived from numerical hydrodynamic turbulent simulations for a Mach number of 0.9 (6.1), as presented in Pan & Scannapieco (2011). Finally, the blue dash-dotted curves represent the expected γ_p/γ_3 ratio for Kolmogorov turbulence without the intermittency correction, scaling simply as $p/3$. The top row shows the results for radio-loud fields, while the measurements for radio-quiet fields are shown at the bottom. Except for the field of HE0238−1904, all nebulae exhibit ESS slope ratios in agreement with expectations for subsonic motions using directly measured velocity maps and/or velocity residual maps after removing a coherent unidirectional gradient. None of the nebulae show signatures of supersonic motions with a Mach number $\gtrsim 6$.

a 2nd-order VSF slope that is consistent with the expected value of 2/3 for Kolmogorov turbulence while three exhibit a flatter VSF. Incidentally, the three nebulae with a flatter VSF are also the smallest in the sample (see Table 4.3). It is possible that the observations do not have a sufficiently large dynamic range for securing a robust constraint on the shape of the VSF (see, e.g., Federrath et al., 2021).

4.3.3   Extended self-similarity (ESS) in turbulent flows

In addition to measuring the 2nd-order VSF slope γ_2, Paper I also explored the presence of ESS, in which a simple power-law function holds between VSFs of different orders on spatial scales that are outside of the inertial range where the Kolmogorov relation applies (see, e.g., Benzi et al., 1993). This ESS is particularly useful for inferring the energy cascade rate when the inertial range is not well established. Compared with the slopes of VSFs of individual orders, the ESS slope ratios are often better constrained with a higher statistical significance thanks to the tight correlation between different orders. In addition, an enhanced level of intermittency in a velocity field will suppress the VSF slopes at higher orders compared with the slopes of lower orders (e.g., Frisch, 1995), making the ESS slope ratios a valuable diagnostic for the underlying gas dynamics. Here we explore the presence or absence of ESS in the QSO nebulae by measuring the VSFs up to order $p = 6$. We obtain the slope ratios γ_p/γ_3 for $p = 1$–6 by fitting a single power-law model to the S'_p vs. S'_3 measurements. As discussed in Paper I, the smoothing effect due to the data PSF does not change the ESS slope ratios. The results are displayed in Figure 4.3, where the data points represent the median values obtained from fitting the 1000 modified bootstrap samples (see Section 4.2.3), and the error bars indicate the 16th and 84th percentiles. The correlation between 2nd- and 3rd-order VSFs for each nebula are displayed in the right-most panels of Figures 4.9–4.16.

Specifically, we measure γ_p/γ_3 using the [O II] $\lambda\lambda\, 3727, 3729$ and [O III] $\lambda\, 5008$ velocity maps as well as their corresponding residual maps after removing a unidirectional velocity

gradient. Figure 4.3 shows the ESS slope ratios, with radio-loud fields in the top row and radio-quiet fields at the bottom. We also overplot the expected γ_p/γ_3 ratios from different theoretical considerations and numerical simulations, including the Kolmogorov expectation of $\gamma_p/\gamma_3 = p/3$ (blue dashed curve), the Kolmogorov turbulence with intermittency correction (solid curve; She & Leveque, 1994), the expectation for supersonic magnetohydrodynamic turbulence (dashed curve; Boldyrev, 2002), and numerical predictions for hydrodynamic turbulence with Mach numbers of $\mathcal{M} = 0.9$ and 6.1 (dash-dotted and dotted curves; Pan & Scannapieco, 2011). In general, the ratio γ_p/γ_3 is expected to be suppressed significantly at larger p's in supersonic flows with a high Mach number. This can be seen in Figure 4.3 where the numerical simulations predict that for gas motions with $\mathcal{M} = 6.1$, γ_p/γ_3 does not increase significantly for $p > 3$, showing a plateau in the γ_p/γ_3 curve (dotted lines).

While the strongest distinguishing power for different scenarios comes in at higher orders, the measurements are also more uncertain. In addition, removing a large-scale gradient from the velocity field can change the γ_p/γ_3 ratios to be more consistent with predictions for lower Mach numbers (e.g., see the trend for PKS0405$-$123 S). Within the 16^{th} and 84^{th} measurement percentile range and considering the results both before and after removing the large-scale velocity gradient, seven out of eight nebulae in our sample show ESS slope ratios consistent with expectations from subsonic turbulence (black solid curve, blue dash-dotted curve, and dash-dotted curve in Figure 4.3). For the nebula surrounding HE0238$-$1904, the γ_p/γ_3 ratios are consistent with the predictions for supersonic magnetohydrodynamic turbulence as presented in Boldyrev (2002), suggesting that the Mach number of gas motions in this field may be higher than that in other nebulae. Given that this field has a constrained γ_2 value that is consistent with the Kolmogorov expectation as discussed above, additional effects (e.g., the presence of a dynamically important magnetic field) might contribute to a relatively small γ_2 in tandem with suppressed γ_p/γ_3 ratios. A more detailed investigation

into the properties of this nebula (e.g., ionization state, interactions with group member galaxies) is needed to further shed light on the possible physical causes for this difference in ESS slope ratios, and a larger sample is required to examine whether the HE0238$-$1904 nebula is a special case. Overall, no system in our sample exhibits ESS slope ratios that indicate gas motions with $\mathcal{M} \gtrsim 6$.

4.4   Discussion

We have shown that the 2nd-order VSF measured for eight QSO nebulae in our sample exhibits a range of slopes. While five of the nebulae in our sample are consistent with the expected slope of $2/3$ for Kolmogorov turbulence, the remaining three exhibit a shallower slope. Despite a range of 2nd-order VSF observed in these QSO nebulae, the measurements suggest that turbulent flows in the [O II] $\lambda\lambda\,3727, 3729$ and [O III] $\lambda\,5008$ line-emitting clouds are subsonic. The subsonic dynamical state of the gas is further corroborated by the ESS slope ratios γ_p/γ_3, which are consistent with theoretical or numerical expectations for subsonic systems with $\mathcal{M} \lesssim 1$ in seven out of eight nebulae. None of the systems shows γ_p/γ_3 measurements that are indicative of highly supersonic flows with $\mathcal{M} \gtrsim 6$.

In addition, we do not observe significant differences between radio-loud and radio-quiet QSO fields in terms of nebula size, line emission luminosity, VSF slopes, VSF amplitude, and turbulent energy heating rate. Recall that five of the nebulae in our sample occur near radio-loud QSOs, while the remaining three reside in radio-quiet halos. The main distinguishing characteristic between radio-loud and radio-quiet QSOs is the presence of powerful jets in radio-loud sources that can result in large-scale structures like radio lobes spanning from tens to thousands of kpc in size (e.g., Mullin et al., 2008). The mechanical energy contained in the collimated jets and the associated inflated bubbles is estimated to be $\sim 10^{41}$–10^{46} erg/s (e.g., Heckman & Best, 2014). If a significant portion of this energy can be deposited into the CGM as kinematic energy, we may expect the VSFs from radio-loud and radio-quiet

fields to exhibit different properties. While previous studies have found that radio jets are the dominant mechanism for driving fast outflows in the inner $\lesssim 10$ kpc regions in radio galaxies (e.g., Nesvadba et al., 2017), a lack of correlation between the observed VSFs and the radio power suggests that the effect of radio jets may be limited to the inner regions and have little influence on the gas kinematics on scales $\gtrsim$tens of kpc. This is in agreement with simulation predictions for the ICM in cool-core clusters (e.g., Yang & Reynolds, 2016). A larger sample with both radio-loud and radio-quiet sources will be helpful to draw robust conclusions regarding the difference (or lack thereof) in the CGM dynamics between these two populations.

In this section, we first discuss the implications for the dynamical state of the gas in the multiphase CGM and infer the energy transfer rate in these QSO host nebulae. We then discuss potential caveats associated with observational limitations, including projection effects, finite nebula sizes, and the small number of systems in the current sample.

4.4.1   Implications for the multiphase CGM dynamics

Based on the velocity dispersion of member galaxies in the QSO host group environment, the halo mass of the QSO hosts in our sample is estimated to be $\approx 10^{13}$–$10^{14} \mathrm{M_\odot}$ (see e.g., Johnson et al., 2018; Helton et al., 2021; Johnson et al., 2022; Liu et al., 2023). This mass range suggests a viral temperature of $T \approx 10^6$–10^7 K for the underlying hot halo (e.g., Mo et al., 2010). Meanwhile, the sound speed of the gas can be calculated by $c_\mathrm{s} = \sqrt{\gamma k_\mathrm{B} T / \mu m_\mathrm{p}}$, where $\gamma = 5/3$ is the adiabatic index for an ideal monatomic gas, k_B is the Boltzmann constant, μ is the mean atomic weight (which is 0.588 for fully ionized gas), and m_p is the proton mass. For the cool gas of $T \approx 10^4$ K, $c_\mathrm{s,cool} \approx 15$ km/s, while for the hot medium of $T \approx 10^6$–10^7 K, $c_\mathrm{s,hot} \approx 150$–$500$ km/s. Therefore, for the nebulae in our sample, the Mach number calculated using the sound speed of the cool gas is $\mathcal{M}_\mathrm{cool} = \sqrt{3}\sigma_\mathrm{pos}/c_\mathrm{s,cool} \approx 7$–$18$, and $\mathcal{M}_\mathrm{hot} = \sqrt{3}\sigma_\mathrm{pos}/c_\mathrm{s,hot} \approx 0.2$–$1.8$ using $c_\mathrm{s,hot}$ for the hot gas. Here σ_pos is the velocity

dispersion in the plane of the sky. As we will discuss below in Section 4.4.3, $\sigma_{\rm pos}$ is typically smaller than the velocity dispersion along the line of sight, and the Mach numbers will be larger ($\mathcal{M}_{\rm cool} \approx 9$–$20$ and $\mathcal{M}_{\rm hot} \approx 0.3$–$2.0$) when estimated using the line-of-sight velocity dispersion.

Given the contrast between the two Mach numbers, $\mathcal{M}_{\rm cool}$ and $\mathcal{M}_{\rm hot}$, the subsonic motions revealed by the VSFs of the nebulae suggest that the [O II] and [O III] emission originates from cool gas clumps embedded in the ambient hot medium. If these cool clumps are in pressure equilibrium with the hot halo, then they can serve as tracers for the kinematics of the volume-filling plasma. The scenario of a dynamically-coupled multiphase gaseous system is supported by absorption line studies on CGM kinematics of $z \sim 2$ star-forming galaxies (e.g., Rudie et al., 2019) as well as by recent measurements in the core regions of nearby galaxy groups and clusters (e.g., Li et al., 2020; Olivares et al., 2022). There has also been an increasing number of theoretical and numerical predictions arguing for a shared dynamical state across different gas phases (e.g., Gaspari et al., 2018; Gronke & Oh, 2018; Schneider et al., 2020; Mohapatra et al., 2022)

The dynamical coupling likely happens due to a combination of physical processes involving cooling, the exchange of mass and momentum between cool and hot phases, and the competition between cool clump formation and cloud crushing at different mass/length scales. Turbulence is expected to facilitate these processes, which in turn further feed into the development of turbulence in the gaseous halo. In the absence of turbulence, the condensed cool clumps tend to settle in more organized structures such as a disk. The extended morphological features of the nebulae in our sample suggest that turbulence is significant in these gaseous halos. Phenomenologically, Gaspari et al. (2018) proposed an empirical criterion of $t_{\rm cool}/t_{\rm eddy} \lesssim 1$ for the condensation and survival of cool gas in clusters and groups, where $t_{\rm cool}$ is the gas cooling time and $t_{\rm eddy}$ is the eddy turnover time. Based on the VSF measurements, we can calculate the eddy turnover time via $t_{\rm eddy} \approx \epsilon^{-1/3} l^{2/3}$, where ϵ is the

energy transfer rate per unit mass at the spatial scale l (for more discussion on ϵ see Section 4.4.2 below). For the nebulae in our sample, we estimate $t_{\mathrm{eddy}} \approx 60$–$150$ Myr at $l \approx 10$ kpc and $t_{\mathrm{eddy}} \approx 150$–$300$ Myr at $l \approx 50$ kpc. While we cannot obtain an estimation for t_{cool} due to the absence of temperature and metallicity measurements of the hot phase, our measured t_{eddy} is in agreement with the estimated values ($t_{\mathrm{eddy}} \approx 100$–$200$ Myr for galaxy groups) that fulfill the gas condensation criterion in Gaspari et al. (2018) (see their Figure 5).

In addition, turbulence in the CGM can also be produced by Kelvin-Helmholtz instability during the accretion of cool gas streams (e.g., Vossberg et al., 2019; Mandelker et al., 2019; Li et al., 2023), and motions of fragmented cool gas clumps in disrupted, turbulent mixing zones near the accreting streams are predicted to be subsonic in numerical simulations (e.g., Aung et al., 2019). Among our sample, the nebula in the field of TXS0206$-$048 exhibits compelling signs of cool, filamentary gas accretion from large scales (Johnson et al., 2022), suggesting that the observed subsonic turbulence may be in part produced through the accreting streams.

Finally, previous studies have identified a correlation between the presence of close companions around the QSOs and the presence of strong, extended nebular line emission (see e.g., a narrow-band imaging survey by Stockton & MacKenty, 1987). In our sample, the morphokinematics of some nebulae (e.g., PKS0405$-$123, HE0238$-$1904, TXS0206$-$048) reveal that part of the line-emitting gas originates from stripped ISM of group member galaxies as indicated by consistent line-of-sight velocities between the galaxies and extended nebulae (see e.g., Johnson et al., 2018; Helton et al., 2021; Liu et al., 2023). It is natural to assume in these cases that the tidal interactions between group member galaxies disturb the gas and enhance turbulence and thermal instabilities in the hot halo, leading to more efficient cooling and cool clump condensation. The stripped ISM can also serve as massive cool gas seeds that facilitate the coagulation of smaller clumps, aiding in subsequent stochastic mass growth in the cool phase (e.g., Gronke et al., 2022). The significance of this environmental

151

effect on the formation of extended nebulae is supported by the fact that the nebulae in PKS0405−123, HE0238−1904, and TXS0206−048 are much larger in area than the nebulae in fields such as J0454−6116 and J2135−5316 where no massive close companions with consistent line-of-sight velocities were found in the nebulae footprint.

4.4.2 Energy transfer rate over seven decades in spatial scale

As described in Paper I, the energy transfer rate per unit mass ϵ can be calculated via the "four-fifths law"(Kolmogorov, 1941; Frisch, 1995):

$$\epsilon = \frac{5}{4}\left[\frac{|\langle \Delta v(r)^3\rangle|}{r}\right] \approx \frac{5}{4}\left[\frac{\langle |\Delta v(r)|^3\rangle}{r}\right].\tag{4.5}$$

For Kolmogorov turbulence, ϵ is a constant at all scales within the inertial range. For VSFs flatter (steeper) than the Kolmogorov expectation, the energy transfer rate would be higher (lower) on smaller spatial scales. Across different nebulae in our sample and on different scales between 10–60 kpc, the estimated ϵ shows a range of values between ≈ 0.02 cm^2 s^{-3} and ≈ 0.2 cm^2 s^{-3}. For nebulae with both [O II] $\lambda\lambda\, 3727, 3729$ and [O III] $\lambda\, 5008$ measurements, the values obtained using these two lines are consistent within uncertainty. This estimated range for ϵ with our sample is comparable to the measurements for Hα filaments in core regions of nearby cool-core clusters (Li et al., 2020; Ganguly et al., 2023) and molecular clouds in nearby H 2 regions (e.g., Hennebelle & Falgarone, 2012). Much lower estimates of $\epsilon \approx 10^{-7}$–10^{-3} cm^2 s^{-3} were obtained for CGM cool clumps probed through absorption line spectroscopy (Rauch et al., 2001; Chen et al., 2023a), and a Milky Way high-velocity cloud (HVC; Marchal et al., 2021).

To gain further insights into the differences between these dynamical systems, we convert the estimated ϵ to a turbulent heating rate per unit volume via $Q_{\mathrm{turb}} = \rho\epsilon$, where ρ is the gas density and can span a wide range for gas in different phases. For the QSO nebulae in
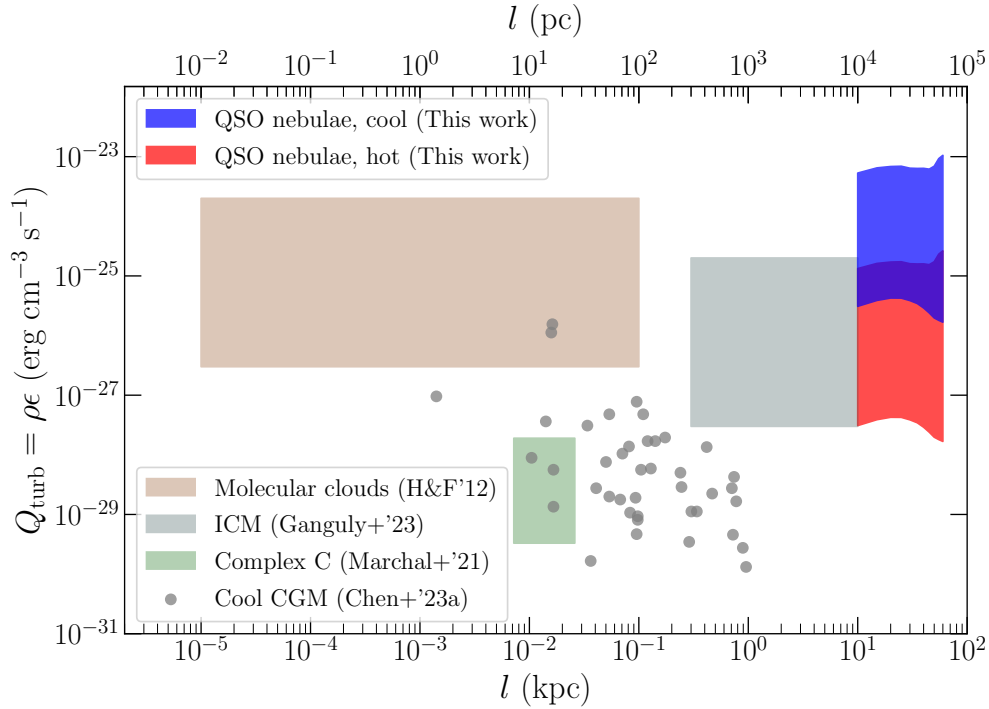
Figure 4.4: Turbulent heating rate Q_{turb} at different scales for different physical systems. The red and blue shaded regions show the estimated Q_{turb} for QSO nebulae at scales of ≈ 10–60 kpc based on our sample. The calculations for the hot and cool gas phases assume densities of 0.01–1 cm^{-3} and 1–40 cm^{-3}, respectively (see text). The lower and upper bounds indicate the 16th–84th percentile ranges for measurements across all eight nebulae. Measurements from Ganguly et al. (2023) for ICM at scales ≈ 0.3–10 kpc are shown by the gray shaded region. Results for star-forming molecular clouds at scales ≈ 0.01–100 pc presented in Hennebelle & Falgarone (2012) are shown by the brown shaded region. Marchal et al. (2021) measured Q_{turb} for a bright concentration location in the HVC Complex C at scales ≈ 6–28 pc, as shown by the green shaded region. The gray points show the results for CGM cool clumps at scales ≈ 10 pc -1 kpc based on absorption line measurements presented in Chen et al. (2023a). The turbulent heating rates in the QSO nebulae, the cool-core cluster ICM, and the star-forming molecular clouds are on average ~ 1000 times higher than that in Complex C and cool gas clumps probed in absorption.

our sample, the [O $\textsc{ii}$] $\lambda\lambda\, 3727, 3729$ doublet line ratios suggest a median upper limit of gas density for the $T \sim 10^4$ K cool phase of $\lesssim 40$ cm^{-3} (Liu et al., 2023), while an estimate of ≈ 1–5 cm^{-3} is obtained assuming pressure equilibrium between typical AGN-illuminated [O $\textsc{ii}$]-emitting gas and the hot halo (Johnson et al., 2022). Based on the [S 2]$\lambda\lambda 6716, 6731$ doublet ratio, observations of spatially extended nebula illuminated by the active galactic nucleus (AGN) in the Teacup galaxy at $z \sim 0.1$ show that the gas density at distances of a few kpc away from the galaxy center is $\lesssim 10$ cm^{-3} (Venturi et al., 2023). Therefore, we adopt a range of 1–40 cm^{-3} for the cool phase gas when calculating Q_{turb} to account for this wide range of uncertainty. For the hot phase with $T \approx 10^6$–10^7 K, we adopt a density range of 0.01–1 cm^{-3} (e.g., Li et al., 2018). We obtain an estimated Q_{turb} of $\approx 10^{-26}$–10^{-22} erg cm^{-3} s^{-1} for the cool gas and $\approx 10^{-28}$–10^{-25} erg cm^{-3} s^{-1} for the hot gas, as shown by the blue and red shaded regions in Figure 4.4. Ganguly et al. (2023) constrained the Q_{turb} of the ICM in the core regions of nearby cool-core clusters to be $\approx 10^{-28}$–10^{-25} erg cm^{-3} s^{-1} (the gray shaded region in Figure 4.4), in agreement with our result for the hot phase. For star-forming molecular clouds, measurements across a wide range of spatial scales of ≈ 0.01–100 pc led to an estimate of $Q_{\text{turb}} \approx 10^{-27}$–$10^{-24}$ erg cm^{-3} s^{-1} as presented in Hennebelle & Falgarone (2012) and shown by the brown shaded region in Figure 4.4. Marchal et al. (2021) measured the density and kinematics of a bright concentration region near the edge of Complex C, an HVC in the Milky Way, which resulted in an estimated $Q_{\text{turb}} \approx 10^{-30}$–$10^{-28}$ erg cm^{-3} s^{-1} as shown by the green shaded region in Figure 4.4. Using non-thermal velocity widths of resolved absorption profiles and clump sizes inferred from photoionization models, Chen et al. (2023a) constrained Q_{turb} to be $\approx 10^{-30}$–10^{-27} erg cm^{-3} s^{-1} for spectrally resolved cool clumps with a size scale of ≈ 10 pc – 1 kpc in the CGM. These are shown by the gray data points in Figure 4.4.

It can be seen that the turbulent heating rates in the QSO nebulae, the cool-core cluster ICM, and the star-forming molecular clouds are on average ~ 1000 times higher than that in

the MW HVC and cool gas clumps probed in absorption. Given that both Complex C and cool absorption clumps are expected to be in relatively quiescent, undisturbed environments (Chen et al., 2023a), a possible explanation for this difference is that feedback due to star formation and AGN activities can significantly elevate the turbulent energy in the gaseous halos. However, caveats remain in this interpretation. As discussed in the previous section, the galaxy environments of the largest extended nebulae hint towards the scenario where tidal/merger interactions play a key role in stirring up the gas and facilitating the formation of multiphase structures, and the presence of a large amount of cool gas near the QSOs can lead to more efficient black hole accretion (e.g., Prasad et al., 2015; Voit et al., 2017). In this case, the elevated turbulent energy might be a precursor for fueling these luminous QSOs instead of a consequence of QSO feedback.

For the first time, we are able to determine turbulent energy transfer rate in the diffuse cosmic gas over seven decades in spatial scale from ~ 0.01 pc to ~ 100 kpc, but the measurements rely on two distinct approaches at different spatial scales. In particular, in the circumgalactic space, where we see three orders of magnitude difference in Q_{turb} from large to small scales, such distinction is also accompanied by differences in the way turbulence energy is determined. The gas turbulence probed in emission likely reflects the relative motions between different line-emitting clumps that trace the hot gas dynamics (as discussed in Section 4.4.1), while high-resolution absorption line studies likely probe turbulence internal to individual clouds. Therefore, the lack of overlapping spatial scales probed by emission and absorption prevents us from forming a consistent picture of turbulent energy cascade in galaxy halos, while systematic uncertainties remain when comparing turbulent flows based on VSF measurements and those from absorption-line analyses. In Paper I, we discussed uncertainties associated with VSF measurements due to either projection effects (see also e.g., von Hoerner, 1951; Xu, 2020) or PSF smoothing (see further discussion in § 4.4.5). While the smallest area accessible in emission measures is limited to the PSF size of the data, the

absorption line technique averages cloud properties over the beam size that is dictated by the black hole accretion disk size (i.e., on the order of $\ll 1$ pc). At the same time, absorption-line analyses are subject to uncertainties in the photo-ionizing background radiation field. Future observations using AO-assisted ground-based IFSs and/or space-based IFSs can extend the small scales probed in the VSFs to $\lesssim 10$ kpc for the line-emitting gas, bridging the gap in spatial scales accessible between emission and absorption studies. A sample of systems with both extended line emission and high-resolution absorption line data will also greatly aid in the investigation of this discrepancy in Q_{turb}.

Finally, we note that these measurements of turbulent motions in QSO nebulae imply that turbulence is insufficient in providing the required energy to offset cooling at tens of kpc scales in the QSO environments. In Section 5.1 of Paper I, we compared the turbulent heating rate and the radiative cooling rate, utilizing measurements from TXS0206$-$048. The calculations considered the gas mass within a 50 kpc radius of a $5 \times 10^{13}\,\mathrm{M}_{\odot}$ halo, assuming an NFW mass profile and that gas of all phases is perfectly coupled dynamically. This approximate evaluation shows that the turbulent heating rate is on par with the luminosity of [O II] or [O III], yet it constitutes only approximately 0.05% of the QSO bolometric luminosity.

4.4.3 Velocity dispersion along the line of sight versus in the plane of the sky

In Figure 4.5, we show the velocity dispersion in the plane of the sky, σ_{pos}, versus the mean velocity dispersion along the line of sight, $\langle \sigma_{\mathrm{los}} \rangle$. σ_{pos} is quantified as the standard deviation of the line-of-sight velocity from spaxels included in the VSF measurements (see discussion in Section 4.2.3 and the velocity maps in Figures 4.9–4.16), and $\langle \sigma_{\mathrm{los}} \rangle$ is the mean line width (obtained through a single-component Gaussian fit) for the same set of spaxels. We show results for both [O II] $\lambda\lambda\, 3727, 3729$ and [O III] $\lambda\, 5008$ emission as they can differ in σ_{pos} and $\langle \sigma_{\mathrm{los}} \rangle$ due to the different footprints of the two lines. The statistical uncertainties of both velocity dispersions estimated through Monte Carlo resampling are small and are
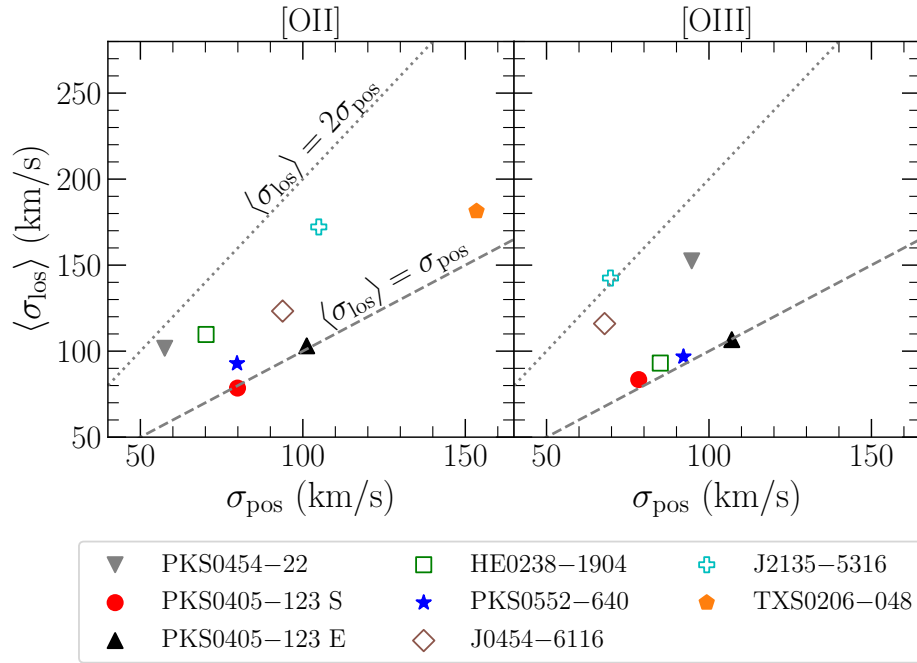
Figure 4.5: The positional velocity dispersion in the plane of the sky, σ_{pos}, versus the mean velocity dispersion along the line of sight, $\langle\sigma_{\mathrm{los}}\rangle$. The left and right panels show measurements using the $[\mathrm{O\,II}]\,\lambda\lambda\,3727, 3729$ and $[\mathrm{O\,III}]\,\lambda\,5008$ emission lines, respectively. The dashed line shows the relation $\sigma_{\mathrm{pos}} = \langle\sigma_{\mathrm{los}}\rangle$, and the dotted line indicates the relation where $\langle\sigma_{\mathrm{los}}\rangle$ is twice the value of σ_{pos}. For all nebulae in our sample, $\sigma_{\mathrm{pos}} \lesssim \langle\sigma_{\mathrm{los}}\rangle$.

not shown in Figure 4.5. The measurements for σ_{pos} before and after removing the unidirectional velocity gradient in the plane of the sky are consistent with each other to within ≈ 20 km/s. Therefore, for clarity, we only show the values obtained using the directly measured [O II] and [O III] velocity maps.

It can be seen that for all nebulae in our sample, $\sigma_{\mathrm{pos}} \lesssim \langle \sigma_{\mathrm{los}} \rangle$. This observation agrees with the general trend seen in spatially-resolved data for H 2 regions where the velocity dispersion along the line of sight exceeds the velocity dispersion in the plane of the sky (e.g., Lagrois & Joncas, 2011; Arthur et al., 2016; García-Vázquez et al., 2023). One possible explanation for this trend is the smoothing effect due to multiple line-emitting clouds along the line of sight contributing to the observed velocity centroid, leading to reduced velocity dispersion in the plane of the sky. In addition, the contribution from bulk/coherent motions along the line of sight will also result in larger σ_{los}. To investigate this possibility, we adopt a simple assumption that $\langle \sigma_{\mathrm{los}} \rangle^2 = [\sigma_{\mathrm{pos}}^2 + (v_{\mathrm{grad,los}} \times L_{\mathrm{los}})^2]$, where $v_{\mathrm{grad,los}}$ is the velocity gradient along the line of sight. We approximate the depth of the nebula L_{los} to be the square root of the nebula size (see Table 4.3), and derive a velocity gradient of $v_{\mathrm{grad,los}} \approx 0.5$–3 km/s/kpc for different nebulae. The range of this derived $v_{\mathrm{grad,los}}$ is in qualitative agreement with the best-fitting velocity gradient in the plane of the sky (see Table 4.4), suggesting that bulk flows along the line of sight may be non-negligible. In contrast, the velocity dispersion across the plane of the sky provides a robust tracer of the underlying velocity variance at scales $\gtrsim 10$ kpc, particularly when a credible model for the coherent shear in the plane of the sky can be obtained with the spatially-resolved velocity measurements, as pointed out by previous studies (e.g., Stewart & Federrath, 2022; García-Vázquez et al., 2023).

4.4.4 Power-law turnover scale for the VSFs

As discussed in Section 4.3.2, the shapes of the VSFs generally do not follow a single power-law across the entire range of scales probed. While additional structures in the VSFs
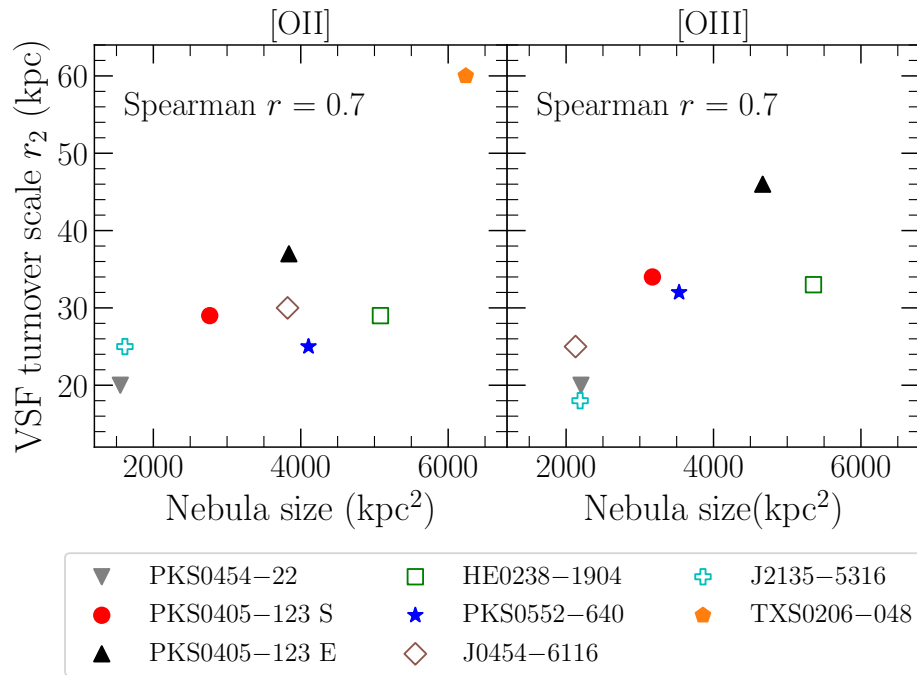
Figure 4.6: Nebula size versus the VSF turnover scale r_2 for all eight nebulae in the sample. The left and right panels show the values using the $[\text{O\,\textsc{ii}}]\,\lambda\lambda\,3727, 3729$ and $[\text{O\,\textsc{iii}}]\,\lambda\,5008$ emission lines, respectively. There is a moderate correlation between nebula size and the VSF turnover scale.

may provide hints for different physical processes present in the nebulae, we caution that the limited nebula size and signal-to-noise can hinder a robust interpretation of these structures.

In particular, we note that there is a moderate correlation (with a Spearman's r coefficient of 0.7) between the VSF turnover scale r_2 (see Section 4.3.2) and the size of the nebula for both the [O II] $\lambda\lambda\, 3727, 3729$ and [O III] $\lambda\, 5008$ emission, as shown in Figure 4.6. This correlation indicates that the deviation of the VSF from a single power-law at larger scales is in part due to the limited nebula size probed by the data given the detection limit. Previous studies have also shown that boundaries of clouds/nebulae can artificially flatten the VSFs at large scales that mimic the signature of energy injection and affect the interpretation of the data (e.g., Ganguly et al., 2023; García-Vázquez et al., 2023). In addition, the smooth transition between the inertial range and the energy injection scale can cause the VSF slopes to taper off at a scale as small as half of the true energy injection scale (Federrath et al., 2021) and further complicate the interpretation of a flattening signal in the VSFs.

Given the abovementioned caveats, we refrain from interpreting r_2 or VSF flattening scales in our sample as indicative of energy injection scales. However, Figure 4.7 indicates no discernible correlations between the constrained 2nd-order power-law slopes (γ_2) and VSF turnover scale (r_2) or nebula size, underscoring the robustness of γ_2 measurements. Measurements from local H 2 regions reported by García-Vázquez et al. (2023) result in larger γ_2 values on average (shown in the blue shaded region in Figure 4.7), suggesting elevated Mach numbers in local H 2 regions and/or increased susceptibility to projection smoothing in their observations (for more discussion of projection effects see Section 4.4.5 below).

4.4.5   Limitations and caveats

A notable limitation in the present study arises from the projection effect inherent in the data. Several studies have investigated how VSFs are affected by the use of projected
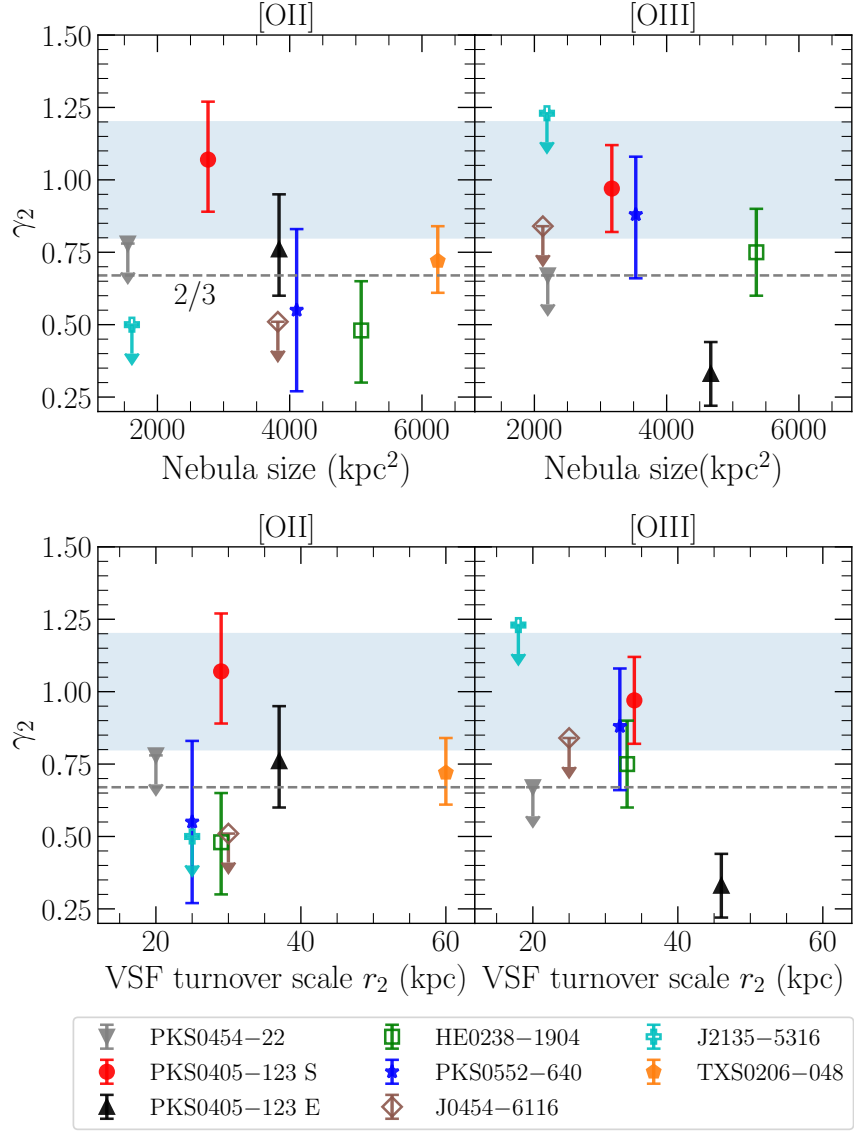
Figure 4.7: *Top row:* Nebula size versus the 2nd-order VSF slope γ_2. *Bottom row:* The VSF turnover scale r_2 versus the 2nd-order VSF slope γ_2. The results based on the [O II] $\lambda\lambda\,3727, 3729$ measurements are shown in the left panels while the results from [O III] $\lambda\,5008$ are shown in the right panels. The horizontal blue shaded regions mark the measurements for local H 2 regions presented in García-Vázquez et al. (2023), which are on average higher than the slopes constrained for QSO nebulae. No discernible correlations are found between the 2nd-order power-law slopes (γ_2) and VSF turnover scale (r_2) or nebulae size.

measurements. Analytically, von Hoerner (1951) derived that for volume-filling gas, the projection effect depends on the spatial scales probed: VSFs are steepened when measuring separation scales smaller than the depth of the cloud along the line of sight, while the VSF slopes recover to the intrinsic value at scales exceeding the cloud depth. This result is sometimes referred to as the "projection smoothing" effect and was independently confirmed by O'dell & Castaneda (1987) and Xu (2020). On the other hand, Zhang et al. (2022) used numerical simulations to show that for spatially confined structures (e.g., isolated filaments), the projection effect flattens the VSFs. As we have discussed in Section 4.4.1, the dynamical state of the nebulae examined in this work indicates that the cool line-emitting gas is embedded in the hot ambient medium and traces the turbulent motions of the hot, volume-filling gas. Therefore, our measurements are more likely affected by the "projection smoothing" effect, suggesting that the intrinsic VSF slopes may be flatter than the values reported in Table 4.4, which still supports our interpretation of the subsonic/transonic gas motions. In addition to whether the gas is volume-filling or spatially confined, in reality, the projection effect will also depend on detailed properties of the system such as density/emissivity fluctuations and the three-dimensional geometry of the gas structure. Detailed investigations using high-resolution numerical simulations are needed to robustly quantify and calibrate the projection effect in more realistic environments.

Another main limitation of the current study is the restricted dynamic range in the VSF measurements, which is confined to approximately one decade or less in projected distance separation. This restriction prevented us from obtaining robust constraints on the VSFs slopes for several systems in our sample. While the largest separation is determined by the nebula size given the detection threshold, the smallest separation accessible in the data is dictated by the spatial sampling (i.e., angular size per spatial pixel) as well as the PSF size. As ground-based observations without adaptive optics (AO) are fundamentally limited by atmospheric seeing, improving the dynamic range towards small scales requires

conducting AO-assisted observations on the ground (e.g., with VLT/ERIS in the infrared and using the Narrow-Field-Mode on VLT/MUSE in the optical) with longer exposure times to reach sufficient signal-to-noise. Alternatively, space-based IFSs such as *JWST*/NIRSpec with unprecedented spatial resolution have also started delivering an increasing sample of spatially-resolved observations of the CGM (e.g., Wylezalek et al., 2022; Veilleux et al., 2023). Finally, with a fixed PSF size, targeting systems at lower redshifts with a higher angular-to-physical size ratio can also help increase the VSF dynamic range. However, few extended ($\gtrsim 50$ kpc) nebulae have been discovered at $z < 0.5$ (e.g., Rupke et al., 2019; Chen et al., 2019; Venturi et al., 2023) and additional effort is required to expand the sample size of low-redshift extended nebulae.

4.5   Conclusion

This paper presents an ensemble study of the turbulent motions in eight extended nebulae surrounding seven QSOs at $z \approx 0.5$–1.1. Using the [O II] $\lambda\lambda\, 3727, 3729$ and/or [O III] $\lambda\, 5008$ emission lines, we measure the line-of-sight velocity fields and construct the velocity structure functions (VSFs). We probed the dynamical state of the gas illuminated by the QSO radiation field at scales ≈ 10–100 kpc. Our main conclusions are:

- Five out of the eight nebulae in our sample have a constrained power-law slope of the 2nd-order VSFs, γ_2, between ≈ 0.3–1.1, while the other three nebulae have loose constraints corresponding to 95% upper limits of $\lesssim 0.5$–1.5, as shown in Figures 4.2 and 4.7 and discussed in Section 4.3.2. To within the 2-σ measurement uncertainty, the slopes are either consistent with the expectation from Kolmogorov turbulence or flatter, suggesting that the gas motions are subsonic.

- Removing a best-fitting unidirectional velocity gradient from the line-of-sight velocity maps flattens the VSFs in general, but also leads to larger uncertainties due to a

reduced dynamic range in the VSFs that can be used for a single power-law fit. The results before and after removing a velocity gradient are consistent within the range of the uncertainty, as shown in Figure 4.2.

- Complementing the measurements for the 2nd-order VSF slopes, γ_2, the ESS slope ratios γ_p/γ_3 for $p = 1$–6 are also in agreement with the expectation of subsonic turbulence, as shown in Figure 4.3 and discussed in Section 4.3.3. The only exception is the nebula surrounding the QSO field HE0238$-$1904, where the γ_p/γ_3 ratios are consistent with the supersonic MHD turbulence prediction by Boldyrev (2002) both before and after removing a uni-directional gradient field. A more detailed investigation of this field and a larger sample size are required to shed light on whether this field is a special case.

- The subsonic motions in the QSO nebulae suggest that the line-emitting cool clouds with $T \sim 10^4$ K are embedded within a hot ambient medium with $T \sim 10^6$–10^7 K. Adopting the sound speed of the hot medium of $c_{\rm s,hot} \approx 500$ km/s, we estimate the Mach number of the cool clouds to be ≈ 0.2–0.5, consistent with the observed VSF properties. The subsonic nature of gas motions supports a scenario where the cool clumps condense out of the hot gas, carrying the turbulent memory of the hot halo and serving as tracers of hot phase dynamics (see Section 4.4.1).

- No discernible differences are seen in VSF properties between radio-loud and radio-quiet QSO fields, suggesting that the collimated jets and their inflated bubbles do not play a critical role in shaping the dynamical state of the gas on $\sim$tens of kpc scales.

- Comparing the mean velocity dispersion along the line of sight, $\langle \sigma_{\rm los} \rangle$, and the velocity dispersion observed in the plane of the sky, $\sigma_{\rm pos}$, we find that $\langle \sigma_{\rm los} \rangle \gtrsim \sigma_{\rm pos}$ for all fields (Figure 4.5). We discuss that projection effects and bulk motion along the line of sight are possible sources for the larger dispersion (see Section 4.4.3).

164

- The turbulent heating rate per unit volume, Q_{turb}, in the QSO nebulae is estimated to be $\sim 10^{-26}$–10^{-22} erg cm^{-3} s^{-1} for the cool phase and $\sim 10^{-28}$–10^{-25} erg cm^{-3} s^{-1} for the hot phase at scales ≈ 10–60 kpc. This range is in agreement with the measurements for intracluster medium and star-forming molecular clouds but is ~ 1000 times higher than that estimated for Milky Way Complex C and cool circumgalactic gas clumps probed in low-ion absorption lines, as shown in Figure 4.4 and discussed in Section 4.4.2. While the difference in Q_{turb} might be a signpost for AGN/stellar feedback, a robust investigation into the systematics of the different measurements is required to shed light on this discrepancy.

Future observations of extended nebulae using AO-assisted IFSs on the ground (e.g., MUSE Narrow-Field-Mode) and/or space-based IFSs (e.g., *JWST*/NIRSpec IFU) will help extend the small scales probed in VSFs to $\lesssim 10$ kpc, improving the robustness of the VSF constraints and bridging the gap between Q_{turb} measured by emission and absorption techniques. The findings of this ensemble study align with the recent emerging picture of the multiphase CGM where different gas phases are intricately connected throughout their formation and evolution history. Turbulence plays a critical role in facilitating nonlinear interactions within the gaseous halos, which in turn promote further developments of turbulence. For shaping the dynamical properties of gas traced by [O II] and [O III] at scales $\gtrsim 10$ kpc, environmental effects (e.g., tidal interactions, galaxy mergers, gas accretion) may dominate over QSO feedback. These findings can be directly compared with high-resolution numerical simulations to shed light on detailed physical mechanisms that govern the driving and development of turbulence in the CGM.

4.6 Appendix

4.6.1 Absence of the luminosity–velocity dispersion relation

For local H 2 regions as well as H 2 galaxies (at both low and high redshifts), a L-σ relation corresponding to the correlation between the luminosity of the region/galaxy in a certain line emission (such as Hα and Hβ) and its velocity dispersion is commonly observed (e.g., Melnick et al., 1987; González-Morán et al., 2021). In our QSO nebulae sample, however, we do not observe such a correlation, as shown in Figure 4.8. The contrast here likely arises from the different emission mechanisms for recombination lines versus collisionally-excited lines, the former of which is more well coupled to the total mass and stellar feedback in the H 2 regions/galaxies. In addition, QSOs are variable and the number of ionization photons output by QSOs is subject to significant changes on timescales of $\lesssim$ tens of Myr (e.g., Schawinski et al., 2015; Sun et al., 2017; Shen, 2021), further weakening a correlation between the luminosity of the surrounding nebulae and the velocity dispersion of the gas.

4.6.2 Measurements for individual nebulae

Here we present the VSFs measurements for individual nebulae in PKS0405$-$123, PKS0552$-$640, and HE0238$-$1904. The measurements for PKS0454$-$22, J0454$-$6116, and J2135$-$5316 can be found in the Appendix of Paper I.
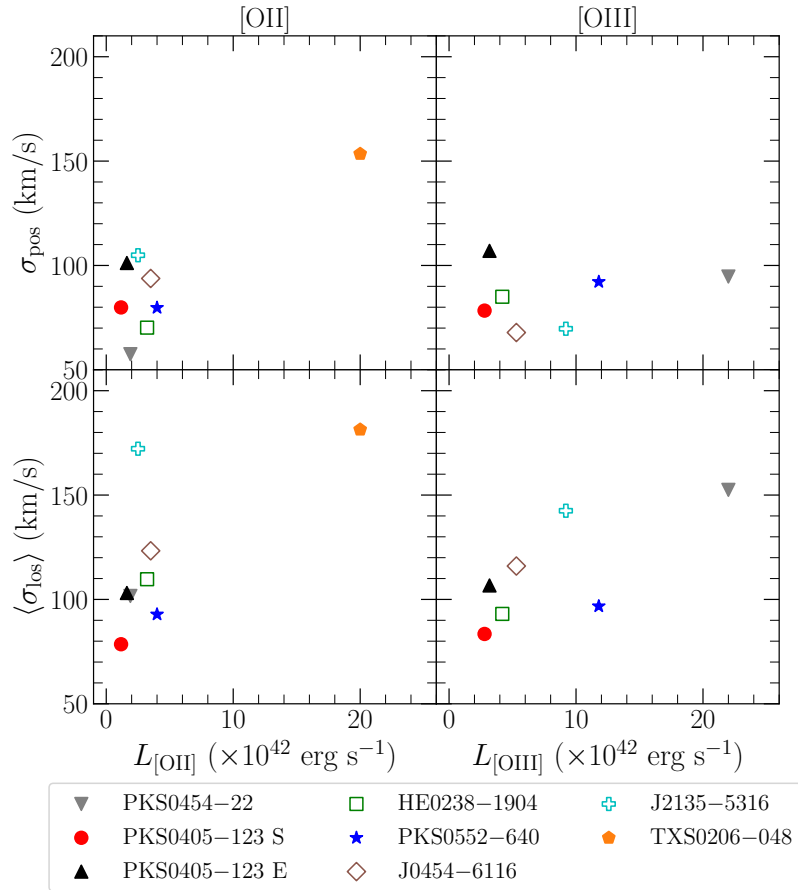
Figure 4.8: The nebula emission line luminosity (for both [O II] $\lambda\lambda\,3727, 3729$ and [O III] $\lambda\,5008$) versus the velocity dispersion, both along the line of sight and in the plane of the sky. We do not observe a $L - \sigma$ correlation using the [O II] and [O III] extended emission surrounding QSOs.
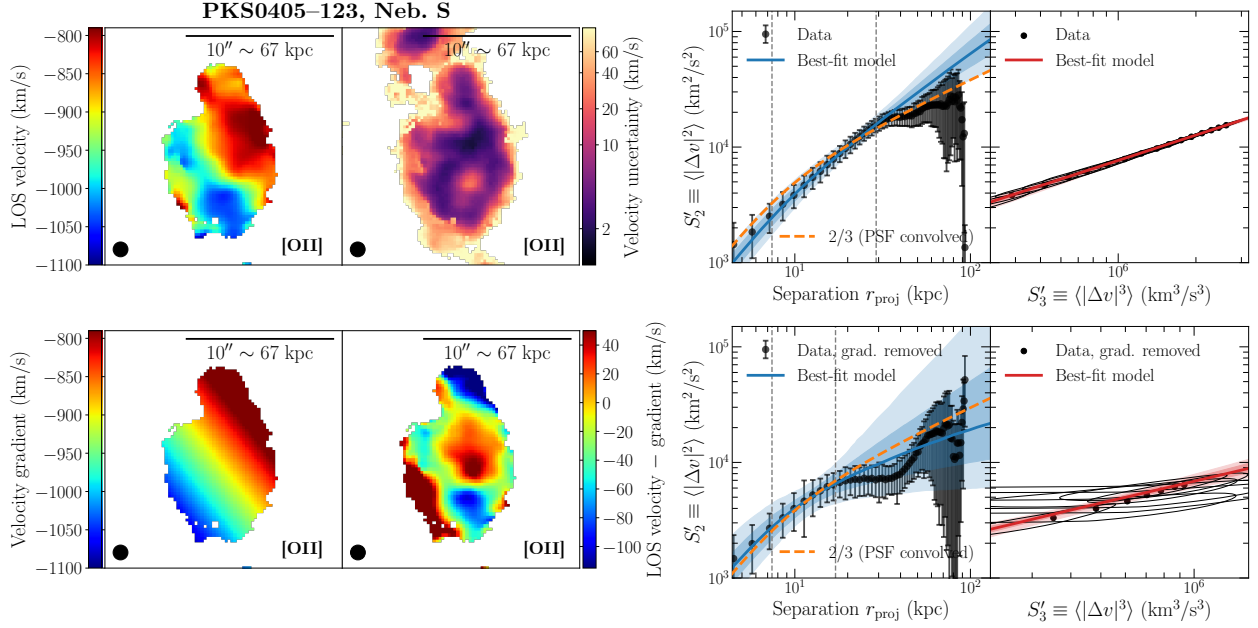
Figure 4.9: *Left-hand panels:* The best-fitting line-of-sight velocity map (top left), the line-of-sight velocity uncertainty (top right), the best-fitting uni-directional velocity gradient map (bottom left), and the residual velocity map after removing the velocity gradient from the line-of-sight velocity map (bottom right) for the southern nebula around PKS0405−123 based on the [O II] $\lambda\lambda\,3727, 3729$ emission. *Right-hand panels:* The observed 2nd-order VSF, S_2', as well as the ESS correlation between S_2' and S_3'. The top row shows the measurements using the best-fitting line-of-sight velocity map shown in the top left panel, and the bottom row shows the results after removing a uni-directional gradient, as shown in the bottom right panel on the left.
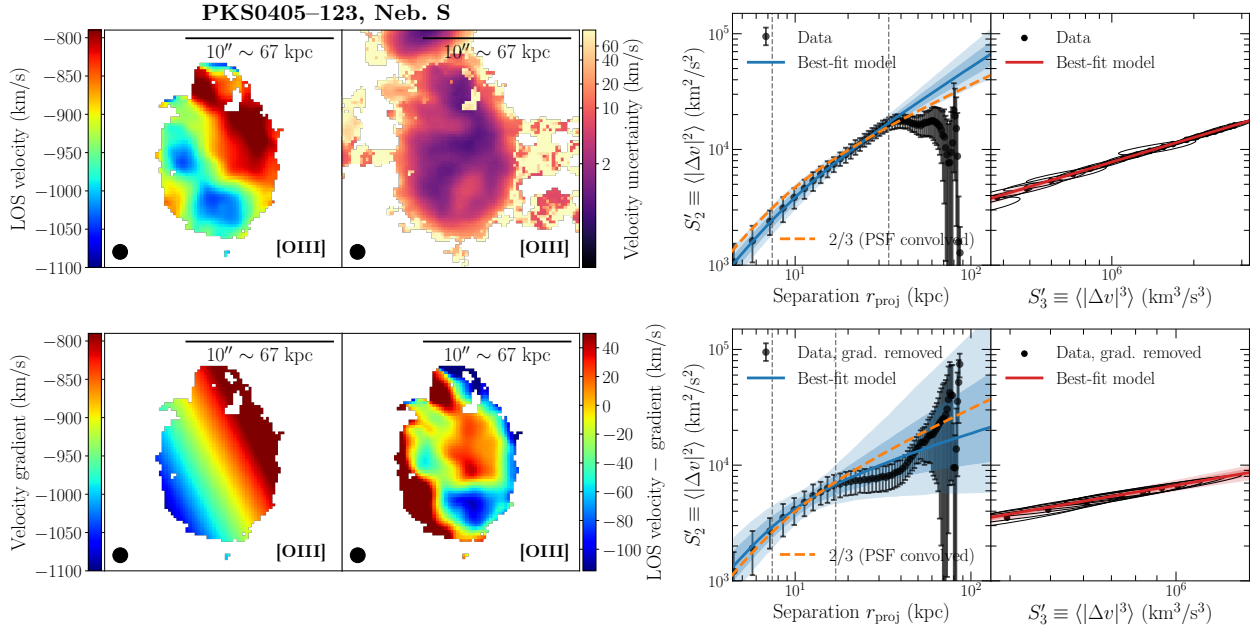
Figure 4.10: Same as Figure 4.9, but for the southern nebula around PKS0405−123 based on the [O III] $\lambda\, 5008$ emission.
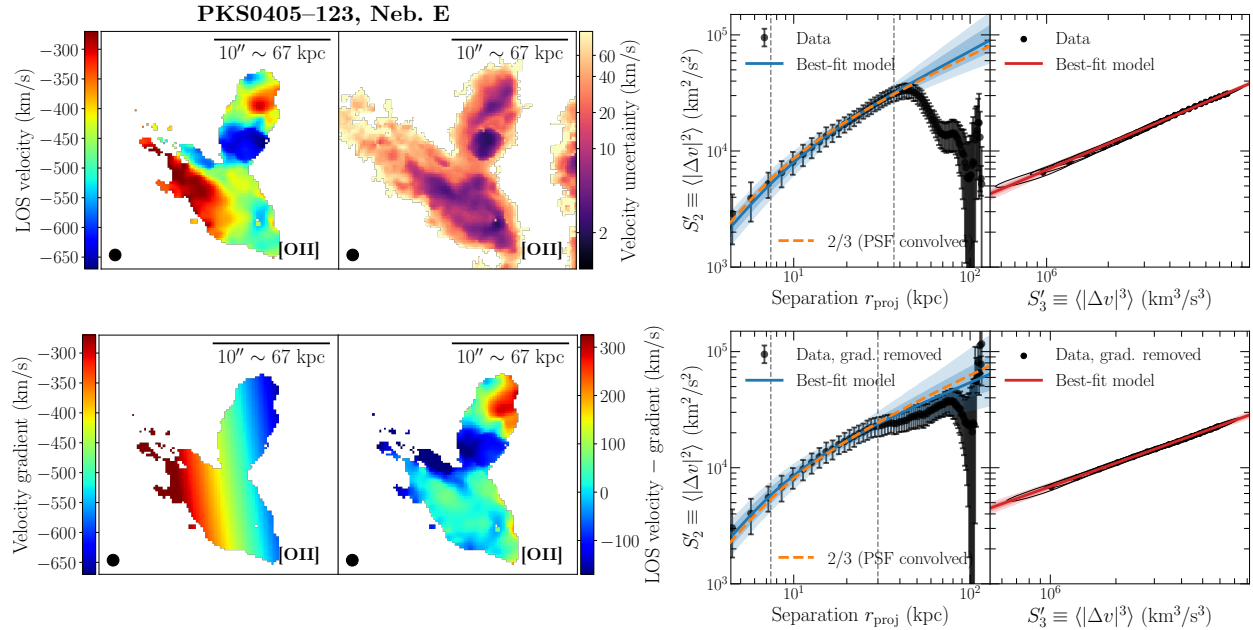

Figure 4.11: Same as Figure 4.9, but for the eastern nebula around PKS0405−123 based on the [O II] $\lambda\lambda\, 3727, 3729$ emission.
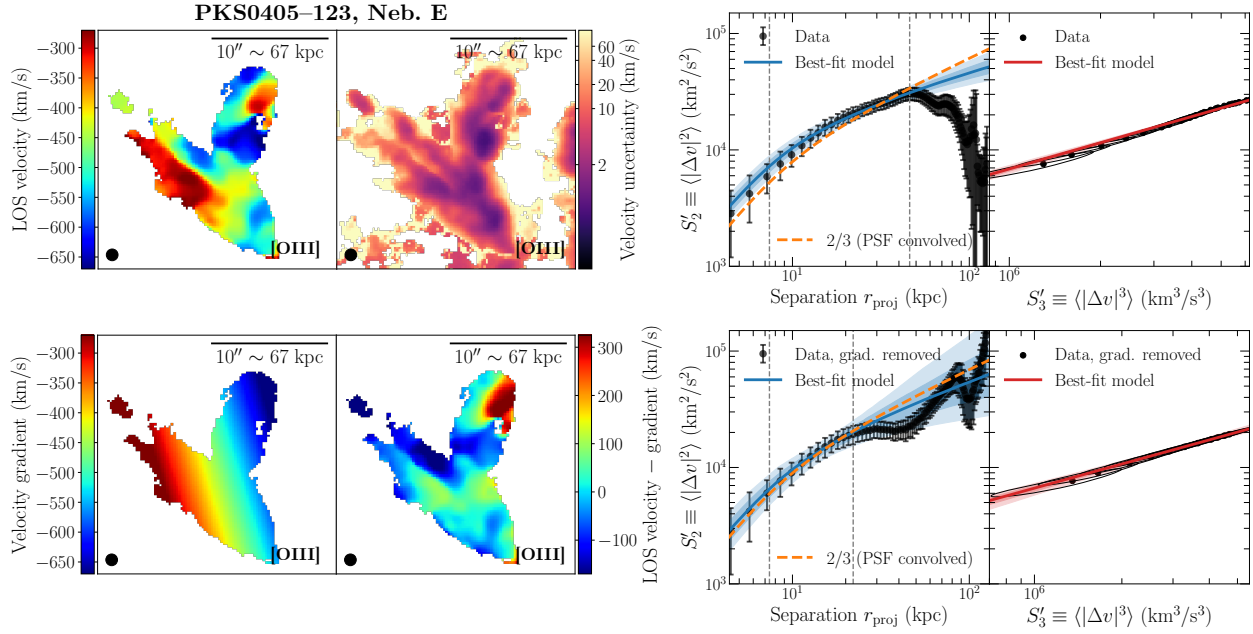
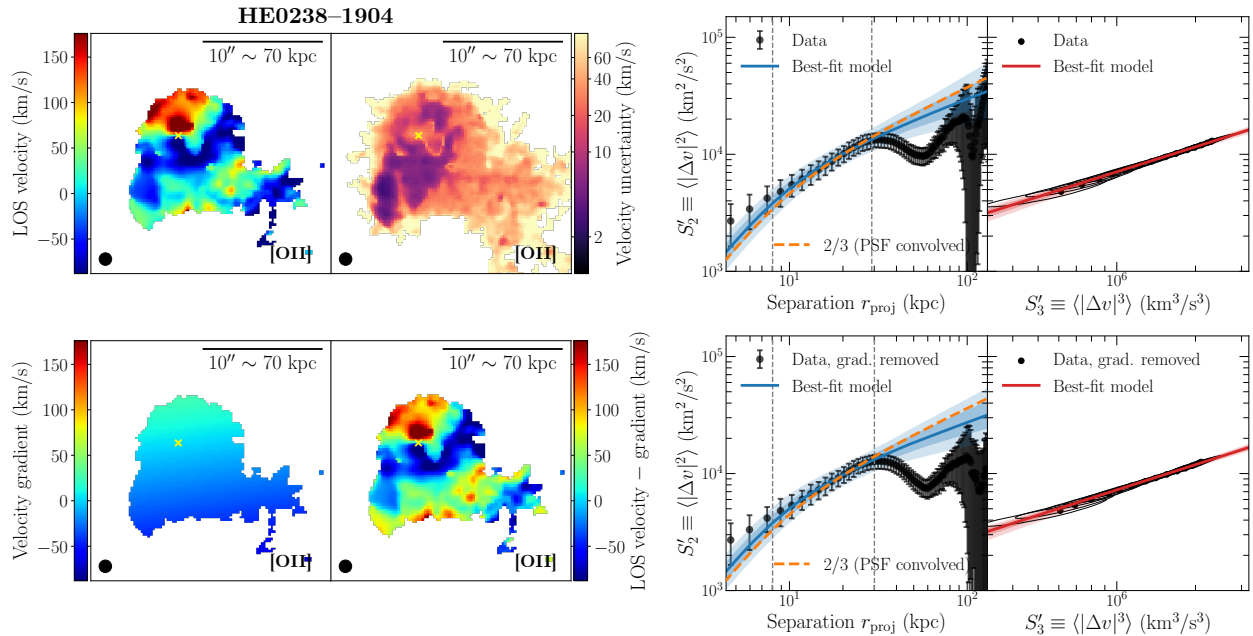Figure 4.12: Same as Figure 4.9, but for the eastern nebula around PKS0405−123 based on the [O III] λ 5008 emission.

Figure 4.13: Same as Figure 4.9, but for the field of HE0238−1904 based on the [O II] λλ 3727, 3729 emission.
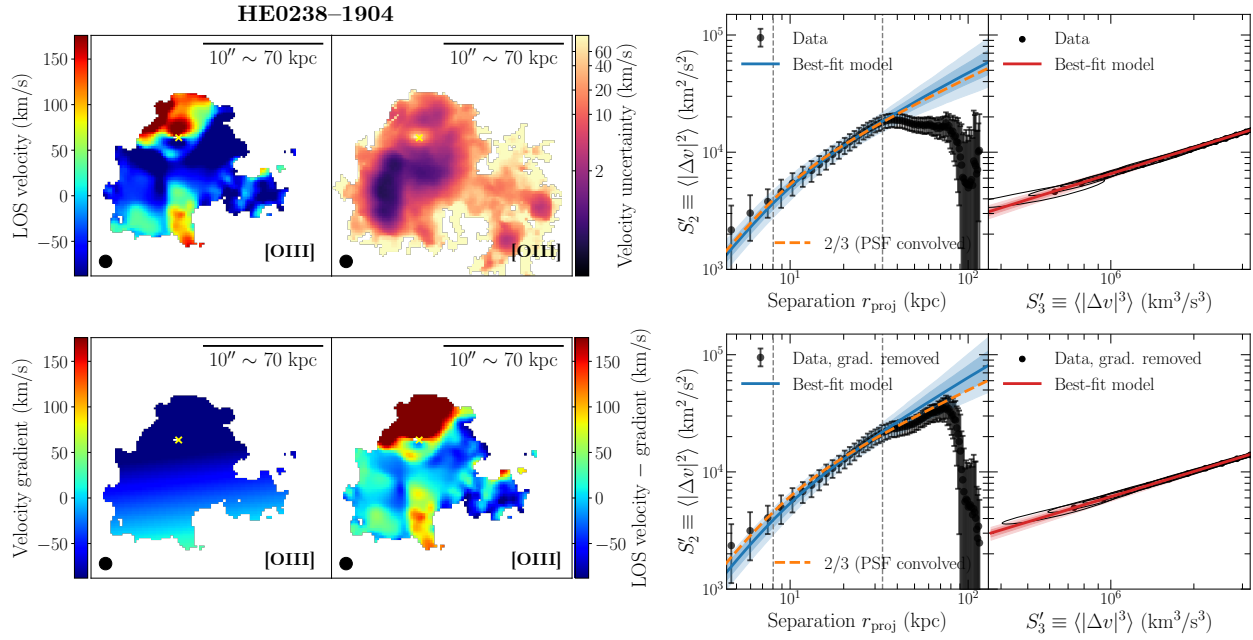
Figure 4.14: Same as Figure 4.9, but for the field of HE0238−1904 based on the [O III] λ 5008 emission.
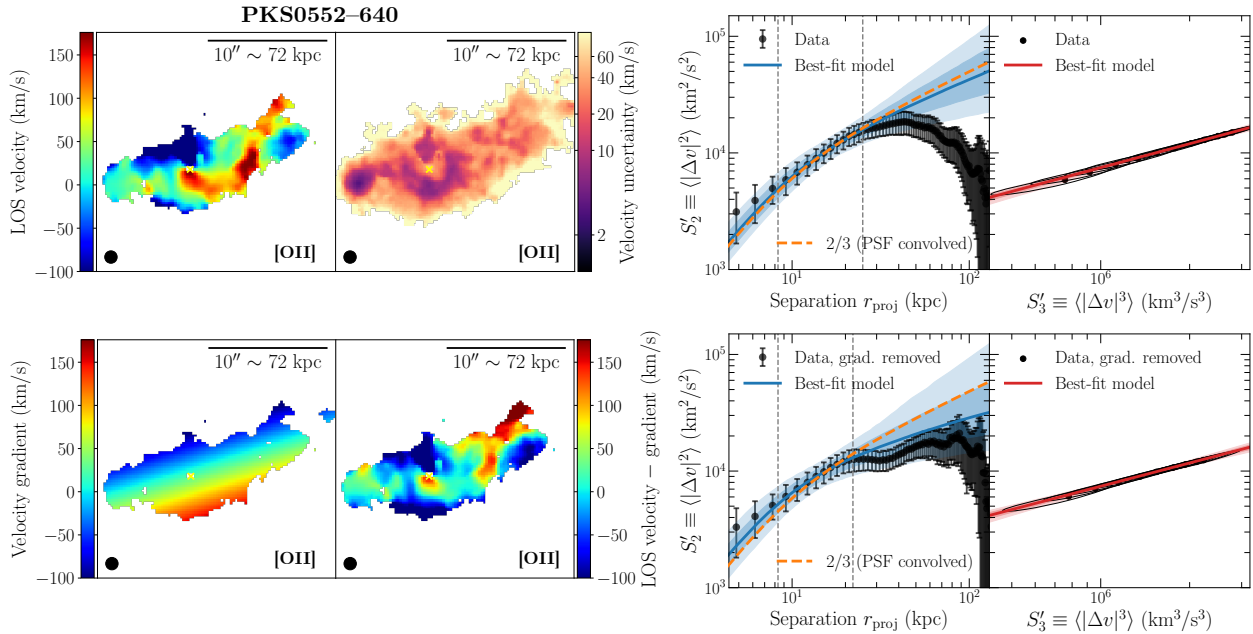

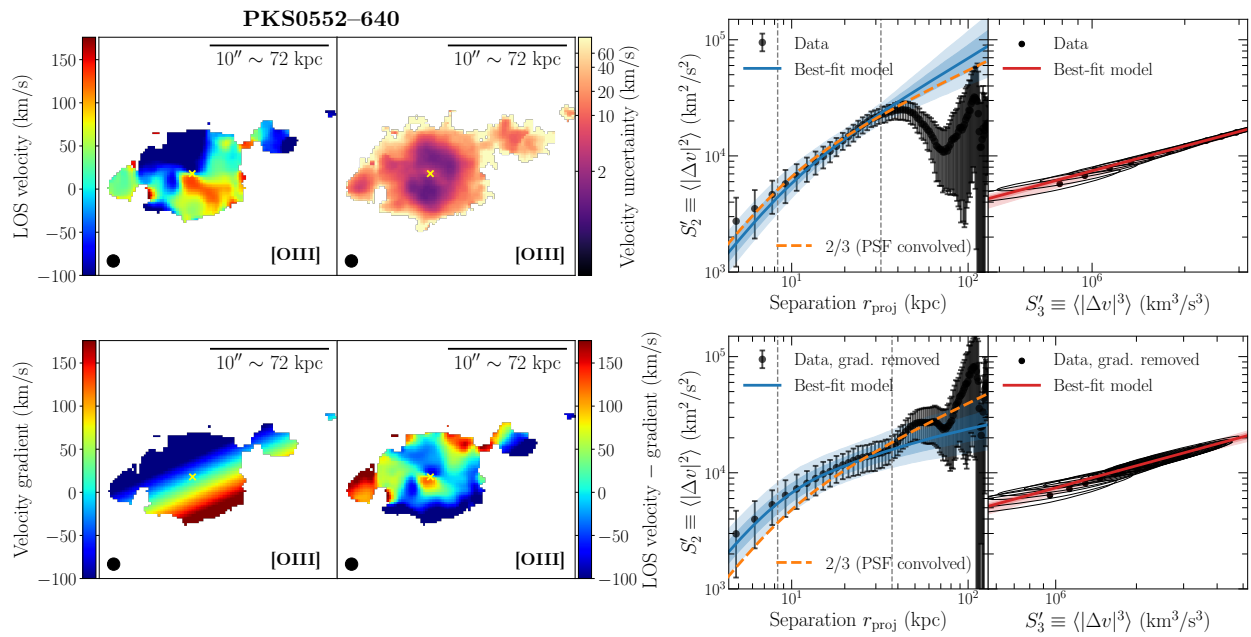Figure 4.15: Same as Figure 4.9, but for the field of PKS0552−640 based on the [O II] λλ 3727, 3729 emission.

Figure 4.16: Same as Figure 4.9, but for the field of PKS0552−640 based on the [O III] $\lambda\,5008$ emission.

CHAPTER 5

CONCLUSIONS AND FUTURE WORK

In summary, this thesis presents detailed studies of CGM gas dynamics based on IFS observations of both active halos with strong black hole accretion and typical non-active, star-forming halos. Using Lyα as a direct tracer for galactic superwinds at $z \approx 3$–4, Chapter 2 not only provides a methodology for extracting unbiased information from spatially-resolved Lyα profiles, it also presents clear-cut examples of star-formation-driven outflows that are now thought to be widespread at high redshifts and are responsible for metal enrichment of the Lyα forest in general. Chapters 3 and 4 use VSF measurements to pinpoint the subsonic nature of gas turbulence in the cool ($T \sim 10^4$ K) phase, which robustly indicates that the cool gas is dynamically coupled to the hot ambient medium. These findings can be directly compared with high-resolution numerical simulations to shed light on detailed physical mechanisms driving galactic outflows and CGM turbulence, as well as the evolution of gas dynamics in general.

Looking forward, the work presented in this thesis also charts a confident path for future observational efforts. As the strongest hydrogen recombination line, Lyα signal will continue to be the main probe of the tenuous CGM in emission, particularly towards higher redshifts and within low-mass halos that constitute the majority of the galaxy population. At redshifts $2 \lesssim z \lesssim 7$, a rich and rapidly increasing sample of extended Lyα nebulae surrounding galaxies spanning a wide range of physical properties has been established by IFS observations through MUSE and KCWI. At lower redshifts, forthcoming space missions, such as the Habitable Worlds Observatory, are anticipated to enhance our capabilities through UV IFS instruments. These tools will enable spatially- and spectrally-resolved Lyα observations originating from the CGM of nearby galaxies. However, despite the burgeoning wealth of the current data archive and the anticipated breakthrough of the future database for local galaxies, interpreting Lyα emission remains challenging due to its resonant nature. To address

these complexities, further investigation across a larger sample is imperative. As evidenced by the in-depth analyses in Chapter 2, a concerted effort is required to conduct detailed, spatially-resolved studies of Lyα signals in tandem with galaxy data. Current observations, including approximately 20 strong-lensing galaxy clusters surveyed by MUSE, have uncovered nearly a dozen lensed arcs with extended Lyα emissions potentially reaching CGM halo scales (e.g., Claeyssens et al., 2022). Future research on this expanded dataset with enhanced spatial resolution via lensing will be instrumental in illuminating the systematic uncertainties inherent in Lyα radiative transfer modeling. Additionally, these analyses will provide valuable constraints on the correlation between Lyα line properties and emissions from other non-resonant lines. Such advancements are crucial for refining our analysis of Lyα observations across both low and high redshifts.

As a key probe for CGM turbulence, the current pilot sample of two-point VSF measurements at $z \gtrsim 0.5$ presented in Chapters 3 and 4 lacks the dynamic range in spatial scales for a robust characterization of the gas flows. The smallest scale accessible is limited by the seeing disk in ground-based observations and the largest scale is dictated by the size of the nebulae over which robust emission signals can be measured. Therefore, a strategic and immediate step forward is to target nebulae at lower redshifts. This approach ensures an increased dynamic range on small scales by amplifying the apparent angular size for a fixed seeing size and on large scales by mitigating the cosmological dimming effect. In this regard, existing data archives of ground-based IFSs already contain a sizable sample suitable for detailed dynamics studies of the CGM. A cross-correlating search using the latest version of the MILLIQUAS quasar catalog (Flesch, 2023) and the ESO data archive yields 355 AGNs at $z \lesssim 0.1$ with existing MUSE observations. Previous research has shown that $\approx 30\%$ of AGN exhibit extended nebulae that are well-suited for in-depth CGM dynamics studies (e.g., Stockton & MacKenty, 1987). Therefore, ~ 100 extended nebulae are anticipated to be discovered within this redshift range from the MUSE archive.
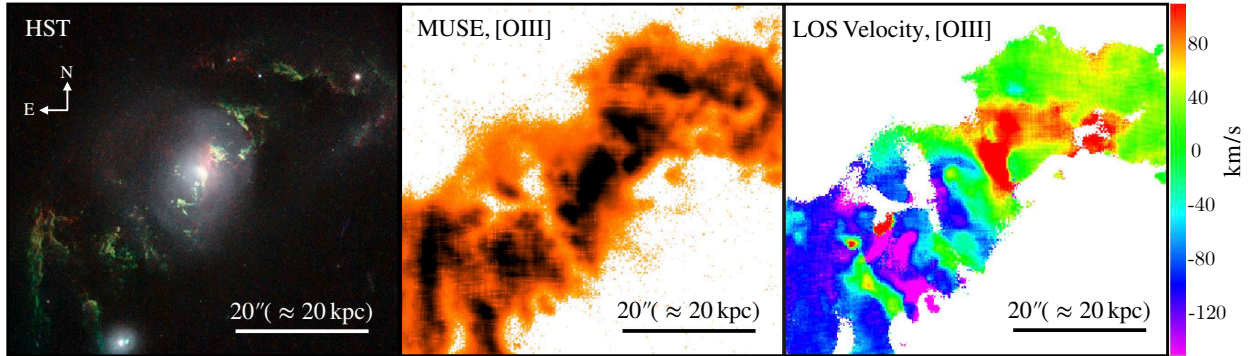
Figure 5.1: Active galaxy UGC 7342 at $z \approx 0.05$, an example from the low-z sample. *Left: HST* color image with [O II] $\lambda\lambda\, 3727, 3729$ emission shown in green and Hα emission in red. *Middle:* continuum-subtracted narrow-band image of the [O III] $\lambda\, 5008$ emission, based on archival MUSE data. *Right:* The line-of-sight velocity measured using the [O III] $\lambda\, 5008$ emission. The velocity map exhibits fluctuations on both large and small scales, revealing the turbulent nature of the gas. This example underlines the power of IFSs in detecting low surface brightness signals and showcases the wide dynamic range in spatial scales accessible through MUSE data at low redshifts.

Figure 5.1 shows an example source UGC 7342, an active galaxy at $z \approx 0.05$, exhibiting extensive gaseous structures in several non-resonant lines including Hβ, [O III] $\lambda\, 5008$ and Hα. With strong emission spanning almost the whole MUSE field of view, this source will enable VSF measurements on scales of $\approx$ 0.6–80 kpc, improving upon the current dynamic range by more than an order of magnitude. The example of UGC 7342 also underlines the power of IFS data in revealing low surface brightness signals, with the MUSE data being approximately $20\times$ deeper than the *HST* narrow-band imaging data, as can be seen from the contrast between the two images in Figure 5.1. The tenfold enhancement in the dynamic range promises a transformative improvement in the VSF measurements, allowing robust characterization of the turbulent energy coupling between $\sim$tens of kpc and sub-kpc scales on a statistical sample in both radio-loud and radio-quite QSO halos. These results will shed light on the impact of AGN and the potential role of radio mode feedback on CGM turbulence.

These future efforts will continue to fill the prominent gap in observational constraints on CGM dynamics. While similar processes in the ICM have been more extensively studied via

detailed X-ray observations, the CGM remains an emergent frontier. Current and upcoming observational studies of the dynamic CGM will catalyze an in-depth exploration of the key factors governing the baryon cycle, from gas infalls/outflows and tidal interactions to magnetic field pressure support and cosmic rays, building a clearer understanding of the impact of stellar/AGN feedback on gas properties and the galaxy-gas ecosystem in general.

REFERENCES

Adelberger K. L., Steidel C. C., Kollmeier J. A., Reddy N. A., 2006, ApJ, 637, 74

Anglés-Alcázar D., Faucher-Giguère C.-A., Kereš D., Hopkins P. F., Quataert E., Murray N., 2017, MNRAS, 470, 4698

Anorve-Zeferino G. A., 2019, MNRAS, 483, 704

Arrigoni Battaia F., Hennawi J. F., Prochaska J. X., Oñorbe J., Farina E. P., Cantalupo S., Lusso E., 2019, MNRAS, 482, 3162

Arthur S. J., Medina S. N. X., Henney W. J., 2016, MNRAS, 463, 2864

Aung H., Mandelker N., Nagai D., Dekel A., Birnboim Y., 2019, MNRAS, 490, 181

Bacon R., et al., 2010, in McLean I. S., Ramsay S. K., Takami H., eds, Society of Photo-Optical Instrumentation Engineers (SPIE) Conference Series Vol. 7735, Ground-based and Airborne Instrumentation for Astronomy III. p. 773508 (`arXiv:2211.16795`), doi:10.1117/12.856027

Bacon R., et al., 2017, A&A, 608, A1

Becker G. D., Rauch M., Sargent W. L. W., 2007, ApJ, 662, 72

Behroozi P. S., Wechsler R. H., Conroy C., 2013, ApJ, 770, 57

Benzi R., Ciliberto S., Tripiccione R., Baudet C., Massaioli F., Succi S., 1993, Phys. Rev. E, 48, R29

Berg D. A., Erb D. K., Auger M. W., Pettini M., Brammer G. B., 2018, ApJ, 859, 164

Bertin E., Arnouts S., 1996, A&AS, 117, 393

Biviano A., et al., 2013, A&A, 558, A1

Böhringer H., et al., 2001, A&A, 369, 826

Boldyrev S., 2002, ApJ, 569, 841

Boldyrev S., 2006, Phys. Rev. Lett., 96, 115002

Bordoloi R., Rigby J. R., Tumlinson J., Bayliss M. B., Sharon K., Gladders M. G., Wuyts E., 2016, MNRAS, 458, 1891

Borisova E., et al., 2016, ApJ, 831, 39

Bouwens R. J., Illingworth G. D., Franx M., Ford H., 2007, ApJ, 670, 928

Brandenburg A., Lazarian A., 2013, Space Sci. Rev., 178, 163

Brinchmann J., Pettini M., Charlot S., 2008, MNRAS, 385, 769

Bruzual G., Charlot S., 2003, MNRAS, 344, 1000

Burkhart B., 2021, PASP, 133, 102001

Cabanac R. A., Valls-Gabaud D., Lidman C., 2008, MNRAS, 386, 2065

Cai Z., et al., 2017, ApJ, 837, 71

Cai Z., et al., 2019, ApJS, 245, 23

Calzetti D., Armus L., Bohlin R. C., Kinney A. L., Koornneef J., Storchi-Bergmann T., 2000, ApJ, 533, 682

Caminha G. B., et al., 2016a, A&A, 587, A80

Caminha G. B., et al., 2016b, A&A, 595, A100

Caminha G. B., et al., 2017, A&A, 607, A93

Cantalupo S., 2017, in Fox A., Davé R., eds, Astrophysics and Space Science Library Vol. 430, Gas Accretion onto Galaxies. p. 195 (`arXiv:1612.00491`), doi:10.1007/978-3-319-52512-9_9

Cantalupo S., Porciani C., Lilly S. J., Miniati F., 2005, ApJ, 628, 61

Cantalupo S., Lilly S. J., Haehnelt M. G., 2012, MNRAS, 425, 1992

Cantalupo S., Arrigoni-Battaia F., Prochaska J. X., Hennawi J. F., Madau P., 2014, Nature, 506, 63

Cantalupo S., et al., 2019, MNRAS, 483, 5188

Carnall A. C., McLure R. J., Dunlop J. S., Davé R., 2018, MNRAS, 480, 4379

Chen H.-W., 2017, Outskirts of Distant Galaxies in Absorption. p. 291, doi:10.1007/978-3-319-56570-5_9

Chen H.-W., Prochaska J. X., Gnedin N. Y., 2007, ApJL, 667, L125

Chen H.-W., Gauthier J.-R., Sharon K., Johnson S. D., Nair P., Liang C. J., 2014, MNRAS, 438, 1435

Chen H.-W., Boettcher E., Johnson S. D., Zahedy F. S., Rudie G. C., Cooksey K. L., Rauch M., Mulchaey J. S., 2019, ApJL, 878, L33

Chen H.-W., et al., 2020, MNRAS, 497, 498

Chen M. C., Chen H.-W., Gronke M., Rauch M., Broadhurst T., 2021, MNRAS, 504, 2629

Chen H.-W., et al., 2023a, arXiv e-prints, p. arXiv:2309.05699

Chen M. C., et al., 2023b, arXiv e-prints, p. arXiv:2310.18406

Chen M. C., et al., 2023c, MNRAS, 518, 2354

Chira R. A., Ibáñez-Mejía J. C., Mac Low M. M., Henning T., 2019, A&A, 630, A97

Claeyssens A., et al., 2019, MNRAS, 489, 5022

Claeyssens A., et al., 2022, A&A, 666, A78

Coe D., et al., 2013, ApJ, 762, 32

Conroy C., 2013, ARA&A, 51, 393

Conroy C., Gunn J. E., 2010, ApJ, 712, 833

Conroy C., Gunn J. E., White M., 2009, ApJ, 699, 486

Cooper T. J., et al., 2021, MNRAS, 508, 4359

Crowther P. A., 2007, ARA&A, 45, 177

Dijkstra M., 2014, PASA, 31, e040

Dijkstra M., 2017, arXiv e-prints, p. arXiv:1704.03416

Dijkstra M., Kramer R., 2012, MNRAS, 424, 1672

Dijkstra M., Haiman Z., Spaans M., 2006, ApJ, 649, 14

Donahue M., Voit G. M., 2022, Phys. Rep., 973, 1

Draine B. T., 2011, Physics of the Interstellar and Intergalactic Medium

Ebeling H., Edge A. C., Henry J. P., 2001, ApJ, 553, 668

Ebeling H., Ma C. J., Kneib J. P., Jullo E., Courtney N. J. D., Barrett E., Edge A. C., Le
    Borgne J. F., 2009, MNRAS, 395, 1213

Eichner T., et al., 2013, ApJ, 774, 124

Eldridge J. J., Stanway E. R., Xiao L., McClelland L. A. S., Taylor G., Ng M., Greis S. M. L., Bray J. C., 2017, PASA, 34, e058

Elíasdóttir Á., et al., 2007, preprint, (`arXiv:0710.5636`)

Epinat B., et al., 2018, A&A, 609, A40

Erb D. K., Steidel C. C., Shapley A. E., Pettini M., Reddy N. A., Adelberger K. L., 2006, ApJ, 646, 107

Erb D. K., et al., 2014, ApJ, 795, 33

Erb D. K., Steidel C. C., Chen Y., 2018, ApJL, 862, L10

Erb D. K., Berg D. A., Auger M. W., Kaplan D. L., Brammer G., Pettini M., 2019, ApJ, 884, 7

Fabian A. C., 2012, ARA&A, 50, 455

Faucher-Giguère C.-A., Oh S. P., 2023, ARA&A, 61, 131

Faucher-Giguère C.-A., Kereš D., Dijkstra M., Hernquist L., Zaldarriaga M., 2010, ApJ, 725, 633

Federrath C., 2013, MNRAS, 436, 1245

Federrath C., Klessen R. S., Iapichino L., Beattie J. R., 2021, Nature Astronomy, 5, 365

Feltre A., Charlot S., Gutkin J., 2016, MNRAS, 456, 3354

Feltre A., et al., 2020, arXiv e-prints, p. arXiv:2007.01878

Ferland G. J., et al., 2017, Rev. Mexicana Astron. Astrofis., 53, 385

Fielding D. B., Ostriker E. C., Bryan G. L., Jermyn A. S., 2020, ApJL, 894, L24

Flesch E. W., 2023, arXiv e-prints, p. arXiv:2308.01505

Florian M. K., et al., 2020, arXiv e-prints, p. arXiv:2006.11387

Foreman-Mackey D., Hogg D. W., Lang D., Goodman J., 2013, PASP, 125, 306

Franx M., Illingworth G. D., Kelson D. D., van Dokkum P. G., Tran K.-V., 1997, ApJL, 486, L75

Frisch U., 1995, Turbulence. The legacy of A.N. Kolmogorov

Frye B., Broadhurst T., 1998, ApJL, 499, L115

Frye B., Broadhurst T., Benítez N., 2002, ApJ, 568, 558

Ganguly S., et al., 2023, Frontiers in Astronomy and Space Sciences, 10, 1138613

García-Vázquez J., Henney W. J., Castañeda H. O., 2023, MNRAS,

Gaspari M., et al., 2018, ApJ, 854, 167

González-Morán A. L., et al., 2021, MNRAS, 505, 1441

Gould A., Weinberg D. H., 1996, ApJ, 468, 462

Grazian A., et al., 2017, A&A, 602, A18

Grete P., O'Shea B. W., Beckwith K., 2021, ApJ, 909, 148

Gronke M., 2017, A&A, 608, A139

Gronke M., Dijkstra M., 2014, MNRAS, 444, 1095

Gronke M., Oh S. P., 2018, MNRAS, 480, L111

Gronke M., Bull P., Dijkstra M., 2015, ApJ, 812, 123

Gronke M., Dijkstra M., McCourt M., Oh S. P., 2016, ApJL, 833, L26

Gronke M., Oh S. P., Ji S., Norman C., 2022, MNRAS, 511, 859

Gutkin J., Charlot S., Bruzual G., 2016, MNRAS, 462, 1757

Ha T., Li Y., Xu S., Kounkel M., Li H., 2021, ApJL, 907, L40

Ha T., Li Y., Kounkel M., Xu S., Li H., Zheng Y., 2022, arXiv e-prints, p. arXiv:2205.00012

Haffert S. Y., Bohn A. J., de Boer J., Snellen I. A. G., Brinchmann J., Girard J. H., Keller
    C. U., Bacon R., 2019, Nature Astronomy, 3, 749

Hansen M., Oh S. P., 2006, MNRAS, 367, 979

Hayes M., 2015, PASA, 32, e027

Heckman T. M., Best P. N., 2014, ARA&A, 52, 589

Heckman T. M., Alexandroff R. M., Borthakur S., Overzier R., Leitherer C., 2015, ApJ, 809,
    147

Helton J. M., Johnson S. D., Greene J. E., Chen H.-W., 2021, MNRAS, 505, 5497

Hennawi J. F., Prochaska J. X., 2013, ApJ, 766, 58

Hennawi J. F., Prochaska J. X., Kollmeier J., Zheng Z., 2009, ApJL, 693, L49

Hennebelle P., Falgarone E., 2012, A&A Rev., 20, 55

Hezaveh Y. D., et al., 2016, ApJ, 823, 37

Hoag A., et al., 2019, MNRAS, 488, 706

Hogan C. J., Weymann R. J., 1987, MNRAS, 225, 1P

Hu Y., Federrath C., Xu S., Mathew S. S., 2022, MNRAS, 513, 2100

Johnson S. D., Chen H.-W., Mulchaey J. S., Tripp T. M., Prochaska J. X., Werk J. K., 2014, MNRAS, 438, 3039

Johnson T. L., et al., 2017, ApJL, 843, L21

Johnson S. D., et al., 2018, ApJL, 869, L1

Johnson S. D., et al., 2022, ApJL, 940, L40

Jullo E., Kneib J.-P., Limousin M., Elíasdóttir Á., Marshall P. J., Verdugo T., 2007, New Journal of Physics, 9, 447

Kaplan S. A., Pikelner S. B., 1970, The interstellar medium

Kassiola A., Kovner I., 1993, ApJ, 417, 450

Kauffmann G., et al., 2003, MNRAS, 346, 1055

Kehrig C., Vílchez J. M., Guerrero M. A., Iglesias-Páramo J., Hunt L. K., Duarte-Puertas S., Ramos-Larios G., 2018, MNRAS, 480, 1081

Kelly P. L., et al., 2018, Nature Astronomy, 2, 334

Kennicutt R. C., Evans N. J., 2012, ARA&A, 50, 531

Kewley L. J., Dopita M. A., Sutherland R. S., Heisler C. A., Trevena J., 2001, ApJ, 556, 121

Kewley L. J., Nicholls D. C., Sutherland R. S., 2019, ARA&A, 57, 511

Kollmeier J. A., Zheng Z., Davé R., Gould A., Katz N., Miralda-Escudé J., Weinberg D. H., 2010, ApJ, 708, 1048

Kolmogorov A., 1941, Akademiia Nauk SSSR Doklady, 30, 301

Kulas K. R., Shapley A. E., Kollmeier J. A., Zheng Z., Steidel C. C., Hainline K. N., 2012, ApJ, 745, 33

Lagrois D., Joncas G., 2011, MNRAS, 413, 721

Lam D., Broadhurst T., Diego J. M., Lim J., Coe D., Ford H. C., Zheng W., 2014, ApJ, 797, 98

Laursen P., Sommer-Larsen J., Andersen A. C., 2009, ApJ, 704, 1640

Leclercq F., et al., 2017, A&A, 608, A8

Leclercq F., et al., 2020, A&A, 635, A82

Leitherer C., et al., 1999, ApJS, 123, 3

Lemaux B. C., et al., 2020, arXiv e-prints, p. arXiv:2007.01310

Li J.-T., Bregman J. N., Wang Q. D., Crain R. A., Anderson M. E., 2018, ApJL, 855, L24

Li Y., et al., 2020, ApJL, 889, L1

Li Y., Luo R., Fossati M., Sun M., Jáchym P., 2023, MNRAS, 521, 4785

Liu Z., et al., 2023, arXiv e-prints, p. arXiv:2309.00053

Livermore R. C., et al., 2012, MNRAS, 427, 688

Lopez S., et al., 2018, Nature, 554, 493

Ma X., Hopkins P. F., Faucher-Giguère C.-A., Zolman N., Muratov A. L., Kereš D., Quataert E., 2016, MNRAS, 456, 2140

Madau P., Dickinson M., 2014, ARA&A, 52, 415

Mandelker N., Nagai D., Aung H., Dekel A., Padnos D., Birnboim Y., 2019, MNRAS, 484, 1100

Marchal A., Martin P. G., Gong M., 2021, ApJ, 921, 11

Martin C. L., Shapley A. E., Coil A. L., Kornei K. A., Bundy K., Weiner B. J., Noeske K. G., Schiminovich D., 2012, ApJ, 760, 127

Maseda M. V., et al., 2017, A&A, 608, A4

Matthee J., Sobral D., Gronke M., Paulino-Afonso A., Stefanon M., Röttgering H., 2018, A&A, 619, A136

McKean J. P., et al., 2007, MNRAS, 378, 109

McNamara B. R., Nulsen P. E. J., 2007, ARA&A, 45, 117

Melnick J., Moles M., Terlevich R., Garcia-Pelayo J.-M., 1987, MNRAS, 226, 849

Melnick J., Tenorio-Tagle G., Telles E., 2021, A&A, 649, A175

Mitchell P. D., Schaye J., 2022, MNRAS, 511, 2948

Mo H., van den Bosch F. C., White S., 2010, Galaxy Formation and Evolution

Mohapatra R., Jetti M., Sharma P., Federrath C., 2022, MNRAS, 510, 2327

Molino A., et al., 2017, MNRAS, 470, 95

Morrissey P., et al., 2018, ApJ, 864, 93

Mortensen K., Keerthi Vasan G. C., Jones T., Faucher-Giguere C.-A., Sanders R., Ellis R. S., Leethochawalit N., Stark D. P., 2020, arXiv e-prints, p. arXiv:2006.00006

Mullin L. M., Riley J. M., Hardcastle M. J., 2008, MNRAS, 390, 595

Muzahid S., et al., 2020, MNRAS, 496, 1013

Nanayakkara T., et al., 2019, A&A, 624, A89

Nesvadba N. P. H., Drouart G., De Breuck C., Best P., Seymour N., Vernet J., 2017, A&A, 600, A121

Neufeld D. A., 1991, ApJL, 370, L85

Newman A., et al., 2019, BAAS, 51, 145

O'dell C. R., Castaneda H. O., 1987, ApJ, 317, 686

Olivares V., et al., 2022, A&A, 666, A94

Orlitová I., Verhamme A., Henry A., Scarlata C., Jaskot A., Oey M. S., Schaerer D., 2018, A&A, 616, A60

Ossenkopf V., Mac Low M. M., 2002, A&A, 390, 307

Osterbrock D. E., Ferland G. J., 2006, Astrophysics of gaseous nebulae and active galactic nuclei

Padoan P., Pan L., Haugbølle T., Nordlund Å., 2016, ApJ, 822, 11

Pan L., Scannapieco E., 2010, ApJ, 721, 1765

Pan L., Scannapieco E., 2011, Phys. Rev. E, 83, 045302

Patrício V., et al., 2016, MNRAS, 456, 4191

Péroux C., Howk J. C., 2020, ARA&A, 58, 363

Péroux C., et al., 2019, MNRAS, 485, 1595

Pettini M., Steidel C. C., Adelberger K. L., Dickinson M., Giavalisco M., 2000, ApJ, 528, 96

Planck Collaboration et al., 2020, A&A, 641, A1

Postman M., et al., 2012, ApJS, 199, 25

Prasad D., Sharma P., Babul A., 2015, ApJ, 811, 108

Qu Z., et al., 2022, MNRAS, 516, 4882

Rauch M., Sargent W. L. W., Womble D. S., Barlow T. A., 1996a, ApJL, 467, L5

Rauch M., Sargent W. L. W., Womble D. S., Barlow T. A., 1996b, ApJL, 467, L5

Rauch M., Sargent W. L. W., Barlow T. A., 2001, ApJ, 554, 823

Rauch M., Sargent W. L. W., Barlow T. A., Simcoe R. A., 2002, ApJ, 576, 45

Rauch M., et al., 2008, ApJ, 681, 856

Rauch M., Becker G. D., Haehnelt M. G., Gauthier J.-R., Ravindranath S., Sargent W. L. W., 2011, MNRAS, 418, 1115

Rauch M., Becker G. D., Haehnelt M. G., Gauthier J.-R., Sargent W. L. W., 2013, MNRAS, 429, 429

Rauch M., Becker G. D., Haehnelt M. G., 2016, MNRAS, 455, 3991

Reddy N. A., Steidel C. C., Pettini M., Adelberger K. L., Shapley A. E., Erb D. K., Dickinson M., 2008, ApJS, 175, 48

Reddy N. A., Pettini M., Steidel C. C., Shapley A. E., Erb D. K., Law D. R., 2012, ApJ, 754, 25

Ribeiro B., et al., 2020, arXiv e-prints, p. arXiv:2007.01322

Richard J., et al., 2020, arXiv e-prints, p. arXiv:2009.09784

Rosati P., et al., 2014, The Messenger, 158, 48

Rubin K. H. R., Weiner B. J., Koo D. C., Martin C. L., Prochaska J. X., Coil A. L., Newman J. A., 2010, ApJ, 719, 1503

Rubin K. H. R., et al., 2018, ApJ, 859, 146

Rudie G. C., Steidel C. C., Pettini M., Trainor R. F., Strom A. L., Hummels C. B., Reddy
N. A., Shapley A. E., 2019, ApJ, 885, 61

Rupke D. S. N., Gültekin K., Veilleux S., 2017, ApJ, 850, 40

Rupke D. S. N., et al., 2019, Nature, 574, 643

Saad T., Cline D., Stoll R., Sutherland J. C., 2017, AIAA Journal, 55, 327

Sanderson K. N., Prescott M. M. K., Christensen L., Fynbo J., Møller P., 2021, ApJ, 923,
252

Savage B. D., Lehner N., Wakker B. P., Sembach K. R., Tripp T. M., 2005, ApJ, 626, 776

Schaerer D., Vacca W. D., 1998, ApJ, 497, 618

Schaerer D., Hayes M., Verhamme A., Teyssier R., 2011, A&A, 531, A12

Schawinski K., Koss M., Berney S., Sartori L. F., 2015, MNRAS, 451, 2517

Schlafly E. F., Finkbeiner D. P., 2011, ApJ, 737, 103

Schneider E. E., Ostriker E. C., Robertson B. E., Thompson T. A., 2020, ApJ, 895, 43

Sersic J. L., 1968, Atlas de Galaxias Australes

Shapley A. E., 2011, ARA&A, 49, 525

Shapley A. E., Steidel C. C., Pettini M., Adelberger K. L., 2003, ApJ, 588, 65

Sharma S., 2017, ARA&A, 55, 213

She Z.-S., Leveque E., 1994, Phys. Rev. Lett., 72, 336

Shen Y., 2021, ApJ, 921, 70

Shibuya T., Ouchi M., Nakajima K., Yuma S., Hashimoto T., Shimasaku K., Mori M., Umemura M., 2014, ApJ, 785, 64

Steidel C. C., Erb D. K., Shapley A. E., Pettini M., Reddy N., Bogosavljević M., Rudie G. C., Rakic O., 2010, ApJ, 717, 289

Steidel C. C., Bogosavljević M., Shapley A. E., Kollmeier J. A., Reddy N. A., Erb D. K., Pettini M., 2011, ApJ, 736, 160

Stewart M., Federrath C., 2022, MNRAS, 509, 5237

Stockton A., MacKenty J. W., 1987, ApJ, 316, 584

Strom A. L., Steidel C. C., Rudie G. C., Trainor R. F., Pettini M., Reddy N. A., 2017, ApJ, 836, 164

Sun A.-L., Greene J. E., Zakamska N. L., 2017, ApJ, 835, 222

Swinbank A. M., Bower R. G., Smith G. P., Wilman R. J., Smail I., Ellis R. S., Morris S. L., Kneib J. P., 2007, MNRAS, 376, 479

Tacconi L. J., et al., 2018, ApJ, 853, 179

Trainor R. F., Steidel C. C., 2012, ApJ, 752, 39

Tumlinson J., Peeples M. S., Werk J. K., 2017, ARA&A, 55, 389

Umetsu K., et al., 2012, ApJ, 755, 56

Vanzella E., et al., 2010, ApJ, 725, 1011

Vanzella E., et al., 2017, MNRAS, 465, 3803

Veilleux S., et al., 2023, ApJ, 953, 56

Venturi G., et al., 2023, arXiv e-prints, p. arXiv:2309.02498

Verhamme A., Schaerer D., Maselli A., 2006, A&A, 460, 397

Verhamme A., Schaerer D., Atek H., Tapken C., 2008, A&A, 491, 89

Voges W., et al., 1999, A&A, 349, 389

Voit G. M., Meece G., Li Y., O'Shea B. W., Bryan G. L., Donahue M., 2017, ApJ, 845, 80

Vossberg A.-C. E., Cantalupo S., Pezzulli G., 2019, MNRAS, 489, 2130

Weilbacher P. M., et al., 2020, A&A, 641, A28

Weiner B. J., et al., 2009, ApJ, 692, 187

Wen Z., O'dell C. R., 1993, ApJ, 409, 262

Whitaker K. E., van Dokkum P. G., Brammer G., Franx M., 2012, ApJL, 754, L29

Wisnioski E., et al., 2015, ApJ, 799, 209

Wisotzki L., et al., 2016, A&A, 587, A98

Wisotzki L., et al., 2018, Nature, 562, 229

Wylezalek D., et al., 2022, ApJL, 940, L7

Xie C., Haffert S. Y., de Boer J., Kenworthy M. A., Brinchmann J., Girard J., Snellen
   I. A. G., Keller C. U., 2020, A&A, 644, A149

Xu S., 2020, MNRAS, 492, 1044

Xue R., et al., 2017, ApJ, 837, 172

Yang H. Y. K., Reynolds C. S., 2016, ApJ, 829, 90

Yang H., et al., 2017, ApJ, 844, 171

Zahedy F. S., Chen H.-W., Rauch M., Wilson M. L., Zabludoff A., 2016, MNRAS, 458, 2423

Zahedy F. S., Chen H.-W., Johnson S. D., Pierce R. M., Rauch M., Huang Y.-H., Weiner B. J., Gauthier J.-R., 2019, MNRAS, 484, 2257

Zahedy F. S., et al., 2021, MNRAS, 506, 877

Zhang C., Zhuravleva I., Gendron-Marsolais M.-L., Churazov E., Schekochihin A. A., Forman W. R., 2022, arXiv e-prints, p. arXiv:2203.04259

Zhuravleva I., et al., 2014, Nature, 515, 85

Zitrin A., et al., 2012, ApJ, 749, 97

ZuHone J. A., Markevitch M., Zhuravleva I., 2016, ApJ, 817, 110

van de Voort F., 2017, in Fox A., Davé R., eds, Astrophysics and Space Science Library Vol. 430, Gas Accretion onto Galaxies. p. 301 (arXiv:1612.00591), doi:10.1007/978-3-319-52512-9_13

von Hoerner S., 1951, ZAp, 30, 17